Magnetite–melt oxybarometry

Dissertation

zur Erlangung der Würde eines

Doktors der Naturwissenschaften

- Dr. rer. nat. -

der Bayreuther Graduiertenschule für Mathematik und Naturwissenschaften

vorgelegt von

Róbert Arató

aus Moskau

Bayreuth, 2017

Table of contents

Abstract

The oxidation state of magmas is a parameter of prime importance in magmatic processes. Despite various existing techniques its reconstruction remains a challenging task, particularly in the case of intrusive rocks. This is because in such rocks the mineral phases that are sensitive to oxygen fugacity were either destroyed or reset at subsolidus conditions, such that accurate estimation of magmatic fO$_2$ is not possible. Thus, the aim of this study is to develop and apply new proxies for magmatic oxidation state (i.e. oxybarometers) that can be used also in rocks that were affected by postmagmatic alteration processes. In this thesis two such independent methods are presented that are based (i) on the partitioning of vanadium, as well as (ii) the exchange of iron and titanium between magnetite and silicate melt. The thesis includes their experimental calibration as well as their first application to natural rocks.

In order to calibrate the new oxybarometers a series of experiments were carried out at varying oxygen fugacities (0.7-4.0 log units above the fayalite-magnetite-quartz buffer), temperatures (800-1000 °C), melt alumina saturation indices (ASI=0.74-1.14), magnetite composition (0.2-14 wt% TiO$_2$) and pressure (1-5 kbar; at H$_2$O saturation). The experiments were performed by equilibrating small ($\leq$20 µm), V-free magnetite grains in V-doped silicate melts (~100 ppm V). Both phases were analyzed by LA-ICP-MS and partition coefficients of vanadium as well as exchange coefficients of Fe and Ti were obtained between magnetite and silicate melt. Attainment of equilibrium was demonstrated by reverse experiments.

The experimental results suggest that D$_V$$^{mgt/melt}$ depends strongly on oxygen fugacity, to a smaller (but still considerable) degree on melt alumina saturation index and temperature. In contrast, magnetite composition and melt water content seem to have negligible effects on vanadium partitioning. Thus, D$_V$$^{mgt/melt}$ can be expressed as a function of oxygen fugacity, temperature and melt composition in the form of a simple equation. This equation reproduces all our experimental D$_V$$^{mgt/melt}$ values within 0.3 log units, and 89% of them within 0.15 log units.

The experimentally calibrated vanadium partitioning oxybarometer was applied to a series of natural rhyolites and dacites. The investigated samples included vitrophyres and holocrystalline rocks in which part of the mineral- and melt assemblage was preserved only as inclusions within phenocrysts. An independent fO$_2$ constraint for vanadium magnetite–melt oxybarometry was obtained via Fe–Ti-oxide oxybarometry, whereas temperature was constrained by zircon saturation thermometry, two-feldspar thermometry and Fe–Ti-oxide thermometry. All analyses

were conducted by laser-ablation ICP-MS. In most of the samples the fO$_2$ values determined via vanadium magnetite–melt oxybarometry agree within 0.5 log units with the oxygen fugacity calculated from Fe-Ti-oxide pairs, except for a few cases where the larger discrepancy can be explained by magma mixing processes. The fO$_2$ value obtained by vanadium partitioning depends significantly on the applied thermometer. Temperatures based on zircon saturation thermometry and two-feldspar thermometry usually agreed within the limits of uncertainty, whereas temperatures obtained via Fe–Ti-oxide thermometry commonly deviated by $\geq$50 °C due to large uncertainties associated with the Fe-Ti-oxide model at T-fO$_2$ conditions typical of most silicic magmas. Therefore, the former two methods are recommended to constrain temperature for vanadium partitioning oxybarometry. The main advantages of this new oxybarometer over classical magnetite–ilmenite oxybarometry are (1) that it can be applied to rocks that do not contain ilmenite, and (2) that it is easier to apply to slowly-cooled rocks such as granites by measuring magnetite-melt pairs in form of inclusions.

Our experimental data was extended by experimental magnetite- and ilmenite-bearing samples from the literature, covering a wide range of oxygen fugacities, temperatures, pressures and silicate melts ranging from basaltic to rhyolitic in composition. Using this extended dataset a further oxybarometer could be calibrated that is based on the partitioning of Fe and Ti between magnetite and melt (i.e. the Fe–Ti exchange coefficient) and is therefore named FeTiMM. In the case of FeTiMM oxygen fugacity was shown to depend solely on the Fe–Ti exchange coefficient and melt composition. The fitting equation based on these two variables yielded fO$_2$ values that mostly agree within 0.5 log units with the fO$_2$, independently constrained by Fe–Ti-oxide oxybarometry, the performance of FeTiMM being similarly good on felsic, mafic and intermediate melts. A first test of the method on natural samples of dacitic to rhyolitic compositions yielded consistent results with Fe–Ti oxide oxybarometry and vanadium partitioning oxybarometry alike. FeTiMM thus opens the door for numerous new applications in various disciplines of Earth Sciences, including the fields of volcanology, igneous petrology, experimental geochemistry, and ore geology. The main advantages of FeTiMM are (1) that it is applicable to both ilmenite-free and ilmenite-bearing samples (2) that it can be applied even to slowly-cooled intrusive rocks such as granites (3) that it is temperature-independent and (4) that it is calibrated to and is therefore applicable to a broad range of melt compositions, spanning the entire range from basalts to rhyolites.

Zusammenfassung

Der Oxidationszustand von Magmas ist ein Parameter von grundlegender Bedeutung in magmatischen Prozessen. Trotz verschiedener existierenden Techniken bleibt die Rekonstruktion von magmatischem fO$_2$ eine herausfordernde Aufgabe, vor allem bei intrusiven Gesteinen. In solchen Gesteinen wurden die Mineralphasen, die empfindlich für Sauerstofffugazität sind, entweder zerstört oder unter Subsolidus-Bedingungen umgewandelt, so dass eine genaue Schätzung des magmatischen fO$_2$ nicht mehr möglich ist. Das Ziel dieser Studie ist, neue Proxies für den magmatischen Oxidationszustand (d.h. Oxybarometer) zu entwickeln und in der Praxis in Gesteinen anzuwenden, welche von postmagmatischen Veränderungsprozessen betroffen sind. In dieser Arbeit werden zwei derartige unabhängige Methoden vorgestellt, die (i) auf der Verteilung von Vanadium sowie (ii) dem Austausch von Eisen und Titan zwischen Magnetit und Silikatschmelze beruhen. Die Arbeit umfasst sowohl ihre experimentelle Kalibrierung als auch ihre erste Anwendung auf natürlichen Gesteinen.

Um die neuen Oxybarometer zu kalibrieren, wurde eine Reihe von Experimenten bei unterschiedlichen Sauerstofffugazitäten (0,7-4,0 Log-Einheiten oberhalb des Fayalit-Magnetit-Quarz-Puffers), Temperaturen (800-1000 ° C), Aluminium-Sättigungsindices (ASI = 0,74-1,14), Magnetitzusammensetzungen (0,2-14 Gew.% TiO$_2$) und Drücken (1-5 kbar, bei H$_2$O-Sättigung) ausgeführt. Die Experimente wurden durch Äquilibrieren von kleinen ($\leq$ 20 μm), V-freien Magnetitkristallen in V-gedopten Silikatschmelzen ($\sim$ 100 ppm V) durchgeführt. Beide Phasen wurden mittels LA-ICP-MS analysiert, und es wurden Verteilungskoeffizienten von Vanadium sowie Austauschkoeffizienten von Fe und Ti zwischen Magnetit und Silikatschmelze berechnet. Die Erreichung des Gleichgewichts wurde durch reverse Experimente nachgewiesen.

Die experimentellen Ergebnisse deuten darauf hin, dass D$_V$$^{Mgt/Schmelze}$ stark von der Sauerstofffugazität und zu einem kleineren Grad vom Aluminium-Sättigungsindex und der Temperatur abhängt. Im Gegensatz dazu scheinen die Magnetitzusammensetzung und der Wassergehalt der Schmelze einen vernachlässigbaren Effekt auf die Vanadiumverteilung zu haben. So kann D$_V$$^{Mgt/Schmelze}$ als Funktion der Sauerstofffugazität, Temperatur und Schmelzzusammensetzung in Form einer einfachen Gleichung ausgedrückt werden. Diese Gleichung reproduziert alle unsere experimentellen D$_V$$^{Mgt/Schmelze}$ Werte innerhalb von 0,3 Log-Einheiten und 89% davon innerhalb von 0,15 Log-Einheiten.

Das experimentell kalibrierte Vanadiumverteilungsoxybarometer wurde auf eine Reihe von natürlichen Rhyoliten und Daziten angewandt. Die untersuchten Proben waren Vitrophyre und holokristalline Gesteine, in welchen ein Teil der Minerale und die Schmelze nur in Form von Einschlüssen in den Phänokristallen erhalten blieben. Ein unabhängiger fO$_2$-Vergleichswert für die Vanadium-Magnetit-Schmelze-Oxybarometrie wurde mittels Fe–Ti-Oxidoxybarometrie erhalten, während die Temperatur durch Zirkonsättigungs-Thermometrie, Zwei-Feldspat-Thermometrie und Fe–Ti-Oxidthermometrie bestimmt wurde. Alle Analysen wurden mithilfe von Laser-Ablations ICP-MS durchgeführt. In den meisten Proben stimmen die durch Vanadium-Magnetit-Schmelz-Oxybarometrie erhaltenen fO$_2$-Werte innerhalb von 0,5 Log-Einheiten mit der aus Fe–Ti-Oxidpaaren berechneten Sauerstofffugazität überein, mit Ausnahme einiger Proben, in denen eine größere Diskrepanz durch Magmamischung erklärt werden kann. Der durch Vanadiumverteilung erhaltene fO$_2$-Wert hängt wesentlich von dem angewandten Thermometer ab. Die Temperaturen, die auf Zirkonsättigungs-Thermometrie und Zwei-Feldspat-Thermometrie basieren, stimmen in der Regel innerhalb der Grenzen der Unsicherheit überein, während die durch Fe–Ti-Oxidthermometrie erhaltenen Temperaturen aufgrund von großen Unsicherheiten, die mit dem Fe–Ti-Oxidmodell verbunden sind, üblicherweise um $\geq 50\,°$C von jenen abweichen. Daher werden die ersten beiden Methoden empfohlen, um die Temperatur für das Vanadiumverteilungs-Oxybarometer zu bestimmen. Die Hauptvorteile dieses neuen Oxybarometers im Vergleich zu klassischer Magnetit–ilmenit-Oxybarometrie sind (1), dass es bei solchen Gesteinen angewendet werden kann, die keinen Ilmenit enthalten, und (2) dass es einfacher ist, die Methode auf langsam auskristallisierte Gesteine wie Granite mittels Messung von Magnetiteinschluss-Schmelzeinschluss-Paaren anzuwenden.

Unsere experimentellen Daten wurden durch experimentelle Magnetit- und Ilmenit-haltige Proben aus der Literatur erweitert, die eine breite Palette von Sauerstofffugazitäten, Temperaturen, Drücken und Schmelzzusammensetzungen abdecken. Durch die Verwendung dieses erweiterten Datensatzes konnte ein weiteres Oxybarometer kalibriert werden, welches auf der Verteilung von Fe und Ti zwischen Magnetit und Schmelze (d.h. dem Fe–Ti-Austauschkoeffizienten) basiert und daher FeTiMM genannt wird. Im Falle von FeTiMM zeigte sich, dass Sauerstofffugazität sich allein durch den Fe–Ti-Austauschkoeffizienten und die Schmelzzusammensetzung beschreiben lässt. Die Regressionsgleichung, die auf diesen beiden Variablen basiert, ergab fO$_2$ Werte, die meistens innerhalb von 0,5 log-Einheiten mit den fO$_2$

Werten übereinstimmen, die mittels Fe–Ti-Oxid-Oxybarometrie ausgerechnet wurden. Außerdem ist die Übereinstimmung bei felsischen, mafischen und intermediären Schmelzen ähnlich gut. Der erste Test der Methode auf natürlichen Proben von dazitischen bis rhyolitischen Zusammensetzungen lieferte konsistente Ergebnisse im Vergleich zu Fe–Ti-Oxid-Oxybarometrie und Vanadiumverteilungs-Oxybarometrie. FeTiMM eröffnet somit zahlreiche neue Anwendungen in verschiedenen Disziplinen der Geowissenschaften, einschließlich der Vulkanologie, der magmatischen Petrologie, der experimentellen Geochemie und der Erzlagerstättenkunde. Die Hauptvorteile von FeTiMM sind (1), dass es sowohl auf ilmenitfreie als auch auf ilmenithaltige Proben anwendbar ist, (2) dass es auch auf langsam gekühlte intrusive Gesteine wie Granite angewendet werden kann, (3) dass es temperaturunabhängig ist und (4) dass es für eine breite Palette von Schmelzzusammensetzungen (von Basalten bis zu Rhyoliten) kalibriert und daher anwendbar ist.

1 Introduction

1.1 The scope of this thesis

Magmatic oxidation state exerts a first order control over magmatic processes. It affects the stability and composition of mafic minerals, the solubility of various volatiles in the magma and also the mineral-melt and the fluid-melt partitioning of various metals. These processes have a strong influence on the mineralizing potential of intrusions; therefore measuring magmatic oxidation state, expressed as oxygen fugacity (fO$_2$), is essential for understanding ore formation. Since the landmark contribution of Ishihara (1977) ore geologists try to distinguish oxidized and reduced granites based on their Fe–Ti oxide content, and a large quantity of papers aimed at relating specific types of ore deposits to oxidized or reduced sources. However, it is often extremely difficult or even impossible to reconstruct fO$_2$ by the currently available methods, especially in the case of intrusive and/or mineralized rocks. Most oxybarometers such as the ones based on Fe–Ti oxides are prone to resetting during slow cooling, whereas empirical redox indicators such as the whole rock Fe(III)/Fe(II) ratio or the presence of anhydrite rarely survive processes of hydrothermal alteration and surficial weathering (Ballard et al., 2002), meaning that their composition does not reflect magmatic conditions anymore. Following the assumption that the partitioning of multivalent elements such as Fe or V between magnetite and melt is sensitive to fO$_2$, we calibrated two oxybarometers experimentally. The ultimate goal of these calibrations was to apply a novel approach that is based on the measurement of natural melt inclusions and magnetite inclusions that were preserved within phenocrysts (e.g. quartz) and thus were protected from subsolidus and hydrothermal alteration. In this way the oxidation state of the above-mentioned "problematic" rocks, comprising many magmatic ore deposits should become accessible.

1.2 The definition of oxygen fugacity and its experimental control

For each substance, the Gibbs free energy G is a function of pressure and temperature:

$$dG = -SdT + VdP \quad (1.1)$$

Where S, T, V and P refer to entropy, temperature, volume and pressure, respectively. At constant temperature, equation 1.1 reduces to:

$$dG = VdP \quad (1.2)$$

8

By integrating equation (1.2) and using the ideal gas law PV=nRT we get:

$$G(P) - G(P_0) = \int_{P_0}^{P} V dP = nRT \int_{P_0}^{P} \frac{1}{P} dP \quad (1.3)$$

and

$$G(P) = G(P_0) + nRT \ln \left(\frac{P}{P^0} \right) \quad (1.4)$$

Where R is the gas constant, T is the temperature in Kelvin and P^0 denotes pressure at standard state (1 bar). However, $\int_{P_0}^{P} V dP$ can only be evaluated for ideal gases. Therefore, a hypothetical pressure – fugacity (f) – is introduced, on which the Gibbs free energy depends in the same way as on the pressure of an ideal gas:

$$G(P) = G(P_0) + nRT \ln \left(\frac{f}{f^0} \right) \quad (1.5)$$

Where f_0 denotes fugacity at standard state (1 bar). Since the activity of component "i" in a mixture is $a_i = \frac{f_i}{f_i^0}$, activity is dimensionless and can be defined as relative to the standard state, whereas fugacity has an absolute value and units of pressure.

Apart from its standard definition as a thermodynamic parameter, oxygen fugacity in geological systems can be described as the potential of multivalent elements to occur in their oxidized or reduced state. In other words, it is a measure of the free energy change between the "oxidized" and the "reduced portions" of an assemblage in a rock or in the buffer capsule (Frost, 1991), as shown in the following example by Frost (1991):

$$2Fe_3O_4 + 3SiO_2 = 3Fe_2SiO_4 + O_2 \quad (1.6)$$
$$\text{magnetite} \qquad \qquad \text{fayalite}$$
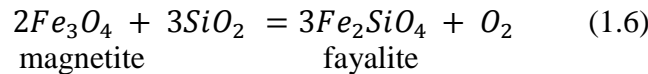
The equilibrium constant of the above equation is the following:

$$K = \frac{(a_{fay})^3 * (a_{O_2})}{(a_{SiO_2})^3 * (a_{mt})^2} \quad (1.7)$$

Where a_i denotes the activity coefficient of component i. Considering pure fayalite, SiO_2 and magnetite (i.e. $a_i=1$) the above equation reduces to:

$$K = a_{O_2} = \frac{fO_2}{fO_2^0} = fO_2 \quad (1.8)$$

Where fO_2^0 marks the standard state oxygen fugacity that equals unity. Since:

$$\log K = \frac{-\Delta G_{FMQ}^0}{2.303 * R * T} \quad (1.9)$$

Then:

$$logfO_2 = \frac{-\Delta G^0_{FMQ}}{2.303*R*T} \quad (1.10)$$

Where ΔG^0_{FMQ} is the standard state Gibbs free energy change of reaction (1.6).

Since the pioneering works of Eugster (1957 and 1959) experimental oxygen fugacity is most commonly controlled by solid-state buffers in double capsule assemblages. In these assemblages fO_2 is imposed by the reaction of two or more solid phases (e.g. fayalite-magnetite-quartz, Ni-NiO, MnO-Mn$_3$O$_4$). Such oxygen controlling equilibria are called fO_2 buffers (Fig. 1.1).
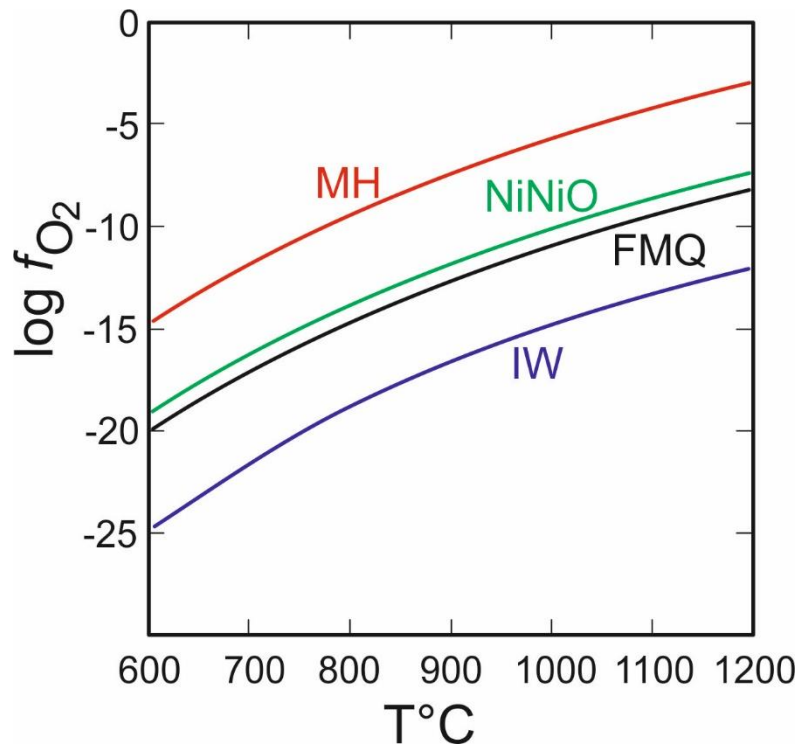
Fig. 1.1 Log oxygen fugacity vs temperature at 1 bar pressure for common buffer assemblages (modified after Frost, 1991). MH = magnetite–hematite buffer, NiNiO = nickel–nickel oxide buffer, FMQ = fayalite–magnetite–quartz buffer, IW= iron–wüstite buffer.

In fO_2-buffered experiments the experimental starting material plus H$_2$O is placed in a H$_2$-permeable (e.g. AuPd) inner capsule that is surrounded by a water-bearing buffer and a less H$_2$-permeable outer capsule (e.g. Au). At experimental p-T conditions H$_2$O dissociates and fO_2 is set in the inner capsule via H$_2$ diffusion. Since oxygen fugacity strongly increases with increasing temperature (Fig. 1.1), it is often expressed as relative to one of the fO_2 buffers. The most commonly used "reference" buffer is the fayalite-magnetite-quartz (FMQ) assemblage, as most igneous rocks formed at oxygen fugacities within a few log units below and above FMQ (Haggerty, 1976).

1.3   Importance of oxygen fugacity in geological systems

1.3.1   *Effect of fO$_2$ on mineral stability*

The control of oxygen fugacity over mineral stability and thus its prime petrological importance has been demonstrated by many authors. Eugster's study (1957) carried the first experimental evidence that some mineral phases are only stable at reduced conditions, whereas others are stable only at oxidized conditions. Some years later Buddington and Lindsley (1964) investigated the effect of oxygen fugacity on the stability of the mineral phases in the FeO-Fe$_2$O$_3$-TiO$_2$ system and found that the composition of the magnetite-ulvöspinel and hematite-ilmenite solid solution series also strongly depends on oxygen fugacity. This pioneering study and a series of subsequent publications (e.g. Carmichael 1967; Stormer 1983; Andersen and Lindsley 1988; Ghiorso and Sack 1991; Lattard et al. 2005; Ghiorso and Evans 2008) form the base of the – until now – most widely used oxybarometer and thermometer, the magnetite–ilmenite method. The stability of mafic minerals including ferromagnesian silicates and oxides was extensively studied by Frost et al. (1988) who calibrated the so called QUILF method based on the fO_2-dependent reaction between quartz, ulvöspinel, ilmenite and fayalite. This method was later further developed (Frost and Lindsley, 1992; Lindsley and Frost, 1992; Andersen et al. 1993) and also applied as an oxybarometer.

Caroll and Rutherford (1985) showed that fO_2 also plays a crucial role in stabilizing different magmatic sulphur-bearing phases, with the occurrence of magmatic anhydrite at high fO_2 and the stability of pyrrhotite at more reducing conditions. This work was also followed by numerous publications (e.g. Luhr et al. 1990; Luhr, 2008; Audétat et al., 2011; Masotta and Keppler, 2015), which further demonstrated the importance of fO_2 in mineral stability studies.

1.3.2   *Effect of fO$_2$ on element partitioning*

The influence of oxygen fugacity in magmatic systems is not restricted to mineral stability. It also affects the solubility and fluid–melt partition coefficients of volatiles as well as the mineral–melt and fluid–melt partition coefficients of various metals that are again interrelated with the above-mentioned mineral stabilities. In silicate melts sulphur is dissolved either as S^{2-} or S^{6+} or a combination of both, depending on magmatic oxygen fugacity (Carroll and Rutherford, 1988). Jugo et al. (2010) showed that the S^{2-} to S^{6+} (sulphide to sulphate) transition takes place in a relatively narrow fO_2 range causing an abrupt increase in sulphur solubility in melts around

FMQ+1. Oxygen fugacity was also shown to strongly affect the fluid-melt partitioning of S, reaching its highest values at low fO$_2$ (Keppler, 2010). Similarly to sulphur, the solubility of nitrogen is also dependent on oxygen fugacity, decreasing strongly with increasing fO$_2$ roughly until the IW buffer where the solubility mechanism changes from chemical (nitrogen dissolved as N^{3-} or NH_3) to physical (nitrogen dissolved as N_2) and the fO$_2$-dependence diminishes (Libourel et al., 2003).

Magmatic oxygen fugacity also significantly influences the sulfide-melt partitioning of many metals at upper mantle (Li and Audétat, 2012) and crustal conditions (Li and Audétat, 2015). Li and Audétat (2012) found that the sulfide-basanite melt partition coefficient of Mo, As and Bi decreases by more than an order of magnitude as fO$_2$ increases from FMQ-3.1 to FMQ+1. A subsequent study (Li and Audétat, 2015) showed similar trends for sulfide-silicate melt partitioning with increasing fO$_2$, with the strongest decrease observed in the case of Mo, Au and Bi (±As).

Although not directly relevant for this study, the solubility and the partitioning of a series of metals was shown to be dependent on the magmatic oxidation state that places important constraints on metal partitioning between different reservoirs of the Earth, especially between the core and the mantle. The explanation for the oxygen fugacity dependence of metal solubility is that all metals are dissolved as ions in silicate melts. Thus, the transition of a neutral atom (e.g. from an alloy) to the silicate melt is accompanied by oxidation according to the following equation (Borisov and Palme, 2000):

$$M + (m/4) \cdot O_2 = MO_{m/2} \text{ (silicate)} \qquad (1.11)$$
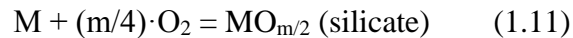
where m is the valence of the metal ion. The equilibrium constant of Equation 1.11 can be written up as $K1 = a_{MO_{m/2}}/[a_M \cdot (f O_2)^{m/4}]$, meaning that the fO$_2$ dependence of a metal's solubility is defined by the valence state of the metal dissolved in the silicate melt (Fig. 1.2). Accordingly, the solubility of noble metals, such as Pd, Au and Ir (Borisov and Palme, 2000) in silicate melt is the least fO$_2$ dependent, whereas Ni and Co solubility (Holzheid et al., 1994) shows steeper slopes on the fO$_2$-solubility plot. Stronger oxygen fugacity dependence was observed in the case of Pt, Ru (Borisov and Palme, 2000), and Os (Fortenfant et al., 2006), and even stronger in the case of Mo, the solubility of which increases by ca. four orders of magnitude as fO$_2$ increases by three log units (Holzheid et al., 1994).
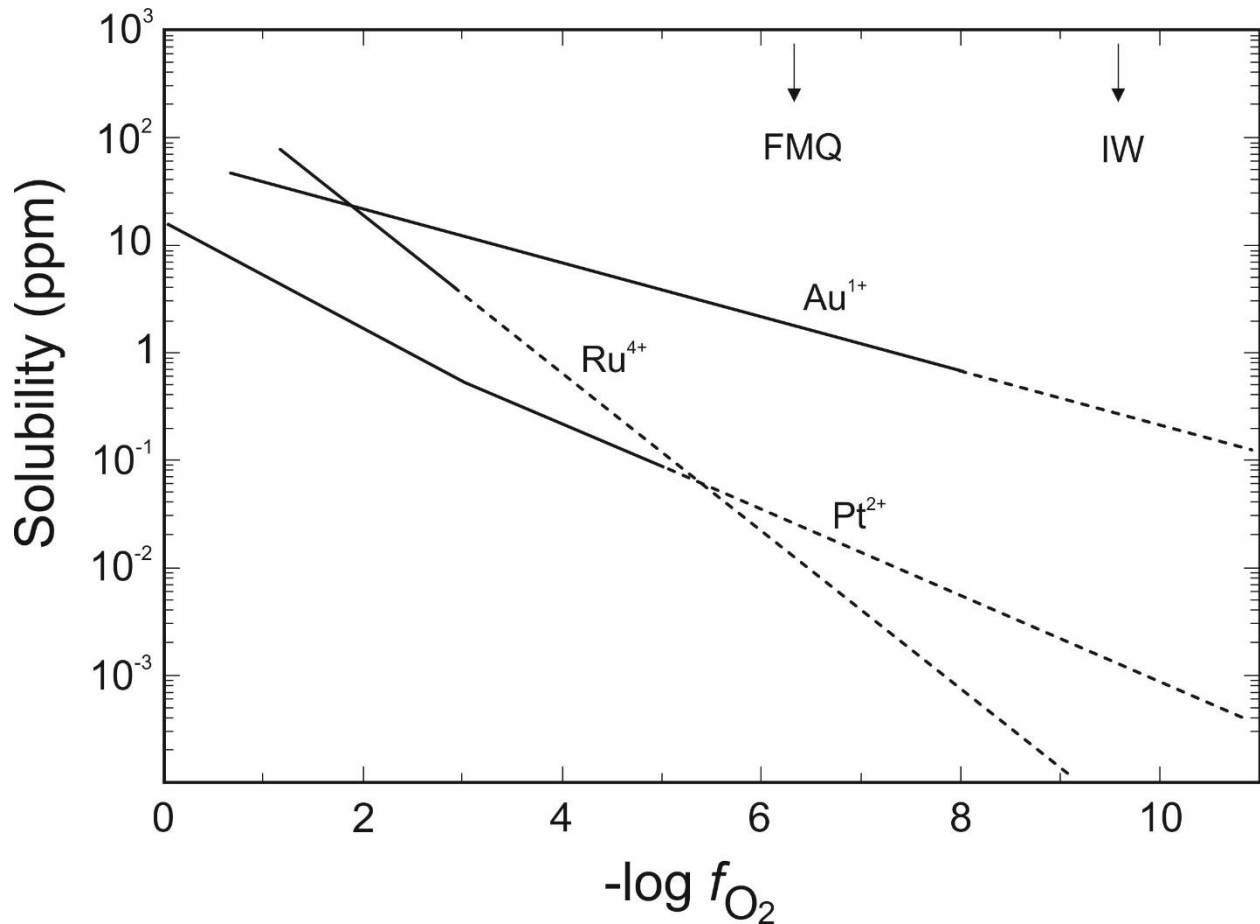
Fig. 1.2 Dependence of noble metal solubilities in an anorthite-diopside eutectic melt on oxygen fugacity (modified after Borisov and Palme, 2000) recalculated to 1400 °C. Solid lines = experimental range, dashed lines = extrapolation. Note the different slopes related to different valence states.

1.3.3 *Effect of fO₂ on ore genesis*

Directly or indirectly related to solubility and partitioning studies, oxygen fugacity was found to exert a strong control over the formation of magmatic ore deposits. A landmark paper of Ishihara (1977) categorized the granitoids of Japan according to their dominant Fe–Ti oxide phase into magnetite-series and ilmenite-series rocks. Based on the characteristic mineral assemblages of the two series Ishihara assumed that magnetite-series rocks are generally more oxidized than ilmenite-series rocks, the fO_2 boundary between the two groups being around the Ni-NiO buffer. Ishihara also found that magnetite-series rocks usually carry porphyry copper-molybdenum deposits whereas the ilmenite-series are usually associated with greisen-type tin-wolframite deposits. In agreement with Ishihara (1977), Lehmann (1990) pointed out that the significant Sn deposits are almost exclusively related to such granites that were categorized as "reduced" based on their Fe^{3+}/Fe^{2+} ratios. This is related to the fact that tin can occur as Sn^{2+} and Sn^{4+} in the melt

13

(Linnen et al., 1996), the latter of which is preferentially incorporated into the mineral phases in granites, whereas the former tends to remain in the melt (Taylor and Wall, 1992 and references therein). This results in a bulk $D_{Sn}^{mineral/melt}<1$ at low fO_2 and thus the enrichment of Sn in evolved melts.

In contrast to tin deposits, more oxidized melts seem to favor the formation of porphyry Mo and Cu deposits. The oxidized nature of Mo-rich deposits was also supported by Candela and Bouton (1990) who showed experimentally and on natural granite-related deposits that magmatic systems with high W/Mo ratios in the silicate melt develop at reduced conditions, whereas high Mo/W ratios are characteristic for oxidized systems. High magmatic fO_2 values (>FMQ+1.5) were also reported from porphyry Mo deposits by Audétat et al. (2011), Audétat (2015) and also by Audétat and Li (2017). Other studies (e.g. Candela 1992; Blevin and Chappell 1992; Hedenquist and Lowenstern, 1994) revealed that magmatic-hydrothermal Cu deposits are usually also related to oxidized calc-alkaline intrusions. This suggested a genetic link between the speciation and solubility of magmatic sulphur (and its influence on the fractionation of chalcophile elements) and processes leading to Cu mineralization. Ballard et al. (2002) showed on a series of ore-bearing and barren intrusions that the Cu±Au deposits are related to the occurences with high zircon Ce^{4+}/Ce^{3+} ratios and therefore to oxidized magmas. According to their interpretation, low magmatic fO_2 leads to early sulphide saturation and the sequestration of sulphides into cumulates and consequently the depletion of Cu in more evolved melts. On the other hand, above ca. FMQ+1 sulphur is present as sulphate in the melt and so chalcophile elements become enriched in the later stages of magma evolution where they tend to partition into hydrothermal fluids. The generally oxidized nature of Cu-bearing calc-alkaline intrusions is also supported by the occurrence of magmatic anhydrite (e.g. Lickfold et al., 2002; Audétat et al., 2004; Stern et al., 2007) at several porphyry copper systems.

Although the compilation of the above-mentioned studies seems to reflect a consistent picture about ore deposit type − magmatic oxidation state relationships, the reader has to bear in mind that magmatic fO_2 of intrusive rocks cannot be measured by currently existing methods and therefore the oxidation state cannot be interpreted in most of the mineralized systems due to the problems described in Section 1.1.

1.4 Magmatic oxybarometers

As described in the previous section, oxygen fugacity is a crucial parameter in magmatic processes. Therefore, it is essential to constrain fO_2 in order to unravel magmatic evolution histories. Methods that were developed with the aim to reconstruct magmatic fO_2 (i.e. oxybarometers) are based on various principles. A group of them is based on mineral equilibria, the most commonly used ones being magnetite–ilmenite oxybarometry (e.g. Buddington and Lindsley, 1964; Carmichael, 1967; Stormer, 1983; Andersen and Lindsley, 1988; Ghiorso and Sack, 1991; Lattard et al., 2005; Ghiorso and Evans, 2008) and the so called QUILF method (Frost and Lindsley, 1992; Lindsley and Frost, 1992; Andersen et al., 1993; Xirouchakis et al., 2001). Other mineral stability/equilibria-based oxybarometers focus on biotite, amphibole, K-feldspar and magnetite (Wones and Eugster, 1965; Wones, 1981), or single-amphibole composition (Ridolfi et al., 2010). Alternative approaches are based on the Fe^{2+}/Fe^{3+} ratio of whole-rocks (Kress and Carmichael, 1989; Putirka, 2016) and Ce anomaly in zircon (Ballard et al., 2002; Trail et al., 2012; Smythe and Brenan, 2016).

1.4.1 Oxybarometers related to Fe–Ti oxides

By far the most commonly used oxybarometer in crustal rocks is based on the equilibrium composition of Fe–Ti oxides. The compositional sensitivity of the magnetite-ulvöspinel solid solution coexisting with the hematite-ilmenite solid solution (Fig. 1.3) to temperature and oxygen fugacity was first demonstrated in the 60's.
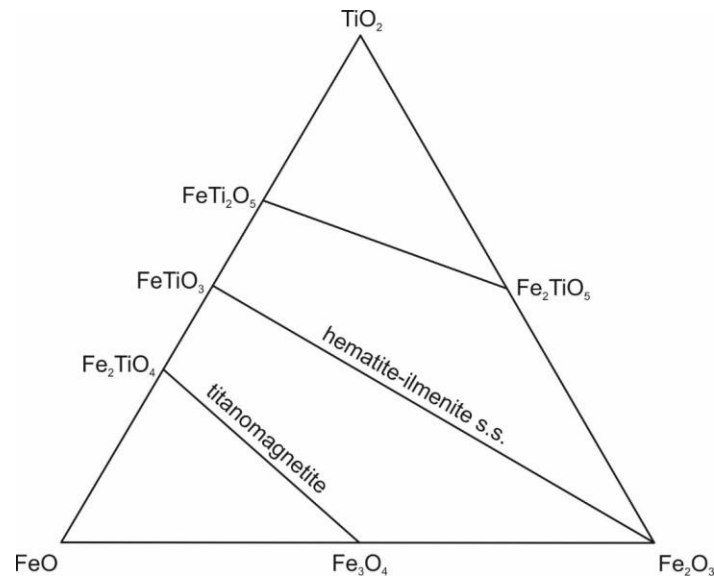
Fig. 1.3 Phases in the system $FeO-Fe_2O_3-TiO_2$, showing the major solid solution series magnetite-ulvöspinel, hematite-ilmenite, and pseudobrookite-$FeTi_2O_6$ in mole percent (modified after Buddington and Lindsley, 1964).

Buddington and Lindsley (1964) experimentally determined the compositions of coexisting Fe–Ti oxides for a wide range of temperatures and oxygen fugacities and applied the experimental calibration to various natural magmatic and metamorphic rocks. They demonstrated that stable Fe–Ti oxide pairs occur according to the following evolution sequence with increasing intensity of oxidation state: ulvöspinel-rich magnetite$_{ss}$+ilmenite$_{ss}$, ulvöspinel-poor magnetite$_{ss}$+ ilmenite$_{ss}$, ulvöspinel-poor magnetite$_{ss}$+ hematite$_{ss}$, hematite$_{ss}$+rutile, where $_{ss}$ refers to solid solution. The authors of that study already pointed out that Fe–Ti oxides commonly show subsolidus re-equilibration features, which preclude the estimation of magmatic fO$_2$ using Fe–Ti oxide phenocrysts in slowly-cooled rocks. Subsequently, Carmichael (1967) successfully applied the magnetite–ilmenite oxybarometer (and thermometer) to a series of SiO$_2$-rich volcanic rocks and also found consistent relationships between fO$_2$ and the stability of ferromagnesian silicates. However, he observed that in some rocks multiple generations of Fe–Ti oxides appear, some of which probably did not form in equilibrium with the others. The equilibrium test for magnetite–ilmenite pairs was later provided by Bacon and Hirschmann (1988), using the Mg/Mn ratio of both oxide phases in order to distinguish between equilibrium and non-equilibrium pairs. A corresponding thermodynamic model for the Fe–Ti oxide thermometer/oxybarometer was developed by Andersen and Lindsley (1985, 1988) as well as by Ghiorso and Sack (1991) and Ghiorso and Evans (2008). The most commonly used calibrations are that of Andersen and Lindsley (1985) and Ghiorso and Evans (2008), yielding often significantly different values especially in terms of temperature. Several factors are responsible for this discrepancy. First, the model of Ghiorso and Evans (2008) is based on a more extensive data set of two-oxide phase equilibria that covers a broad range of experimental conditions between 800 °C and 1300 °C, and between NNO–3 and NNO+3. Second, the model of Ghiorso and Evans (2008) accounts for the configurational entropy changes related to both the short-range cation order and the $R\bar{3}$-$R\bar{3}c$ order-disorder transition of the rhombohedral phase, whereas the model of Andersen and Lindsley (1985) does not. These modifications result in differences in fO$_2$ and T estimation since the latter model assumes an ordered $R\bar{3}$ structure for the hematite-ilmenite solid solution. This, however, is not accurate at oxygen fugacities above NNO+1 and at temperatures of 700-900 °C where ilmenite has a cation-disordered structure. Therefore, the model of Ghiorso and Evans (2008) provides a more reliable estimate of fO$_2$ at conditions typical for many natural silicic magmas.

The study of Ghiorso and Evans (2008) also shows that the temperature estimates based on magnetite–ilmenite pairs have significantly larger uncertainties at oxidized conditions, whereas oxygen fugacity can be accurately constrained throughout the whole temperature range, making Fe–Ti oxides an excellent indicator of the oxidation state provided that they are unaltered and in equilibrium with each other.

As demonstrated by Carmichael (1967), the stability and composition of ferromagnesian silicates depends on fO_2 and T. Following up on that, Frost et al. (1988) showed that in Fe-rich metamorphic and highly evolved igneous rocks where fayalite can coexist with quartz and Fe–Ti oxides the uncertainty of the oxide-based fO_2 and T estimate can be reduced by an order of magnitude using the following equilibrium reaction:

$$SiO_2(qtz) + 2Fe_2TiO_4(usp) = 2FeTiO_3(ilm) + Fe_2SiO_4(fay) \qquad (1.12)$$

Rocks that contain all four minerals are scarce, however, subsequent studies (e.g. Frost and Lindsley, 1992; Lindsley and Frost, 1992) extended the calibration of QUILF by several equilibria involving augite, pigeonite and orthopyroxene in the system Fe-O-CaO-MgO-SiO$_2$-TiO$_2$. This extension made QUILF applicable to a broader range of rock compositions, facilitating the estimation of fO_2 using independent equilibria even where not all included minerals are present. An advantage of the method is that it enables the estimation of fO_2 even in rocks in which Fe–Ti oxides suffered subsolidus alteration, provided that a number of parameters (e.g. pressure) can be estimated. The QUILF model was further extended with titanite-bearing equilibria by Xirouchakis et al. (2001) that facilitated to put closer constraints on fO_2 and T.

A different approach to estimate fO_2 was presented by Wones and Eugster (1965) based on biotite-alkali feldspar-magnetite equilibria, which was further advanced by the studies of Wones (1981, 1989), Carmichael and Ghiorso (1990), Frost (1991), Ghiorso and Sack (1991), and Andersen et al. (1993). This oxybarometer is based on the following equilibrium:

$$annite + 1/2\ O_2 = sanidine + magnetite + H_2O \qquad (1.13)$$
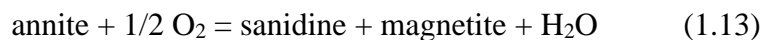
, which leads to a continuous reaction where, at higher fO_2, biotite becomes more Mg-rich at the expense of components released to K-feldspar and magnetite. From equation 1.13 it is clear that the estimation of fO_2 requires the knowledge of magmatic (and unaltered) biotite, alkali feldspar and magnetite compositions as well as the H$_2$O fugacity.

1.4.2 Alternative oxybarometers

The most straightforward way of measuring the oxidation state of volcanic glasses is based on the Fe^{2+}/Fe^{3+} or Fe^{2+}/Fe^{tot} (ΣFe) ratio of volcanic glasses. This approach makes use of the fact that Fe is a redox sensitive element present in most of the melts in wt% amount. Measurement of Fe^{2+}/Fe^{3+} is routinely done by wet chemistry (e.g. Gaillard et al., 2001), Mössbauer spectroscopy (e.g. Wilke et al., 2002) or XANES (e.g. Botcharnikov et al., 2005), and fO_2 is most commonly calculated via an empirical relationship of Kress and Carmichael (1991), however, newer calibrations (e.g. Jayasuria et al., 2004; Putirka et al., 2016) also exist. An important limitation of this oxybarometer is that it can be applied only to glasses, as Mg-bearing silicates tend to stabilize Fe^{2+} even at higher fO_2, making whole rock Fe^{2+}/Fe^{3+} ratio an inaccurate proxy of magmatic oxidation state in crystallized rocks (Frost, 1991).

Similarly to the Fe^{2+}/Fe^{3+} ratio the V/Sc ratio of volcanic glasses is also characteristic for the magmatic oxidation state (Aeolus Lee et al., 2005). The basis of this oxybarometer is that V and Sc show similar geochemical behaviour during mantle melting, as evidenced by their similar enrichments in continental crust, arc magmas and MORB relative to primitive mantle (Sun & McDonough, 1989; McDonough & Sun, 1995; Rudnick & Fountain, 1995), they are both mildly incompatible during the formation of MORB and arc lavas, and they are not mobile in fluids. On the other hand, the difference between the two elements is that the partitioning of V is redox-sensitive, whereas that of Sc is not, thus the V/Sc ratio is dependent mainly on fO_2 (Lee et al., 2005).

As shown by Scaillet and Evans (1999), the mg-number of hornblende (and orthopyroxene) can also be used to estimate magmatic fO_2. Later studies by Ridolfi et al. (2010) and Ridolfi and Renzulli (2011) derived empirical relationships between (calcic) amphibole mg-number and fO_2 based on large datasets of single amphibole compositions. The application of this oxybarometer is complicated by the fact that the presence of sulphur significantly affects the mg-number of hornblende. In the field of sulfide crystallization the mg-number is larger in sulphur-bearing charges as compared with sulphur free charges (Scaillet and Evans, 1999). At higher fO_2 (fO_2>NNO+1·3) the difference diminishes, however, at even more oxidizing conditions sulphur destabilizes hornblende.

Another approach for estimating fO_2 is related to the partitioning of redox sensitive trace elements, such as Ce and V. As shown by Ballard et al. (2002), the Ce^{4+}/Ce^{3+} ratio of zircon can

be used as a proxy for magmatic oxidation state, based on the fact that zircon is a common and resistant accessory mineral in intermediate to silicic rocks that preferably incorporates Ce^{4+} over Ce^{3+}. The study of Ballard et al. (2002) used the Ce^{4+}/Ce^{3+} ratio of zircon only for relative comparison whereas Trail et al. (2011, 2012) presented the experimental calibration of the method that facilitates the quantitative assessment of fO_2 via the following equation:

$$\ln\left(\frac{Ce}{Ce^*}\right)_D = (0.1156 \pm 0.0050) \times \ln(fO_2) + 13860 \pm \frac{708}{T(K)} - 6.125 \pm 0.484 \quad (1.14)$$

, where $\left(\frac{Ce}{Ce^*}\right)_D = \frac{D_{Ce}^{zrc/melt}}{\sqrt{D_{La}^{zrc/melt} \times D_{Pr}^{zrc/melt}}}$. As pointed out in Trail et al. (2012), 50 °C uncertainty in

the estimation of temperature propagates to 1.5 log units uncertainty in the estimation of fO_2. Due to experimental difficulties the melt composition effect was not evaluated in that study, representing a great source of uncertainty. The calibration of Smythe and Brenan (2015) and Smythe et al. (2016) significantly improved the precision of that oxybarometer as it also captured the strong effect of melt composition and melt H_2O content on Ce valence state (and partitioning), which in turn make the application on natural samples difficult. Nevertheless, this calibration reduced the range of fO_2 estimates on Hadean zircons from 12 (!) log units (Trail et al., 2011) to ca. 3.5 log units (Smythe et al., 2016).

1.5   Element partitioning between magnetite and silicate melt

As described in the section 1.4.1, the Fe and Ti content of magnetite coexisting with ilmenite is an extremely sensitive measure of magmatic oxidation state. Furthermore, an important feature of magnetite is that its structure can distort to accommodate a large range of cations, including those of transition metals such as Fe, Ni, Mn, Zn, Ti, Cr, Co, Ru, Ir, Rh and V (Righter et al., 2006). This opens various opportunities to estimate fO_2 via the partitioning of redox sensitive elements between magnetite and melt. The main focus of this study is thus the partitioning of vanadium and iron (the latter being compared with the partitioning of titanium). The structure and composition of magnetite and melt can have a significant effect on the partitioning of the previously mentioned elements, thus this section aims at summarizing the basic knowledge about these two media as well as the behaviour of V, Fe and Ti in them.

1.5.1 *Magnetite structure*

The following description is based on a recent summary about the crystal chemistry of the magnetite-ulvöspinel series by Bosi et al (2009). Spinels have the general formula of AB_2O_4, where A and B denote cations of either 2+ and 3+ valence ($A^{2+}B^{3+}_2O_4$, so-called 2-3 spinels) or of 4+ and 2+ valence ($A^{4+}B^{2+}_2O_4$, so-called 4-2 spinels). Spinel structure (space group $Fd\overline{3}m$) is generally described as a slightly distorted cubic close packed (CCP) array of anions. The cations fill the interstices within the oxygen framework, on l6 octahedral and 8 tetrahedral sites (Fig. 1.4). This cation occupancy results in two different cation distribution schemes. In the normal spinel cation A occupies the tetrahedral site and the two B cations occupy the octahedral sites (general formula: AB_2O_4); whereas in inverse spinel one of the B cations occupies the tetrahedral site and the remaining A and B cations fill the octahedral sites, giving the general formula $B(AB)O_4$. Both ideal magnetite (Fe_3O_4) and ulvöspinel (Fe_2TiO_4) have inverse spinel structure, with the structural formulae $(Fe^{3+})(Fe^{2+}Fe^{3+})O_4$ and $(Fe^{2+})(Fe^{2+}Ti^{4+})O_4$, respectively. Complete solid solution between magnetite and ulvöspinel exists at temperatures above 600 °C (Price 1981). The intermediate compositions, known as titanomagnetite ($Fe^{2+}_{1+x}Fe^{3+}_{2-2x}Ti_xO_4$), are formed by the replacement of two Fe^{3+} cations by Fe^{2+} and Ti^{4+}. For the sake of simplicity, in this study I refer to the magnetite-ulvöspinel solid solution as magnetite.
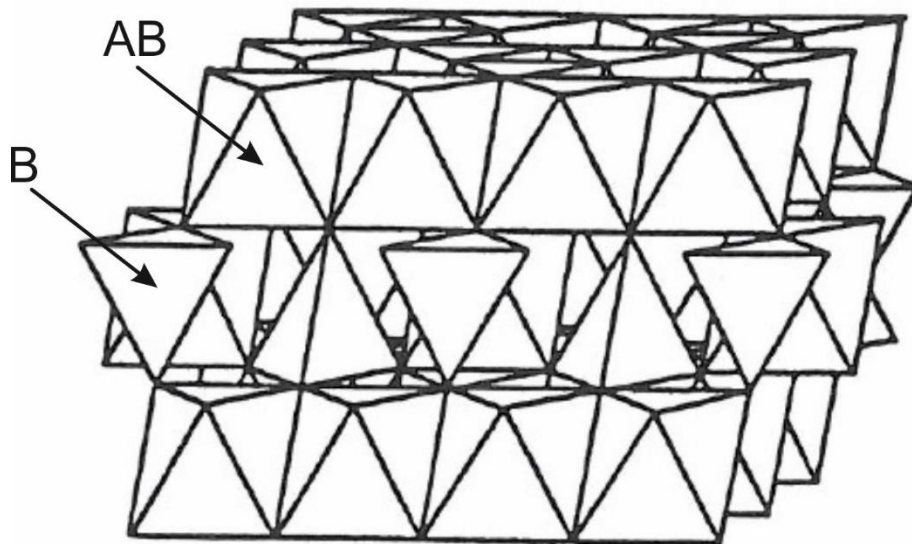
Fig. 1.4 Spinel structure: alternating layers of octahedral and tetrahedral polyhedra (modified after Waychunas, 1991). B and AB indicate the distribution of A and B type cations in the inverse spinel structure.

1.5.2   *Structure of the silicate melt and its description*

The structure of silicate melts can be considered as a network of SiO_4^{4-} tetrahedra that are linked at their corners similarly to crystalline SiO_2 varieties. Beyond adjacent tetrahedra, the medium- or intermediate range structure contains rings of tetrahedra and other interconnected units (Henderson et al., 2006). The incorporation of Al^{3+} and other trivalent elements (e.g. Fe^{3+}) into the silicate network is facilitated by low field strength elements (e.g. alkalis) that charge balance Al^{3+} (Mysen and Toplis, 2007). These cations can be most simply categorized as either network formers (Si, Al, Ti, partly Fe^{3+}) or network modifiers (Na, K, Ca, Mg, Fe^{2+} etc.). The addition of network modifiers to the silicate melt results in the formation of non-bridging oxygens (abbreviated as NBO). The ratio of non-bridging oxygens and the tetrahedrally coordinated cations (T) provides a convenient way to compare physical and chemical properties of glasses and melts (e.g. Mysen et al., 1981; Mysen and Virgo, 1985), high NBO/T denoting a more depolymerized melt. If the amount of low field strength elements is enough to charge balance Al^{3+}, the melt can be considered fully polymerized, but further addition of network modifiers leads to the depolymerization of the melt. This depolymerization increases with increasing peralkalinity, thus, properties that depend on melt polymerization are also correlated with peralkalinity (e.g. Mysen and Toplis, 2007). Mysen and Toplis (2007) also showed that even though melt viscosity shows a maximum around the metaluminous join, the polymerization of the melt continuously increases as melt composition changes from peralkaline to peraluminous. Based on these statements, one can similarly well apply the melt alumina saturation index (ASI) to account for the melt composition effect on trace element partitioning. ASI or A/NK (Shand, 1943) can be calculated from the following molecular ratio: $Al_2O_3/(Na_2O+K_2O)$. In the case of more complex melt compositions this ratio can be extended by other elements such as Ca and Mg resulting in the melt descriptors $A/CNK=Al_2O_3/(CaO+Na_2O+K_2O)$ and $A/MCNK=Al_2O_3/(MgO+CaO+Na_2O+K_2O)$ respectively. According to this classification rocks with ASI<1 are termed peralkaline, the ones with ASI>1 but A/CNK<1 metaluminous, and rocks with A/CNK>1 peraluminous.

Universal melt descriptors such as NBO/T or ASI are routinely used to express the effect of melt composition on trace element partitioning and solubility (e.g. Mysen and Virgo, 1981; Linnen et al., 1996; Righter and Drake, 1997; Zajacz, 2015). However, as pointed out by O'Neill and Eggins (2002) and also Burnham and O'Neill (2016) these melt descriptors fail to capture the

melt composition effect in some cases partly because they treat certain elements (e.g. Mg and Ca) as identical despite their different geochemical behaviour.

1.5.3   *Vanadium partitioning between magnetite and melt*

Vanadium can become strongly concentrated in magnetite because of the similar ionic radii of V^{3+} (0.65 Å) and Fe^{3+} (0.67 Å), as well as V^{4+} (0.61 Å) and Ti^{4+} (0.64 Å). Consequently, V occurs in most natural magnetites in amounts that are measurable by conventional analytical methods (e.g. LA-ICP-MS, EPMA). Vanadium concentrations in silicate melts are distinctly lower and generally decrease with increasing SiO_2 content; highly evolved rhyolite melts may contain less than 1 ppm V. Previous studies have shown that vanadium partitioning between spinel and silicate melt, $D_V^{sp/melt}$, can be used as a proxy for magmatic oxidation state, and several calibrations have been developed (Irving, 1978; Horn et al., 1994; Canil, 1999, 2002; Righter et al., 2006a; Righter et al., 2006b; Mallmann and O'Neill, 2009). The basis of using V partitioning for oxybarometry is that vanadium is present (at least partly) in different oxidation state in spinel and the coexisting silicate melt, therefore its partitioning between the two reservoirs involves oxygen (eqs. 1.15 and 1.16). The valence state of V can range from 0 to +5, however, as suggested by several authors (e.g. Toplis and Corgne, 2002) it occurs dominantly as V^{3+}, V^{4+} or V^{5+} in the silicate melt at the conditions relevant for the Earth's crust. According to the calculations of Toplis and Corgne (2002) the dominant valence state of V at FMQ is 4+, however, with increasing fO_2, the relative proportion of V^{4+} in the silicate melt falls and the portion of V^{5+} begins to increase significantly until it dominates above NNO+2 (Fig. 1.5).
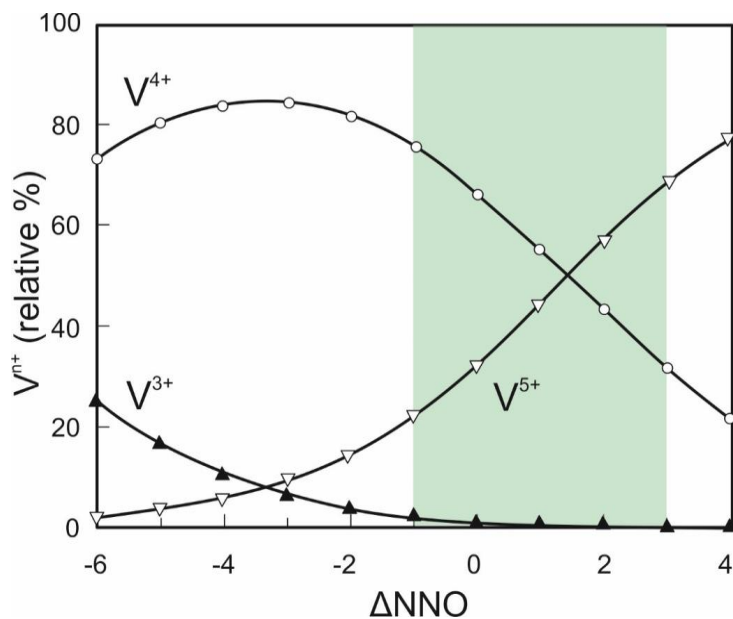
Fig. 1.5 Calculated variations of the relative proportions of V^{n+} as a function of fO_2 (modified after Toplis and Corgne, 2002). The green field marks the fO_2 conditions relevant for the Earth's crust.

On the other hand, Righter et al. (2006b) showed that the valence of V is always lower in magnetite than in the silicate melt. At upper crustal conditions it is predominantly V^{3+} and occupies only the octahedral sites in magnetite but may be present in minor amounts also as octahedrally coordinated V^{4+} in titanomagnetite (Toplis and Corgne, 2002; Righter et al., 2006a). The dominant reactions describing the partitioning of V between magnetite and melt are the following:

$$VO_{5/2}^{melt} = VO_{3/2}^{mgt} + 0.5O_2 \tag{1.15}$$

$$VO_2^{melt} = VO_{3/2}^{mgt} + 0.25O_2 \tag{1.16}$$

From the above two equations it is clear that the partitioning of vanadium will remain fO_2 dependent even where all V in the melt is oxidized to V^{5+}. This is in agreement with the partitioning study of Mallmann and O'Neill (2009) where they demonstrated that $D_V^{sp/melt}$ changes as a function of oxidation state over the entire range of fO_2 relevant for the Earth's crust (Fig. 1.6).
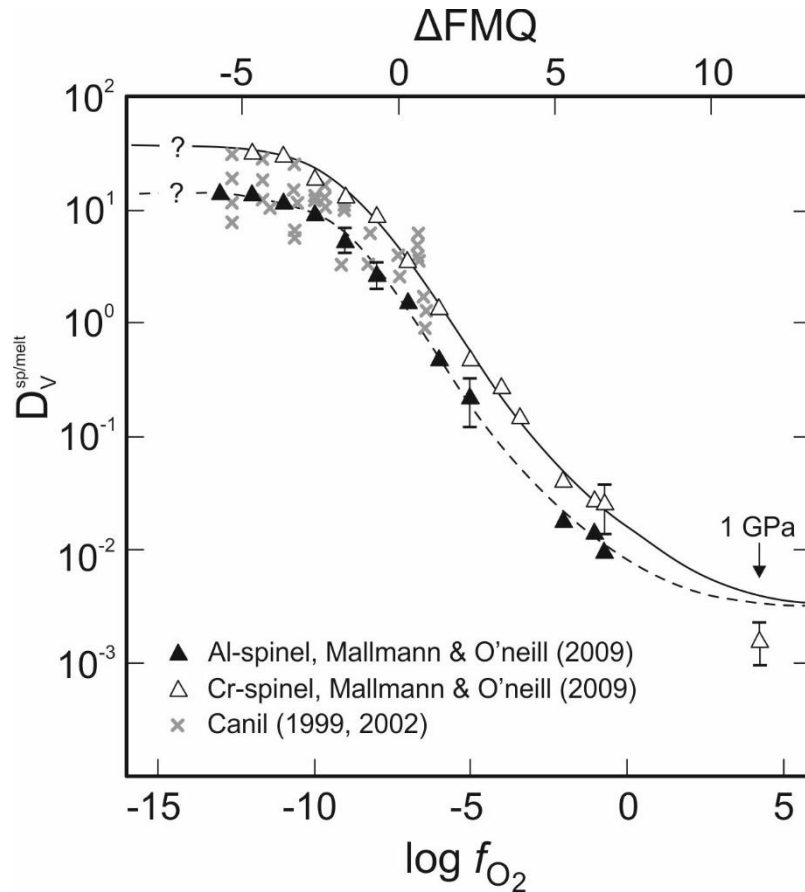
Fig. 1.6 The fO_2 dependence of V partitioning between spinel and melt (modified after Mallmann and O'Neill, 2009).

1.5.4 Iron and titanium solubility in silicate melt

Previous studies mainly focused on the solubility of Fe and Ti, which in turn has a significant influence on their partitioning behaviour between the melt and mineral phases. Gaillard et al. (2001) demonstrated that the solubility of iron in metaluminous rhyolitic glasses strongly increases with increasing oxygen fugacity. Furthermore, that study showed that melt composition also affects the Fe^{3+}/Fe^{2+} ratio and – although not stated specifically in the paper – the solubility of Fe (FeO_{tot}). A preliminary study of Siersch (2014) and also the present study investigated this melt composition effect more in detail and found that it is significant at peralkaline compositions, but seems to diminish/change slope somewhere around ASI=1 (Fig. 1.7).
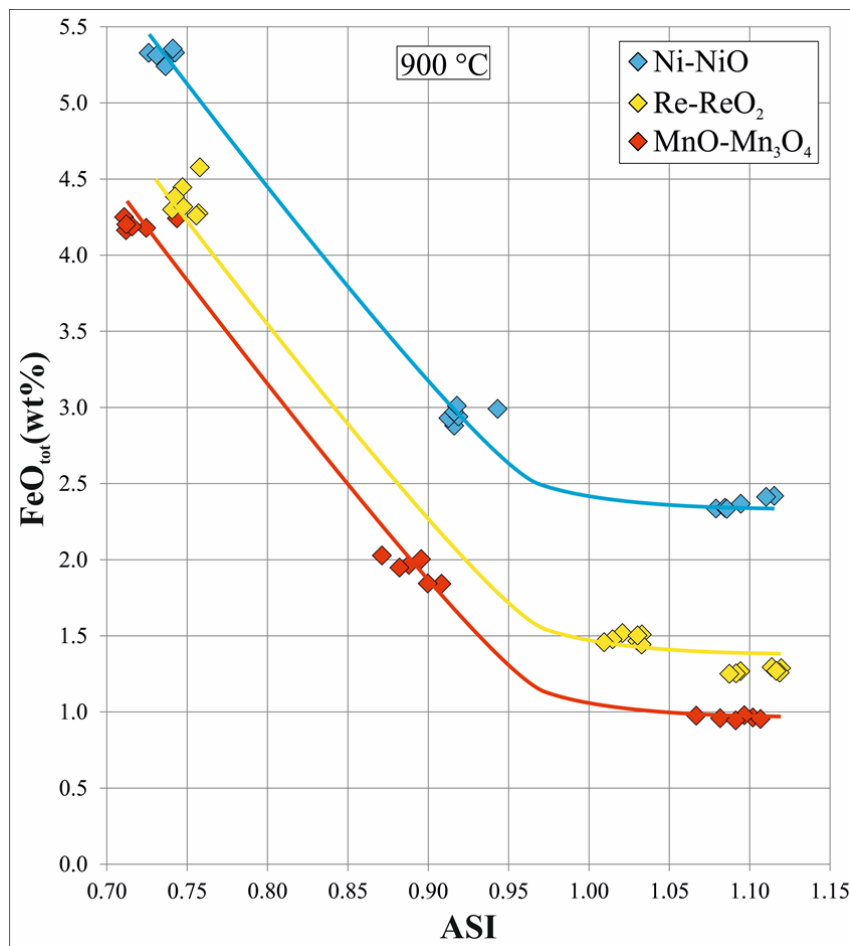
Fig. 1.7 Magnetite solubility as a function of alumina saturation index, temperature and oxygen fugacity. Solid lines represent interpreted solubility trends based on the experimental data.

The solubility of rutile and therefore that of Ti in silicate melt was investigated in detail by Kularatne and Audétat (2014). The authors of that study found that Ti solubility is strongly dependent on temperature as well as on the melt composition in the peralkaline ASI range.

However, the melt composition effect was shown to disappear over an ASI value of 1 in a similar manner as in the case of iron.

2   Experimental procedures and analytical methods

2.1   Experiments

For the calibration of the two new oxybarometers presented in chapters 6 and 8 a series of experiments was carried out at the experimental facilities of the Bayerisches Geoinstitut. The vast majority of the experiments was done in cold-seal pressure vessels (CSPV), but in order to extend the pressure range, piston cylinder was also used. The experimental data set consists of fifty-four experiments at 1–5 kbar and 800–1000 °C, with oxygen fugacity fixed either at the Ni-NiO, Re-ReO$_2$ or MnO-Mn$_3$O$_4$ buffer, i.e. 0.7, 2.5 and 4 log units above the fayalite-magnetite-quartz (FMQ) buffer, respectively.

2.1.1   Starting materials and sample design

The following starting glasses were used in our experiments: (i) Synthetic haplogranite glasses with initial alumina saturation indices (ASI) of 0.8, 1.0 and 1.1, and (ii) natural obsidians from New Zealand, China and Armenia. The haplogranites were prepared from analytical grade SiO$_2$, Al(OH)$_3$, Na$_2$CO$_3$ and K$_2$CO$_3$. The SiO$_2$ content was fixed at the 2 kbar haplogranite eutectic melt composition (Qz$_{35}$Ab$_{40}$Or$_{25}$; Johannes and Holtz, 1996), whereas ASI was changed by varying Al$_2$O$_3$, Na$_2$O and K$_2$O at a constant Na/K-ratio. After mixing, the powders were filled into Pt crucibles and decarbonated/dehydrated in a muffle furnace by heating to 1100 °C at a rate of 100 °C/hour. After two hours at 1100 °C the glasses were quenched in air. The recovered samples were homogenized and freed of gas bubbles by grinding them in an agate mortar to a grain size of <63 mm. Aliquots of these glass powders (plus of similarly prepared powders of natural obsidians) were doped with ca. 1000 ppm V by mixing them thoroughly with VO$_2$ powder (< 20 μm) and remelting them in the oven at 1600 °C and atmospheric pressure for 4 hours. Then, the resulting glasses were powdered, mixed at a 1:9-ratio with V-free glass powder and melted once more at 1600 °C for 4 hours to obtain glasses with ca. 100 ppm V. Some of these glasses were further diluted with V-free counterparts to produce starting glasses containing ca. 10 ppm V, which were used to test Henry's law.

Stoichiometric magnetite with a constant grain size of 10-20 µm was synthetized hydrothermally from analytical-grade Fe_3O_4 powder dispersed in an aqueous solution that additionally contained a few grains of oxalic acid to prevent formation of hematite. Furthermore, Ti-bearing magnetite (with 6 and 12 wt% TiO_2, respectively) was synthetized in a gas-mixing furnace at 1300 °C and fO_2 corresponding to the NiNiO buffer using run times of 24 h. The densely sintered pellets were then crushed in an agate mortar to <20 µm grain size, similar to that of the Ti-free magnetite.
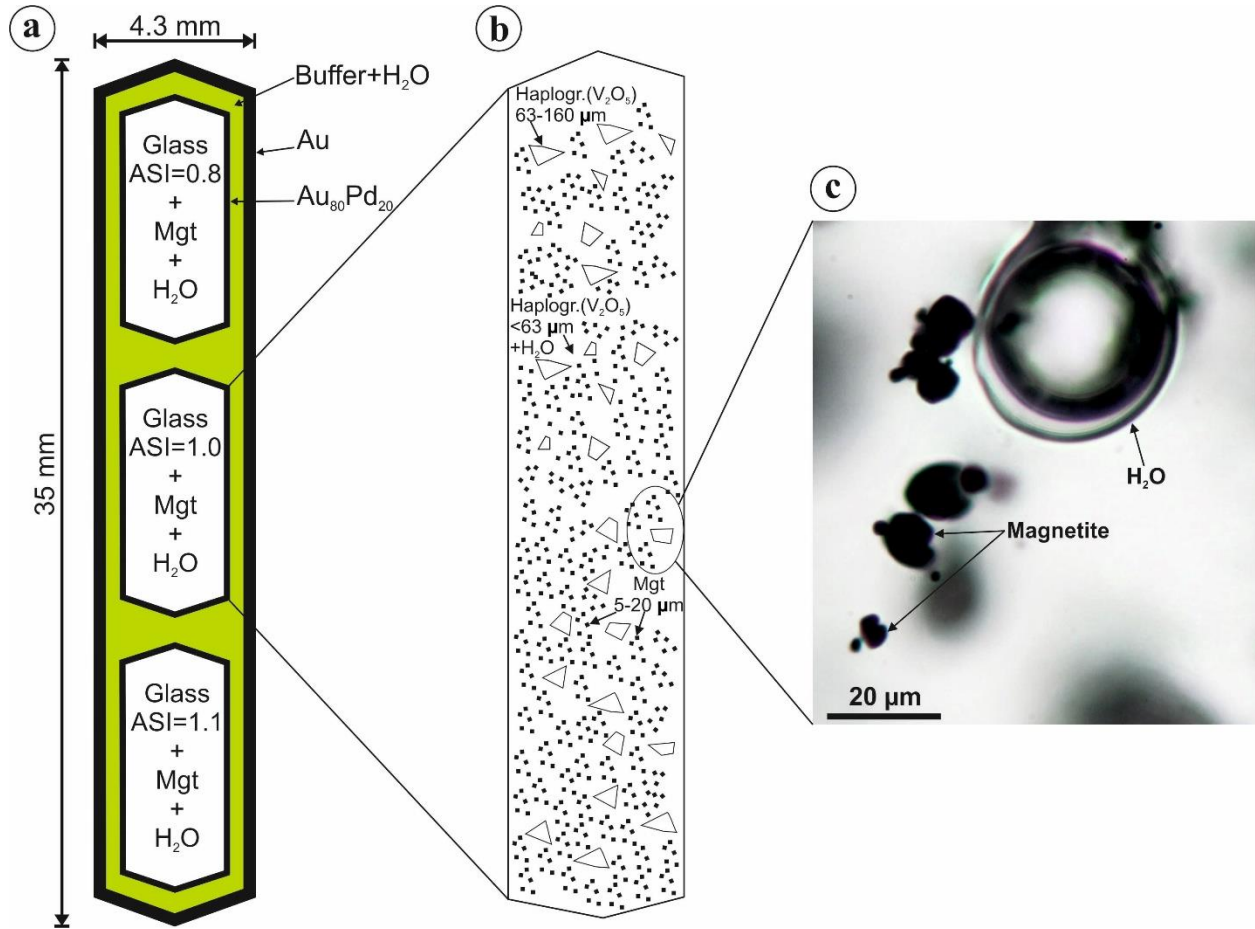
Fig. 2.1 a Schematic drawing of a typical capsule setup used in the CSPV experiments. **b** Schematic drawing of a typical inner capsule. **c** Transmitted light photomicrograph of a typical run product

The crushed haplogranite glasses were mixed with magnetite powder to produce the starting material used for the partitioning experiments (Fig. 2.1b). The silicate glass was added in two grain size fractions of <63 mm and 63–160 mm, respectively, in order to obtain magnetite-free glass domains of 50–100 mm size that could be later easily analysed by LA-ICP-MS. These glass fractions were mixed with magnetite powder – which later partly dissolved in the melt during the experiments – at a weight ratio of 2:2:1. Water was pipetted to the mixture such that it contained

26

ca. 10% excess H_2O at the given experimental p-T conditions (Johannes and Holtz, 1996). The experimental charges usually consisted of three inner $Au_{80}Pd_{20}$ capsules (3.0 mm O.D. and 2.7 mm I.D.) that contained the sample material (Fig. 2.1a). These were placed in an outer Au capsule (4.3 mm O.D. and 4.0 mm I.D.) containing the fO_2 buffer + H_2O. Excess H_2O in both inner and outer capsules was necessary to set the fO_2 value corresponding to the buffer. Attainment of equilibrium was demonstrated by reverse runs. In the forward runs V-bearing melt was equilibrated with V-free magnetite, whereas in the reverse runs V-bearing magnetite was equilibrated with V-free melt. After the experiments the recovered samples were cleaned, dried, and weighed to check for potential leaks during the experiments. After opening the outer capsule, the pH of the quench fluid was tested by pH paper, and the integrity of the buffer was checked under the microscope. Runs in which one of the buffer components became exhausted were discarded. Pieces of magnetite-bearing silicate glasses recovered from the inner capsules were prepared as doubly-polished, ca. 200 mm thick mounts for LA-ICP-MS analysis (Fig. 2.1c). Special attention was paid to fluid bubbles in the run product as these served as a proof of water saturation.

2.1.2   Rapid-quench cold-seal pressure vessel experiments

The cold-seal pressure vessel is a widespread experimental apparatus used to investigate systems at the conditions characteristic for the Earth's upper crust. In this study I used vertical vessels, the upper part of which (i.e. the autoclave) was positioned in a furnace during the experiments (Fig. 2.2a). The majority of the experiments was conducted using conventional autoclaves made of Inconel 713LC super alloy and water as pressure medium, which was supplied by capillary tubing (Fig. 2.2) through the cone seal. In contrast, the TZM alloy (Ti- and Zr-reinforced molybdenum) pressure vessel – that was used for the run at 1000°C – was operated with Ar as pressure medium.

The applied setup was similar to that of Matthews et al. (2003). The autoclave was attached to the lower part of the vessel (the so called extension tube) by a double cone, and at this joint the assemblage was constantly kept at room temperature via circulating cooling water. The sample was fixed on the tip of a support rod equipped with a steel plug such that it could be moved within the vessel by a magnet ring outside the extension tube (Fig. 2.2b). In this way the sample was held at the upper end of the autoclave during the experiment by fixing the magnet just beneath the joint. The samples were heated isobarically to 800–1000 °C at 1 or 2 kbar within 30–

50 min. The temperature was determined via thermocouples placed into an external borehole of the vessels, whereas pressure was measured by a pressure gauge. Uncertainties in temperature and pressure are estimated at ±10 °C and ±50 bar, respectively. The experiment duration varied between 2 and 22 days, which durations were demonstrated by the reverse experiments of this study and those of Zhang and Audétat (2011) to be sufficiently long to reach equilibrium between magnetite and melt. At the end of the experiment the sample was in situ quenched by dropping the magnet, causing the experimental charges to cool below the glass transition temperature within 2–3 s.
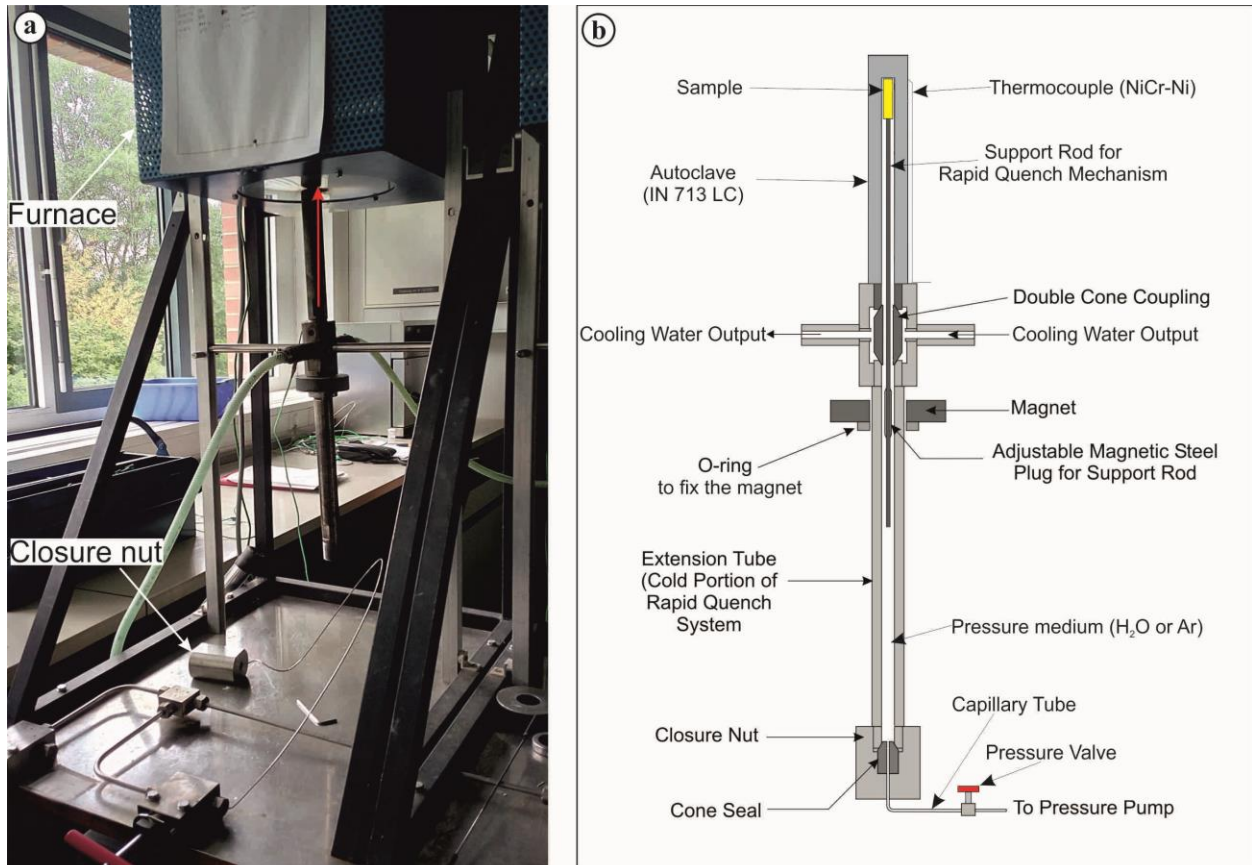
Fig. 2.2 a Cold-seal pressure vessel at the Bayerisches Geoinstitut in open state. The red arrow indicates the position of the autoclave's lower end during the experiment. **b** Schematic sketch of the CSPV (Modified after Matthews et al., 2003)

2.1.3 Piston cylinder experiment

One single run (RA-V37) was conducted in an end-loaded piston cylinder apparatus in order to test the potential effect of pressure on magnetite–melt partitioning. 1/2-inch MgO–NaCl assemblies and stepped graphite heaters were used. The experimental conditions were set to 800 °C and 5 kbar, and fO_2 was buffered by the Ni-NiO buffer. Temperature was measured by a type

"S" (Pt/Pt$_{90}$Rh$_{10}$) thermocouple. Uncertainties in recorded pressure and temperature are considered ±0.5 kbar and ±20 °C, respectively. The sample was isobarically heated to the desired run temperature at a pressure of ca. 4.5 kbar, and subsequently pressurized to the final value of 5 kbar (i.e., ''hot-piston in''). The run was stopped by switching off the power, which resulted in cooling below 100 °C within less than 10 s. For this run, a triple-capsule design was used. Two samples with different ASI were contained in inner Au$_{80}$Pd$_{20}$ capsules (1.6 mm O.D. and 1.2 mm I.D.), which themselves were placed together with Ni-NiO and H$_2$O into an outer Pt$_{95}$Rh$_5$ capsule (5.0 mm O.D. and 4.4 mm I.D.) lined with a slightly smaller gold capsule (4.3 mm O.D. and 4.0 mm I.D.). The latter approach was applied to reduce H$_2$-loss through the PtRh alloy.

2.2   Natural samples

The experimentally developed oxybarometers presented in chapters 6 and 8 were tested on an extensive set of natural silicic rocks (chapters 3.3, 7 and 8.4). The compilation consists partly of donated material and partly of specimens that were collected by Andreas Audétat. While compiling the sample set the aim was to represent a range of fO$_2$, temperature, and melt composition as wide as possible covering different geological settings (see 7.7 for detailed sample description). Nevertheless, all of these samples can be categorised as rhyolites or dacites, meaning that FeTiMM – which should be also applicable for more mafic compositions – could not be tested yet on natural samples more mafic than dacite.

From each sample polished thick sections of approximately 300-400 µm thickness were prepared. These were carefully investigated under the petrographic microscope to search for fresh Fe–Ti oxide microphenocrysts, feldspar phenocrysts and quenched silicate melt, or, if these were not present, for Fe–Ti oxide-, feldspar- and melt inclusions preserved within quartz and feldspar phenocrysts.

Areas with measurable inclusions/mineral phases were cut out of each section by means of a diamond saw, and the pieces were then assembled on a glass mount for LA-ICP-MS analysis. Before the measurements, a detailed map was prepared of each mount on an A3 sized scan image.

2.3 Analytical methods

2.3.1 *Optical microscopy*

Experimental samples were investigated under stereomicroscope and polarisation microscope as well. The stereomicroscope was used to check if both buffer phases as well as some excess water was present in the outer capsule after the experiment. The thick sections of the experimental run products were always studied with polarisation microscope. Reflected light was used to detect possible inhomogeneity in magnetite crystals or unwanted mineral phases in the sample such as hematite or ilmenite. By means of transmitted light I could observe the water bubbles in the run product and also search for areas that were well suited for the later LA-ICP-MS analyses.

The thick sections made of natural samples were investigated under polarisation microscope to search for fresh Fe–Ti oxide microphenocrysts, feldspar phenocrysts and quenched silicate melt in fresh volcanic samples. Where the matrix was altered or crystallized and/or the phenocrysts were altered, inclusions of the Fe–Ti oxides, feldspars and melt preserved within quartz and feldspar phenocrysts were selected for analysis. Special attention was paid to signs of magma mixing such as resorption- or alteration features, or multiple generations of individual mineral phases that are the usual signs of non-equilibrium conditions and are of great importance for interpreting thermobarometry data.

2.3.2 *LA-ICP-MS*

The experimental run products as well as the natural samples of this study were analysed by means of laser ablation inductively coupled mass spectrometry (LA-ICP-MS) using a similar equipment as described by Günther et al. (1998). The instrument consisted of a GeolasPro 193 nm ArF Excimer Laser (Coherent, USA) coupled with an Elan DRC-e (Perkin Elmer, Canada) quadrupole mass spectrometer. The ICP-MS was tuned to a ThO/Th rate of 0.05–0.1% and a Ca^{2+}/Ca^+ rate of 0.1–0.2% according to measurements on NIST SRM 610 glass (Jochum et al., 2011). The sample chamber was flushed with He gas at a rate of 0.4 l/min, to which 5 ml/min H_2 gas was added on its way to the ICP-MS.

The experimental run products were analysed using the following settings: The element menu included ^{23}Na, ^{25}Mg, ^{27}Al, ^{29}Si, ^{39}K, ^{49}Ti, ^{51}V, ^{53}Cr, ^{55}Mn, ^{57}Fe, ^{62}Ni, ^{66}Zn, ^{140}Ce and ^{185}Re, with dwell times ranging from 10 to 50 ms. The laser beam was operated at 10 Hz frequency and a

constant energy density of 10 J/cm^2 at the sample surface. The applied laser pit size was usually 30–40 mm for the silicate glasses and 15–30 mm for the magnetite clusters.

A number of considerations were made specifically for the measurement of the run products: For each magnetite–melt pair we analysed the glass first and an adjacent area containing both magnetite and glass afterwards. Only areas with small magnetite clusters were selected for the latter purpose because large accumulations of magnetite showed chemical heterogeneity and may have failed to completely equilibrate with the melt. The composition of magnetite was obtained by numerically subtracting glass of the first part of the signal until no Na was left in the second, mixed part of the signal. Fe, Ti, Mn and V partition strongly into the magnetite, therefore the residual signals of these elements are well-resolved, whereas the signals of Al and Mg are not, as these elements occur in higher amounts in the glass. External standardization was based on NIST SRM 610 glass, which was measured twice before and after each block of 8−14 unknowns. For precise determination of the alumina saturation index (ASI), a second, matrix-matched external standard in the form of a natural obsidian glass from Armenia was used to calculate the concentrations of Na, K and Al. This obsidian glass has been thoroughly characterized by independent analyses with electron microprobe and LA-ICP-MS, using the NIST SRM 610 (Jochum et al., 2011), NIST SRM 621 and BAM-S005-A (Yang et al., 2012) standards.

Data reduction was done by means of in-house Excel spreadsheets. Internal standardization of the silicate glass analyses was done by normalizing the sum of Na_2O, MgO, Al_2O_3, SiO_2, K_2O, TiO_2 and FeOtot to 100%. The melt compositions were calculated on an anhydrous basis, as the water content was found to have no effect on vanadium, iron and titanium partitioning (see sections 6.4 and 8.2). By ignoring the valence state of iron in the most Fe-rich glasses (4 wt% FeOtot) an error of max. 0.4% was introduced in the concentration of all other elements analysed. Magnetite analyses were calculated by normalizing the sum of Fe_3O_4, MnO (typically around 1 wt%) and TiO_2 (typically around 0.6 wt%) to 100 wt%. Furthermore, some uncertainty was introduced by the fact that Al_2O_3 is not included in this sum, which is due to the inability to reliably subtract the Al_2O_3 contribution of ablated silicate glass from the mixed signal. However, the error introduced by not taking into account Al_2O_3 in the normalization procedure should be small, since magnetites in rhyolites rarely contain more than 3 wt% Al_2O_3 (Ghiorso and Evans, 2008).

matrix glasses, and 15-30 µm for the exposed Fe–Ti-oxide microphenocrysts, whereas for inclusions it was always chosen such that the complete inclusion volume was sampled including some host material. Feldspars and melt inclusions / matrix glasses were usually measured before analysing the Fe–Ti-oxide inclusions / microphenocrysts. The co-ablation of the host material was treated in a similar sense as in the case of experimental samples. The composition of Fe–Ti-oxide inclusions was obtained by numerically subtracting the contribution of the host crystal (usually quartz or feldspar) from the mixed signal by assuming that the magnetite did not contain Si. Sometimes however, this correction was not sufficient, as the Fe–Ti-oxide inclusions were commonly trapped together with a small amount of silicate melt. In the case of quartz-hosted inclusions, a second correction could be applied in which melt of the same composition as coexisting melt inclusions was numerically subtracted from the signal by assuming no Na in the magnetite. The composition of silicate melt inclusions was obtained by using an internal standard (usually Al_2O_3; see below) and subtracting host quartz from the mixed signal until the value (usually Al_2O_3) of the internal standard was reached. The external standardisation of the natural sample analyses was similar as in the case of experimental samples with the slight but important difference that a natural, homogenous ilmenite from Labrador collected by Tony Morse (KI-2193; major element composition given in Janssen et al. 2010) was used to accurately determine the major element composition of the Fe–Ti oxides. Using this natural standard, the calculated Ti content of the magnetite changed by ≤3% relative to the value that would have been obtained by applying only NIST glass. This gives an estimate of the error introduced by using only the NIST glass for quantifying the trace element content of the Fe–Ti-oxides. Agreement between Fe–Ti-oxide compositions determined by LA-ICP-MS versus electron microprobe was demonstrated on three natural samples containing ±homogeneous Fe–Ti-oxide populations.

Data reduction was done similarly to that of experimental samples. Internal standardization of the silicate glass and exposed glassy melt inclusions was obtained by normalizing the sum of Na_2O, MgO, Al_2O_3, SiO_2, K_2O, TiO_2, MnO and FeO_{tot} to 100 %. For crystallized melt inclusions and unexposed glassy melt inclusions (which were always hosted in quartz) Al concentration was used as internal standard that was estimated from whole rock or homogenized melt inclusion literature data, or was taken from analyses of exposed, glassy melt inclusions from the same sample. The SiO_2 concentration of melt inclusions was then calculated by difference assuming a total of 100 wt % major element oxides. All the options mentioned before, but especially using

the whole rock Al content as an internal standard, introduce some error in the glass composition calculations if the major element composition of the melt inclusions does not match exactly the composition of the rock matrices or whole rocks that were used as internal standard. However, in all cases where such a comparison could be made, no significant compositional differences in the major element concentrations were found. All concentrations – including the standards – were calculated on a volatile-free basis. Magnetite analyses were calculated by normalizing the sum of FeO, Fe_3O_4, TiO_2, Al_2O_3, MnO, MgO, V_2O_5, ZnO, Nb_2O_3 and Cr_2O_3 to 100 wt%, whereby the FeO/Fe_3O_4-ratio was calculated from stoichiometric constraints in the same manner as it is done for electron microprobe analyses.

3   Results and discussion

In this section I give a brief summary of the results and their interpretation. The results presented here have all been published or are in press but this section does not exactly follow the structure of the manuscripts. For detailed information please see the manuscripts in Sections 6, 7, and 8.

3.1   Vanadium partitioning between magnetite and melt

Magnetite-melt partitioning experiments showed that at fixed alumina saturation index and temperature the partition coefficient of vanadium between magnetite and melt ($D_V^{mgt/melt}$) decreases by 1.5-1.7 log units as fO_2 increases from values corresponding to the Ni-NiO to those corresponding to the MnO-Mn$_3$O$_4$ buffer (Fig. 3.1). This strong oxygen fugacity dependence renders the application of $D_V^{mgt/melt}$ as an oxybarometer feasible. Furthermore, $D_V^{mgt/melt}$ decreases with increasing temperature at a fixed fO_2 (Fig. 3.1), however, the net temperature effect is actually positive if we consider that absolute fO_2 increases with temperature (Fig. 1.1).
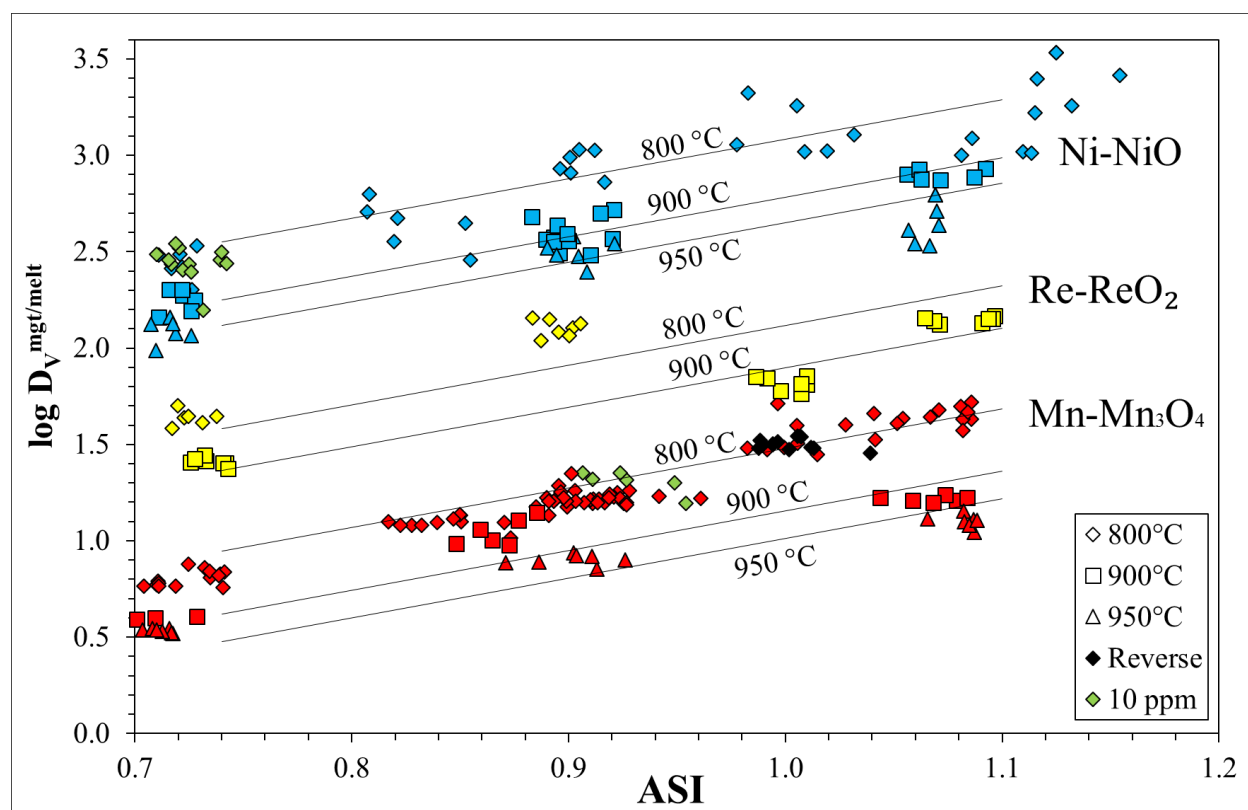
Fig. 3.1 Summary of experimental results as a function of oxygen fugacity buffer, temperature and melt composition. ASI= molar Al$_2$O$_3$/(CaO+Na$_2$O+K$_2$O). Colors indicate different fO_2 buffers (shown on the right); symbol shapes mark different temperatures. The solid lines represent fits through the data points calculated from the regression equation given in equation (3.1). 10 ppm refers to 10 ppm VO$_2$ in the starting glass, as opposed to the concentration of 100 ppm VO$_2$ used in all other runs.

Melt alumina saturation index also affects $D_V^{mgt/melt}$ significantly, as increasing ASI from 0.74 to 1.14 results in a 0.6-0.8 log units increase in $D_V^{mgt/melt}$. The large scatter of vanadium partition coefficients obtained at high ASI, Ni-NiO buffer and 800 °C seems to reflect problems to reach equilibrium.

The dependence of $D_V^{mgt/melt}$ on oxygen fugacity is related to a change in vanadium valence during its partitioning between magnetite and melt. The dominant valence of vanadium in magnetite was shown to be V^{3+}, substituting for $Fe^{3+} \pm Cr^{3+}$, Al^{3+} in the octahedral site (Toplis and Corgne, 2002; Righter et al., 2006b). In contrast, the dominant valence of vanadium in (basaltic) silicate melts at geologically realistic fO_2 conditions is either V^{4+} or V^{5+}, their relative proportion being dependent on fO_2 (Toplis and Corgne, 2002). The results of Mallmann and O'Neill (2009) suggest that over the fO_2 range covered in the present study (FMQ+0.7 - FMQ+4.0) $D_V^{mgt/melt}$ should vary approximately linearly with oxygen fugacity. This interpretation is in good agreement with the results of the present study, for which reason a linear dependence of $D_V^{mgt/melt}$ on oxygen fugacity is assumed. Considering this and also the temperature and melt composition dependence of vanadium partitioning, our data can be described by the following equation:

$$\log D_V^{mgt/melt} = 0.3726 * \frac{10,000}{T(K)} + 2.0465 * ASI - 0.4773 * \Delta FMQ - 2.1214 \ (3.1)$$

, or if the regression is performed for ΔFMQ:

$$\Delta FMQ = -2.0511 * \log D_V^{mgt/melt} + 0.7809 * \frac{10,000}{T} + 4.2367 * ASI - 4.4767 \ (3.2)$$

The use of more silicic melts and the observed strong melt composition dependence as well as the significantly lower temperatures (mostly 800-950 °C) in our experiments compared to previous investigations (1100-1300 °C) are likely the reasons why our $D_V^{mgt/melt}$ values are 1-3 orders of magnitude higher than those obtained in previous studies (e.g. Canil, 1999; Righter et al., 2006a; Righter et al., 2006b). Therefore, a direct comparison of our method and previous calibrations is not possible.

3.2 Iron and titanium partitioning between magnetite and melt

Iron solubility in silicic melts has been shown to depend on fO$_2$ (Gaillard et al., 2001). A series of magnetite-melt partitioning experiments presented in this study have shown that magnetite solubility (and thus Fe partitioning between magnetite and silicate melt) depends also strongly on temperature and melt composition. However, TiO$_2$ solubility shows a similar melt composition (ASI) dependence (Kularatne and Audétat, 2014) but it is not affected by fO$_2$. Therefore, if the partition coefficient of Fe ($D_{Fe}^{mgt/melt}$) is divided by that of Ti ($D_{Ti}^{mgt/melt}$) the melt composition dependence can be significantly reduced. The resulting Fe–Ti exchange coefficient ($D_{Fe-Ti}^{mgt/melt}$) is mainly controlled by oxygen fugacity and to a small extent by melt composition (which is again fO$_2$ dependent), whereas the effects of temperature, pressure and magnetite composition are negligible (Fig. 3.2).
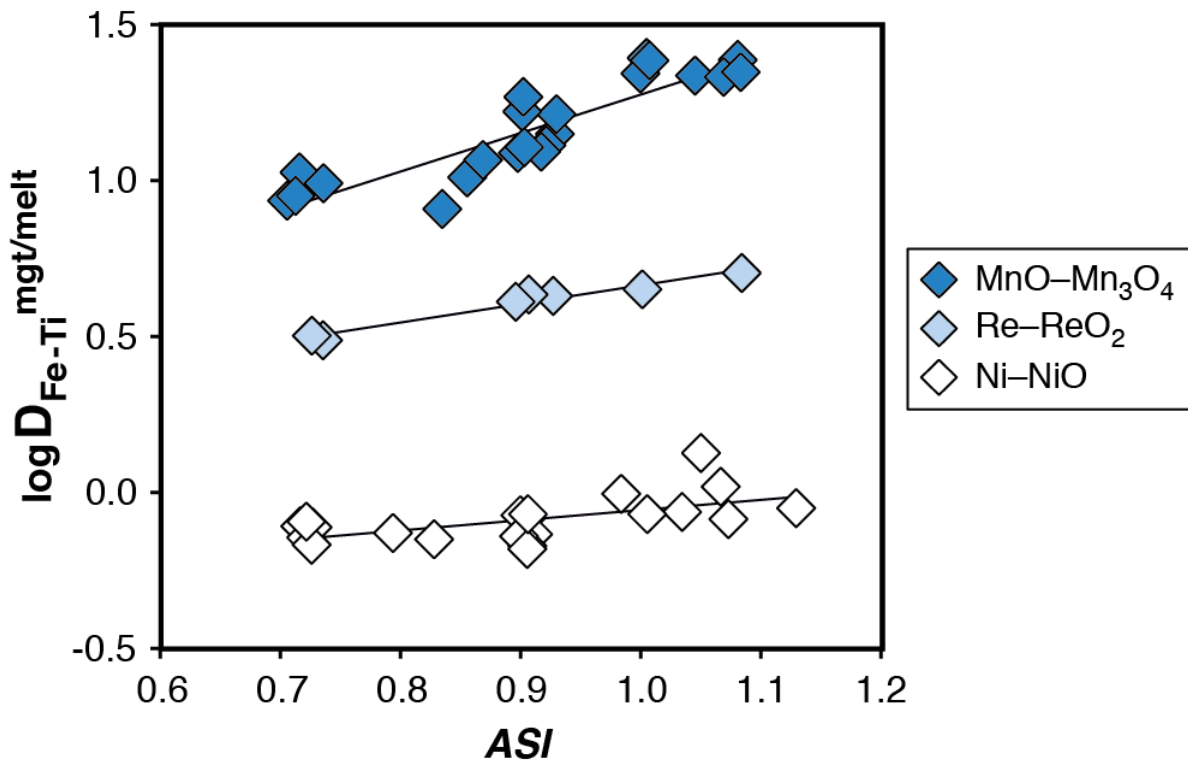
Fig. 3.2 Dependence of the Fe–Ti exchange coefficient between magnetite and rhyolitic melt on fO$_2$ and melt alumina saturation index. $D_{Fe-Ti}^{mgt/melt}$ refers to ($D_{FeOtot}^{mgt/melt}$)/($D_{TiO2}^{mgt/melt}$), whereas ASI refers to molar Al$_2$O$_3$ /(CaO + Na$_2$O + K$_2$O). The dataset comprises magnetite–melt pairs from 50 different experiments performed at three different oxygen fugacity buffers, temperatures of 800-1000°C, pressures of 100-500 MPa, with melt ASI values of 0.71-1.12, and magnetite compositions of 0.2-14 wt% TiO$_2$.

In a second step, my own data set was extended by 59 experiments from 14 different studies performed at 750-1100 °C, 0.1-700 MPa, oxygen fugacities of -1.3 to +5.5 log units relative to the fayalite-magnetite-quartz buffer (FMQ-1.3 to FMQ+5.5), with melt compositions of 48-79 wt% SiO_2 and ASI=0.3-1.3, and magnetite compositions of 0.01-28 wt% TiO_2. After adding this data to the set of own experiments a similar oxygen fugacity and melt composition dependence could be observed as in the case of using solely my own data. This extended data set is described by the following equation:

$$\Delta FMQ = (\log(D_{FeOtot}^{mgt/melt}/D_{TiO_2}^{mgt/melt}) + 0.137*AMCNK + 0.102)/(0.288*AMCNK + 0.054) \quad \text{(Eq. 3.3)}$$

, where AMCNK= molar $Al_2O_3/(CaO+Na_2O+K_2O+MgO)$. The literature experiments were all ilmenite-saturated such that fO_2 could be independently constrained via magnetite–ilmenite oxybarometry. The comparison of the fO_2 values given by the new oxybarometer (named FeTiMM) with ones obtained via magnetite–ilmenite oxybarometry shows a good agreement (Fig. 3.3) for all rock compositions investigated. This makes FeTiMM a simple and universally applicable oxybarometer.
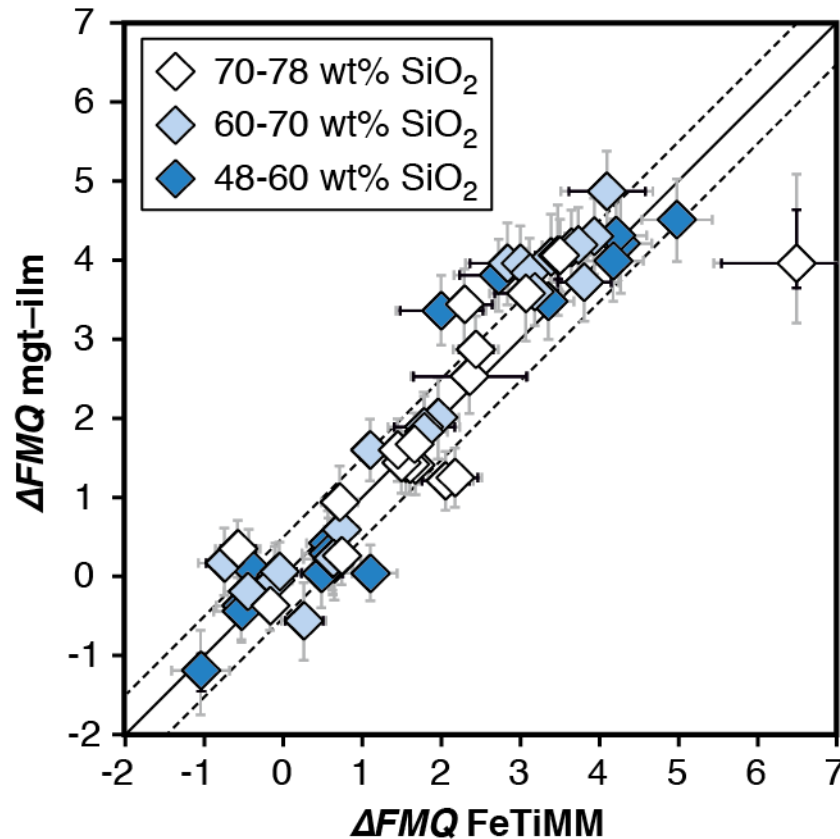
Fig. 3.3 Performance of FeTiMM on ilmenite-saturated experimental samples. Oxygen fugacities (expressed in log units relative to the FMQ buffer) obtained via FeTiMM are compared with ones obtained via magnetite–ilmenite oxybarometry using the model of Ghiorso and Evans (2008). The data are divided into three groups according to melt SiO_2 content. Black error bars (in most cases smaller than the symbol size) denote the analytical error, whereas the grey error bars show the overall error that includes both the analytical scatter and the error inherent to the model.

3.3 Application of the new oxybarometers to natural silicic rocks

The first application of the vanadium partitioning oxybarometer and FeTiMM to natural rhyolites and dacites returned very promising results. Investigated samples included vitrophyres and holocrystalline rocks in which part of the mineral- and melt assemblage was preserved only in form of inclusions within phenocrysts. Oxygen fugacity was always independently constrained by magnetite–ilmenite oxybarometry, whereas temperature was calculated (only needed for vanadium partitioning oxybarometry) using zircon saturation thermometry, two-feldspar thermometry and Fe–Ti-oxide thermometry. In most of the samples the fO$_2$ values determined via vanadium magnetite–melt oxybarometry (Fig. 3.4a) and FeTiMM (Fig. 3.4b) agree within 0.5 log units with the oxygen fugacity calculated from Fe–Ti-oxide pairs, except for a few cases where the larger discrepancy can be explained by magma mixing processes. However, using the equilibrium test based on the exchange coefficient of Mn and Mg between magnetite and melt, disequilibrium magnetite-melt pairs can now be detected and discarded.
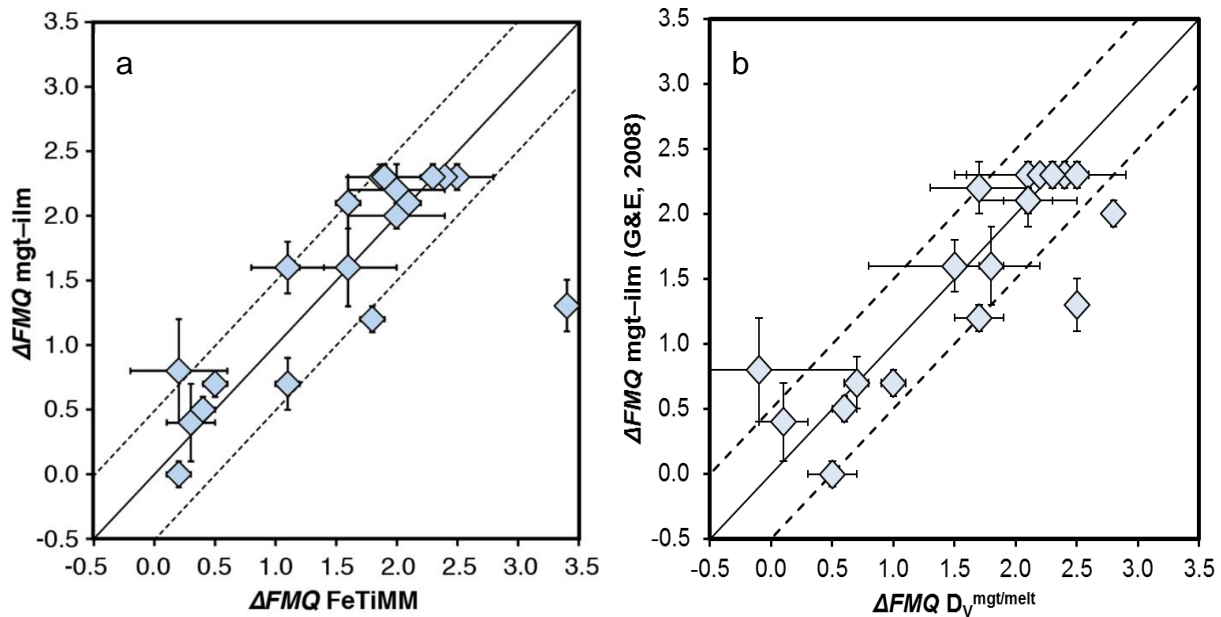
Fig. 3.4 a Comparison of fO$_2$ values (reported in log units relative to the fayalite-magnetite-quartz buffer) obtained via FeTiMM versus Fe–Ti oxide oxybarometry using the model of Ghiorso and Evans (2008) **b** Comparison of fO$_2$ values (reported in log units relative to the fayalite-magnetite-quartz buffer) obtained via vanadium magnetite–melt partitioning oxybarometry versus Fe–Ti oxide oxybarometry using the model of Ghiorso and Evans (2008). Error bars indicate 1 sigma standard deviations of the calculated fO$_2$ averages.

The fO$_2$ values obtained via vanadium partitioning depend significantly on the applied thermometer. Temperatures obtained via zircon saturation thermometry and two-feldspar thermometry usually agreed within the limits of uncertainty, whereas temperatures obtained via

Fe–Ti-oxide thermometry commonly deviated by ≥50 °C due to large uncertainties associated with the Fe–Ti-oxide model at T-fO_2 conditions typical of most silicic magmas. Therefore, the former two methods are recommended to constrain temperature for vanadium partitioning oxybarometry. The main advantages of both new oxybarometers over classical magnetite–ilmenite oxybarometry are (1) that they can be applied to both ilmenite-free and ilmenite-bearing samples (2) that they are easier to apply to slowly-cooled rocks such as granites by measuring magnetite-melt pairs in form of inclusions. Further advantages of FeTiMM are (3) that it is temperature-independent and (4) that it is calibrated to and is therefore applicable to a broad range of melt compositions, spanning the entire range from basalts to rhyolites.

4 References

Aeolus Lee, C.T. (2005) Similar V/Sc Systematics in MORB and Arc Basalts: Implications for the Oxygen Fugacities of their Mantle Source Regions. *J. Petrol.* **46**, 2313-2336.

Andersen, D.J. and Lindsley, D.H. (1985) New (and final!) models for the Ti-magnetite/ilmenite geothermometer and oxygen barometer. In: Abstract AGU 1985 Spring Meeting Eos Transactions. American Geophysical Union. **66**, 416.

Andersen, D.J. and Lindsley, D.H. (1988) Internally consistent solution models for Fe-Mg-Mn-Ti oxides: Fe–Ti oxides. *Am. Mineral.* **73**, 714-726.

Andersen, D.J., Lindsley, D.H. and Davidson, P.M. (1993) QUILF: A pascal program to assess equilibria among Fe–Mg–Mn–Ti oxides, pyroxenes, olivine, and quartz. *Comput. Geosci.* **19**, 1333-1350.

Audétat, A. (2015) Compositional evolution and formation conditions of magmas and fluids related to porphyry Mo mineralization at Climax, Colorado. *J. Petrol.* **56**, 1519-1546.

Audétat, A. and Li, W. (2017) The genesis of Climax-type porphyry Mo deposits: Insights from fluid inclusions and melt inclusions. *Ore Geol. Rev.* **88**, 436-460.

Audétat, A., Pettke, T. and Dolejš, D. (2004) Magmatic anhydrite and calcite in the ore-forming quartz-monzodiorite magma at Santa Rita, New Mexico (USA): genetic constraints on porphyry-Cu mineralization. *Lithos* **72**, 147-161.

Audétat, A., Dolejs, D. and Lowenstern, J.B. (2011) Molybdenite Saturation in Silicic Magmas: Occurrence and Petrological Implications. *J. Petrol.* **52**, 891-904.

Bacon, C.R. and Hirschmann, M.M. (1988) Mg/Mn partitioning as a test for equilibrium between coexisting Fe-Ti oxides. *Am. Mineral.* **73**, 57-61.

Ballard, J.R., Palin, M.J. and Campbell, I.H. (2002) Relative oxidation states of magmas inferred from Ce(IV)/Ce(III) in zircon: application to porphyry copper deposits of northern Chile. *Contrib. Mineral. Petrol.* **144**, 347-364.

Blevin, P.L. and Chappell, B.W. (1992) The role of magma sources, oxidation states and fractionation in determining the granite metallogeny of eastern Australia. *Transactions of the Royal Society of Edinburgh: Earth Sciences* **83**, 305-316.

Borisov, A. and Palme, H. (2000) Solubilities of noble metals in Fe-containing silicate melts as derived from experiments in Fe-free systems. *Am. Mineral.* **85**, 1665-1673.

Bosi, F., Halenius, U. and Skogby, H. (2009) Crystal chemistry of the magnetite-ulvospinel series. *Am. Mineral.* **94**, 181-189.

Botcharnikov, R.E., Koepke, J., Holtz, F., McCammon, C. and Wilke, M. (2005) The effect of water activity on the oxidation and structural state of Fe in a ferro-basaltic melt. *Geochim. Cosmochim. Acta* **69**, 5071-5085.

Buddington, A. and Lindsley, D. (1964) Iron-titanium oxide minerals and synthetic equivalents. *J. Petrol.* **5**, 310-357.

Burnham, A.D. and O'Neill, H.S.C. (2016) The effect of melt composition on mineral-melt partition coefficients: The case of beryllium. *Chem. Geol.* **442**, 139-147.

Candela, P.A. (1992) Controls on ore metal ratios in granite-related ore systems: an experimental and computational approach. *Earth and Environmental Science Transactions of The Royal Society of Edinburgh* **83**, 317-326.

Candela, P.A. and Bouton, S.L. (1990) The influence of oxygen fugacity on tungsten and molybdenum partitioning between silicate melts and ilmenite. *Econ. Geol.* **85**, 633-640.

Canil, D. (1999) Vanadium partitioning between orthopyroxene, spinel and silicate melt and the redox states of mantle source regions for primary magmas. *Geochim. Cosmochim. Acta* **63**, 557-572.

Canil, D. (2002) Vanadium in peridotites, mantle redox and tectonic environments: Archean to present. *Earth Planet. Sci. Lett.* **195**, 75-90.

Carmichael, I.S.E. (1967) The iron-titanium oxides of salic volcanic rocks and their associated ferromagnesian silicates. *Contrib. Mineral. Petrol.* **14**, 36-64.

Carmichael, I. and Ghiorso, M. (1990) Controls on oxidation-reduction relations in magmas. *Rev Mineral, Min Soc America, Washington, DC* **24**, 191-212.

Carroll, M. and Rutherford, M. (1985) Sulfide and sulfate saturation in hydrous silicate melts. *Journal of Geophysical Research: Solid Earth* **90**.

Carroll, M. and Rutherford, M.J. (1988) Sulfur speciation in hydrous experimental glasses of varying oxidation state--results from measured wavelength shifts of sulfur X-rays. *Am. Mineral.* **73**, 845-849.

Eugster, H.P. (1957) Heterogeneous Reactions Involving Oxidation and Reduction at High Pressures and Temperatures. *The Journal of Chemical Physics* **26**, 1760-1761.

Eugster, H.P. (1959) Reduction and oxidation in metamorphism. *Researches in geochemistry* **1**, 397-426.

Fortenfant, S.S., Dingwell, D.B., Ertel-Ingrisch, W., Capmas, F., Birck, J.L. and Dalpé, C. (2006) Oxygen fugacity dependence of Os solubility in haplobasaltic melt. *Geochim. Cosmochim. Acta* **70**, 742-756.

Frost, B.R. (1991) Introduction to oxygen fugacity and its petrologic importance. *Rev. Mineral. Geochem.* **25**, 1-9.

Frost, B.R. and Lindsley, D. (1992) Equilibria among Fe–Ti oxides, pyroxenes, olivine, and quartz: Part II. Application. *Am. Mineral.* **77**, 1004-1004.

Frost, B.R., Lindsley, D.H. and Andersen, D.J. (1988) Fe–Ti oxide-silicate equilibria; assemblages with fayalitic olivine. *Am. Mineral.* **73**, 727-740.

Gaillard, F., Scaillet, B., Pichavant, M. and Bény, J.-M. (2001) The effect of water and fO$_2$ on the ferric–ferrous ratio of silicic melts. *Chem. Geol.* **174**, 255-273.

Ghiorso, M.S. and Sack, O. (1991) Fe–Ti oxide geothermometry: thermodynamic formulation and the estimation of intensive variables in silicic magmas. *Contrib. Mineral. Petrol.* **108**, 485-510.

Ghiorso, M.S. and Evans, B.W. (2008) Thermodynamics of rhombohedral oxide solid solutions and a revision of the Fe–Ti two-oxide geothermometer and oxygen-barometer. *Am. J. Sci.* **308**, 957-1039.

Günther, D., Audétat, A., Frischknecht, R. and Heinrich, C.A. (1998) Quantitative analysis of major, minor and trace elements in fluid inclusions using laser ablation–inductively coupled plasmamass spectrometry. *J. Anal. At. Spectrom.* **13**, 263-270.

Haggerty, S. (1976) Oxidation of opaque mineral oxides in basalts. *Oxide minerals*, Hg1-Hg100.

Henderson, G.S., Calas, G. and Stebbins, J.F. (2006) The structure of silicate glasses and melts. *Elements* **2**, 269-273.

Holzheid, A., Borisov, A. and Palme, H. (1994) The effect of oxygen fugacity and temperature on solubilities of nickel, cobalt, and molybdenum in silicate melts. *Geochim. Cosmochim. Acta* **58**, 1975-1981.

Horn, I., Foley, S.F., Jackson, S.E. and Jenner, G.A. (1994) Experimentally determined partitioning of high field strength- and selected transition elements between spinel and basaltic melt. *Chem. Geol.* **117**, 193-218.

Irving, A.J. (1978) A review of experimental studies of crystal/liquid trace element partitioning. *Geochim. Cosmochim. Acta* **42**, 743-770.

Ishihara, S. (1977) The magnetite-series and ilmenite-series granitic rocks. *Mining Geol.* **27**, 293-305.

Janssen, A., Putnis, A., Geisler, T. and Putnis, C.V. (2010) The experimental replacement of ilmenite by rutile in HCl solutions. *Mineral. Mag.* **74**, 633-644.

Jayasuriya, K.D., O'neill, H.S.C., Berry, A.J. and Campbell, S.J. (2004) A Mössbauer study of the oxidation state of Fe in silicate melts. *Am. Mineral.* **89**, 1597-1609.

Jochum, K.P., Weis, U., Stoll, B., Kuzmin, D., Yang, Q., Raczek, I., Jacob, D.E., Stracke, A., Birbaum, K., Frick, D.A., Günther, D. and Enzweiler, J. (2011) Determination of reference values for NIST SRM 610-617 glasses following ISO guidelines. *Geostand. Geoanal. Res.* **35**, 397-429.

Johannes, W. and Holtz, F. (1996) *Petrogenesis and experimental petrology of granitic rocks.* Springer. 335 pp.

Jugo, P.J., Wilke, M. and Botcharnikov, R.E. (2010) Sulfur K-edge XANES analysis of natural and synthetic basaltic glasses: Implications for S speciation and S content as function of oxygen fugacity. *Geochim. Cosmochim. Acta* **74**, 5926-5938.

Keppler, H. (2010) The distribution of sulfur between haplogranitic melts and aqueous fluids. *Geochim. Cosmochim. Acta* **74**, 645-660.

Kress, V.C. and Carmichael, I.S. (1989) The lime-iron-silicate melt system: Redox and volume systematics. *Geochim. Cosmochim. Acta* **53**, 2883-2892.

Kress, V.C. and Carmichael, I.S. (1991) The compressibility of silicate liquids containing Fe2O3 and the effect of composition, temperature, oxygen fugacity and pressure on their redox states. *Contrib. Mineral. Petrol.* **108**, 82-92.

Lattard, D., Sauerzapf, U. and Käsemann, M. (2005) New calibration data for the Fe–Ti oxide thermo-oxybarometers from experiments in the Fe–Ti-O system at 1 bar, 1,000-1,300°C and a large range of oxygen fugacities. *Contrib. Mineral. Petrol.* **149**, 735-754.

Lehmann, B. (1990) Metallogeny of tin (Lecture Notes in Earth Sciences 32). 211 pp.

Li, Y. and Audétat, A. (2012) Partitioning of V, Mn, Co, Ni, Cu, Zn, As, Mo, Ag, Sn, Sb, W, Au, Pb, and Bi between sulfide phases and hydrous basanite melt at upper mantle conditions. *Earth Planet. Sci. Lett.* **355-356**, 327-340.

Li, Y. and Audétat, A. (2015) Effects of temperature, silicate melt composition, and oxygen fugacity on the partitioning of V, Mn, Co, Ni, Cu, Zn, As, Mo, Ag, Sn, Sb, W, Au, Pb, and Bi between sulfide phases and silicate melt. *Geochim. Cosmochim. Acta* **162**, 25-45.

Libourel, G., Marty, B. and Humbert, F. (2003) Nitrogen solubility in basaltic melt. Part I. Effect of oxygen fugacity. *Geochim. Cosmochim. Acta* **67**, 4123-4135.

Lickfold, V., Cooke, D.R., Smith, S.G. and Ullrich, T.D. (2003) Endeavour copper-gold porphyry deposits, Northparkes, New South Wales: Intrusive history and fluid evolution. *Econ. Geol.* **98**, 1607-1636.

Lindsley, D.H. and Frost, B.R. (1992) Equilibria among Fe–Ti oxides, pyroxenes, olivine, and quartz; Part I, Theory. *Am. Mineral.* **77**, 987-1003.

Linnen, R.L., Pichavant, M. and Holtz, F. (1996) The combined effects of fO$_2$ and melt composition on SnO$_2$ solubility and tin diffusivity in haplogranitic melts. *Geochim. Cosmochim. Acta* **60**, 4965-4976.

Linnen, R.L., Pichavant, M. and Holtz, F. (1996) The combined effects of f O2 and melt composition on SnO 2 solubility and tin diffusivity in haplogranitic melts. *Geochim. Cosmochim. Acta* **60**, 4965-4976.

Luhr, J.F. (1990) Experimental phase relations of water-and sulfur-saturated arc magmas and the 1982 eruptions of El Chichón volcano. *J. Petrol.* **31**, 1071-1114.

Luhr, J.F. (2008) Primary igneous anhydrite: Progress since its recognition in the 1982 El Chichón trachyandesite. *J. Volcanol. Geotherm. Res.* **175**, 394-407.

Mallmann, G. and O'Neill, H.S.C. (2009) The crystal/melt partitioning of V during mantle melting as a function of oxygen fugacity compared with some other elements (Al, P, Ca, Sc, Ti, Cr, Fe, Ga, Y, Zr and Nb). *J. Petrol.* **50**, 1765-1794.

Masotta, M. and Keppler, H. (2015) Anhydrite solubility in differentiated arc magmas. *Geochim. Cosmochim. Acta* **158**, 79-102.

Matthews, W., Linnen, R.L. and Guo, Q. (2003) A filler-rod technique for controlling redox conditions in cold-seal pressure vessels. *Am. Mineral.* **88**, 701-707.

McDonough, W.F. and Sun, S.-S. (1995) The composition of the Earth. *Chem. Geol.* **120**, 223-253.

Mysen, B.O. and Virgo, D. (1985) Structure and properties of fluorine-bearing aluminosilicate melts: the system Na2O-Al2O3-SiO2-F at 1 atm. *Contrib. Mineral. Petrol.* **91**, 205-220.

Mysen, B.O. and Toplis, M.J. (2007) Structural behavior of Al3+ in peralkaline, metaluminous, and peraluminous silicate melts and glasses at ambient pressure. *Am. Mineral.* **92**, 933-946.

Mysen, B.O., Virgo, D. and Kushiro, I. (1981) The structural role of aluminum in silicate melts; a Raman spectroscopic study at 1 atmosphere. *Am. Mineral.* **66**, 678-701.

O'Neill, H.S.C. and Eggins, S.M. (2002) The effect of melt composition on trace element partitioning: an experimental investigation of the activity coefficients of FeO, NiO, CoO, MoO 2 and MoO 3 in silicate melts. *Chem. Geol.* **186**, 151-181.

Price, G. (1981) Diffusion in the titanomagnetite solid solution series. *Mineral. Mag* **44**, 195-200.

Putirka, K. (2016) Rates and styles of planetary cooling on Earth, Moon, Mars, and Vesta, using new models for oxygen fugacity, ferric-ferrous ratios, olivine-liquid Fe-Mg exchange, and mantle potential temperature. *Am. Mineral.* **101**, 819-840.

Ridolfi, F. and Renzulli, A. (2011) Calcic amphiboles in calc-alkaline and alkaline magmas: thermobarometric and chemometric empirical equations valid up to 1,130°C and 2.2 GPa. *Contrib. Mineral. Petrol.* **163**, 877-895.

Ridolfi, F., Renzulli, A. and Puerini, M. (2010) Stability and chemical equilibrium of amphibole in calc-alkaline magmas: an overview, new thermobarometric formulations and application to subduction-related volcanoes. *Contrib. Mineral. Petrol.* **160**, 45-66.

Righter, K. and Drake, M.J. (1997) Metal-silicate equilibrium in a homogeneously accreting earth: new results for Re. *Earth Planet. Sci. Lett.* **146**, 541-553.

Righter, K., Leeman, W.P. and Hervig, R.L. (2006) Partitioning of Ni, Co and V between spinel-structured oxides and silicate melts: Importance of spinel composition. *Chem. Geol.* **227**, 1-25.

Righter, K., Sutton, S.R., Newville, M., Le, L., Schwandt, C.S., Uchida, H., Lavina, B. and Downs, R.T. (2006) An experimental study of the oxidation state of vanadium in spinel and basaltic melt with implications for the origin of planetary basalt. *Am. Mineral.* **91**, 1643-1656.

Rudnick, R.L. and Fountain, D.M. (1995) Nature and composition of the continental crust: a lower crustal perspective. *Rev. Geophys.* **33**, 267-309.

Scaillet, B. and Evans, B.W. (1999) The 15 June 1991 eruption of Mount Pinatubo. I. Phase equilibria and pre-eruption P–T–fO2–fH2O conditions of the dacite magma. *J. Petrol.* **40**, 381-411.

Shand, S.J. (1943) Eruptive rocks: their genesis, composition, classification, and their relation to ore deposits with a chaper on meteorites.

Siersch, N. (2014) Magnetite solubility in hydrous rhyolite melts at 700-900 °C and 200 MPa. *Master's report BGI*.

Smythe, D.J. and Brenan, J.M. (2015) Cerium oxidation state in silicate melts: Combined fO_2, temperature and compositional effects. *Geochim. Cosmochim. Acta* **170**, 173-187.

Smythe, D.J. and Brenan, J.M. (2016) Magmatic oxygen fugacity estimated using zircon-melt partitioning of cerium. *Earth Planet. Sci. Lett.* **453**, 260-266.

Stern, C.R., Funk, J.A., Skewes, M.A. and Arévalo, A. (2007) Magmatic anhydrite in plutonic rocks at the El Teniente Cu-Mo deposit, Chile, and the role of sulfur-and copper-rich magmas in its formation. *Econ. Geol.* **102**, 1335-1344.

Stormer, J.C. (1983) The effects of recalculation on estimates of temperature and oxygen fugacity from analyses of multicomponent iron-titanium oxides. *Am. Mineral.* **68**, 586-594.

Sun, S.-S. and McDonough, W.-s. (1989) Chemical and isotopic systematics of oceanic basalts: implications for mantle composition and processes. *Geological Society, London, Special Publications* **42**, 313-345.

Taylor, J.R. and Wall, V.J. (1992) The behavior of tin in granitoid magmas. *Econ. Geol.* **87**, 403-420.

Toplis, M.J. and Corgne, A. (2002) An experimental study of element partitioning between magnetite, clinopyroxene and iron-bearing silicate liquids with particular emphasis on vanadium. *Contrib. Mineral. Petrol.* **144**, 22-37.

Trail, D., Watson, E.B. and Tailby, N.D. (2011) The oxidation state of Hadean magmas and implications for early Earth's atmosphere. *Nature* **480**, 79-82.

Trail, D., Bruce Watson, E. and Tailby, N.D. (2012) Ce and Eu anomalies in zircon as proxies for the oxidation state of magmas. *Geochim. Cosmochim. Acta* **97**, 70-87.

Wilke, M., Behrens, H., Burkhard, D.J. and Rossano, S. (2002) The oxidation state of iron in silicic melt at 500 MPa water pressure. *Chem. Geol.* **189**, 55-67.

Wones, D. (1981) Mafic silicates as indicators of intensive variables in granitic magmas. *Mining Geol.* **31**, 191-212.

Wones, D.R. (1989) Significance of the assemblage titanite+ magnetite+ quartz in granitic rocks. *Am. Mineral.* **74**, 744-749.

Wones, D. and Eugster, H. (1965) Stability of biotite–experiment theory and application. *Am. Mineral.* **50**, 1228-1272.

Xirouchakis, D., Lindsley, D.H. and Frost, B.R. (2001) Assemblages with titanite (CaTiOSiO4), Ca-Mg-Fe olivine and pyroxenes, Fe-Mg-Ti oxides, and quartz: Part II. Application. *Am. Mineral.* **86**, 254-264.

Zajacz, Z. (2015) The effect of melt composition on the partitioning of oxidized sulfur between silicate melts and magmatic volatiles. *Geochim. Cosmochim. Acta* **158**, 223-244.

Zhang, L. and Audétat, A. (2011) Vanadium partitioning between hydrous rhyolite melt and magnetite. *Annual report of the Bavarian Geoinstitute* **25**, 77-79.

5 List of manuscripts and statement of the author's contribution

1 Arató, R. and Audétat, A. (2017): Experimental calibration of a new oxybarometer for silicic magmas based on vanadium partitioning between magnetite and silicate melt. Geochim. Cosmochim. Acta, 209, 284-295.

The research idea was from my supervisor, Andreas Audétat (AA). In that study I carried out the partitioning experiments and prepared the samples for analysis. AA did all the LA-ICP-MS analyses. I evaluated the data. We did the interpretation and wrote the manuscript together.

2 Arató, R. and Audétat, A. (2017): Vanadium magnetite–melt oxybarometry of natural, silicic magmas: a comparison of various oxybarometers and thermometers. Contrib. Mineral. Petrol., 172(7).

The research idea was from AA. The samples for that study were collected by AA. Sample preparation was done partly by Raphael Njul, partly by AA and partly by myself. AA did all the LA-ICP-MS analyses. I evaluated the data. We did the interpretation and wrote the manuscript together.

3 Arató, R. and Audétat, A. (2017): FeTiMM – a new oxybarometer for mafic to felsic magmas, Geochemical Perspectives Letters, in press.

The research idea was from AA. In that study I carried out the partitioning experiments and prepared the samples for analysis. AA did all the LA-ICP-MS analyses. I evaluated the data and compiled the literature data for the calibration. We did the interpretation and wrote the manuscript together.

6 Experimental calibration of a new oxybarometer for silicic magmas based on vanadium partitioning between magnetite and silicate melt

Róbert Arató*, Andreas Audétat

Bayerisches Geoinstitut, Universität Bayreuth, 95440 Bayreuth, Germany

Abstract

Partition coefficients of vanadium between magnetite and rhyolitic silicate melt, $D_V^{mgt/melt}$, were experimentally determined as a function of oxygen fugacity (0.7-4.0 log units above the fayalite-magnetite-quartz buffer), temperature (800-1000 °C), melt aluminum saturation index (ASI=0.74-1.14), magnetite composition (0.2-14 wt% TiO_2) and pressure (1-5 kbar; at H_2O saturation). Experiments were performed by equilibrating small ($\leq$20 μm), V-free magnetite grains in V-doped silicate melts (~100 ppm V) and then analyzing both phases by LA-ICP-MS. Attainment of equilibrium was demonstrated by several reversal experiments. The results suggest that $D_V^{mgt/melt}$ depends strongly on fO_2, increasing by 1.5-1.7 log units from the MnO-Mn_3O_4 buffer to the Ni-NiO buffer, and to lesser (but still considerable) extents on melt alumina saturation index (ASI; increasing by 0.3-0.7 log units over 0.4 ASI units) and temperature (increasing by 0.3-0.7 log units over a 200 °C interval at a fixed fO_2 buffer). Magnetite composition and melt water content seem to have negligible effects. The data were fitted by the following linear regression equation:

$$\log D_V^{mgt/melt} = 0.3726 * \frac{10{,}000}{T} + 2.0465 * ASI - 0.4773 * \Delta FMQ - 2.1214$$

, in which temperature is given in K, ASI refers to molar $Al_2O_3/(CaO+Na_2O+K_2O)$ and ΔFMQ refers to the deviation of fO_2 (in log units) from the fayalite-magnetite-quartz buffer. This equation reproduces all of our data within 0.3 log units, and 89% of them within 0.15 log units. The main advantages of this new oxybarometer over classical magnetite–ilmenite oxybarometry are (1) that it can be applied to rocks that do not contain ilmenite, and (2) that it is easier to apply to slowly-cooled rocks such as granites.

* Author to whom correspondence should be addressed (robert.arato@uni-bayreuth.de)

6.1 Introduction

Oxygen fugacity (fO$_2$) is an important parameter in magmatic systems that affects the stability of mineral phases and fluid species (Lindsley and Frost, 1992; Keppler, 1993; Jugo et al., 2010). Furthermore, it affects mineral-melt and fluid-melt partition coefficients of many metals (Candela and Bouton, 1990; Taylor and Wall, 1992; Peiffert et al., 1994; Linnen et al., 1996; Jugo et al., 1999) and thus the mineralizing potential of intrusions (Ishihara, 1981; Lehmann, 1990; Blevin et al., 1996).

The most commonly applied method to constrain oxygen fugacity in intermediate to silicic rocks is Fe-Ti oxide thermobarometry (e.g. Buddington and Lindsley, 1964; Carmichael, 1967; Stormer, 1983; Andersen and Lindsley, 1988; Ghiorso and Sack, 1991; Lattard et al., 2005; Ghiorso and Evans, 2008). Other approaches are based on mineral reactions involving olivine, pyroxene, and/or sphene (Frost and Lindsley, 1992; Lindsley and Frost, 1992; Andersen et al., 1993; Xirouchakis et al., 2001), or biotite, K-feldspar and magnetite (Wones and Eugster, 1965; Wones, 1981). Most recently, oxygen fugacity has been estimated also from amphibole compositions (Ridolfi et al., 2009).

However, despite the various techniques listed above, reconstruction of magmatic fO$_2$ in Si-rich igneous rocks remains a challenging task, particularly in the case of intrusive rocks. There are only few intrusive rocks that contain unaltered assemblages of the above mentioned minerals, because in most cases the minerals were either destroyed or reset at subsolidus conditions, such that fO$_2$ estimation is either not possible anymore or leads to erroneous results. Furthermore, many samples contain only one Fe-Ti-oxide phase (magnetite or ilmenite), preventing application of the classical magnetite–ilmenite oxybarometry. The main goal of this study was to develop an oxybarometer that is based on phases which commonly occur as inclusions within quartz phenocrysts and thus were protected from subsolidus alteration. This oxybarometer can be applied to any silicic rock that contains magnetite, independent of whether or not the magma was saturated also in ilmenite.

For mineral–melt oxybarometry it is essential to focus on an element whose concentration varies as a function of oxygen fugacity in either the silicate melt or in a coexisting mineral phase, or to different extents in both. Further requirements are that the element of interest occurs in measurable amounts (i.e. above the detection limit of LA-ICP-MS measurements) in both phases, and that its concentration does not depend strongly on other factors such as mineral

composition or melt composition. Previous studies have shown that vanadium partitioning between magnetite and silicate melt, $D_V^{mgt/melt}$, fulfills the above-mentioned requirements, and several calibrations have been developed (Irving, 1978; Horn et al., 1994; Canil, 1999, 2002; Toplis and Corgne, 2002; Righter et al., 2006a; Righter et al., 2006b; Mallmann and O'Neill, 2009). However, most of these studies focused on mafic to ultramafic systems at very high temperatures, which are not applicable to upper crustal rhyolitic magmas. The aim of the current study is to fill this gap by developing an experimental calibration of the vanadium magnetite–melt oxybarometer at P-T-x conditions that are relevant for silicic, upper crustal magmas. Such an oxybarometer would be useful not only for rocks lacking ilmenite, but also for slowly-cooled rocks such as granites because both silicate melt and to a lesser degree magnetite commonly occur as inclusions within quartz phenocrysts (e.g., Anderson et al., 2000; Audétat and Pettke, 2006; Audétat, 2015; Zhang and Audétat, 2017). If such inclusions are not intersected by later cracks and are analyzed as entities by laser-ablation ICP-MS (LA-ICP-MS), their original compositions – and thus $D_V^{mgt/melt}$ partition coefficients and corresponding fO_2 values – can be reconstructed.

6.2 Experimental methods

The following starting glasses were used in our experiments: (i) Synthetic haplogranite glasses with aluminum saturation indices (ASI) of 0.7, 0.9 and 1.1, and (ii) natural obsidians from New Zealand, China and Armenia. The haplogranites were prepared from analytical grade SiO_2, $Al(OH)_3$, Na_2CO_3 and K_2CO_3. Their SiO_2 content was fixed at the value corresponding to the 2 kbar haplogranite eutectic melt composition ($Qz_{35}Ab_{40}Or_{25}$; Johannes and Holtz, 1996), and ASI was changed by varying Al_2O_3, Na_2O and K_2O at a constant Na/K-ratio. The powders were mixed, filled into Pt crucibles and decarbonated/dehydrated in a muffle furnace by heating to 1100 °C at a rate of 100 °C/hour. After keeping them at this temperature for two hours they were quenched in air. The recovered samples were homogenized and freed of gas bubbles by grinding them in an agate mortar to a grain size of <63 µm. Aliquots of these glass powders (plus of similarly prepared powders of natural obsidians) were then doped with ~1000 ppm V by mixing them thoroughly with VO_2 powder (< 20 µm) and remelting them in the oven at 1600 °C and atmospheric pressure for 4h. After this, the resulting glasses were powdered, mixed at a 1:9-ratio with V-free glass powder and melted once more at 1600 °C for 4 hrs to obtain glasses with V-

contents of ~100 ppm. Some of these glasses were further diluted with V-free counterparts to produce starting glasses containing ~10 ppm V, which were used to test Henry's law.

Stoichiometric magnetite with a constant grain size of 10-20 μm was synthetized hydrothermally from analytical-grade Fe_3O_4 powder dispersed in an aqueous solution that additionally contained a few grains of oxalic acid to prevent formation of hematite. The dispersion was filled into gold capsules of 4.3 mm O.D., 4.0 mm I.D. and 40 mm length, which subsequently were arc-welded and placed in rapid-quench cold-seal pressure vessels, where they were subjected to 800 °C and 2 kbar for 2.5 days. The resulting material was dried and checked under the polarizing microscope. Two compositions of Ti-bearing magnetite (6 and 12 wt% TiO_2, respectively) were synthetized in a gas-mixing furnace at 1300 °C and fO_2 corresponding to the NiNiO buffer using run times of 24 h. The densely sintered pellets were then crushed in an agate mortar to a grain size <20 μm.

Crushed, V-doped haplogranite glasses were mixed with magnetite powder to produce the starting material used for the partitioning experiments. In order to obtain magnetite-free glass domains of 50-100 μm size that are easily analyzable by LA-ICP-MS, the silicate glass was added in two grain size fractions of <63 μm and 63-160 μm, respectively. These glass fractions were mixed with magnetite powder – which partly dissolved in the melt during the experiments – at a weight ratio of ~2:2:1.

Fifty-four experiments were carried out in rapid-quench cold-seal pressure vessels at 1-2 kbar and 800-1000 °C, with oxygen fugacity fixed either at Ni-NiO, Re-ReO$_2$ or MnO-Mn$_3$O$_4$ buffer, i.e., 0.7, 2.5 and 4 log units above the fayalite-magnetite-quartz (FMQ) buffer, respectively (Table 6.1). This range of conditions is representative for most upper crustal silicic magma chambers, except that no experiments were conducted at temperatures <800 °C due to slow diffusion rates. An experimental charge usually consisted of three inner $Au_{80}Pd_{20}$ capsules (3.0 mm O.D. and 2.7 mm I.D.) that contained the haplogranite melts + magnetite + excess H_2O, and which were placed in an outer Au capsule (4.3 mm O.D. and 4.0 mm I.D.) containing the fO_2 buffer + H_2O (Fig. 6.1). In the first run we also tested an inner Pt capsule and an inner $Pd_{75}Ag_{25}$ capsule, which were deemed less useful due to Fe-uptake and embrittlement, respectively, although the obtained $D_V^{mgt/melt}$ data agreed with those obtained in the $Au_{80}Pd_{20}$ capsule. The capsules were loaded into rapid-quench cold-seal pressure vessels pressurized with water (for details regarding the design, see Matthews et al., 2003) and heated isobarically to 800-1000 °C at
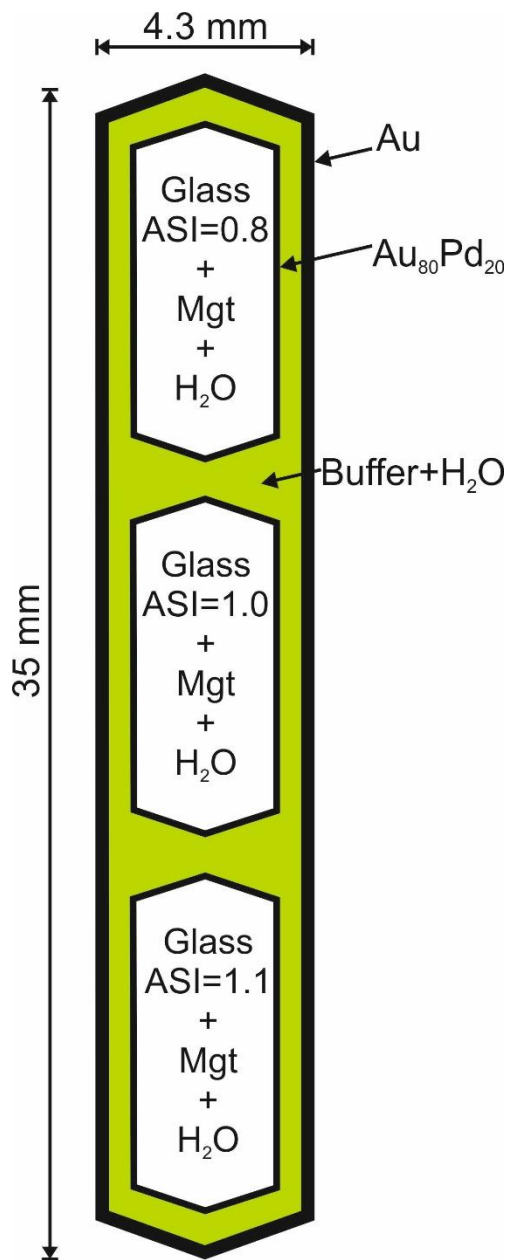
Fig. 6.1 Schematic drawing of a typical capsule setup. Samples with contrasting alumina saturation index (ASI; = molar $Al_2O_3/(CaO+Na_2O+K_2O)$) are contained within three inner $Au_{80}Pd_{20}$ capsules, which are placed together with fO_2 buffers (Ni-NiO, Re-ReO$_2$ or MnO-Mn$_3$O$_4$) and H_2O in an outer Au capsule.

1 or 2 kbar within 30-50 minutes. Uncertainties in temperature and pressure are estimated at ±10 °C and ±50 bar, respectively. The experiments lasted between 2 and 22 days, which durations were demonstrated to be sufficiently long to reach equilibrium between magnetite and melt (Zhang and Audétat, 2011; see below). This is further supported by the fact that no compositional gradients are observed in our experimental glasses. The experiments were stopped by rapid in-situ quenching, causing the experimental charges to cool below the glass transition temperature within 2-3 seconds. One experiment (RA-V37) was conducted in an end-loaded piston cylinder using ½-inch MgO–NaCl assemblies and stepped graphite heaters. The experimental conditions were 800 °C and 5 kbar, at an oxygen fugacity controlled by the Ni-NiO buffer. Temperature was measured by a type "S" (Pt/Pt$_{90}$Rh$_{10}$) thermocouple. Uncertainties in recorded pressure and temperature are considered ±0.5 kbar and ±20 °C, respectively. The sample was isobarically heated to the desired run temperature at a pressure of ca. 4.5 kbar, and subsequently pressurized to the final value of 5 kbar (i.e., "hot-piston in"). The run was terminated by switching off the power, which resulted in cooling below 100 °C within less than 10 seconds. For this run, a triple-capsule design was used. Two samples with different ASI were contained in inner $Au_{80}Pd_{20}$ capsules (1.6 mm O.D. and 1.2 mm I.D.), which themselves were placed together with Ni-NiO and H_2O into an outer Pt$_{95}$Rh$_5$ capsule (5.0 mm O.D. and 4.4 mm I.D.) that was lined with a slightly smaller gold capsule (4.3 mm O.D. and 4.0 mm I.D.). The latter was necessary to reduce H_2-loss through the PtRh alloy.

Recovered samples were cleaned, dried, and weighed to check for potential leaks during the experiments. After opening the outer capsule, the pH of the quench fluid was tested by pH paper, and the integrity of the buffer was checked under the microscope. Runs in which one of the buffer components became exhausted were discarded. Fragments of magnetite-bearing silicate glasses recovered from the inner capsules were prepared as doubly-polished, ca. 200 µm thick mounts for LA-ICP-MS analysis.

6.3   Analytical methods

The run products were analyzed by LA-ICP-MS using a system consisting of a GeolasPro 193 nm ArF Excimer Laser (Coherent, USA) attached to an Elan DRC-e (Perkin Elmer, Canada) quadrupole mass spectrometer. The ICP-MS was tuned to a ThO/Th rate of 0.05-0.1 % and a Ca^{2+}/Ca^+ rate of 0.1-0.2 % according to measurements on NIST SRM 610 glass (Jochum et al., 2011). The sample chamber was flushed with He gas at a rate of 0.4 l/min, to which 5 ml/min H_2 gas was added on its way to the ICP-MS. The following isotopes were analyzed: ^{23}Na, ^{25}Mg, ^{27}Al, ^{29}Si, ^{39}K, ^{49}Ti, ^{51}V, ^{53}Cr, ^{55}Mn, ^{57}Fe, ^{62}Ni, ^{66}Zn, ^{140}Ce and ^{185}Re, with dwell times ranging from 10 to 50 ms. The laser beam was operated at 10 Hz frequency and a constant energy density of 10 J/cm^2 at the sample surface. Laser pit size was 40-30 µm for the silicate glasses and 15-30 µm for the magnetites. For each magnetite–melt pair the glass was measured first, followed by analysis of an adjacent area containing both magnetite and glass (Fig. 6.3).

Only areas with few, scattered magnetites were selected for this purpose because large accumulations of magnetite may have failed to completely equilibrate with the melt. The composition of magnetite was obtained by numerically subtracting glass of the first part of the signal until no Na was left in the second, mixed part of the signal. Since Fe, Ti, Mn and V partition strongly into the magnetite the residual signals of these elements are well-resolved, whereas the signal of Al and Mg is not, as these elements occur in higher amounts in the glass.

External standardization was based on NIST SRM 610 glass, which was measured twice before and after each block of 8-14 unknowns. Special attention was paid to precise determination of the aluminum saturation index (ASI) of the silicate glasses. For this purpose, a second, matrix-matched external standard in the form of a natural obsidian glass from Armenia was used to calculate the concentrations of Na, K and Al. This obsidian glass was thoroughly characterized by independent analyses with electron microprobe and LA-ICP-MS, using the NIST SRM 610

(Jochum et al., 2011), NIST SRM 621 and BAM-S005-A (Yang et al., 2012) standards. The raw signals were integrated and converted to element concentrations using in-house sheets of the Excel software. Internal standardization of the silicate glass analyses was obtained by normalizing the sum of Na_2O, MgO, Al_2O_3, SiO_2, K_2O, TiO_2 and FeO_{tot} to 100 %. The melts were calculated on an anhydrous basis, as the water content was found to have no effect on vanadium partitioning (see below). In the most Fe-rich glasses (4 wt% FeO_{tot}) the ignorance of the valence state of iron introduces an error of $\leq 0.4\%$ in the concentration of all other elements analyzed. Magnetite analyses were calculated by normalizing the sum of Fe_3O_4, MnO (typically ≤ 1 wt%) and TiO_2 (typically ≤ 0.6 wt%) to 100 wt%. Some uncertainty is introduced by the fact that Al_2O_3 is not included in this sum, which is due to the inability to reliably subtract the contribution of ablated silicate glass from the mixed signal. However, magnetites in rhyolites rarely contain more than 3 wt% Al2O3 (Ghiorso and Evans, 2008), hence the error introduced by not taking into account Al_2O_3 in the normalization procedure should be small.

Table 6.1 Overview of experiments and obtained results

Experiment	Glass type[a]	ASI[b]	V in starting glass (µg/g)	fO_2 buffer[c]	days	P (kbar)	T (°C)	Capsule (inner/ outer)	n[d]	V in mgt avg (µg/g)	V in mgt stdev[e] (µg/g)	V in melt avg (µg/g)	V in melt stdev[f] (µg/g)	$D_V^{mgt/melt}$ avg	$D_V^{mgt/melt}$ stdev[g]
RA-V03a	Haplogranite	0.72	100	MHO	7	2	800	AuPd/Au	7	300	20	47	2	6.3	0.2
RA-V03b	Haplogranite	0.93	100	MHO	7	2	800	AuPd/Au	7	370	60	20	3	18	1
RA-V03c	Haplogranite	1.08	100	MHO	7	2	800	AuPd/Au	7	730	150	15	4	48	5
RA-V04	Haplogranite	0.73	10	NNO	7	2	800	AuPd/Au	7	92	15	0.34	0.05	280	60
RA-V05a	Obsidian N.Z.	0.74	100	MHO	7	2	800	AuPd/Au	7	310	30	43	4	7.4	0.4
RA-V05b	Obsidian C.	0.85	100	MHO	7	2	800	AuPd/Au	6	480	80	35	5	14	1
RA-V05c	Obsidian A.	1.00	100	MHO	7	2	800	AuPd/Au	7	570	240	16	5	35	5
RA-V07a	Haplogranite	0.84	100	MHO	7	2	800	AuPd/Au	6	400	70	26	12	13	1
RA-V07b	Haplogranite	0.93	10	MHO	7	2	800	AuPd/Au	6	47	10	2.2	0.5	22	3
RA-V07c	Haplogranite	1.04	100	MHO	7	2	800	AuPd/Au	6	1800	500	38	12	47	7
RA-V08a	Haplogranite	0.90	100	MHO	7	2	800	Pt/Au	6	390	50	20	2	19	3
RA-V08b	Haplogranite	0.92	100	MHO	7	2	800	PdAg/Au	6	280	30	16	1	17	1
RA-V08c	Haplogranite	0.90	100	MHO	7	2	800	AuPd/Au	6	340	30	20	2	18	1
RA-V09a	Haplogranite	1.00	0[h]	MHO	7	2	800	AuPd/Au	6	1000	100	30	1	34	2
RA-V09b	Haplogranite	1.02	0[h]	MHO	7	2	800	AuPd/Au	6	14000	1000	430	30	34	2
RA-V09c	Haplogranite	0.90	100	MHO	7	2	800	AuPd/Au	6	390	50	22	2	17	2
RA-V10a	Haplogranite	0.72	100	NNO	7	2	800	AuPd/Au	7	1900	700	6.8	2.0	280	60
RA-V10b	Haplogranite	0.91	100	NNO	7	2	800	AuPd/Au	6	1600	300	1.7	0.2	980	150
RA-V10c	Haplogranite	1.11	100	NNO	7	2	800	AuPd/Au	4	1600	800	1.6	0.8	1200	400
RA-V11a	Haplogranite	0.73	100	RRO	7	2	800	AuPd/Au	6	960	60	21	2	47	4
RA-V11b	Haplogranite	0.90	100	RRO	7	2	800	AuPd/Au	7	970	180	7.1	1.0	140	10
RA-V12a	Haplogranite	0.72	100	NNO	7	2	900	AuPd/Au	7	1600	300	8.4	0.9	190	30
RA-V12b	Haplogranite	0.90	100	NNO	7	2	900	AuPd/Au	6	1100	400	1.4	0.4	860	290
RA-V12c	Haplogranite	1.07	100	NNO	7	2	900	AuPd/Au	5	1400	400	1.6	0.4	980	110
RA-V13a	Haplogranite	0.91	100	NNO	7	2	900	AuPd/Au	3	980	160	2.2	0.5	450	90
RA-V13b	Haplogranite	0.91	100	NNO	7	2	900	AuPd/Au	3	1500	100	3.3	0.1	460	40
RA-V13c	Haplogranite	0.90	100	NNO	7	2	900	AuPd/Au	4	1200	100	3.4	0.4	360	20
RA-V15a	Obsidian C.	0.82	100	NNO	7	2	800	AuPd/Au	6	1300	300	1.4	0.2	930	250
RA-V15b	Obsidian A.	1.00	100	NNO	7	2	800	AuPd/Au	6	1600	400	1.1	0.2	1500	500

RA-V15c	Haplogranite	1.13	100	NNO	7	2	800	AuPd/Au	5	8300	3900	3.4	0.6	2400	1000
RA-V17a	Haplogranite	0.72	100	NNO	7	2	900	AuPd/Au	6	1700	300	8.9	0.6	190	30
RA-V17b	Haplogranite	0.90	100	NNO	7	2	900	AuPd/Au	6	790	50	2.0	0.2	390	40
RA-V17c	Haplogranite	1.07	100	NNO	7	2	900	AuPd/Au	6	1700	200	2.0	0.2	850	50
RA-V18a	Haplogranite	0.70	100	MHO	7	2	900	AuPd/Au	6	320	20	76	3	4.2	0.1
RA-V18b	Haplogranite	0.87	100	MHO	7	2	900	AuPd/Au	6	410	30	34	4	12	2
RA-V18c	Haplogranite	1.07	100	MHO	7	2	900	AuPd/Au	6	670	120	38	7	18	1
RA-V19a	Haplogranite	0.72	100	NNO	3	1	950	AuPd/Au	6	2100	400	16	4	130	20
RA-V19b	Haplogranite	0.90	100	NNO	3	1	950	AuPd/Au	6	1800	400	5.1	0.8	340	50
RA-V19c	Haplogranite	1.07	100	NNO	3	1	950	AuPd/Au	6	1300	300	2.8	0.3	480	120
RA-V21a	Haplogranite	0.93	100	RRO	2	1.5	1000	AuPd/Au	6	810	40	27	2	30	1
RA-V21b	Haplogranite	0.91	100	RRO	2	1.5	1000	AuPd/Au	6	730	50	28	1	26	1
RA-V25a	Haplogranite	0.73	100	RRO	4	2	900	AuPd/Au	7	1400	200	51	6	28	1
RA-V25b	Haplogranite	1.00	100	RRO	4	2	900	AuPd/Au	7	1200	200	11	2	100	10
RA-V25c	Haplogranite	1.09	100	RRO	4	2	900	AuPd/Au	7	1300	200	8.7	1.4	150	10
RA-V28	Haplogranite	0.92	100	MHO	7	1	800	AuPd/Au	7	560	150	30	4	19	4
RA-V29a	Haplogranite	0.71	100	MHO	2.5	1	950	AuPd/Au	7	280	10	77	2	3.7	0.1
RA-V29b	Haplogranite	0.90	100	MHO	2.5	1	950	AuPd/Au	7	390	50	46	5	8.5	0.5
RA-V29c	Haplogranite	1.08	100	MHO	2.5	1	950	AuPd/Au	7	630	50	46	4	14	1
RA-V30a	Haplogranite	0.79	100	NNO	22	1	800	AuPd/Au	7	1800	800	6.1	1.8	280	60
RA-V30b	Haplogranite	1.04	100	NNO	22	1	800	AuPd/Au	7	1200	500	1.3	0.3	970	250
RA-V31a	Haplogranite	0.91	100	NNO	4	1	900	AuPd/Au	11	1000	400	1.8	0.4	540	130
RA-V31b	Haplogranite	1.10	100	NNO	4	1	900	AuPd/Au	7	1800	600	1.6	0.2	1100	300
RA-V37a	Haplogranite	0.90	100	NNO	3	5	800	AuPd/Au/PtRh	6	660	120	1.6	0.7	520	330
RA-V37b	Haplogranite	1.08	100	NNO	3	5	800	AuPd/Au/PtRh	6	1000	500	0.59	0.12	1800	700

[a] Obsidian N.Z., C. and A. refer to natural obsidians from New-Zealand, China and Armenia, respectively

[b] ASI= molar $Al_2O_3/(CaO+Na_2O+K_2O)$

[c] MHO=MnO-Mn_3O_4, RRO=Re-ReO_2, NNO=Ni-NiO

[d] number of analyzed magnetite-melt pairs

[e] 1σ standard deviation, calculated from n magnetite analyses

[f] 1σ standard deviation, calculated from n melt analyses

[g] 1σ standard deviation, calculated from n partition coefficients

[h] reverse experiments, V initially in magnetite

6.4 Results

Recovered samples consist of grains or clusters of magnetite embedded in optically transparent silicate glass (Fig. 6.2). The presence of large, isolated bubbles filled with
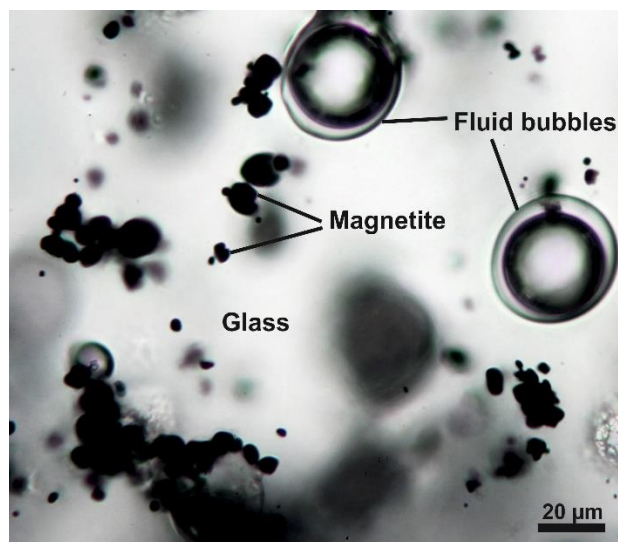
Fig. 6.2 Transmitted-light photomicrograph of a typical run product (run RA-V25). The presence of aqueous fluid bubbles proves that the sample was water-saturated.
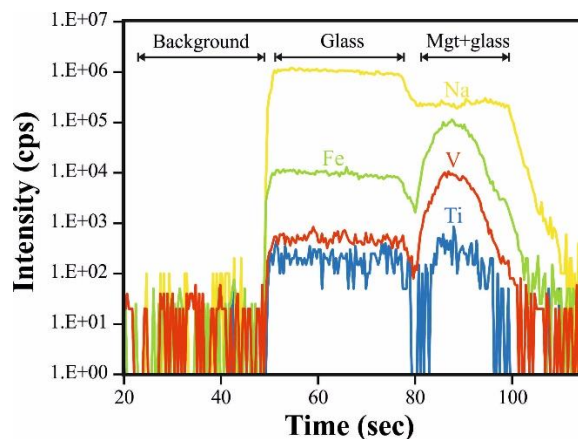
Fig. 6.3 LA-ICP-MS signal of silicate glass (ablated with 40 μm pit size) and an adjacent magnetite inclusion within silicate glass (ablated with 20 μm pit size) from experiment RA-V25c. The contribution of silicate glass in the second, mixed signal is numerically subtracted by removing element intensities in the same proportions as they occur in the first signal until no Na is left (see text). Concentrations of vanadium in the silicate glass and magnetite are 9 μg/g and 1300 μg/g, respectively.

aqueous fluid suggests that the experiments were saturated with an aqueous fluid phase, which is necessary to reach the fO_2 imposed by the external buffer. Neutral pH was found in all samples, meaning that there was no CO_2 (e.g. because of incomplete decarbonation of the glass), which could have changed the fO_2 and the fluid composition to acidic. The use of a coarse glass grain size fraction in the starting material resulted in magnetite-free areas of up to 100 μm size, which facilitated contamination-free LA-ICP-MS analyses. At the same time, these areas were small enough to allow complete equilibration with magnetite, as demonstrated by the absence of any compositional gradients. Due to partial dissolution of magnetite in the silicate melt during the experiments, all run product glasses contain appreciable amounts of Fe (0.5-6.0 wt% FeO$_{tot}$). An overview of conducted experiments and obtained results is provided in Table 6.1 and in Figure 6.4. Attainment of equilibrium was demonstrated by five reverse runs in a preliminary study (Zhang and Audétat, 2011) and two reverse runs in the present study. In the forward runs V-

bearing melt was equilibrated with V-free magnetite, whereas in the reverse runs V-bearing magnetite was equilibrated with V-free melt. The following forward vs. reverse run pairs were conducted in the preliminary study of Zhang and Audétat (2011): One pair each at Ni-NiO, Re-ReO$_2$ and MnO-Mn$_3$O$_4$ at 800 °C, 2 kbar, 7 days; one at Ni-NiO, 750 °C, 2 kbar, 10 days; and one at Ni-NiO, 850 °C, 2 kbar, 7 days. In all cases, the D$_V$$^{mgt/melt}$ values obtained in forward experiments agreed within uncertainty with the results from reverse experiments. One sigma standard deviations of all the obtained partition coefficients (including measurements from both forward and reverse runs) were ≤14% relative in the case of the Re-ReO$_2$ and MnO-Mn$_3$O$_4$-buffered runs and the Ni-NiO run conducted at 850 °C, and 20-50 % relative in the other two Ni-NiO-buffered runs. Similarly, the two reverse runs conducted in the present study (RA-V09a, b; conducted at 800 °C, MnO-Mn$_3$O$_4$ buffer) produced results that are perfectly consistent with those obtained during forward runs (Fig. 6.4; Table 6.1).

Adherence to Henry's law is demonstrated by the fact that results obtained from experiments conducted with ~100 ppm V in the starting glass are within uncertainty the same as those obtained from experiments conducted with only ~10 ppm V in the starting glass (Fig. 6.4). With the exception of some data obtained at 800 °C at the Ni-NiO buffer (see below) the D$_V$$^{mgt/melt}$ values are thus considered reliable.

At fixed ASI and temperature, D$_V$$^{mgt/melt}$ decreases by 1.5-1.7 log units as fO$_2$ increases from the Ni-NiO to the MnO-Mn$_3$O$_4$ buffer (Fig. 6.4). The strong influence of fO$_2$ renders application of D$_V$$^{mgt/melt}$ as an oxybarometer feasible. For any given oxygen fugacity buffer D$_V$$^{mgt/melt}$ decreases with increasing temperature (Fig. 6.4). However, this includes a large change in absolute fO$_2$ values because fO$_2$ increases with increasing temperature along each buffer curve (Frost, 1991). If one accounts for the effect of changing absolute oxygen fugacity, the net temperature effect actually turns out positive, with D$_V$$^{mgt/melt}$ increasing by 0.5-0.8 log units per 100 °C (supplementary Fig. 6.S1). However, since it is more practical to express fO$_2$ relative to a specific buffer (e.g., FMQ) we use this notation also for our overall regression equation (see below), resulting in a negative temperature term.

Another important parameter that affects D$_V$$^{mgt/melt}$ is the melt aluminum saturation index. Increasing ASI from 0.74 to 1.14 results in a 0.6 log units increase in D$_V$$^{mgt/melt}$ at 950 °C, and a 0.8 log units increase at 800 °C (Fig. 6.4). The large scatter of vanadium partition coefficients obtained in the Ni-NiO buffer at 800 °C appears to reflect problems to reach equilibrium. In this

case we consider the maximum values as most representative because failure to reach equilibrium results in artificially low $D_V^{mgt/melt}$ values.
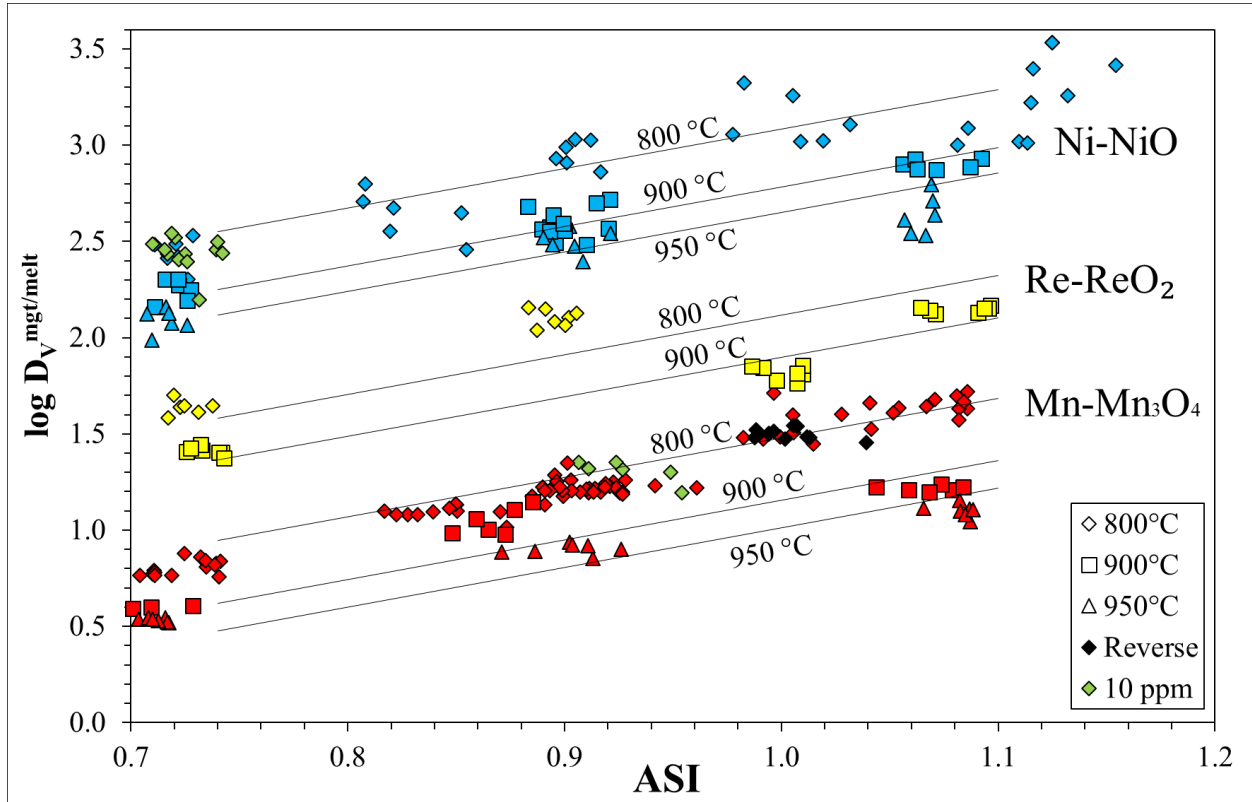
Fig. 6.4 Summary of experimental results as a function of oxygen fugacity buffer, temperature and melt composition. ASI= molar $Al_2O_3/(CaO+Na_2O+K_2O)$. Colors indicate different fO_2 buffers (shown on the right); symbol shapes indicate different temperatures. The solid lines represent fits through the data points using the linear regression given in equation (6.5). For the data at Ni-NiO and 800 °C only the maximum values are considered reliable. 10 ppm refers to 10 ppm VO_2 in the starting glass, as opposed to the concentration of 100 ppm VO_2 used in all other runs.

The effect of magnetite TiO_2 content on vanadium partitioning was tested at 900 °C at the Ni-NiO buffer, and at 1000 °C at the Re-ReO$_2$ buffer. For these experiments, two magnetite compositions containing 6 and 12 wt% TiO_2, respectively, were synthetized at 1300 °C in the gas mixing furnace and then equilibrated with V-bearing melt in the same manner as the other experiments. Although the TiO_2 content of the magnetite changed significantly during the experiments, it is evident that at the investigated T-fO_2 conditions the presence of up to 14 wt% TiO_2 does not significantly affect $D_V^{mgt/melt}$ (Fig. 6.5).
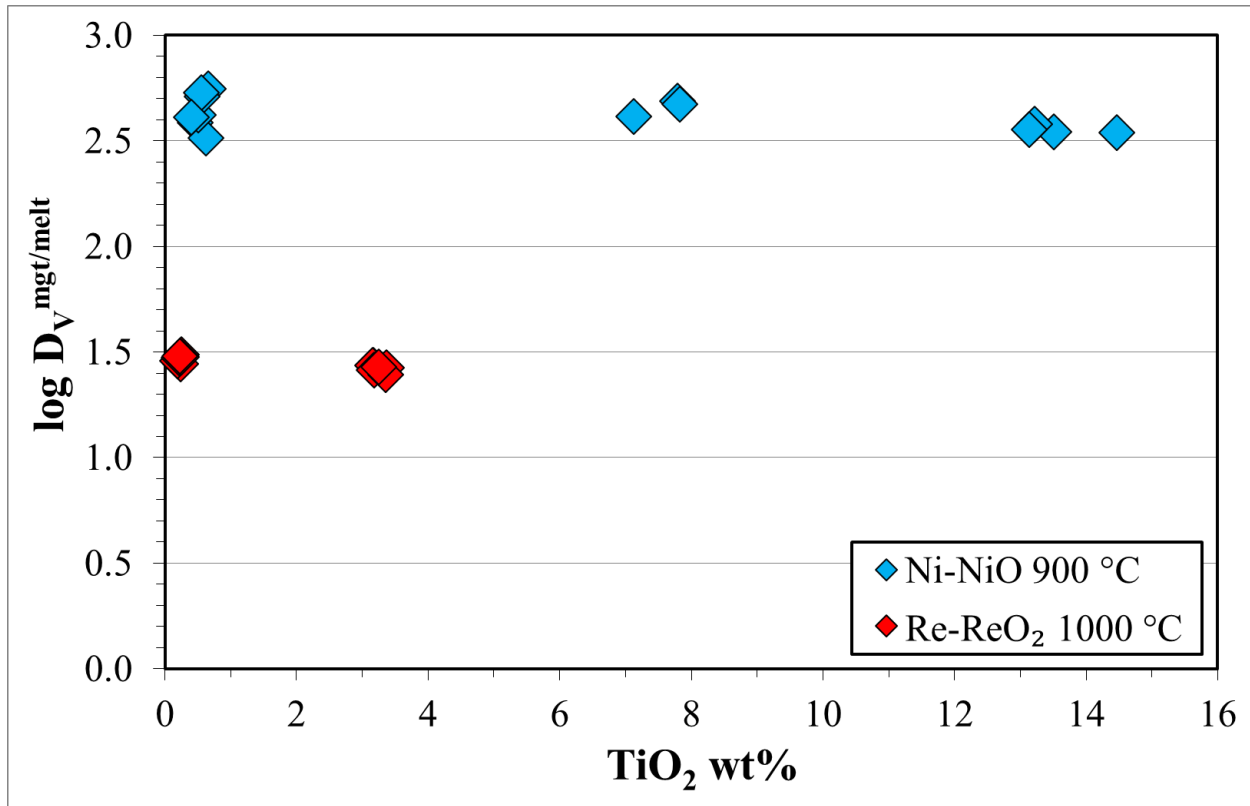
Fig. 6.5 Effect of magnetite TiO_2 content on $D_V^{mgt/melt}$ at two different temperatures and oxygen fugacity buffers.

The potential influence of pressure and melt H_2O content was investigated simultaneously, because at higher pressure, higher H_2O content is needed for H_2O saturation. Three runs were run at the Ni-NiO buffer at 800 °C (1, 2 and 5 kbar respectively), two runs at the Ni-NiO buffer at 900 °C (1 and 2 kbar), and two runs at the MnO-Mn_3O_4 buffer at 800 °C (1 and 2 kbar). Corresponding H_2O contents were ~4.0 wt% at 1 kbar, ~6.0 wt% at 2 kbar, and ~10 wt% at 5 kbar (Johannes and Holtz, 1996). Due to the higher viscosity and slower diffusion at low water contents the experiments conducted at 1 kbar were run for up to 22 days. The results (Fig. 6.6) suggest that at conditions relevant for upper crustal magma chambers there is no detectable combined effect of pressure/ melt water content on $D_V^{mgt/melt}$.
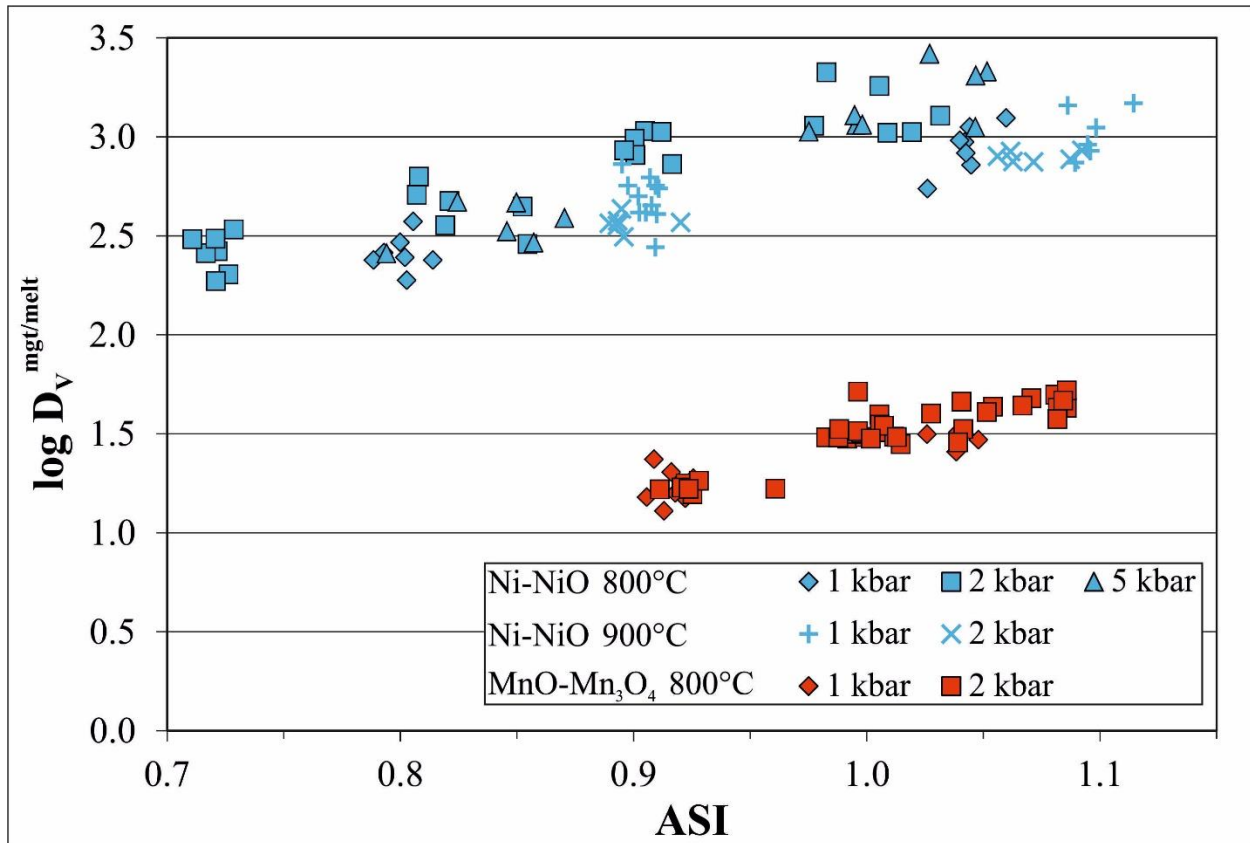
Fig. 6.6 Effect of pressure on $D_V{}^{mgt/melt}$ at various alumina saturation indices, temperatures and oxygen buffers. ASI= molar $Al_2O_3/(CaO+Na_2O+K_2O)$.

6.5 Discussion

In general, the $D_V{}^{mgt/melt}$ values obtained in the present study are reproducible and vary regularly with temperature and ASI, suggesting that equilibrium was attained. Exceptions are three runs conducted at 800 °C at the Ni-NiO buffer (RA-V10c, RA-V15b,c and RA-V30b), which show an unusually large scatter (Fig. 6.4). In these experiments attainment of equilibrium appears to have been hindered by a combination of (1) low temperatures, (2) lower average bond strength in the melt (e.g. Mysen et al., 2007) and (3) high partition coefficients (please note: V was initially in the melt), for which reason we regard anomalously low $D_V{}^{mgt/melt}$ values in these runs as not reliable.

The dependence of $D_V{}^{mgt/melt}$ on oxygen fugacity is related to a change in vanadium valence between magnetite and melt. The dominant valence of vanadium in magnetite is V^{3+}, substituting for $Fe^{3+}\pm Cr^{3+}$, Al^{3+} in the octahedral site (Toplis and Corgne, 2002; Righter et al., 2006b). In contrast, the dominant valence of vanadium in (basaltic) silicate melts at geologically realistic fO_2 conditions is either V^{4+} or V^{5+}, depending on fO_2 (Toplis and Corgne, 2002): V^{4+} is dominant

60

(~80%) at FMQ, whereas V^{5+} becomes dominant above ~FMQ+2.7. At extremely reducing conditions (<FMQ-8) V^{3+} becomes dominant. Consequently, the dependence of $D_V^{mgt/melt}$ on oxygen fugacity flattens out at extremely reduced conditions, but it flattens out also at very oxidized conditions (Mallmann and O'Neill, 2009) because other substitution mechanisms (e.g. Beattie, 1993) become dominant. The results of Mallmann and O'Neill suggest that over the comparatively small fO_2 range covered in the present study (FMQ+0.7 - FMQ+4.0) $D_V^{mgt/melt}$ should vary approximately linearly with oxygen fugacity. This interpretation is in good agreement with the results of the present study (Fig. 6.7), for which reason a linear dependence of $D_V^{mgt/melt}$ on oxygen fugacity is assumed.
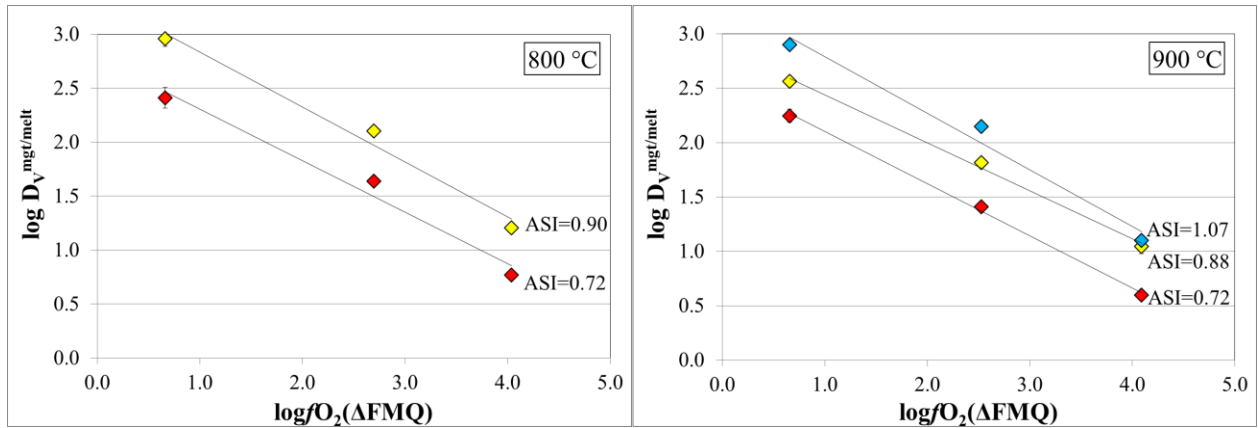
Fig. 6.7 Effect of oxygen fugacity on $D_V^{mgt/melt}$ at various alumina saturation indices, temperatures and oxygen buffers. Each data point corresponds to the average of all partition coefficients of one experiment and the corresponding error bars (in most cases smaller than the symbol size) represent 1 sigma standard deviations. ΔFMQ = relative to the fayalite-magnetite-quartz buffer. Solid lines represent linear fits through the data points.

Linear regression of our experimental data yields an average slope of log $D_V^{mgt/melt}$ vs. ΔFMQ of -0.4773 (±0.0044). This value can be explained by a combination of the following two reactions:

$$VO_{5/2}^{melt} = VO_{3/2}^{mgt} + 0.5O_2 \tag{6.1}$$

$$VO_2^{melt} = VO_{3/2}^{mgt} + 0.25O_2 \tag{6.2}$$

If the valence of V in the silicate melt is strongly dominated by V^{5+} (i.e., equation 6.1), then a 0.5 log unit decrease in fO_2 would correspond to one log unit increase in $D_V^{mgt/melt}$. On the other hand, if V^{4+} dominates (equation 6.2), the same change in the partition coefficient requires only 0.25 log unit decrease in fO_2. The fact that the value of 0.4773 is much closer to 0.5 than to 0.25 suggests that the dominant valence state of vanadium in the silicate melts of our experiments is probably V^{5+}, although the proportion of V^{5+} relative to V^{4+} certainly varied across the

investigated fO_2 range and accurate interpretation additionally depends on knowledge of the individual magnetite–melt partition coefficients for each valence state.

There has been no systematic study about the temperature effect on vanadium partitioning in which the effect of temperature could be clearly separated from other factors. Righter et al. (2006a) observed that $D_V^{spinel-melt}$ decreased with increasing temperature at the Ni-NiO buffer, but they observed no effect at NiNiO+3. In contrast, our study suggests that temperature has significant effect both at relatively reduced (Ni-NiO) and relatively oxidized (MnO-Mn$_3$O$_4$) conditions (Fig. 6.4). This trend persists also after subtracting the effect of temperature on absolute fO_2 along a given oxygen fugacity buffer (supplementary Fig. 6.S1). The contrasting observations can have two reasons: (1) we used much simpler spinel compositions (i.e. magnetite), allowing better separation of the effects of fO_2 versus temperature, or (2) the experiments of Righter et al (2006a) were carried out at higher temperatures (1150-1325 °C), where the effect of temperature may become difficult to resolve.

Evidence regarding the effect of melt composition on $D_V^{mgt/melt}$ has been ambiguous. Canil (1999) noticed a large variation of $D_V^{mgt/melt}$ in their experimentally investigated mafic and ultramafic compositions, but it is not clear whether this is due to changes in melt composition or due to corresponding changes in magnetite composition. In contrast, Toplis and Corgne (2002) argued for no significant compositional control in their basaltic andesitic to andesitic compositions, and also Mallmann and O'Neill (2009) did not invoke any compositional effect. The results of the present study suggest that the degree of melt polymerization has a rather strong effect, with $D_V^{mgt/melt}$ increasing by 0.6-0.8 log units as ASI changes from 0.74 to 1.14. The use of more silicic (=more polymerized) melts and distinctly lower temperatures (mostly 800-950 °C) in our experiments compared to previous investigations (1100-1300 °C) is likely the reason why our $D_V^{mgt/melt}$ values are 1-3 orders of magnitude higher than obtained in previous studies (e.g. Canil, 1999; Righter et al., 2006a; Righter et al., 2006b). A rigorous comparison with previous experimental data is thus not possible.

 Previous studies on mafic systems have identified major effects of magnetite composition on $D_V^{mgt/melt}$ (Nielsen et al., 1994; Canil, 1999, 2002; Righter et al., 2006b; Mallmann and O'Neill, 2009). Fortunately, spinels in rhyolitic magmas are compositionally much simpler than those of mafic magmas, containing negligible amounts of Cr$_2$O$_3$ and only minor amounts of MgO (typically $\leq$1 wt%, Ghiorso and Evans, 2008) and Al$_2$O$_3$ (typically $\leq$3 wt%; Ghiorso and Evans,

2008). The only two elements that are commonly present in substantial amounts are TiO_2 (up to 18 wt% at 1000 °C at NiNiO; Lattard et al., 2005) and – more rarely – MnO (up to 5 wt%; Audétat, 2015). The TiO_2 content decreases with decreasing temperature and increasing fO_2 (e.g. Ghiorso and Evans, 2008). As mentioned above, V^{4+} could potentially substitute for Ti^{4+} (Toplis and Corgne, 2002), whereas vanadium substitution for Mn^{2+} appears unlikely. We thus investigated only the effect of TiO_2 on magnetite–melt partitioning. The results show no discernable effect of up to 12 wt% TiO_2 on $D_V^{mgt/melt}$ (Fig. 6.5).

Vanadium partitioning between magnetite and melt can be expressed as an exchange with ferric and ferrous iron (equations 6.3 and 6.4; corresponding to equations 6.1 and 6.2 above):

$$VO_{2.5}^{melt} + 2FeO^{mgt} = VO_{1.5}^{mgt} + 2FeO_{1.5}^{melt} \qquad (6.3)$$

$$VO_2^{melt} + FeO^{mgt} = VO_{1.5}^{mgt} + FeO_{1.5}^{melt} \qquad (6.4)$$
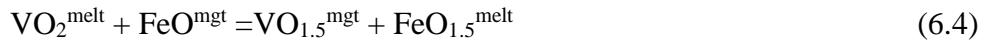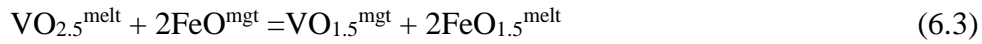
Hence, any parameter that affects the ferric-to-ferrous ratio in the silicate melt could potentially affect also $D_V^{mgt/melt}$. The most important parameter is fO_2, but also melt composition has been shown to be important (Kress and Carmichael, 1988). In fact, the decrease of $D_V^{mgt/melt}$ with decreasing ASI may be a consequence of changing Fe^{3+}/Fe^{2+} in the silicate melt, as this ratio has been shown to decrease with decreasing degree of melt polymerization at constant fO_2 (Dickenson and Hess, 1986). Another parameter that potentially affects Fe^{3+}/Fe^{2+} in the silicate melt is the melt water content, although no consensus has been found yet regarding this topic (Moore et al., 1995; Baker and Rutherford, 1996; Gaillard et al., 2001; Wilke et al., 2002; Humphreys et al., 2015). The results of our experiments conducted at 1-5 kbar (corresponding to 4-10 wt% H_2O; Johannes and Holtz, 1996) show no evidence for any effect of melt water content (or pressure) on $D_V^{mgt/melt}$ (Fig. 6.6).

The overall dependence of $D_V^{mgt/melt}$ on oxygen fugacity (ΔFMQ), temperature and melt composition observed in our study can be expressed in the form of the following multi-variable linear regression equation:

$$\log D_V^{mgt/melt} = 0.3726 * \frac{10,000}{T(K)} + 2.0465 * ASI - 0.4773 * \Delta FMQ - 2.1214 \quad (6.5)$$

This equation was obtained by least square fitting to 261 experimental data points, using the R software package (R Core Team, 2016). Details of the regression statistics can be found in supplementary Table 6.S1. Partition coefficients that were suspected to represent non-equilibrium conditions were excluded from the regression dataset. As discussed above, this was
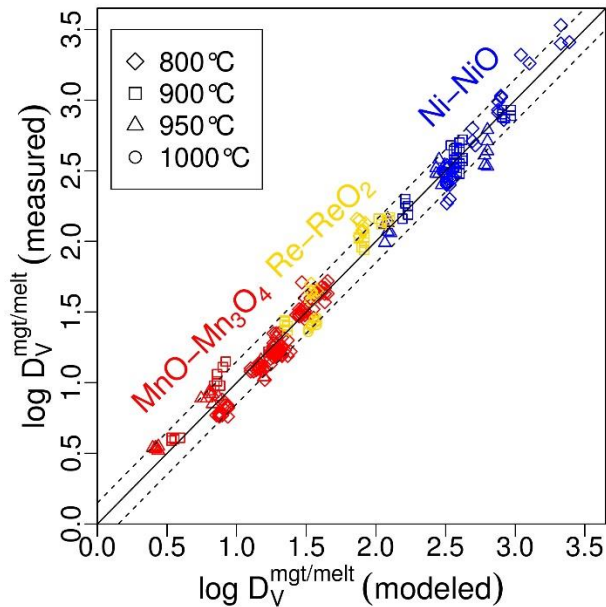
Fig. 6.8 Comparison of 261 measured $D_V^{mgt/melt}$ partition coefficients with corresponding values predicted by our linear regression equation. Not included are a few data points at 800 °C and Ni-NiO that appear to have not reached equilibrium (see text). The dashed lines represent 0.15 log units deviation from the 1:1 correspondence (solid line). Colors refer to indicated oxygen fugacity buffers.

done only for some values in three runs carried out at 800 °C at the Ni-NiO buffer, but the regression would be virtually the same if these values had been kept. Comparison of the experimental with the calculated values show excellent agreement, with all data points being reproduced within 0.3 log units, and 89% of the data points being reproduced within 0.15 log units (Fig. 6.8). At this point we like to emphasize that it is not recommended to apply this new approach to melt compositions and T-fO$_2$ conditions far outside the range used in this study.

6.6 Conclusions and future perspectives

The experimental data presented in this study allowed identification of the main factors controlling vanadium partitioning between magnetite and melt in silicic magmas. $D_V^{mgt/melt}$ is most strongly affected by fO$_2$, changing by 1.5-1.7 log units between the Ni-NiO and MnO-Mn$_3$O$_4$ buffers. This result thus confirms earlier studies noting a strong dependence of vanadium partitioning on oxygen fugacity. Two other major parameters are temperature and melt composition (ASI), whereas magnetite composition (TiO$_2$ content) and melt water content (pressure) appear to have no discernible effect. Our data are well described by a linear regression equation that considers the effects of fO$_2$ (expressed relative to FMQ), temperature and melt composition (ASI) on $D_V^{mgt/melt}$.

As mentioned in the introduction, the main motivation of this study was to develop an oxybarometer that is applicable for slowly-cooled rocks such as granites, via analysis of melt inclusions and magnetite inclusions preserved within quartz phenocrysts. However, since it requires only the presence of magnetite and silicate melt, the method can also be applied to

volcanic samples that lack ilmenite. The advantage in slowly-cooled rocks is that it is based on phases that commonly occur in the form of inclusions within phenocrysts. By drilling out entire, individual inclusions by LA-ICP-MS and integrating the obtained signals, any mineralogical changes that occurred within the inclusions (e.g., crystallization of the trapped silicate melt; exsolution of ilmenite lamella from magnetite) after their entrapment will be reversed and original compositions are obtained. In principle, the analysis of melt inclusions provides information on temperature (via zircon saturation temperature), ASI and the vanadium content of the silicate melt, whereas the analysis of coeval magnetite inclusions gives the vanadium content of the magnetite, which can be combined with the former to obtain $D_V^{mgt/melt}$. However, in the case of slowly-cooled, crystallized melt inclusions in quartz the reconstruction of ASI is problematic because these inclusions commonly lost Na after their entrapment (Zajacz et al., 2008; Audétat and Lowenstern, 2014). A potential solution to this problem is to use the ASI of corresponding whole rocks, but the validity of this approach needs to be tested.

The method can be also applied to rapidly quenched volcanic samples, in which case both magnetite phenocryst–glassy matrix and magnetite inclusion–glassy melt inclusion pairs may be used to obtain fO_2. However, caution should be exercised if the former approach (V partitioning between magnetite phenocrysts and matrix) wants to be used for samples containing crystallized matrix because the composition of both magnetite and matrix may have changed during cooling. Certainly, this approach should not be used if the magnetite phenocrysts show visible exsolution features or signs of alteration. Further difficulties could arise in highly evolved samples, where the vanadium content of the silicate melt may be too low to be detected in normal-sized melt inclusions, and in strongly peraluminous samples (ASI >1.1), where the melt composition effect on $D_V^{mgt/melt}$ may become increasingly non-linear. Again, we stress that the method should not be used to compositions outside the calibration range.

The new oxybarometer was extensively tested in a separate publication on 22 rhyolites and dacites, for which fO_2 could be independently constrained via magnetite–ilmenite oxybarometry. The results suggest that the new method provides accurate fO_2 values (≤0.5 log units deviation) if the analyzed magnetites and silicate melts can unambiguously be demonstrated to have coexisted with each other, but they also reveal that many samples record more complex histories than what it looks like at first sight.

6.7   Acknowledgements

6.8   References

Andersen, D.J. and Lindsley, D.H. (1988) Internally consistent solution models for Fe-Mg-Mn-Ti oxides: Fe-Ti oxides. *Am. Mineral.* **73**, 714-726.

Andersen, D.J., Lindsley, D.H. and Davidson, P.M. (1993) QUILF: A pascal program to assess equilibria among Fe–Mg–Mn–Ti oxides, pyroxenes, olivine, and quartz. *Comput. Geosci.* **19**, 1333-1350.

Anderson, A.T., Davis, A.M. and Lu, F. (2000) Evolution of Bishop Tuff rhyolitic magma based on melt and magnetite inclusions and zoned phenocrysts. J. Petrol. **41**, 449-473.

Audétat, A. (2015) Compositional evolution and formation conditions of magmas and fluids related to porphyry Mo mineralization at Climax, Colorado. *J. Petrol.* **56**, 1519-1546.

Audétat, A. and Pettke, T. (2006) Evolution of a Porphyry-Cu Mineralized Magma System at Santa Rita, New Mexico (USA). J. Petrol. **47**, 2021-2046.

Audétat, A. and Lowenstern, J.B. (2014) Melt inclusions. In Geochemistry of mineral deposits (ed. S. D. Scott). *Treatise on Geochemistry 2nd ed.* **13**, 143-173.

Baker, L.L. and Rutherford, M.J. (1996) The effect of dissolved water on the oxidation state of silicic melts. *Geochim. Cosmochim. Acta* **60**, 2179-2187.

Beattie, P. (1993) On the occurrence of apparent non-Henry's Law behaviour in experimental partitioning studies. Geochim. Cosmochim. Acta **57**, 47-55.

Blevin, P.L., Chappell, B.W. and Allen, C.M. (1996) Intrusive metallogenic provinces in eastern Australia based on granite source and composition. *Geological Society of America Special Papers* **315**, 281-290.

Buddington, A. and Lindsley, D. (1964) Iron-titanium oxide minerals and synthetic equivalents. *J. Petrol.* **5**, 310-357.

Candela, P.A. and Bouton, S.L. (1990) The influence of oxygen fugacity on tungsten and molybdenum partitioning between silicate melts and ilmenite. *Econ. Geol.* **85**, 633-640.

Canil, D. (1999) Vanadium partitioning between orthopyroxene, spinel and silicate melt and the redox states of mantle source regions for primary magmas. *Geochim. Cosmochim. Acta* **63**, 557-572.

Canil, D. (2002) Vanadium in peridotites, mantle redox and tectonic environments: Archean to present. *Earth Planet. Sci. Lett.* **195**, 75-90.

Carmichael, I.S.E. (1967) The iron-titanium oxides of salic volcanic rocks and their associated ferromagnesian silicates. *Contrib. Mineral. Petrol.* **14**, 36-64.

Dickenson, M. and Hess, P. (1986) The structural role and homogeneous redox equilibria of iron in peraluminous, metaluminous and peralkaline silicate melts. *Contrib. Mineral. Petrol.* **92**, 207-217.

Frost, B.R. (1991) Introduction to oxygen fugacity and its petrologic importance. *Rev. Mineral. Geochem.* **25**, 1-9.

Frost, B.R. and Lindsley, D. (1992) Equilibria among Fe-Ti oxides, pyroxenes, olivine, and quartz: Part II. Application. *Am. Mineral.* **77**, 1004-1004.

Gaillard, F., Scaillet, B., Pichavant, M. and Bény, J.-M. (2001) The effect of water and fO_2 on the ferric–ferrous ratio of silicic melts. *Chem. Geol.* **174**, 255-273.

Ghiorso, M.S. and Sack, O. (1991) Fe-Ti oxide geothermometry: thermodynamic formulation and the estimation of intensive variables in silicic magmas. *Contrib. Mineral. Petrol.* **108**, 485-510.

Ghiorso, M.S. and Evans, B.W. (2008) Thermodynamics of rhombohedral oxide solid solutions and a revision of the Fe-Ti two-oxide geothermometer and oxygen-barometer. *Am. J. Sci.* **308**, 957-1039.

Horn, I., Foley, S.F., Jackson, S.E. and Jenner, G.A. (1994) Experimentally determined partitioning of high field strength- and selected transition elements between spinel and basaltic melt. *Chem. Geol.* **117**, 193-218.

Humphreys, M.C.S., Brooker, R.A., Fraser, D.G., Burgisser, A., Mangan, M.T. and McCammon, C. (2015) Coupled interactions between volatile activity and Fe oxidation state during arc crustal processes. *J. Petrol.* **56**, 795-814.

Irving, A.J. (1978) A review of experimental studies of crystal/liquid trace element partitioning. *Geochim. Cosmochim. Acta* **42**, 743-770.

Ishihara, S. (1981) The granitoid series and mineralization. *Econ. Geol. 75th Anniv. Vol.*, 458-484.

Jochum, K.P., Weis, U., Stoll, B., Kuzmin, D., Yang, Q., Raczek, I., Jacob, D.E., Stracke, A., Birbaum, K., Frick, D.A., Günther, D. and Enzweiler, J. (2011) Determination of reference values for NIST SRM 610-617 glasses following ISO guidelines. *Geostand. Geoanal. Res.* **35**, 397-429.

Johannes, W. and Holtz, F. (1996) *Petrogenesis and experimental petrology of granitic rocks.* Springer. 335 pp.

Jugo, P., Candela, P. and Piccoli, P. (1999) Magmatic sulfides and Au:Cu ratios in porphyry deposits: an experimental study of copper and gold partitioning at 850 °C, 100 MPa in a haplogranitic melt–pyrrhotite–intermediate solid solution–gold metal assemblage, at gas saturation. *Lithos* **46**, 573-589.

Jugo, P.J., Wilke, M. and Botcharnikov, R.E. (2010) Sulphur K-edge XANES analysis of natural and synthetic basaltic glasses: Implications for S speciation and S content as function of oxygen fugacity. *Geochim. Cosmochim. Acta* **74**, 5926-5938.

Keppler, H. (1993) Influence of fluorine on the enrichment of high field strength trace elements in granitic rocks. *Contrib. Mineral. Petrol.* **114**, 479-488.

Kress, V.C. and Carmichael, I.S.E. (1988) Stoichiometry of the iron oxidation reaction in silicate melts. *Am. Mineral.* **73**, 1267-1274.

Lattard, D., Sauerzapf, U. and Käsemann, M. (2005) New calibration data for the Fe-Ti oxide thermo-oxybarometers from experiments in the Fe-Ti-O system at 1 bar, 1,000-1,300°C and a large range of oxygen fugacities. *Contrib. Mineral. Petrol.* **149**, 735-754.

Lehmann, B. (1990) *Metallogeny of tin (Lecture Notes in Earth Sciences 32)*. Springer. 211 pp.

Lindsley, D.H. and Frost, B.R. (1992) Equilibria among Fe-Ti oxides, pyroxenes, olivine, and quartz; Part I, Theory. *Am. Mineral.* **77**, 987-1003.

Linnen, R.L., Pichavant, M. and Holtz, F. (1996) The combined effects of fO$_2$ and melt composition on SnO$_2$ solubility and tin diffusivity in haplogranitic melts. *Geochim. Cosmochim. Acta* **60**, 4965-4976.

Mallmann, G. and O'Neill, H.S.C. (2009) The crystal/melt partitioning of V during mantle melting as a function of oxygen fugacity compared with some other elements (Al, P, Ca, Sc, Ti, Cr, Fe, Ga, Y, Zr and Nb). *J. Petrol.* **50**, 1765-1794.

Matthews, W., Linnen, R.L. and Guo, Q. (2003) A filler-rod technique for controlling redox conditions in cold-seal pressure vessels. *Am. Mineral.* **88**, 701-707.

Moore, G., Righter, K. and Carmichael, I. (1995) The effect of dissolved water on the oxidation state of iron in natural silicate liquids. *Contrib. Mineral. Petrol.* **120**, 170-179.

Mysen, B.O. and Toplis, M.J. (2007) Structural behavior of Al^{3+} in peralkaline, metaluminous,

and peraluminous silicate melts and glasses at ambient pressure. *Am. Mineral.* **92**, 933-946.

Nielsen, R.L., Forsythe, L.M., Gallahan, W.E. and Fisk, M.R. (1994) Major- and trace-element magnetite–melt equilibria. *Chem. Geol.* **117**, 167-191.

Peiffert, C., Cuney, M. and Nguyen-Trung, C. (1994) Uranium in granitic magmas: Part 1. Experimental determination of uranium solubility and fluid-melt partition coefficients in the uranium oxide-haplogranite-H$_2$O-Na$_2$CO$_3$ system at 720–770° C, 2 kbar. *Geochim. Cosmochim. Acta* **58**, 2495-2507.

R Core Team (2016) R: A language and environment for statistical computing. R Foundation for Statistical Computing, Vienna, Austria.

Ridolfi, F., Renzulli, A. and Puerini, M. (2009) Stability and chemical equilibrium of amphibole in calc-alkaline magmas: an overview, new thermobarometric formulations and application to subduction-related volcanoes. *Contrib. Mineral. Petrol.* **160**, 45-66.

Righter, K., Leeman, W.P. and Hervig, R.L. (2006a) Partitioning of Ni, Co and V between spinel-structured oxides and silicate melts: Importance of spinel composition. *Chem. Geol.* **227**, 1-25.

Righter, K., Sutton, S.R., Newville, M., Le, L., Schwandt, C.S., Uchida, H., Lavina, B. and Downs, R.T. (2006b) An experimental study of the oxidation state of vanadium in spinel and basaltic melt with implications for the origin of planetary basalt. *Am. Mineral.* **91**, 1643-1656.

Stormer, J.C. (1983) The effects of recalculation on estimates of temperature and oxygen fugacity from analyses of multicomponent iron-titanium oxides. *Am. Mineral.* **68**, 586-594.

Taylor, J.R. and Wall, V.J. (1992) The behavior of tin in granitoid magmas. *Econ. Geol.* **87**, 403-420.

Toplis, M.J. and Corgne, A. (2002) An experimental study of element partitioning between magnetite, clinopyroxene and iron-bearing silicate liquids with particular emphasis on vanadium. *Contrib. Mineral. Petrol.* **144**, 22-37.

Wilke, M., Behrens, H., Burkhard, D.J. and Rossano, S. (2002) The oxidation state of iron in silicic melt at 500 MPa water pressure. *Chem. Geol.* **189**, 55-67.

Wones, D. (1981) Mafic silicates as indicators of intensive variables in granitic magmas. *Mining Geology* **31**, 191-212.

Wones, D. and Eugster, H. (1965) Stability of biotite–experiment theory and application. *Am. Mineral.* **50**, 1228-&.

Xirouchakis, D., Lindsley, D.H. and Frost, B.R. (2001) Assemblages with titanite (CaTiOSiO$_4$), Ca-Mg-Fe olivine and pyroxenes, Fe-Mg-Ti oxides, and quartz: Part II. Application. *Am. Mineral.* **86**, 254-264.

Yang, Q.-C., Jochum, K.P., Stoll, B., Weis, U., Kuzmin, D., Wiedenbeck, M., Traub, H. and Andreae, M.O. (2012) BAM-S005 type A and B: New silicate reference glasses for microanalysis. *Geostand. Geoanal. Res.* **36**, 301-313.

Zajacz, Z., Halter, W.E., Pettke, T. and Guillong, M. (2008) Determination of fluid/melt partition coefficients by LA-ICPMS analysis of co-existing fluid and silicate melt inclusions: Controls on element partitioning. *Geochim. Cosmochim. Acta* **72**, 2169-2197.

Zhang, D. and Audétat, A. (2017) What Caused the Formation of the Giant Bingham Canyon Porphyry Cu-Mo-Au Deposit? Insights from Melt Inclusions and Magmatic Sulfides. **112**, 221-244.

Zhang, L. and Audétat, A. (2011) Vanadium partitioning between hydrous rhyolite melt and magnetite. *Annual report of the Bavarian Geoinstitute* **25**, 77-79

6.9   Supplementary information
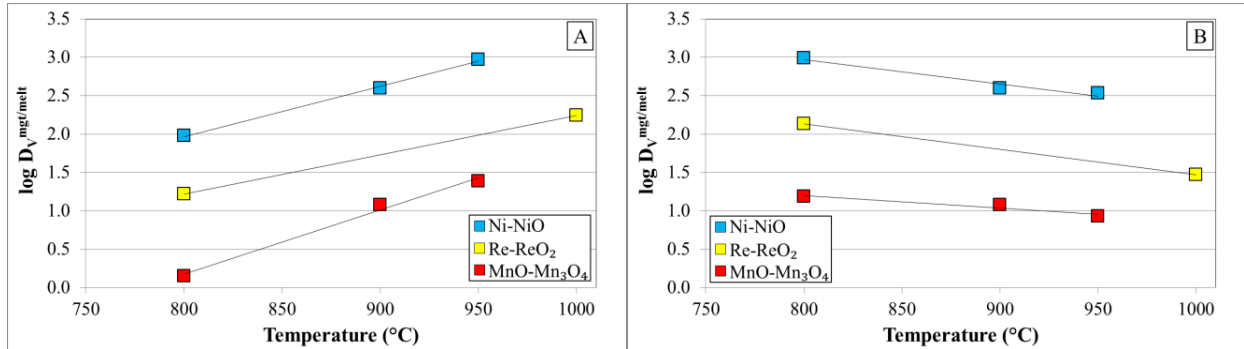
Fig. 6.S1 Effect of temperature on DVmgt/melt at constant pressure (2 kbar) and ASI (0.90). (A) Without considering the effect of changing absolute fO2 along a given oxygen buffer. (B) After subtracting the effect of changing absolute fO2. 1σ standard deviations are always smaller, than the symbol size.

Table 6.S1 Regression summary

lm(formula=logD ~ 10000/T + ASI + dFMQ)

Residuals:

	Min	1Q	Median	3Q	Max
					0.296786
	-0.27094	-0.07555	-0.00601	0.068696	

Coefficients:

	Estimate	Std. Error	t value	Pr(>|t|)	
(Intercept)	-2.12144	0.123484	-17.18	<2e-16	***
10000/T	0.372565	0.012744	29.23	<2e-16	***
ASI	2.046525	0.0505	40.52	<2e-16	***
dFMQ	-0.47726	0.004369	-109.23	<2e-16	***

Signif. codes: 0 '***' 0.001 '**' 0.01 '*' 0.05 '.' 0.1 ' ' 1

Residual standard error: 0.1008 on 257 degrees of freedom
Multiple R-squared: 0.9798, Adjusted R-squared: 0.9796
F-statistic: 4160 on 3 and 257 DF, p-value: < 2.2e-16

7 Vanadium magnetite–melt oxybarometry of natural, silicic magmas: a comparison of various oxybarometers and thermometers

Róbert Arató[*], Andreas Audétat

Bayerisches Geoinstitut, Universität Bayreuth, 95440 Bayreuth, Germany

Abstract

In order to test a recently developed oxybarometer for silicic magmas based on partitioning of vanadium between magnetite and silicate melt, a comprehensive oxybarometry and thermometry study on 22 natural rhyolites to dacites was conducted. Investigated samples were either vitrophyres or holocrystalline rocks in which part of the mineral- and melt assemblage was preserved only as inclusions within phenocrysts. Utilized methods include vanadium magnetite–melt oxybarometry, Fe-Ti-oxide thermometry and -oxybarometry, zircon saturation thermometry, and two-feldspar thermometry, with all analyses conducted by laser-ablation ICP-MS. Based on the number of analyses, the reproducibility of the results and the certainty of contemporaneity of the analyzed minerals and silicate melts the samples were grouped into three classes of reliability. In the most reliable (n=5) and medium reliable (n=10) samples, all fO$_2$ values determined via vanadium magnetite–melt oxybarometry agree within 0.5 log units with the fO$_2$ values determined via Fe-Ti-oxide oxybarometry, except for two samples of the medium reliable group. In the least reliable samples (n=7), most of which show evidence for magma mixing, calculated fO$_2$ values agree within 0.75 log units.

Comparison of three different thermometers reveals that temperatures obtained via zircon saturation thermometry agree within the limits of uncertainty with those obtained via two-feldspar thermometry in most cases, whereas temperatures obtained via Fe-Ti-oxide thermometry commonly deviate by ≥50 °C due to large uncertainties associated with the Fe-Ti-oxide model at T-fO$_2$ conditions typical of most silicic magmas. Another outcome of this study is that magma mixing is a common but easily overlooked phenomenon in silicic volcanic rocks,

---

[*] Róbert Arató ; robert.arato@uni-bayreuth.de

which means that great care has to be taken in the application and interpretation of thermometers and oxybarometers.

7.1 Introduction

Oxygen fugacity is an important thermodynamic parameter in magmatic systems, given that it exerts a first-order control on phase equilibria (e.g. Lindsley and Frost 1992; Keppler 1993; Jugo et al. 2010) as well as on mineral-melt and fluid-melt partition coefficients of many ore-forming metals (Candela and Bouton 1990; Taylor and Wall 1992; Peiffert et al. 1994; Linnen et al. 1996; Jugo et al. 1999) and thus the mineralizing potential of intrusions (Ishihara 1981; Lehmann 1990; Blevin et al. 1996).

The most commonly applied method to constrain oxygen fugacity in intermediate to silicic rocks is Fe-Ti oxide oxybarometry (e.g. Buddington and Lindsley 1964; Carmichael 1967; Stormer 1983; Andersen and Lindsley 1988; Ghiorso and Sack 1991; Lattard et al. 2005; Ghiorso and Evans 2008). Other approaches are based on mineral reactions involving olivine, pyroxene, and/or sphene (Frost and Lindsley 1992; Lindsley and Frost 1992; Andersen et al. 1993; Xirouchakis et al. 2001), or biotite, K-feldspar and magnetite (Wones and Eugster 1965; Wones 1981). Most recently, oxygen fugacity was estimated also from amphibole compositions (Ridolfi et al. 2009).

Despite the various existing techniques, reconstruction of magmatic fO$_2$ in silica-rich igneous rocks remains a challenging task, particularly in the case of intrusive members. There are only a few intrusive rocks that contain unaltered assemblages of the above mentioned minerals, because in most cases the necessary minerals were either destroyed or reset at subsolidus conditions, such that accurate estimation of magmatic fO$_2$ is not possible. This study applies a novel approach that is based on the measurement of melt inclusions and magnetite inclusions that were preserved within quartz phenocrysts and thus were protected from subsolidus- and hydrothermal alteration. If they are not intersected by later cracks and are analyzed as entities by laser-ablation ICP-MS (LA-ICP-MS), their original compositions – and thus $D_V^{mgt/melt}$ partition coefficients and corresponding fO$_2$ values – can be reconstructed also for slowly-cooled samples such as granites. Previous studies have shown that V partitioning between spinel-group minerals and silicate melt is a strong function of oxygen fugacity, thus, several calibrations have been developed to use $D_V^{sp/melt}$ as an fO$_2$ proxy (Irving 1978; Horn et al. 1994; Canil 1999; Canil 2002; Righter et al.

2006a; Righter et al. 2006b; Mallmann and O'Neill 2009). However, most of these studies focused on mafic to ultramafic systems at very high temperatures, which cannot be applied well to upper crustal rhyolitic magmas. A recent experimental calibration of the V magnetite–melt oxybarometer at P-T-x conditions relevant for silicic, upper crustal magmas by Arató and Audétat (2016) fills this gap. The study of Arató and Audétat (2016) showed that the partitioning of V depends strongly on oxygen fugacity, temperature and melt composition, whereas magnetite composition and pressure (or melt water content) have a negligible effect on $D_V^{mgt/melt}$. The above-mentioned dependence of V partitioning can be summarized in the following linear equation obtained by linear regression:

$$\Delta FMQ = -2.0511 * \log D_V^{mgt/melt} + 0.7809 * \frac{10,000}{T} + 4.2367 * ASI - 4.4767 \ (7.1)$$

, in which temperature is given in K, ASI refers to molar $Al_2O_3/(CaO+Na_2O+K_2O)$, and ΔFMQ refers to the deviation of fO_2 (in log units) from the fayalite-magnetite-quartz buffer. The intrinsic error associated with this model (i.e., the residual standard error of the regression) is ± 0.2091. The coefficients in this equation are slightly different from those that we would get by rearranging the equation reported in Arató and Audétat (2016); however, this difference results in less than 0.1 log unit difference in the predicted fO_2 (i.e., less than the overall error of the model).

The current study presents the first application of this oxybarometer on an extensive set of natural silicic rocks, where it is compared with the commonly applied magnetite-ilmenite (mgt-ilm) oxybarometer of Ghiorso and Evans (2008). A comparison with the mgt-ilm oxybarometer of Andersen and Lindsley (1985) was also made (Fig. 7.3c; supplementary Table 7.S1), but the calibration of Ghiorso and Evans (2008) is considered more reliable because (i) it is based on a more extensive experimental dataset, and (ii) because it accounts for the configurational entropy changes related to both the short-range cation order and the $R\overline{3}c$-$R\overline{3}$ order-disorder transition of the rhombohedral phase. In the beginning of this study we focused mainly on crystal-bearing obsidians (vitrophyres) because they have a high chance to contain fresh Fe-Ti-oxides, and because magnetite–melt partition coefficients of vanadium ($D_V^{mgt/melt}$) can easily be obtained by analyzing magnetite and ilmenite phenocrysts and the surrounding, glassy matrix. However, it soon became clear that some vitrophyres do not contain equilibrium mineral–melt assemblages, for which reason we extended our search to devitrified/crystallized samples containing well-

preserved silicate melt inclusions and coexisting (but spatially separate) inclusions of Fe-Ti-oxides within quartz and feldspar phenocrysts. Results of both types of samples are presented below. Furthermore, the study also includes a comparison of different thermometers, namely the mgt-ilm thermometer (Ghiorso and Evans 2008), the two-feldspar thermometer (Putirka 2008) and the zircon saturation thermometer (Watson and Harrison, 1983) aiming at identifying the most reliable one for use as temperature constraint for magnetite–melt V oxybarometry in silicic magmas.

7.2 Methods

A considerable array of silicic igneous rocks was investigated in the study. The aim was to cover a wide range of oxygen fugacities and temperatures, as well as to represent different melt compositions and geological settings (see Table 7.1 for sample list and Appendix for detailed sample description). In some samples all oxybarometers and thermometers could be applied simultaneously; however, lack of some mineral phases (or very low concentration of V in some highly evolved melts) facilitated application of only some methods in other samples.

Polished thick sections of approximately 300-400 µm thickness were prepared from each sample. These were carefully investigated under the petrographic microscope to search for fresh Fe-Ti oxide microphenocrysts, feldspar phenocrysts and quenched silicate melt, or, if these were not present, for Fe-Ti oxide-, feldspar- and melt inclusions preserved within quartz and feldspar phenocrysts (Fig. 7.1). Special attention was paid to signs of magma mixing and other characteristics that could reflect non-equilibrium conditions, such as more evolved melt inclusion compositions than matrix compositions, resorption- or alteration features, or multiple generations of individual mineral phases. Samples that showed any of these features were treated with special caution and were marked as "medium reliable" or "least reliable", depending on the severity of the signs.
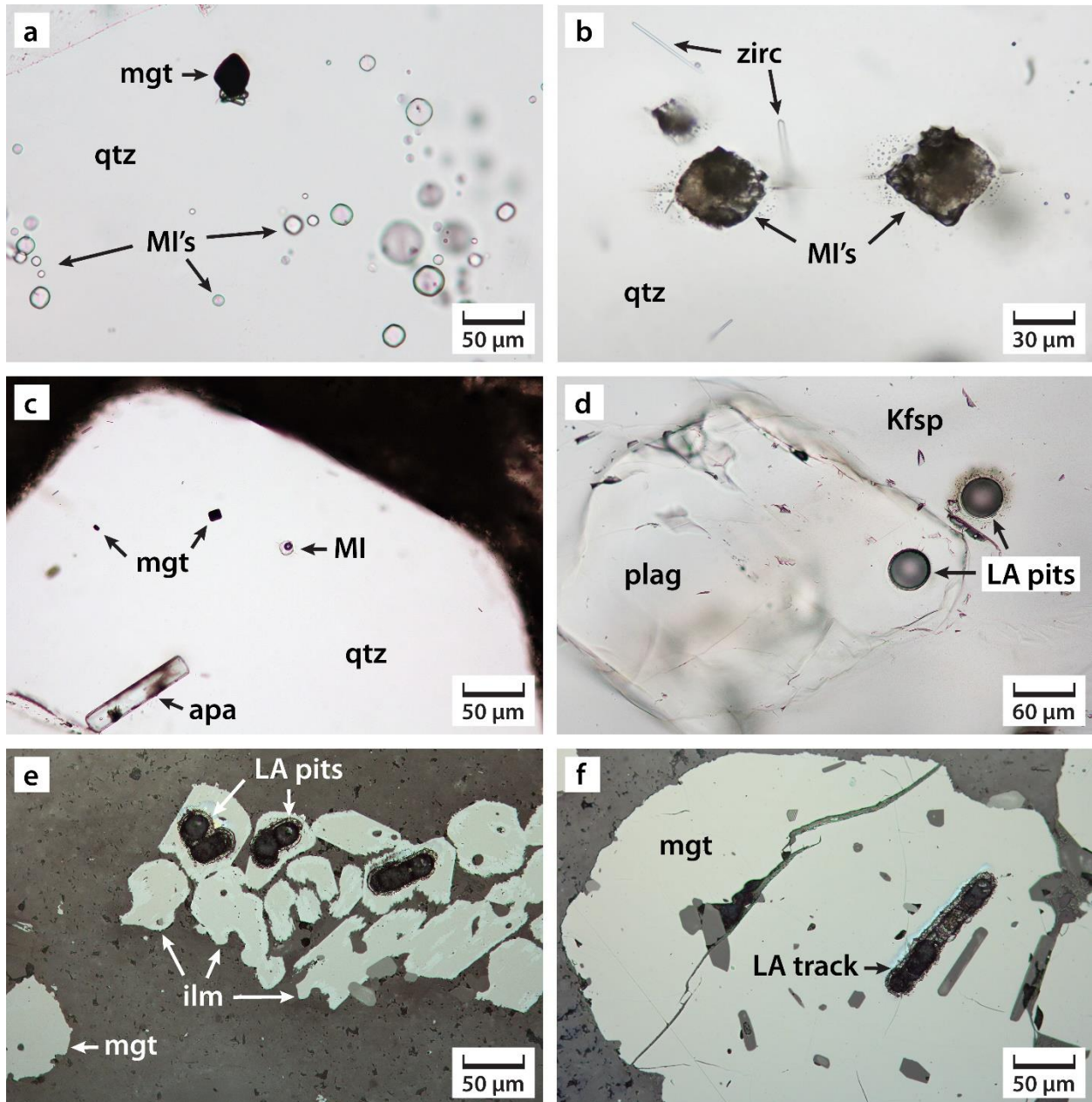
Fig. 7.1 Photomicrographs of various kinds of samples analyzed in this study. a Glassy melt inclusions (MI's) and a coeval magnetite inclusion (mgt; with two smaller, unknown minerals attached at its lower end) within a quartz phenocryst from the air fall tuff of Pine Grove, Utah. b Two crystallized melt inclusions (MI's) and several zircon needles (zirc) within a quartz phenocryst from the Lordsburg rhyolite, New Mexico. c A glassy melt inclusion (MI), two coeval magnetite inclusions (mgt), and an apatite inclusion (apa) within a quartz phenocryst from the Lordsburg rhyolite. d A plagioclase inclusion (plag) within a potassic feldspar phenocryst (Kfsp) from Parinacota, Chile. e Cluster of ilmenite crystals (ilm) and a single magnetite microphenocryst (mgt) from "The Dyke", Colorado. Notice the partly altered rims of the ilmenite crystals and the laser-ablation ICP–MS pits in the unaltered interiors. (f) magnetite microphenocryst from "The Dyke". Images a–d were taken in transmitted light; images e–f in reflected light.

Areas with measurable inclusions/mineral phases were cut out of each section by means of a diamond saw, and the pieces were then assembled on a glass mount for LA-ICP-MS analysis. Before the measurements, a detailed map was prepared of each mount on an A3 sized scan

image. All measurements were carried out by LA-ICP-MS (see below). Traditionally, Fe-Ti oxide pairs are measured by electron microprobe. However, we performed comparative tests on samples with homogeneous populations of Fe-Ti-oxides and found that LA-ICP-MS returns within error the same element concentrations as the electron microprobe (supplementary Table 7.S2). A major advantage of LA-ICP-MS is that it allows to analyze entire, unmixed Fe-Ti-oxide inclusions hosted within other phenocrysts and to reconstitute their original composition by integrating the signal, which approach was essential for this study and would not have been possible by using the electron microprobe.

Table 7.1 Overview of investigated samples and obtained results. Underlined temperature values were utilized to calculate fO2 via V partitioning oxybarometry (plotted in Fig. 7.3)

Sample name	mineralogy[a]	matrix	T zirc[b] (°C) (utilized ASI)	T two-fsp[c] (°C) (based on)	T mgt-ilm[d] (°C) (based on)	log fO$_2$ mgt-ilm[d] (ΔFMQ) (based on)	log fO$_2$ V-partitioning[e] (ΔFMQ) (based on)
Most reliable samples							
Oravita hyalodacite	plag, qtz, bio, amph, px, mgt, ilm, zirc, po	glassy	750 ± 10 (mx 0.96)	-	800 ± 60 (mp)	0.4 ± 0.3 (mp)	0.1 ± 0.2 (mp)
Mount Rano vitrophyre	plag, px, mgt, ilm, zirc	glassy	830 ± 10 (mx 1.01)	-	860 ± 10 (mp)	0.5 ± 0.1 (mp)	0.8 ± 0.1 (mp)
Parinacota vitrophyre	qtz, plag, Kfsp, bio, px, mgt, ilm, tit, zirc, po	glassy	720 ± 10 (mx 0.99) 720 ± 10 (MI 0.99)	730 ± 10 (fsp in fsp)	720 ± 80 (mp)	2.2 ± 0.2 (mp)	1.7 ± 0.4 (mp) 1.8 ± 0.2 (mp, MI)
Hideaway Park tuff	qtz, Kfsp, plag, bio, mgt, ilm, ap, zirc, tit, moly	altered	760 ± 10 (MI 1.04)	740 ± 10 (fsp in fsp)	670 ± 10 (incl)	1.2 ± 0.1 (incl)	1.7 ± 0.2 (incl)
Cottonwood tuff	qtz, plag, bio, amph, px mgt, ilm, po, zirc, ap	glassy	750 ± 30 (mx 1.01) 750 ± 10 (MI 0.98)	-	770 ± 50 (mp)	1.6 ± 0.3 (mp)	1.8 ± 0.1 (mp) 1.1 ± 0.3 (incl); 1.5 ± 0.3[f]
Medium reliable samples							
Lordsburg rhyolite	qtz, plag, Kfsp, bio, mgt, ilm, zirc, ap	altered	680 ± 10 (MI 1.05)	750 ± 30 (Kfsp+plag in qtz)	560 ± 20 (mgt incl, ilm mp)	2.3 ± 0.1 (mgt incl, ilm mp)	2.1 ± 0.5 (incl)
Lordsburg granodiorite	qtz, plag, Kfsp, bio, amph, mgt, ilm, tit, zirc, all	crystallized	770 (mx 0.98)	-	720 ± 30 (mp)	2.3 ± 0.1 (mp)	2.4 ± 0.1 (mp)
Smelter Knolls rhyolite	qtz. plag, Kfsp, bio, mgt, ilm, zirc, tit, fl, all	crystallized	670 ± 10 (MI 1.06) 690 (mx 1.01)	660 ± 40 (fsp pc)	710 ± 30 (mp) 630 ± 10 (incl)	2.3 ± 0.1 (incl) 2.3 ± 0.1 (mp)	2.5 ± 0.4 (incl)[g] 1.1 ± 0.5 (incl)[h]
Banco Bonito vitrophyre	qtz, plag, Kfsp, bio, px, mgt ilm, zirc, ap, po	glassy	760 ± 10 (mx 1.02) 740 ± 10 (MI 0.97)	-	800 ± 20 (mp)	2.1 ± 0.1 (mp)	2.1 ± 0.2 (mp)
Santa Rita rhyodacite (SR15)	qtz, plag, Kfsp, amph, bio, mgt, ilm, zirc, ap, anhy, tit, po	crystallized	710 ± 10 (MI 1.03) 760 ± 20 (mx 1.03)	840 ± 20 (Kfsp+plag in qtz)	770 (mp); 600 (incl)	2.3 (incl); 2.0 (mp)	2.2 ± 0.7 (incl) 2.5 ± 0.3 (mp)

	Minerals[a]	Texture	T zircon[b]	T fsp[c]	T mgt-ilm[d]	ASI	ΔFMQ[e]
Santa Rita rhyodacite (SR9)	qtz, plag, Kfsp, amph, bio, mgt, ilm, zirc, ap, anhy, tit, po	altered	725 ± 10 (MI 1.02)				2.2 ± 0.1 (incl)
The Dyke	qtz, Kfsp, plag, amph, bio, mgt, ilm, zirc, po	crystallized	730 ± 10 (MI 1.10)	790 ± 40 (fsp in fsp)	720 ± 80 (mp) 630 ± 10[i]	2.3 ± 0.1 (mp) 2.3 ± 0.1[i]	2.3 ± 0.3 (incl) 2.3 ± 0.3 (mp, MI)
Nomlaki tuff	plag, amph, px, mgt, ilm, zirc	glassy	790 ± 10 (mx 1.09)	-	810 ± 10 (mp)	2.0 ± 0.1 (mp)	2.8 ± 0.2 (mp)
Amalia tuff	qtz, plag, Kfsp, mgt, ilm, ti, zirc, ap, amph, px, moly, po	altered	N/A[j]	680 ± 30 (fsp pc)	770 ± 50 (incl)	1.6 ± 0.2 (incl)	1.5 ± 0.7 (incl) 1.6 ± 1.0 (mp, MI)
Kos granite enclave	qtz, plag, Kfsp, bio, mgt, ilm, zirc, ap, mon	crystallized	720 ± 20 (MI 1.13)	720 ± 30 (fsp pc)	590 ± 20 (mp)	1.3 ± 0.2 (mp)	2.5 ± 0.1 (mp, MI)
Least reliable samples							
Los Humeros vitrophyre	plag, mgt, ilm, px, zirc, ol	glassy	840 ± 10 (mx 0.98)	-	850 ± 30 (mp)	0.0 ± 0.1 (mp)	0.6 ± 0.1 (mp)
Glass Creek Dome vitrophyre	qtz, plag, Kfsp, mgt, ilm, ap, zirc, all, po	glassy	840 ± 20 (mx 0.97)	-	940 ± 140 (mp)	0.8 ± 0.4 (mp)	-0.1 ± 0.8 (mp)
Glass Creek Flow vitrophyre	qtz, plag, Kfsp, mgt, ilm, ap, zirc, all, po	glassy	870 ± 10 (mx 1.01)	910 ± 50 (fsp pc)	930 ± 30 (mp)	0.7 ± 0.1 (mp)	1.3 ± 0.1 (mp)
Mono #12 vitrophyre	qtz, plag, Kfsp, mgt, ilm, ap, zirc, all, po	glassy	770 ± 10 (mx 0.98)	-	880 ± 40 (mp)	0.7 ± 0.2 (mp)	1.4 ± 0.1 (mp)
Tunnel Spring Tuff	qtz, Kfsp, plag, bio, mgt, ilm, zirc, po	altered	660 ± 10 (MI 1.07)	760 ± 50 (fsp in fsp)	660 ± 40 (incl) 630 ± 10 (mp)	2.1 ± 0.2 (incl) 2.3 ± 0.2 (mp)	2.1 ± 0.4 (incl) 1.1 ± 0.3 (mp, MI)
Samples with temperature constraint only							
Blackfoot lava field vitrophyre	qtz, Kfsp, plag, biot, mgt, ilm, ap, zirc	glassy	770 ± 10 (MI 1.07)	720 ± 20 (fsp pc)	780 ± 10 (mp)	0.4 ± 0.1 (mp)	-
Pine Grove tuff	qtz, plag, Kfsp, bio, zirc, xe, mon, moly	altered	700 ± 10 (MI 0.99)	690 ± 10 (fsp in fsp)	-	-	-

abbreviations: ASI – aluminum saturation index; ΔFMQ – relative to the fayalite-magnetite-quartz buffer; incl – inclusion; MI – melt inclusion; mp – microphenocryst; pc – phenocryst; all – allanite; anhy – anhydrite; ap – apatite; bio – biotite; fl – fluorite; fsp – feldspar; ilm – ilmenite; Kfsp – potassic feldspar; mgt – magnetite; mon – monazite; ol – olivine; plag – plagioclase; po – pyrrhotite; px – pyroxene; qtz – quartz; tit – titanite; xe – xenotime; zirc – zircon; moly – molybdenite.

[a] including both minerals mentioned in the literature and minerals indentified in the present study; underlined minerals were analyzed

[b] calculated using the model of Watson and Harrison (1983); if several values are reported, the underlined result is considered more reliable.

[c] calculated using equation 27b of Putirka (2008)

[d] calculated using the model of Ghiorso and Evans (2008)

[e] calculated using the model of Arató and Audétat (2016)

[f] MI in feldspar and mgt in quartz

[g] MI and mgt in feldspar

[h] MI and mgt in quartz

[i] magnetite inclusions; ilmenite microphenocrysts

[j] peralkaline rock; zircon saturation thermometry model of Watson and Harrison (1983) is not applicable

The LA-ICP-MS system used for the measurements consists of a GeolasPro 193 nm ArF Excimer Laser (Coherent, USA) attached to an Elan DRC-e (Perkin Elmer, Canada) quadrupole

mass spectrometer. The ICP-MS was tuned to a ThO/Th rate of 0.05-0.1 % and a Ca^{2+}/Ca^+ rate of 0.1-0.2 % according to measurements on NIST SRM 610 glass (Jochum et al. 2011). The sample chamber was flushed with He gas at a rate of 0.4 l/min, to which 5 ml/min H_2 gas was added on its way to the ICP-MS. The following isotopes were analyzed: [11]B, [23]Na, [25]Mg, [27]Al, [29]Si, [39]K, [43]Ca, [49]Ti, [51]V, [53]Cr, [55]Mn, [57]Fe, [66]Zn, [85]Rb, [88]Sr, [89]Y, [90]Zr, [93]Nb, [98]Mo, [133]Cs, [137]Ba, [140]Ce, [178]Hf, [232]Th and [238]U, using dwell times ranging from 10 to 50 ms. The laser beam was operated at 10Hz frequency and an energy of 5-10 J/cm^2 at the sample surface. The laser pit size was usually 30-40 μm for exposed feldspars and silicate glasses, and 15-30 μm for exposed Fe-Ti-oxides, whereas for inclusions it was always chosen such that the complete inclusion volume was sampled.
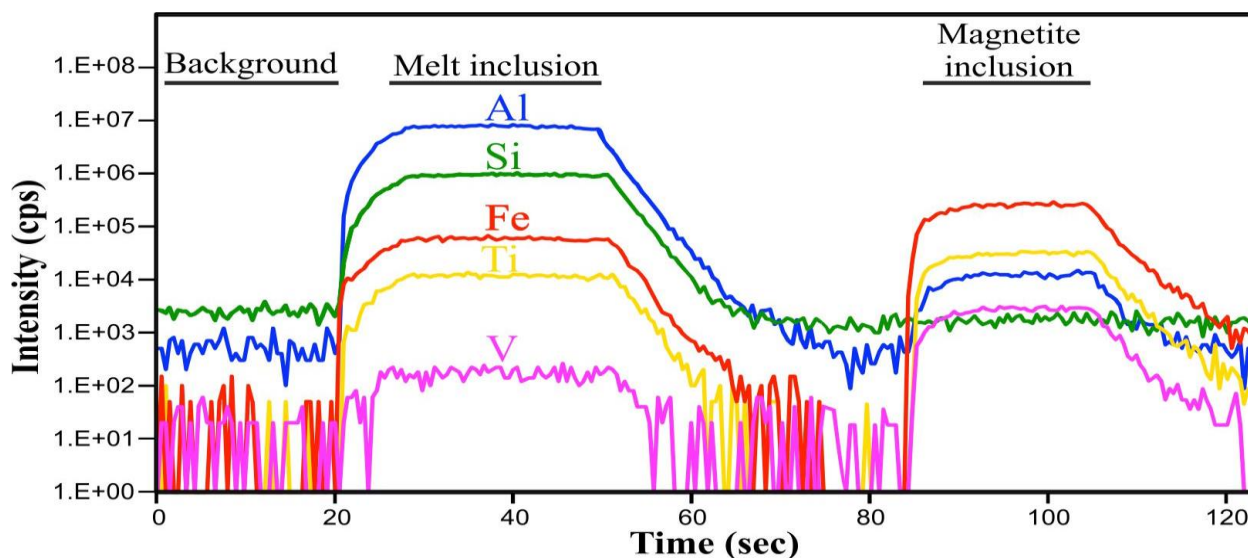
Fig 7.2 LA-ICP-MS signals of an exposed, glassy silicate melt inclusion in a quartz phenocryst (ablated with 50 μm pit size) and of an exposed magnetite inclusion in a feldspar phenocryst (ablated with 20 μm pit size), both from the Amalia Tuff, New Mexico. The silicate melt contains 77 wt% SiO_2, 12 wt% Al_2O_3, 1.5 wt% FeO_{tot}, 0.13 wt% TiO_2, and 0.7 ppm V; the magnetite contains 85 wt% FeO_{tot}, 4.4 wt% TiO_2, and 150 ppm V.

Feldspars and melt inclusions / matrix glasses were usually measured first, followed by analysis of the Fe-Ti-oxide inclusions / microphenocrysts (Fig. 7.2). When measuring inclusions, co-ablation of the host crystal is unavoidable. The composition of silicate melt inclusions was obtained by using an internal standard (usually Al_2O_3; see below) and subtracting host quartz from the mixed signal until the value of the internal standard was reached. The composition of Fe-Ti-oxide inclusions was obtained by numerically subtracting host crystal (usually quartz or feldspar) until there was no Si left in the signal. Sometimes however, this correction was not sufficient, as the Fe-Ti-oxide inclusions were commonly trapped together with a small amount of

silicate melt. In the case of quartz-hosted inclusions a second correction was thus applied in which melt of the same composition as coexisting melt inclusions was numerically subtracted from the signal until no Na was left.

External standardization was based on NIST SRM 610 glass, which was measured twice before and after each block of up to 14 unknowns. Special attention was paid to precise determination of the aluminum saturation index (ASI) of the silicate glasses. For this purpose, a second, matrix-matched external standard in the form of a natural obsidian glass from Armenia was used to calculate the concentrations of Na, K and Al. This obsidian glass was thoroughly characterized via independent analyses obtained by electron microprobe and LA-ICP-MS, using the NIST SRM 610 (Jochum et al. 2011), NIST SRM 621 and BAM-S005-A (Yang et al. 2012) standards. Similarly, a natural, homogenous ilmenite from Labrador collected by Tony Morse (KI-2193; major element composition given in Janssen et al. 2010) was used to accurately determine the major element composition of the Fe-Ti oxides. Using this natural standard, the Ti content of the magnetite changed by $\leq 3\%$ relative to the value that we would have obtained via NIST glass. This gives an estimate of the error introduced by using the NIST glass for quantifying the trace element content of the Fe-Ti-oxides. Agreement between Fe-Ti-oxide compositions determined by LA-ICP-MS versus electron microprobe was demonstrated on three natural samples containing $\pm$homogeneous Fe-Ti-oxide populations (supplementary Table 7.S2).

The raw signals were integrated and converted to element concentrations using in-house Excel sheets. Internal standardization of the silicate glass and exposed glassy melt inclusions was obtained by normalizing the sum of Na_2O, MgO, Al_2O_3, SiO_2, K_2O, TiO_2, MnO and FeO_{tot} to 100 %. Ignorance of the potential presence of ferric iron in the silicate melt introduces a maximum error of. 0.4% to our most Fe-rich glasses (4 wt% FeO_{tot}), which error is propagated to all other elements due to the normalization to 100 wt%. For crystallized melt inclusions and unexposed glassy melt inclusions (which always were hosted in quartz) Al was used as internal standard, the concentration of which was estimated from whole rock or homogenized melt inclusion (Hideaway Park Tuff) literature data, or was taken from analyses of exposed, glassy melt inclusions. All these options, but especially using the whole rock Al content as an internal standard, introduce some error to the glass composition calculations if the major element composition of the melt inclusions does not match exactly the composition of the rock matrices or whole rocks that were used as internal standard. However, in all cases where such a

comparison could be made, no significant compositional differences in the major element concentrations were found (Supplementary Table 7.S3). The SiO_2 concentration of melt inclusions was calculated by difference assuming a total of 100 wt % major element oxides. All concentrations – including the standards – were calculated on a volatile-free basis. Magnetite analyses were calculated by normalizing the sum of FeO, Fe_3O_4, TiO_2, Al_2O_3, MnO, MgO, V_2O_5, ZnO, Nb_2O_3 and Cr_2O_3 to 100 wt%, whereby the FeO/Fe_3O_4-ratio was calculated from stoichiometric constraints in the same manner as it is done for electron microprobe analyses.

In the few samples in which intergrown magnetite-ilmenite pairs were available, only these data were considered for thermometry and oxybarometry. In all other cases the Fe-Ti oxide pairs were randomly paired, and each pair was then tested for equilibrium via the method of Bacon and Hirschmann (1988). Pairs that did not pass this test were eliminated. These tests revealed that most samples contain different generations of oxides, only some of which were in equilibrium with each other. The equilibrium pairs were then used to calculate fO_2 and temperature with the model of Ghiorso and Evans (2008). For comparison purpose, fO_2 and temperature were calculated also with the model of Andersen and Lindsley (1985) using the ILMAT spreadsheet (Lepage 2003). For each sample, an average and a 1σ standard deviation was calculated from the individual fO_2 and temperature values.

In samples in which fresh feldspar phenocrysts or well-preserved feldspar inclusions in quartz were present, temperatures were calculated by two-feldspar thermometry using the method of Putirka (2008, his eq. 27b). This method was applied for (i) feldspar grains enclosed within an other feldspar (usually plagioclase inclusions in potassium feldspar), (ii) for plagioclase and potassium feldspar inclusions within quartz phenocrysts, and (iii) for randomly picked feldspar phenocrysts. A disadvantage of the latter two approaches is that in this case the feldspars typically cannot be proved to have been in equilibrium with each other; hence they were considered as less reliable.

In all samples we additionally constrained temperature with the zircon saturation thermometer of Watson and Harrison (1983). This approach is suitable for this study because all of the investigated samples (and nearly all silicic magmas in general) are saturated in zircon (Table 7.1). Although several new calibrations of the zircon saturation thermometer have been published recently (e.g. Boehnke et al. 2013; Gervasoni et al. 2016), they seem to involve poorer fits at the low-temperature end of the calibration, with the result that temperatures calculated for

highly evolved, silicic magmas such as those investigated in this study turn out to be mostly subsolidus (400-660 °C; Table 7.S1). We thus prefer the original calibration of Watson and Harrison (1983) for applications on evolved granites and rhyolites. It should be noted that the approach via measuring Zr concentrations in melt inclusions or glassy matrix is more reliable than the common approach via whole rock Zr contents because the latter depends also on the timing of zircon saturation and the amount of inherited zircons in the magma. A significant limitation of the calibration of Watson and Harrison (1983) is that it cannot be applied for peralkaline magmas.

The V magnetite–melt oxybarometer was preferentially applied to pairs of coexisting (but spatially separate) magnetite inclusions and melt inclusions (Fig. 7.1a, c), or to pairs of magnetite microphenocryst and surrounding glassy or fine-grained rock matrix. Where such pairs were not available, magnetite inclusions were paired with rock matrix, or magnetite microphenocrysts were paired with melt inclusions to calculate fO_2. However, results from these latter combinations are considered less reliable because there is the danger of coupling non-equilibrium pairs. After eliminating outliers from both groups, magnetite inclusion/microphenocryst analyses were randomly paired with melt inclusion/matrix analyses, and a V partition coefficient was calculated for each pair. According to equation (7.1), calculation of fO_2 additionally requires input of melt ASI and temperature. For the latter, we used the results mostly obtained from zircon saturation thermometry (because we consider those as most reliable in most cases; see below), except for a peralkaline sample for which two-feldspar temperature was utilized instead, and some reduced samples with severe signs of magma mixing where mgt-ilm thermometry results were applied. The melt ASI was either constrained by analyses of glassy rock matrix or exposed, glassy melt inclusions, or was taken from published whole rock or homogenized melt inclusion analyses if the rock matrix and melt inclusions were crystallized. After obtaining an fO_2 for each magnetite–melt pair, an average and 1σ standard deviation was calculated for every sample.

7.3   Results

An overview of the mineralogical characteristics of the investigated samples and the obtained thermobarometric results is given in Table 7.1. A more detailed version of this table is provided in supplementary Table 7.S1, whereas the full analytical data set is given in supplementary

Tables 7.S3 and 7.S4. Each sample will be discussed in more detail below. For the comparison between V magnetite–melt oxybarometry and mgt-ilm oxybarometry, the samples were grouped into three different classes according to a petrographic and a statistical factor. The "most reliable samples" are those for which no evidence for magma mixing was observed and for which at least two measurements were obtained from each melt, magnetite and ilmenite. The "medium reliable samples" have either (i) at least one phase (melt, magnetite, ilmenite) that could be measured only once, (ii) a large scatter in the composition of one of the phases, or (iii) inclusion data had to be coupled with phenocryst data to calculate fO_2. The "least reliable samples" show clear signs of magma mixing; thus, calculated oxygen fugacities or temperatures may be erroneous. Additionally, two samples are described that allowed only comparison of thermometers but not of oxybarometers because the V content of the silicate melt was below the detection limit. All Fe-Ti-oxide temperatures and fO_2 values mentioned in the following sections were calculated with the model of Ghiorso and Evans (2008), whereas corresponding results obtained with the model of Andersen and Lindsley (1985) are listed in Fig. 7.3c. Unless stated differently, zircon saturation temperatures were used as temperature input for V partitioning oxybarometry.

Most reliable samples

Oraviţa hyalodacite

Only Fe-Ti oxide microphenocrysts and the matrix were analyzed in this sample. The matrix contains both glassy and finely crystalline areas; however, both show the same, homogeneous major- and trace element (i.e. Rb/Sr and Cs/Ba ratios) composition. Very reproducible V concentrations were observed also in the magnetite microphenocrysts, although the major element composition varied slightly (by a few percent) in both magnetite and ilmenite. These variations result in some scatter of the calculated mgt-ilm fO_2 values (FMQ+0.4±0.3) and temperatures (800±60 °C), but within error they agree well with the fO_2 constrained via V partitioning (FMQ+0.1±0.2) and with the temperature constrained via zircon saturation (750±10 °C).

Mount Rano

The fresh, idiomorphic nature of feldspars and Fe-Ti oxides, as well as the optically homogenous, glassy matrix of the Mount Rano vitrophyre show no evidence of magma mixing. The glassy matrix is compositionally very homogenous, as shown by only one percent scatter in

ASI and only a few percent scatter in the Rb/Sr and Cs/Ba ratios. The analyses of the Fe-Ti oxides show only one generation of each phase. The fO_2 values obtained via V partitioning (FMQ+0.8±0.1) agree within 0.3 log units with those obtained via mgt-ilm oxybarometry (FMQ+0.5 ± 0.1). The average zircon saturation temperature (830±10 °C) is 30 °C lower than the average Fe-Ti oxide temperature (860±10 °C). Even if this slight difference cannot be interpreted geologically, as it lies within the uncertainty of both thermometers, one would obtain an even better agreement between the two oxybarometers if the temperatures obtained from mgt-ilm thermometry were used as temperature input for V partitioning oxybarometry (FMQ+0.6±0.1).

Parinacota

Six out of eight analyzed melt inclusions and all three glass analyses show very similar trace element compositions in this vitrophyre, which generally supports the statement of Hora et al. (2012) that the investigated unit is homogenous and free of magma mixing. On the other hand, we observed two distinct magnetite and ilmenite populations and two melt inclusions that have higher Rb/Sr and Cs/Ba ratios than the glassy matrix, which is indicative of magma mixing. Nevertheless, temperatures obtained from two-feldspar thermometry (730±10 °C), zircon saturation thermometry (720±0 °C) and mgt-ilm thermometry (720±80 °C) match perfectly, and oxygen fugacities calculated via V mgt/melt partitioning (using magnetite phenocrysts combined with matrix: FMQ+1.7±0.4 or melt inclusions: FMQ+1.8±0.2) agree within 0.5 log units with those calculated via mgt-ilm oxybarometry (FMQ+2.2±0.2).

Hideaway Park tuff

Both magnetite and ilmenite were present as microphenocrysts and as inclusions in quartz. However, due to the altered appearance of magnetite phenocrysts we used only inclusions to constrain fO_2 and temperature via Fe-Ti-oxide thermobarometry. In contrast, Mercer et al. (2015) obtained temperature and fO_2 from phenocrysts, which might be the reason for the significant difference between their and our oxygen fugacity values (FMQ+0.4±0.3 versus FMQ+1.2±0.1). Since our magnetite and ilmenite inclusions pass the equilibrium test of Bacon and Hirschmann (1988), but the microphenocryst pairs do not (Mercer et al. 2015), we consider the inclusion-based values more reliable. Corresponding fO_2 values (FMQ+1.2±0.1) agree within 0.5 log units with the fO_2 values constrained via V magnetite–melt partitioning (FMQ+1.7±0.2).

Temperatures obtained via mgt-ilm thermometry (670±10 °C) are significantly lower than those constrained via two-feldspar thermometry (740±10 °C) and zircon saturation thermometry (760±0 °C), which can be explained by the large uncertainty associated with mgt-ilm thermometry at low temperatures and oxidized conditions (see below).
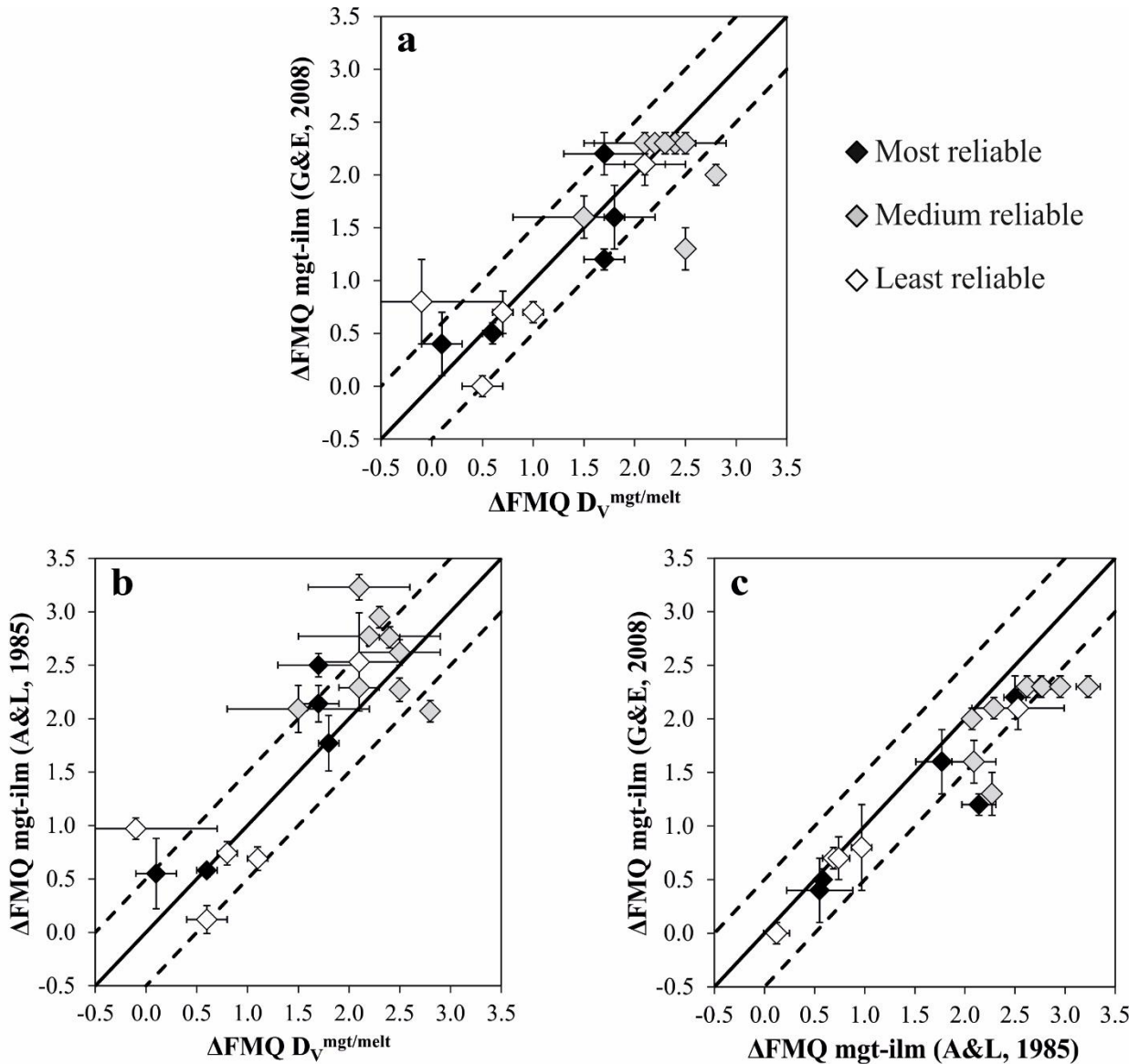
Fig. 7.3 Comparison of fO_2 values (reported in log units relative to the fayalite-magnetite-quartz buffer) obtained via (a) vanadium magnetite–melt partitioning oxybarometry (Arató and Audétat, 2016) versus Fe-Ti oxide oxybarometry using the model of Ghiorso and Evans (2008) (b) vanadium magnetite–melt partitioning oxybarometry (Arató and Audétat, 2016) versus Fe-Ti oxide oxybarometry using the model of Andersen and Lindsley (1985), and (c) Fe-Ti oxide oxybarometry using the model of Andersen and Lindsley (1985) versus the model of Ghiorso and Evans (2008). Notice the increasing mismatch in (b) and (c) at high fO_2 values, where the model of Ghiorso and Evans (2008) generally returns lower values. The data points are grouped into three levels of reliability based on criteria discussed in the text. The solid line represents the 1:1 correspondence; the dashed lines 0.5 log units deviation. Error bars indicate 1 sigma standard deviations of the calculated fO_2 averages. The temperatures utilized for V partitioning oxybarometry are listed in Table 7.1.

Cottonwood Wash tuff

Comparison of the oxybarometry results is not straightforward in this sample, as the dacitic whole rock composition differs significantly from the rhyolitic composition of the glassy matrix and melt inclusions. This may explain the good agreement of matrix-based V partitioning fO_2 values (FMQ+1.8±0.1) with the ones derived from phenocrystic magnetite-ilmenite pairs (FMQ+1.6±0.3), and their disagreement with the inclusion-based V partitioning fO_2 values (FMQ+1.1±0.3). A probable explanation for this difference is that the analyzed magnetite inclusions were trapped at a relatively early stage where they were in equilibrium with a less evolved melt, whereas the analyzed melt inclusions formed at some later stage in the magma evolution. This interpretation is supported by the fact that feldspar-hosted melt inclusions are less evolved (based on their Rb/Sr ratio) and yield more consistent fO_2 values (FMQ+1.4±0.3) if combined with magnetite inclusions. The analyzed Fe-Ti-oxide microphenocrysts, on the other hand, continuously re-equilibrated until the time of magma eruption. In this sample the mgt-ilm temperatures (770±50 °C) agree well with the zircon saturation temperatures obtained from both melt inclusions (750±10 °C) and matrix (750±30 °C).

Medium reliable samples

Lordsburg rhyolite

Due to the lack of geochemical data and the altered nature of this rhyolite sample we used the Al_2O_3 content of a single, exposed, glassy melt inclusion as internal standard for unexposed and/or crystallized melt inclusions, which may have introduced a considerable uncertainty to the melt inclusion data. The V content of the analyzed melt inclusions varied significantly, resulting in a relatively big scatter in calculated V magnetite–melt fO_2 values (FMQ+2.1±0.5). Despite these uncertainties and the fact that magnetite inclusions had to be coupled with ilmenite microphenocrysts to calculate oxygen fugacity via Fe-Ti oxide oxybarometry (FMQ+2.3±0.1), the results of the two independent oxybarometers agree well. Calculated temperatures are less consistent, as the two-feldspar temperatures are significantly higher (750±30 °C) than those obtained via zircon saturation (680±10 °C), whereas the mgt-ilm thermometer yields subsolidus temperatures (560±20 °C). It has to be noted that two-feldspar temperatures based on feldspar inclusions in quartz appear to be less reliable than temperatures obtained from feldspar inclusions within feldspar (see below).

Lordsburg granodiorite

The unsteady signal of the matrix analysis and the small number of Fe-Ti oxide equilibrium pairs (compared to the total number of measured grains) in this sample are not ideal, but the oxygen fugacity obtained via mgt-ilm oxybarometry (FMQ+2.3±0.1) and V partitioning oxybarometry (FMQ+2.4±0.1) agree well with each other, and they are also rather similar to the fO_2 values obtained from the Lordsburg rhyolite. Temperatures obtained via mgt-ilm thermometry (720±30 °C) are ca. 50 °C lower than those obtained via zircon saturation thermometry (770 °C), but in this particular case neither result is considered particularly reliable because Fe-Ti-oxide temperatures are associated with a large uncertainty at these conditions (see below) and Zr is too inhomogeneously distributed in the crystalline rock matrix to allow reliable measurement.

Smelter Knolls rhyolite

The Smelter Knolls rhyolite contains abundant Fe-Ti oxides as inclusions in quartz, feldspar and biotite phenocrysts, as well as in the form of individual microphenocrysts. The magnetite microphenocrysts and the inclusions in biotite have fairly similar compositions, but the magnetite inclusions in feldspar and a single magnetite inclusion in quartz are more iron-rich and aluminum-poor, with the feldspar-hosted ones containing about 50% more V_2O_5 than all the other magnetites. Furthermore, there is a factor of four to nine difference in the V-concentration of the quartz hosted- and feldspar hosted melt inclusions. Obviously, these differences result in diverse V partitioning fO_2 values, namely FMQ+1.1±0.5 for inclusions (melt and magnetite) in quartz, and FMQ+2.5±0.4 for inclusions in feldspar. The latter value is in fairly good agreement with microphenocryst-based and inclusion-based mgt-ilm oxybarometry results (FMQ+2.3±0.1 and 2.3±0.0, respectively). The zircon saturation temperatures (670±0 °C) agree well with the two-feldspar temperatures (660±40 °C) reported in the literature (Turley and Nash 1980), both of them plotting close to the water-saturated granite solidus at three kbar (Ebadi and Johannes 1991). Inclusion-based mgt-ilm temperatures are subsolidus (630±0 °C), whereas the average phenocryst-based temperatures (710±0 °C) are about fifty degrees higher than the zircon saturation and two-feldspar temperatures.

Amalia Tuff

The Amalia Tuff contains large amounts of Fe-Ti oxide inclusions (in K-feldspar, plagioclase and quartz) and microphenocrysts, as well as melt inclusions (in quartz) available for oxybarometry. Melt inclusion compositions are well reproducible with respect to

incompatible/compatible trace element ratios and the V content, but the major elements show significant variations, with ASI values ranging from 0.79 to 0.91, which might be related to loss of Na from some inclusions. This, and also the twenty-fold variation in V content of magnetite result in a relatively big scatter in the calculated fO_2 values (FMQ+1.5±0.7). Although these values cover an fO_2 range of more than 1.5 log units, the average is close to the fO_2 obtained from inclusions via mgt-ilm oxybarometry (FMQ+1.6±0.2). It should be noted that none of the analyzed magnetite-ilmenite microphenocryst pairs passed the equilibrium test (and thus were not considered), and that only two equilibrium pairs were identified amongst the inclusions. As the zircon saturation thermometer of Watson and Harrison (1983) is not calibrated for peralkaline compositions, only the two-feldspar temperatures (680±30 °C) can be compared with the mgt-ilm temperatures, the latter being about 90 °C higher (770±50 °C).

Banco Bonito vitrophyre

The melt inclusions of this sample seem to record the complex evolution history of the volcanic field, since their Rb/Sr and Cs/Ba ratios, as well as their V concentrations and ASI values vary considerably. In contrast, the matrix glasses are very homogeneous with respect to all elements, and are most probably in equilibrium with the rim overgrowths of plagioclase crystals (Eichler 2012). For this reason we focused on the glassy matrix and the phenocrysts to reconstruct temperature and oxygen fugacity. The mgt-ilm method yielded basically the same fO_2 value (FMQ+2.1±0.0) as the V partitioning oxybarometer (FMQ+2.1±0.2), whereas the mgt-ilm temperatures (800±20 °C) are 40 °C higher (but within error still the same) than those obtained via zircon saturation thermometry (760±30 °C).

Santa Rita rhyodacite dike

We investigated two samples (SR15, SR9) from two rhyodacite dikes. The abundance of Fe-Ti oxide phenocrysts and mineral- and melt inclusions in quartz phenocrysts of sample SR15 provide an excellent opportunity to compare different oxybarometers and thermometers. In contrast, both the matrix and the Fe-Ti oxides of sample SR9 are altered, hence, only magnetite inclusions and melt inclusions preserved within quartz phenocrysts could be used in this sample. The composition of the crystallized melt inclusions was constrained by using the whole rock Al_2O_3 concentration reported in (Jones et al. 1967) as internal standard. In sample SR15, a similar Al_2O_3 content was determined for the fine-grained matrix via LA-ICP-MS. The V content shows a certain variation in both the matrix and the melt inclusions, varying by an order of

magnitude in the latter. This is why the $f\mathrm{O}_2$ value (FMQ+2.2±0.7) calculated from V partitioning between magnetite inclusions and melt inclusions in quartz show an unusually high standard deviation of 0.7 log units. The average oxygen fugacity calculated from V partitioning between magnetite microphenocrysts and matrix composition (FMQ+2.5±0.3) is slightly higher and shows a smaller standard deviation. The mgt-ilm oxybarometer could be applied only to a single magnetite-ilmenite pair in the case of magnetite and ilmenite microphenocrysts (FMQ+2.0), and a single pair in the case of inclusions (FMQ+2.3), whereas all other pairs failed the equilibrium test (Bacon and Hirschmann 1988). Corresponding oxygen fugacities agree well with those obtained via V partitioning in the case of inclusions, but differ by 0.5 log units in the case of microphenocrysts (FMQ+2.5±0.3). In contrast to sample SR15, the six quartz-hosted melt inclusions analyzed from sample SR9 showed well-reproducible compositions, irrespective of their position in the quartz phenocryst (core, middle growth zone, rim). The V partitioning $f\mathrm{O}_2$ values (FMQ+2.2±0.1) agree well with those obtained from SR15 and show a much smaller scatter. They also agree well with the $f\mathrm{O}_2$ values of FMQ+2.0 to FMQ+2.6 (NNO+1.3 to NNO+1.9) reported by Audétat and Pettke (2006). The interpretation of temperatures obtained via different thermometers is not straightforward. Matrix-based zircon saturation temperatures (760±20 °C) are in good agreement with the value obtained from magnetite-ilmenite microphenocrysts (770 °C). Melt inclusion-based zircon saturation temperatures are somewhat lower (710±10 °C); however, it is possible that these melt inclusions record an earlier, slightly cooler stage of the magma evolution than the matrix because the latter is less evolved (i.e., has lower Rb/Sr and Cs/Ba ratios) than the melt inclusions, hence there was magma mixing involved. Temperatures obtained via Fe-Ti-oxide thermometry from inclusions in quartz are below the granite solidus. On the other hand, feldspar inclusions within quartz phenocrysts return surprisingly high temperatures (840±20 °C), which – as pointed out already in the section on Lordsburg – may be due to some general problem associated with quartz-hosted feldspar inclusions (see below).

The Dyke

Despite the large width of the dike (several tens of meters) the groundmass of the rock is relatively fine-grained, and the Fe-Ti-oxide microphenocrysts look fresh. Magnetite was found also as inclusion within quartz phenocrysts, but no coexisting ilmenite inclusions were found. Melt was analyzed in the form of crystallized melt inclusions in quartz, whereas the rock matrix was too heterogeneous to provide reliable V and Zr concentrations. Hence, a comparison of results obtained from inclusions only versus microphenocrysts plus matrix was not possible in this case. Nevertheless, microphenocryst-based mgt-ilm fO$_2$ values (FMQ+2.3±0.0) are very similar to those obtained from inclusion-based V partitioning (FMQ+2.3±0.2), and they agree also with values obtained by pairing magnetite inclusions with ilmenite microphenocrysts (FMQ+2.3±0.0), and pairing melt inclusions with magnetite microphenocrysts (FMQ+2.3±0.3). This suggests that oxygen fugacity remained rather constant throughout the evolution recorded by the analyzed phases. The thermometry results are less consistent. Melt inclusion-based zircon saturation temperatures (730±30 °C) show only small scatter and plot close to the average value obtained from magnetite and ilmenite microphenocrysts (720±80 °C), but the two-feldspar thermometer yields temperatures that are ca. 50 °C higher in average (790±40 °C). The good match between Fe-Ti oxide temperatures and zircon saturation temperatures is probably a coincidence, as the former span a large range from <700 °C to >800 °C. The high two-feldspar temperatures might be the related to an earlier stage of feldspar crystallization.

Nomlaki Tuff

The Nomlaki Tuff contains Fe-Ti-oxide microphenocrysts set in a glassy matrix. The compositions of the matrix glass and Fe-Ti oxides suggest that our sample belongs to the more evolved, cooler part of the tuff, for which Poletski (2010) obtained an average mgt-ilm temperature of 850 °C using the calibration of Andersen and Lindsley (1985). Recalculation of those temperatures using the calibration of Ghiorso and Evans (2008) results in about 40 °C lower values (810±0 °C), which agree well with the zircon saturation temperatures (790±10 °C). Oxygen fugacities obtained via V partitioning (FMQ+2.8±0.2) are significantly higher than those obtained via mgt-ilm (FMQ+2.0±0.0), but there is no obvious explanation for this discrepancy.

Kos granite enclave

A rigorous comparison of the two oxybarometers in this sample is complicated by the fact that melt composition could be obtained only from quartz-hosted melt inclusions, whereas Fe-Ti oxides were present only in the form of microphenocrysts in interstices of the holocrystalline matrix. Oxygen fugacity values calculated from V partitioning between magnetite microphenocrysts and quartz-hosted melt inclusions (FMQ+2.5±0.1) are more than one log unit higher than the values obtained from magnetite-ilmenite microphenocryst pairs (FMQ+1.3±0.2). The former is in good agreement with mgt-ilm fO_2 values published for the tuff, whereas the latter agrees with values published for holocrystalline granite enclaves (Bachmann 2010). However, based on the fact that magnetite-ilmenite pairs from the granite enclaves always return subsolidus temperatures (our study and Bachmann 2010) and that large variation in oxygen fugacity within the same magma body are rather unlikely, we believe that the data obtained from magnetite-ilmenite pairs in the enclaves are not reliable. Temperatures obtained via zircon saturation thermometry on melt inclusions and via two-feldspar thermometry are around 720 °C, which is in good agreement with the literature data (Bachmann 2010).

Least reliable samples

Los Humeros

This sample from the Los Humeros volcanic center is a vitrophyre from a rhyolitic lava flow. The four glass analyses and two magnetite-ilmenite pairs analyzed from this sample show rather reproducible compositions. However, the common occurrence of sieve-textured plagioclase cores and the presence of a small enclave containing olivine crystals provide clear evidence for magma mixing. This probably explains the slight mismatch between fO_2 values obtained via V partitioning (FMQ+0.6±0.1) and those obtained via magnetite-ilmenite pairs (FMQ+0.0±0.1), as the composition of the silicate melt may have changed immediately before or during magma eruption. The temperatures obtained via zircon saturation thermometry (840±10 °C) agree well with those obtained via Fe-Ti oxides (850±30 °C), which may be due to the better reliability of mgt-ilm thermometry at more reduced conditions ($\leq$Ni-NiO buffer; Ghiorso and Evans, 2008). The agreement between the two oxybarometers gets slightly better if mgt-ilm temperatures are used as input for V partitioning oxybarometry (FMQ+0.5±0.1).

Samples from the Mono-Inyo volcanic field

In this study we investigated three vitrophyre samples, collected from (i) the Glass Creek dome, (ii) the Glass Creek flow, and (iii) the Mono Dome #12 (Bailey 1989), all of them marked as "enclave-bearing" by Bray (2014). Compositionally, the samples can be classified as rhyolite (i and (ii) and rhyodacite (iii), based on whole rock compositions. The oxygen fugacity values obtained from V partitioning via zircon saturation thermometry (FMQ-0.1±0.8; FMQ+1.3±0.1; FMQ+1.4±0.1) do not agree with those obtained from magnetite-ilmenite pairs (FMQ+0.8±0.4; FMQ+0.7±0.1; FMQ+0.7±0. 2), which likely is a consequence of magma mixing. Interestingly, the Fe-Ti oxides yield values around FMQ+0.7 in all three vitrophyres, whereas V partitioning records an oxygen fugacity of ca. FMQ+1.35 in two samples, and values around either FMQ+0.7 or FMQ -1 in the third sample. Omitting the two most reducing values (which might not represent equilibrium), the remaining oxygen fugacities cluster at FMQ+0.7 and FMQ+1.35, only the first of which is in agreement with literature data. Despite being abundant, it is highly possible that the latter group does not represent equilibrium, but rather partially reset/oxidized magnetite and melt compositions, as also shown by the high variation in magnetite compositions (Carmichael, 1967). Zircon saturation temperatures (840±20 °C; 870±10 °C; 770±10 °C) are at least 60 °C lower than those obtained from Fe-Ti oxide pairs (940±140 °C; 930±30 °C; 880±40 °C). This may be explained by the intrusion of a hotter, more mafic magma batch into the silicic magma chamber immediately before the eruption, which led to complete (Mono #12, Glass Creek Flow) or partial (Glass Creek Dome) resetting of the Fe-Ti oxide compositions (notice the big scatter of the mgt-ilm temperatures in the Glass Creek Dome sample), but occurred at a too short time scale to reset the zircon saturation thermometer. In the Glass Creek Flow sample, the two-feldspar method yields a huge scatter of temperatures (820-960 °C), which again seems to be due to magma mixing. These observations and the fact that the mgt-ilm thermometer yields more reliable values at reduced (≤Ni-NiO buffer) conditions (Ghiorso and Evans, 2008) explain why one obtains a better agreement between the two oxybarometers in the Mono #12 and Glass Creek Flow samples if the mgt-ilm temperatures are used as input for V partitioning oxybarometry (Table 7.1).

Tunnel Spring Tuff

Zircon saturation temperatures (660±10 °C; obtained from melt inclusions within quartz cores) and mgt-ilm temperatures (660±40 °C; obtained from inclusions, too) of the Tunnel Spring Tuff scatter around the water saturated granite solidus at three kbar, whereas two-feldspar thermometry yields distinctly higher temperatures ~760±50 °C. These results are in good agreement with a previous study (Audétat 2013), where zircon saturation thermometry yielded temperatures of 630-660 °C in the core of two quartz phenocrysts, and temperatures of 720-770 °C in their rim, which, together with a rimward increase in the concentration of compatible elements (Sr, Ba) and decrease in the concentration of incompatible elements (Rb, Cs), provides clear evidence for a stage of magma rejuvenation during the formation of the quartz crystals. The results of this study suggest that the analyzed feldspars crystallized after the rejuvenation event, whereas the analyzed melt inclusions and Fe-Ti-oxide inclusions crystallized earlier.

Similarly to the Kos granite, the analytical data do not allow a rigorous comparison of the two oxybarometers because Fe-Ti-oxide inclusion pairs do not pass the equilibrium test, and because the matrix could not be analyzed. Despite the apparent Mg/Mn disequilibrium, the magnetite-ilmenite inclusion pairs yield similar fO_2 values (FMQ+2.1±0.2) as those obtained from Fe-Ti-oxide microphenocrysts (FMQ+2.3±0.2). The V partitioning method returns similar fO_2 values only if magnetite inclusions are paired with melt inclusions (FMQ+2.1±0.4), but not so if melt inclusions are paired with magnetite microphenocrysts (FMQ+1.1±0.3). The latter may be explained by non-equilibrium due to magma rejuvenation.

Samples that allowed only comparison of thermometers

Blackfoot lava field vitrophyre

Only few Fe-Ti oxides were available in this sample, yielding a mgt-ilm fO_2 of FMQ+0.4±0.0. Unfortunately, this value could not be compared with V partitioning oxybarometry because the V content of the matrix glass was below the detection limit of ~0.1 ppm V. Temperatures obtained via zircon saturation thermometry (770±0 °C) and mgt-ilm thermometry (780±10 °C) are a few tens of degrees higher than those obtained by two-feldspar thermometry (720±20 °C).

Pine Grove Tuff

Although the Pine Grove Tuff contains abundant glassy melt inclusions and several Fe-Ti-oxide inclusions and thus would have been suitable for oxybarometry, the V content of the glass was below the detection limit, precluding the application of V partitioning oxybarometry on this sample. On the other hand, consistent values were obtained by two-feldspar thermometry (690±10 °C) and zircon saturation thermometry (700±10 °C), which results overlap with previously published ranges of mgt-ilm temperatures (650-700 °C; Keith and Shanks, 1988) and zircon saturation temperatures (707-724 °C; Audétat et al., 2011).

7.4 Discussion

The fO$_2$ values obtained via the newly developed V partitioning oxybarometer are in reasonable agreement with both the Fe-Ti oxide oxybarometer model of Andersen and Lindsley (1985) and that of Ghiorso and Evans (2008), but they fit better with the latter model, especially at high oxygen fugacities (above FMQ+2; Fig. 7.3). There are several differences between the two models that can explain the difference. First, the model of Ghiorso and Evans (2008) is based on a more extensive data set of two-oxide phase equilibria that covers a broad range of experimental conditions between 800 °C and 1300 °C, and between NNO−3 and NNO+3. Second, the model of Ghiorso and Evans (2008) accounts for the configurational entropy changes related to both the short-range cation order and the R$\overline{3}$c-R$\overline{3}$ order-disorder transition of the rhombohedral phase, which are not considered by the model of Andersen and Lindsley (1985). These modifications are important because previous models considered only ilmenite compositions close to the FeTiO$_3$ endmember, where they have an ordered R$\overline{3}$ structure. This, however, is not the case for oxygen fugacities above NNO+1 and at temperatures of 700-900 °C, which conditions apply for the majority of our samples. Therefore, we believe that the model of Ghiorso and Evans (2008) provides a more reliable estimate of fO$_2$ at conditions typical of natural silicic magmas.

The error bars plotted in Fig. 7.3 show only the scatter caused by compositional variation of the analyzed Fe-Ti-oxides and silicate melts. They do not include any analytical uncertainty nor any uncertainties inherent to the calibrations of either method. An analytical error of three percent in the determination of the ASI value would cause the fO$_2$ obtained via V partitioning to shift by ~0.15 log units, an error of three percent in measured V concentrations would cause a shift of ~ 0.1 log units, and a 30 °C error in the temperature determination a shift of ~ 0.2 log units.

Additionally, an uncertainty of 0.2 log (residual standard error of the linear regression) units is introduced by the experimental calibration of the V oxybarometer itself. Taking into account all these effects, the overall accuracy of the V partitioning oxybarometer is estimated at ±0.5 log units.
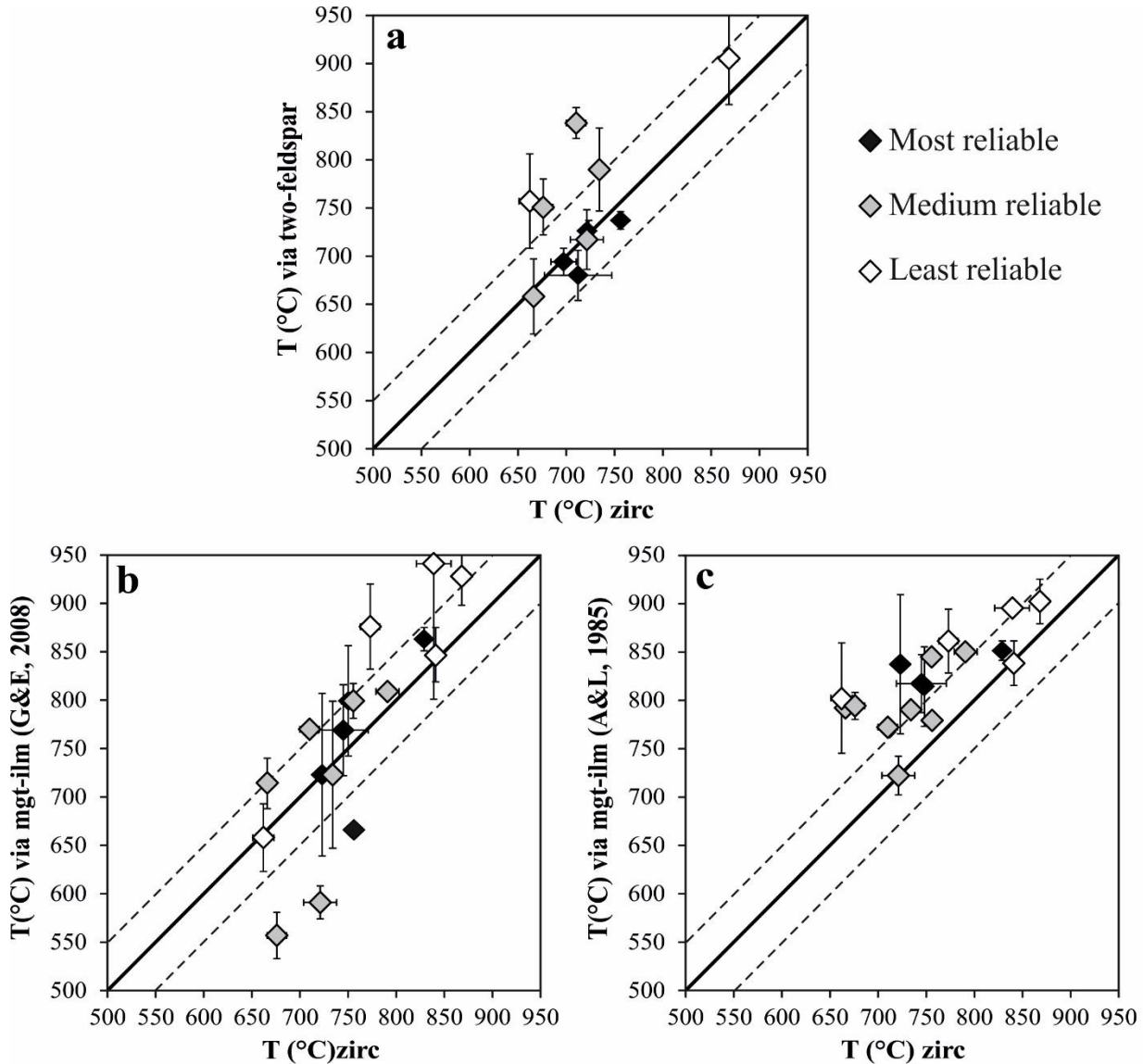
Fig. 7.4 Comparison of temperatures calculated via four different methods. **a** zircon saturation temperatures (Watson and Harrison, 1983) versus twofeldspar temperatures (Eq. 27b of Putirka, 2008); **b** zircon saturation temperatures versus magnetite–ilmenite temperatures obtained with the model of Ghiorso and Evans (2008), and c zircon saturation temperatures vs. magnetite–ilmenite temperatures obtained with the model of Andersen and Lindsley (1985). The data points are grouped into three levels of reliability based on criteria discussed in the text. The two most divergent two-feldspar values from the "medium reliable" data points plotted in (a) were obtained from feldspar inclusions in quartz. The dashed lines denote 50 °C deviations from the 1:1 correspondence

Although the uncertainty associated with the calibration of the model of Ghiorso and Evans (2008) was not specifically stated by the authors, it can be estimated at ±0.5 log units based on

their Figs. 10 and 27. An analytical error of three percent in the determination of the ilmenite fraction in ilmenite leads to an uncertainty of 0.2 log units fO_2 at the T-fO_2 conditions typical of natural, silicic magmas, whereas a three percent error in the determination of the ulvöspinel fraction in magnetite leads to an uncertainty of 0.1 log units. Thus, in terms of analytical- and calibration-derived uncertainties the two approaches have similar accuracies (not taking into account the substantial discrepancy between different Fe-Ti-oxide oxybarometry models).

Apart from these analytical- and calibration-derived uncertainties there is in most cases uncertainty introduced by the choice of analyzed Fe-Ti-oxides and silicate melts. Obviously, if the analyzed phases were not in equilibrium with each other, then the result will likely be wrong independent of how accurate the applied method is. In the case of mgt-ilm oxybarometry one can use the method of Bacon and Hirschmann (1988) to identify non-equilibrium pairs, whereas in the case of V partitioning oxybarometry careful petrography and/or a sufficient number of analyses (to be able to identify potential outliers or multiple generations of magnetite or melt) are needed to demonstrate equilibrium. The analyzed samples have been divided into "most reliable", "medium reliable" and "least reliable" dominantly based on this latter principle.

The most reliable samples are those that do not show any evidence for magma mixing and from which multiple analyses of all three phases required for both V partitioning and Fe-Ti oxide oxybarometry (i.e., magnetite, ilmenite, melt) were obtained, showing little compositional variation. Oxygen fugacities calculated via the two independent oxybarometers agree within 0.5 log units in all samples of this group (Fig. 7.3a), which is well satisfactory considering the relatively large uncertainties associated with both methods. Although the "medium reliable" samples are more likely to yield discrepant results, the results actually agree well with each other (Fig. 7.3a), except for two samples: the Kos granite enclave and the Nomlaki Tuff. In the case of the Kos granite enclave the analyzed magnetite and ilmenite microphenocrysts probably re-equilibrated at subsolidus conditions – a common process in granites. In contrast, there is no obvious explanation for the discrepancy observed in the Nomlaki Tuff (which is the "medium reliable" data point in Fig. 7.3a that plots only slightly outside the 0.5 log units envelope). Even the "least reliable" samples show a correspondence in the calculated fO_2 values within ≤0.75 log units (Fig. 7.3a), which is better than expected given the strong signs of magma mixing present in these samples. Compared to the recently calibrated oxybarometer of Putirka (2016) based on ferric-ferrous ratios of silicate melts equilibrated with olivine, which has a model error of 0.75-1

log units, the agreement of the two oxybarometers in this study is fairly promising. It should be mentioned that the V partitioning oxybarometer could not be applied to some highly evolved silicic rocks (Pine Grove Tuff and Blackfoot lava field vitrophyre) due to extremely low V contents in the silicate melt (<0.1 ppm V).

Application of the V partitioning oxybarometer requires input of temperature. However, as shown in Fig. 7.4, different thermometers (zircon saturation, mgt-ilm and two-feldspar) commonly yield results that differ by as much as 200 °C. A major source of error in mgt-ilm thermometry lies in the fact that at oxygen fugacities greater than ~NNO+1 the isotherms are very closely spaced in the magnetite vs. ilmenite compositional diagram (Ghiorso and Evans, 2008; their Figure 14 being reproduced with permission in supplementary Figure 7.S1), leading to a calibration uncertainty of at least 50-100 °C. At oxygen fugacities greater than ~NNO+2.5 the calibration uncertainty reaches even 200-400 °C (cf. Fig. 26 of Ghiorso and Evans, 2008). The close spacing of the isotherms also means that the Fe-Ti oxide thermometer is very sensitive to analytical errors in the determination of the ulvöspinel component of magnetite.

Calibration uncertainties are significantly smaller in the case of zircon saturation thermometry and two-feldspar thermometry, although other problems exist, such as the difficulty to experimentally grow or dissolve zircons in low-temperature silicic melts due to slow diffusion and sluggish nucleation, and the common Na-loss of natural quartz-hosted feldspar inclusions. The calibration uncertainty of the zircon saturation model of Watson and Harrison (1983) is about five percent relative, i.e., ±35°C at 700 °C and ±40 °C at 800 °C (Boehnke et al., 2013; their Fig. 7), and the calibration uncertainty of the two-feldspar thermometer of Putirka (2008; his equation 27b) is reported at ±30 °C. Therefore, these two thermometers are expected to provide more reliable temperature estimates for most of the natural silicic magmas than mgt-ilm thermometry. This conclusion is supported by the data plotted in Fig. 7.4, which show mostly good agreement (within 50 °C) between zircon saturation temperatures and two-feldspar temperatures (Fig. 7.4a; exceptions are two samples in which the feldspars were analyzed as inclusions in quartz, and one sample that shows strong signs of magma mixing), and less good agreement between zircon saturation temperatures and mgt-ilm temperatures, especially if the model of Andersen and Lindsley (1988) is used (Figs. 7.4b, c). The reason for the discrepant results obtained from feldspars analyzed as inclusions within quartz phenocrysts is not clear, but potentially the feldspar inclusions exchanged alkalies via post-entrapmental Na diffusion through

quartz, similar to the process that leads to the ubiquitous Na-deficiency in quartz-hosted, crystallized melt inclusions (e.g. Audétat et al. 2000; Audétat and Pettke 2003; Zajacz et al. 2008; Audétat and Lowenstern 2014). This explanation is supported by the fact that the feldspar compositions are conspicuously non-stoichiometric in both samples in which large discrepancies between zircon saturation temperatures and two-feldspar temperatures based on feldspar inclusions in quartz were noticed (Lordsburg rhyolite and Santa Rita granodiorite), showing A/CNK ratios significantly over unity in both feldspar phases. We conclude that the temperatures required for V partitioning oxybarometry should preferably be obtained by zircon saturation thermometry (in metaluminous and peraluminous rocks) or, where fresh feldspars are available, by two-feldspar thermometry on feldspar inclusions within feldspar phenocrysts.

The goal of this study was to test the reliability of a new oxybarometer that is applicable also to slowly-cooled rocks such as granites, in which mgt-ilm oxybarometry is difficult to apply because Fe-Ti-oxides easily re-equilibrate during cooling. As demonstrated on the Hideaway Park tuff, the Smelter Knolls rhyolite and the Tunnel Spring tuff (plus by previous work on the Chalk Mountain rhyolite at Climax, Colorado; Audétat, 2015), the problem of subsolidus re-equilibration and phase separation could in principle be solved by analyzing both magnetite and ilmenite inclusions preserved within quartz phenocrysts. However, the chance of finding both types of inclusions in the same growth zone of a given quartz phenocryst is extremely small, for which reason one would have to rely on randomly paired inclusions that are not known to have been in equilibrium with each other. In contrast, melt inclusions are much more common, hence the chance of finding pairs of coeval magnetite inclusions and melt inclusions is much higher (although they still can be rather difficult to find). This is why we aimed at developing an oxybarometer that is based on mineral–melt partitioning rather than on mineral–mineral partitioning. As is true for most thermometers and (oxy)barometers, the reliability of the results obtained via V partitioning oxybarometry depends critically on the quality of the petrographic control on the analyzed phases.

7.5 Conclusions

The results of this extensive test on natural samples demonstrate that the newly developed V partitioning oxybarometer provides $f\mathrm{O}_2$ values that agree well (within ≤0.5 log units) with those obtained via Fe-Ti oxide oxybarometry using the model of Ghiorso and Evans (2008), provided that care is taken to identify coeval magnetite–melt pairs. The accuracy of the method depends on several factors: (i) the accuracy of reconstructed temperature, (ii) the accuracy of reconstructed melt composition (in particular the aluminum saturation index, the Zr content, and the V content), and (iii) the accuracy of reconstructed magnetite composition. Most critically, however, it depends on the carefulness of conducted petrography to verify that the analyzed magnetites and melts were in equilibrium with each other. A comprehensive comparison of different thermometers (zircon saturation thermometry, two-feldspar thermometry, Fe-Ti-oxide thermometry) reveals that Fe-Ti-oxide thermometry does not provide reliable results at $f\mathrm{O}_2$ above ~NNO+1 and temperatures below ~900 °C, which conditions apply for most natural, silicic rocks. More reliable is zircon saturation thermometry, which can be applied for metaluminous and peraluminous rocks (but not to peralkaline rocks) and is associated with an uncertainty of ca. ±35 °C at 700 °C, and two-feldspar thermometry if applied to feldspar intergrowths in rapidly-quenched, volcanic samples, with an associated uncertainty of ca. ±30 °C.

The new V magnetite–melt partitioning oxybarometer has the advantage that it can be applied to samples that do not contain ilmenite, and that it can be applied to slowly cooled silicic rocks such as granites, in which unshielded Fe-Ti-oxides extensively re-equilibrated at subsolidus temperatures. For the latter application one has to focus on magnetite and melt inclusions preserved within quartz phenocrysts, whose original compositions can be obtained by analyzing the inclusions as entities by LA-ICP-MS and integrating the resulting signals.

7.6 Acknowledgments

and an anonymous reviewer significantly contributed to the final version of the manuscript and are gratefully appreciated.

7.7 Appendix

Samples

Four samples were kindly provided by the Smithsonian Institution (NMNH 117450-58 Los Humeros volcano – Mexico; NMNH 117455-27 Mount Rano – Indonesia; NMNH 117462-1 Blackfoot Lava Field – USA; NMNH 116377-38a Nomlaki Tuff – USA), one by Sorin Silviu Udubasa (Oravita area – Romania) and one by John Hora (Parinacota volcano – Chile). Additional vitrophyres (Inyo-Mono craters, Banco Bonito volcano – both USA), silicic tuffs (Winter Park, Smelter Knolls, Guaje, Pine Grove, Crystal Peak, Lordsburg, Chalk Mountain, Amalia and Cottonwood – all USA) and fine-grained porphyritic rocks (Santa Rita rhyodacite dikes, Lordsburg rhyolite and granodiorite, Topaz Mountain, The Dyke – all USA) were collected by Andreas Audétat, whereas a sample from Kos (Greece) was kindly donated by Thomas Pettke.

Sample description

Oraviţa hyalodacite

Unfortunately, there is no detailed description (such as exact locality, rock unit, etc.) available for this specimen. Most probably it stems from one of the Permian rhyolitic flow units of the Oraviţa area in Romania. Publications about these Permian volcanics in the area are mainly in Romanian language and/or not accessible for the public, but a recent paper (Seghedi 2011) describes the Lower Permian volcanic occurrences of the neighboring Sirinia basin. The exclusively rhyolitic composition (74-80% SiO_2) and the glass-rich, dominantly hyaline texture of Sirinia basin rhyolites – similarly to our sample – let us to suggest that they are genetically related.

Mount Rano

The Mount Rano volcano is located on the southwestern part of the North Maluku Island, Indonesia. The volcano forms part of the Late Cretaceous-Eocene Oha Formation (Hakim and Hall 1991), consisting of basalts and andesites. However, our vitrophyre sample, which stems

from the southwestern flank of Mount Rano and was kindly provided by the Smithsonian institution (NMNH 117455-27), has a rhyolitic composition.

Parinacota

The Parinacota volcano is located in Chile, Central Andes, and its evolution can be subdivided into five main stages, spanning from 163 ka until 5 ka (K-Ar; Hora et al. 2007). A detailed description of the geochemistry, petrography and evolution history can be found in Wörner et al. (1988) and in Hora et al. (2007). Our sample stems from the Rhyodacite Dome Plateau sequence (47-40 ka), which represents the second stage of the volcano's evolution history. In contrast to most other magmas produced at this stage, the rhyodacite sample originates from one of the non-mixing endmember reservoirs. This sample was thoroughly investigated in a case study involving a test of multiple thermometers (Hora et al. 2013). Despite some high amphibole–plagioclase temperatures obtained from glomerocrysts, the temperature estimates obtained by Hora et al. (2013) from phenocrysts/microphenocrysts provide convincing evidence that this unit is homogenous and free of magma mixing.

Hideaway Park tuff

The Hideaway Park tuff (also referred to as Winter Park tuff) is an extrusive volcanic unit of Oligocene age (27.77 ± 0.34 Ma, sanidine K-Ar; Mercer et al. 2015) that is genetically related to the Red Mountain intrusive complex in Colorado, USA, which hosts the giant Urad-Henderson porphyry Mo deposit. Its mineralogy and geochemistry is described in detail by Mercer et al. (2015), who provided also an extensive set of mineral- and melt inclusion analyses. In order to calculate the composition of the crystallized melt inclusions, the average Al_2O_3 content from all homogenized melt inclusions and pumice glasses analyzed by Mercer et al. (2015) was used as internal standard (13.30 wt % Al_2O_3).

Cottonwood Wash tuff

The Cottonwood Wash tuff belongs to the Indian Peak volcanic field that was active from ca. 30 to 29 Ma (plagioclase K-Ar; Best 2013) and comprises tens of calderas and related ash flow sheets that cover about 50000 km^2 across the Utah-Nevada state line, USA. The Cottonwood Wash tuff formed during a super-eruption 31.13 million years ago (plagioclase K-Ar; Best 2013), producing about 2000 km^3 of crystal-rich, dacitic tuff, with a fairly homogenous composition over its entire extent. A detailed description about the geochemistry, petrography

and mineralogy of the volcanic units of the Indian Peak volcanic field can be found in Best et al. (1989) and Best (2013). The rapidly quenched, fresh, glassy matrix and the presence of abundant Fe-Ti oxide microphenocrysts allow easy application of the mgt-ilm oxybarometer and the V partitioning oxybarometer. At the same time, the latter method could be applied also to inclusions, as both magnetite inclusions (in quartz) and melt inclusions (in quartz and feldspar) were available.

Lordsburg rhyolite

The Lordsburg mining district is located in the Pyramid Mountains, a north-trending range of Lower Cretaceous to middle Tertiary volcanic and plutonic rocks in the Basin and Range province of southwestern New Mexico, southwest of the city of Lordsburg. The Paleocene intrusive rocks of the area include a granodiorite stock (58.8 ± 2 Ma, biotite K-Ar; Thorman and Drewes 1978), rhyolitic vents, breccia pipes and dikes, the first two formations of which were investigated in this study. Although some early studies have been conducted on these rock units (Lasky 1938; Flege 1959; Thorman and Drewes 1978), nothing has been published about their major- and trace element composition.

Lordsburg granodiorite

This sample was collected from the most widespread intrusive unit of the Pyramid Mountains – the granodiorite – , which intruded also the previously described Lordsburg rhyolite. The lack of quartz phenocrysts precluded any inclusion-based thermometry and oxybarometry. However, due to the relatively unaltered nature of this rock (unlike the Lordsburg rhyolite) the relevant information was obtained from the composition of fresh-looking microphenocrysts and the fine-grained rock matrix.

Smelter Knolls rhyolite

The Smelter Knolls rhyolite belongs to a bimodal association of silica-rich, often topaz-bearing rhyolites and contemporaneous basalts and basaltic andesites of Cenozoic age that are widespread in the Basin and Range province and along the Rio Grande Rift in Western USA and Mexico (Christiansen et al. 1986). Thorough geological, geochemical and age data about these topaz rhyolites can be found in the comprehensive study of Christiansen et al. (1986), whereas the detailed description of the Smelter Knolls complex was published by Turley and Nash (1980). The Smelter Knolls represent a single rhyolite flow-dome complex measuring 5 km in

diameter and 2.2 km^3 in volume, located north of the city of Delta in Utah, USA. The dome complex formed at 3.4 ± 0.1 Ma based on sanidine K-Ar dating (Turley and Nash 1980). A recent study on the Black Rock Desert volcanic field (Johnsen et al. 2010) − which includes the Smelter Knolls − contains a large amount of whole rock geochemical data, from which the average Al_2O_3 content of Smelter Knolls rhyolite was used as an internal standard for our melt inclusion analyses.

Amalia Tuff

The Questa caldera and the cogenetic volcanic and intrusive rocks of the Latir volcanic field in northern New Mexico, USA, were extensively studied by Lipman (1988), Johnson and Lipman (1988), Johnson et al. (1989), and Czamanske et al. (1990). Most of the Latir volcanic units and associated intrusive rocks were emplaced within a few million years (28-26 Ma), including the eruption of the only major ash flow tuff − the Amalia Tuff − 26.5 Ma ago (sanidine K-Ar; Lipman et al. 1986). This peralkaline, rhyolitic tuff can be subdivided into two subunits, and the upper sequence − according to similarities in composition and mineralogy − is thought to represent the erupted portion of resurgent peralkaline intrusions of the Questa caldera. Although plutons at exposed levels are texturally discrete and of contrasting composition, regional gravity data (Cordell et al. 1985) suggest that the entire Questa caldera is underlain by cogenetic batholithic rocks of 10 by 20 km size at shallow depth. The Amalia Tuff sample investigated in the present study was collected from an outflow sheet 40 km SW of the caldera rim near the town of Tres Piedras.

Banco Bonito vitrophyre

The Banco Bonito Flow forms part of the East Fork Member of the Valles Rhyolite in New Mexico, USA. It represents the youngest volcanic unit of the Valles caldera complex that was active between 45 ka and 35 ka (ESR ages, ^{21}Ne exposure ages, regional constraints; (Goff and Gardner 2004; Ogoh et al. 1993; Phillips et al. 1997). Detailed descriptions of the mineralogy, petrography and geochemistry of the East Fork Member can be found in Eichler (2012). Based on the trace element geochemistry of the phenocrysts and the volcanic glass, the East Fork Member rhyolites had a complex evolution history, starting with fractional crystallization of a basalt, followed by magma ascent to lower crustal levels and crustal assimilation, and finally fractional crystallization in a granitic magma chamber in the upper crust.

Santa Rita rhyodacite dike

The porphyry-copper deposit at Santa Rita (Chino Mine) in southwestern New Mexico formed during the Laramide orogeny (45–75 Ma) as a result of subduction along an Andean-type continental margin. There were several stages of the igneous activity in the region, starting with dioritic to quartz-dioritic sills intruded into the Precambrian basement rocks, followed by the eruption of basaltic–andesitic to andesitic magma and the formation of mafic dikes, and subsequently the intrusion of granodioritic to quartz-monzodioritic magma. The last stage of magmatic activity is represented by dikes of rhyodacitic to rhyolitic composition, which cut across all other lithologies. Details on the geology and petrography of the complex can be found in Rose and Baltosser (1966) and Jones et al. (1967), whereas more recent studies (Audétat and Pettke 2006) focus on the chemical analysis of mineral and melt inclusions. We investigated two samples (SR15, SR9) from two rhyodacite dikes.

The Dyke

The West Elk laccolite cluster occupies the northern part of the West Elk Mountains, northwestern Gunnison County, Colorado. The laccoliths are located along a dike swarm related to a NNE-SSW trending, at least 40 km long fracture zone (Godwin and Gaskill 1964). The mafic, early stage of each stock is crosscut by SiO_2-rich dikes or stock-internal granodiorites (Mutschler et al. 1981). "The Dyke" represents this second stage and forms a prominent outcrop of ca. 2.5 km length south of Ruby Peak. There are no age data available from The Dyke, but considering that it intrudes the Early Eocene Wasatch formation and the genetically related Crested Butte laccolith and Paradise stock, which yielded biotite K-Ar ages of 29.0 ± 1.1 Ma and 29.1 ± 1.0 Ma, respectively (Obradovich et al. 1969), it is probable that The Dyke granite formed in the Oligocene.

Nomlaki Tuff

This sample was kindly provided by the Smithsonian Institution (NMNH 116377-38a). The Nomlaki Tuff (4.2 to 3.6 Ma) formed by a Plinian eruption in the Pliocene and covers areas in California, Nevada, Utah, Arizona and New Mexico. The deposits consist of widespread ash-fall and proximal ash-flow units and are commonly used as marker horizons in the region (Knott and Sarna-Wojcicki 2001). Information about the distribution and regional correlation of the Late Cenozoic tuffs of the Central Coast Ranges of California can be found in Sarna-Wojcicki et al. (1984), in Knott and Sarna-Wojcicki (2001) and in Poletski (2010). Whole-rock geochemical

data can be found in Knott and Sarna-Wojcicki (2001), whereas an extensive dataset regarding the geochemistry of glass fragments and pumices, as well as regarding mgt-ilm thermometry results – both from the occurrences in the Sacramento Valley – are published in Poletski (2010). Poletski (2010) distinguished two chemo-types within the tuff based on the major element composition of glass shards and magnetite-ilmenite microphenocryst thermometry results, and explained the phenomenon by a zoned magma chamber, containing a more evolved and cooler magma in its upper part, and a less evolved, hotter magma at its bottom.

Kos granite enclave

The geochemical evolution of the Kos Plateau Tuff and related magma chamber processes have been exceptionally well studied. Petrographic observations (Keller 1969), sanidine Ar-Ar dating (Smith et al. 1996), zircon U-Pb dating (Bachmann et al. 2007), melt inclusion analysis (Bachmann et al. 2009), and a recent comprehensive study on the Kos Plateau Tuff (Bachmann 2010) all contributed to a comprehensive understanding of the region's magmatism. The Kos Plateau Tuff formed 160,000 years ago (Smith et al. 1996), and represents one of the largest Quaternary explosive eruptions. The non-welded tuff consists mainly of juvenile ash, different types of pumice, and lithic fragments, and locally contains equigranular granitic enclaves. The rhyolitic magma most probably evolved from a more mafic parent dominantly by fractional crystallization, as shown by the lack of inherited zircons (Bachmann et al. 2007). The magma was probably in a crystal mush state before the eruption, with some completely crystallized units at the edge of the magma body having been entrained in the form of granitic enclaves. The system was partly reheated by injection of a more mafic magma batch, which triggered the eruption and resulted in the formation of andesitic bands within pumice, plagioclase overgrowths on K-feldspar, and inverse zonations in plagioclases (Bachmann 2010).

Los Humeros

This sample was obtained from the Smithsonian Institution (NMNH 117450-58). The Los Humeros volcanic center of Pleistocene age (K-Ar) is located 180 km east of Mexico City and represents the easternmost expression of the late Tertiary to Quaternary Mexican Neovolcanic Belt (Ferriz and Mahood 1984). The volcanic province can be characterized by a series of lava flows, large eruptions (resulting in large scale ignimbrite deposition) and subsequent caldera collapse and dome-forming events. The most common compositions are rhyolitic and rhyodacitic, however, andesites and basalts (the latter mainly at the last stage of volcanism)

occur as well. A detailed description of the volcanics in the region can be found in Ferriz and Mahood (1984). Our sample was obtained from the Smithsonian Institution (NMNH 117450-58).

Samples from the Mono-Inyo volcanic field

The Long Valley Volcanic Field is located at the intersection of the Sierra Nevada and the Basin and Range tectonic province in east-central California. Volcanism in the region started about 4 million years ago (Gilbert et al. 1968) and continued in multiple phases until recently. It can be separated into a pre-caldera and a post-caldera episode, the first of which peaked at 0.76 ka with the eruption of the Bishop Tuff, followed by a caldera collapse and the formation of multiple craters along the N-S trending Mono-Inyo fissure system (Bailey, 2004). The composition of magmas erupted from the Mono-Inyo crater system ranges from basaltic to rhyolitic, with a compositional gap between trachyandesite and dacite, and includes several high-silica varieties containing andesitic inclusions. These andesitic inclusions lie on the mixing line between finely porphyritic rhyolites and typical post-caldera mafic magmas. Their xenocryst assemblage is identical to the phenocryst assemblage of the host rhyolites, which provides strong evidence for the involvement of mafic magma and magma mixing during silicic eruptions (Varga et al. 1990). Extensive geochemical datasets, detailed geological observations and interpretation of the complex geological evolution of the region can be found in Bailey (2004) and in Bray (2014).

Tunnel Spring Tuff

The Tunnel Spring Tuff was erupted 35.4 million years ago (K-Ar age) from a vent that probably was close to Crystal Peak, Utah, where the tuff forms a canyon fill of more than 400 m thickness (Steven 1989). The P-T-x history of the parental magma was investigated by Audétat (2013) based on zircon saturation thermometry of melt inclusions and Ti-in-quartz thermobarometry.

Blackfoot lava field vitrophyre

The Blackfoot lava field is located in southeastern Idaho, USA. It is characterized by bimodal volcanism, consisting of five rhyolitic domes located in a predominantly basaltic volcanic field. The rhyolites, which belong to the group of Cenozoic Topaz Rhyolites (Christiansen 1986), contain inclusions of older basalts and andesites, but they are older than the basalts exposed on the surface. Our vitrophyre sample was kindly provided by the Smithsonian Institution (NMNH 117462-1) and was collected on the northern side of a rhyolite dome named China Hat (also referred to as China Cap or Middle Cone), the age of which was determined at 61±6 ka (sanidine

K-Ar; Pierce et al. 1982). The geology of the lava field, including whole rock data, is described in Christiansen et al. (1986).

Pine Grove Tuff

The Pine Grove intrusions and associated tuffs are located in the southern Wah Wah Mountains, southern Utah, USA. Whole rock and K-feldspar K-Ar data suggests that the Pine Grove system, which consists of rhyolitic (and partly dacitic) tuffs, and intrusions ranging from rhyolitic to mafic compositions, formed 23 to 22 m.y. ago (Keith et al. 1986). According to Keith et al. (1986) the tuffs were erupted from a magma chamber that was intruded by a trachyandesitic magma multiple times, and was compositionally zoned from dacite to rhyolite. Detailed petrography and K-Ar age data of the Pine Grove system can be found in Keith et al. (1986), an extensive dataset of melt inclusion analyses was published by Lowenstern et al (1994), whereas thermometry and oxybarometry data can be found in Keith and Shanks (1988) and Audétat et al. (2011). Our sample was collected from the rhyolitic air-fall unit.

7.8   References

Andersen DJ, Lindsley DH (1985) New (and final!) models for the Ti-magnetite/ilmenite geothermometer and oxygen barometer. In: Abstract AGU 1985 Spring Meeting Eos Transactions. American Geophysical Union. 66(18):416

Andersen DJ, Lindsley DH (1988) Internally consistent solution models for Fe-Mg-Mn-Ti oxides: Fe-Ti oxides. Am Mineral 73:714-726

Andersen DJ, Lindsley DH, Davidson PM (1993) QUILF: A pascal program to assess equilibria among Fe–Mg–Mn–Ti oxides, pyroxenes, olivine, and quartz. Comput Geosci 19(9):1333-1350

Arató R, Audétat A (2016) Experimental calibration of a new oxybarometer for silicic magmas based on vanadium partitioning between magnetite and silicate melt, submitted

Audétat A (2013) Origin of Ti-rich rims in quartz phenocrysts from the Upper Bandelier Tuff and the Tunnel Spring Tuff, southwestern USA. Chem Geol 360-361:99-104

Audétat A (2015) Compositional evolution and formation conditions of magmas and fluids related to porphyry Mo mineralization at Climax, Colorado. J Petrol 56(8):1519-1546

Audétat A, Pettke T, Dolejs D (2004) Magmatic anhydrite and calcite in the ore-forming quartz-monzodiorite magma at Santa Rita, New Mexico (USA): genetic constraints on porphyry-Cu mineralization. Lithos 72(3):147-161.

Audétat A, Dolejs D, Lowenstern JB (2011) Molybdenite Saturation in Silicic Magmas: Occurrence and Petrological Implications. J Petrol 52(5):891-904

Audétat A, Günther D, Heinrich C (2000) Magmatic-hydrothermal evolution in a fractionating granite: A microchemical study of the Sn-WF-mineralized Mole Granite (Australia). Geochim Cosmochim Acta 64(19):3373-3393

Audétat A, Lowenstern JB (2014) Melt inclusions. In: Scott SD (ed) Geochemistry of mineral deposits. Treatise on Geochemistry 2nd ed., 13, pp 143-173

Audétat A, Pettke T (2003) The magmatic-hydrothermal evolution of two barren granites: a melt and fluid inclusion study of the Rito del Medio and Canada Pinabete plutons in northern New Mexico (USA). Geochim Cosmochim Acta 67(1):97-121

Audétat A, Pettke T (2006) Evolution of a Porphyry-Cu Mineralized Magma System at Santa Rita, New Mexico (USA). J Petrol 47(10):2021-2046

Bachmann O (2010) The petrologic evolution and pre-eruptive conditions of the rhyolitic Kos Plateau Tuff (Aegean Arc). Open Geosci 2(3):270-305

Bachmann O, Charlier BLA, Lowenstern JB (2007) Zircon crystallization and recycling in the magma chamber of the rhyolitic Kos Plateau Tuff (Aegean arc). Geology 35(1):73-76

Bachmann O, Wallace PJ, Bourquin J (2009) The melt inclusion record from the rhyolitic Kos Plateau Tuff (Aegean Arc). Contrib Mineral Petrol 159(2):187-202

Bacon CR, Hirschmann MM (1988) Mg/Mn partitioning as a test for equilibrium between coexisting Fe-Ti oxides. Am Mineral 73(1-2):57-61

Bailey R (1989) Geologic map of Long Valley Caldera, Mono-Inyo craters volcanic chain and vicinity, Eastern California, scale 1:62,500. US Geol Surv Geophys Invest Map I—1993:11

Bailey RA (2004) Eruptive history and chemical evolution of the precaldera and postcaldera basalt-dacite sequences, Long Valley, California: Implications for magma sources, current seismic unrest, and future volcanism. USGS Prof Pap 1692:75 pp

Best M (2013) The 36–18 Ma Indian Peak–Caliente ignimbrite fi eld and calderas, southeastern Great Basin, USA: Multicyclic super-eruptions. Geosphere 9(4):864-950

Best MG, Christiansen EH, Blank RH (1989) Oligocene caldera complex and calc-alkaline tuffs and lavas of the Indian Peak volcanic field, Nevada and Utah. Geol Soc Am Bull 101(8):1076-1090

Blevin PL, Chappell BW, Allen CM (1996) Intrusive metallogenic provinces in eastern Australia based on granite source and composition. Geol Soc Am Spec Pap 315:281-290

Boehnke P, Watson EB, Trail D, Harrison TM, Schmitt AK (2013) Zircon saturation re-revisited. Chem Geol 351:324-334

Bray BA (2014) Mafic replenishment of multiple felsic reservoirs at the Mono domes and Mono Lake islands, California. MSc thesis. McGill University

Buddington A, Lindsley D (1964) Iron-titanium oxide minerals and synthetic equivalents. J Petrol 5(2):310-357

Candela PA, Bouton SL (1990) The influence of oxygen fugacity on tungsten and molybdenum partitioning between silicate melts and ilmenite. Econ Geol 85(3):633-640

Canil D (1999) Vanadium partitioning between orthopyroxene, spinel and silicate melt and the redox states of mantle source regions for primary magmas. Geochim Cosmochim Acta 63(3):557-572

Canil D (2002) Vanadium in peridotites, mantle redox and tectonic environments: Archean to present. Earth Planet Sci Lett 195(1):75-90

Carmichael ISE (1967) The iron-titanium oxides of salic volcanic rocks and their associated ferromagnesian silicates. Contrib Mineral Petrol 14:36-64

Christiansen EH, Sheridan MF, Burt DM (1986) The geology and geochemistry of Cenozoic topaz rhyolites from the western United States. Geol Soc Am Spec Pap 205:1-82

Cordell L, Long CL, Jones DW (1985) Geophysical expression of the batholith beneath Questa caldera, New Mexico. J Geophys Res 90(B13):11263-11269

Ebadi A, Johannes W (1991) Beginning of melting and composition of first melts in the system Qz-Ab-Or-H2O-CO2. Contrib Mineral Petrol 106(3):286-295

Eichler C (2012) Petrogenesis of the East Fork Member Rhyolites, Valles Caldera, New Mexico, USA. MSc thesis. University of Nevada

Ferriz H, Mahood GA (1984) Eruption rates and compositional trends at Los Humeros Volcanic Center, Puebla, Mexico. J Geophys Res 89(B10):8511-8524

Flege RF (1959) Geology of Lordsburg Quadrangle, Hidalgo County, New Mexico. New Mexico Bur Mines and Mineral Resources Bull (62):36 pp

Frost BR (1991) Introduction to oxygen fugacity and its petrologic importance. Rev Mineral Geochem 25(1):1-9

Frost BR, Lindsley D (1992) Equilibria among Fe-Ti oxides, pyroxenes, olivine, and quartz: Part II. Application. Am Mineral 77:1004-1004

Gervasoni F, Klemme S, Rocha-Júnior ERV, Berndt J (2016) Zircon saturation in silicate melts: a new and improved model for aluminous and alkaline melts. Contrib Mineral Petrol 171(3):1-12

Ghiorso MS, Evans BW (2008) Thermodynamics of rhombohedral oxide solid solutions and a revision of the Fe-Ti two-oxide geothermometer and oxygen-barometer. Am J Sci 308(9):957-1039

Ghiorso MS, Sack O (1991) Fe-Ti oxide geothermometry: thermodynamic formulation and the estimation of intensive variables in silicic magmas. Contrib Mineral Petrol 108:485-510

Gilbert C, Christensen M, Al-Rawi Y, Lajoie K (1968) Structural and volcanic history of Mono basin, California-Nevada. Geol Soc Am Mem 116:275-330

Godwin L, Gaskill D (1964) Post-Paleocene West Elk laccolithic cluster, west-central Colorado. Geological Survey Research 1964, US Geol Surv Profess Pap 501-C:3 pp

Goff F, Gardner J (2004) Late Cenozoic geochronology of volcanism and mineralization in the Jemez Mountains and Valles caldera, north central New Mexico. In: Mack GH, KA G (eds) The Geology of New Mexico. New Mexico Geol Soc Spec Publ, 11:295-312

Hakim A, Sufni, Hall R (1991) Tertiary volcanic rocks from the Halmahera Arc, Eastern Indonesia. J Southeast Asian Earth Sci 6:271-287

Hora JM, Kronz A, Möller-McNett S, Wörner G (2013) An Excel-based tool for evaluating and visualizing geothermobarometry data. Comput Geosci 56:178-185

Hora JM, Singer BS, Wörner G (2007) Volcano evolution and eruptive flux on the thick crust of the Andean Central Volcanic Zone: 40Ar/39Ar constraints from Volcan Parinacota, Chile. Geol Soc Am Bull 119(3-4):343-362

Horn I, Foley SF, Jackson SE, Jenner GA (1994) Experimentally determined partitioning of high field strength- and selected transition elements between spinel and basaltic melt. Chem Geol 117(1):193-218

Irving AJ (1978) A review of experimental studies of crystal/liquid trace element partitioning. Geochim Cosmochim Ac 42(6):743-770

Ishihara S (1981) The granitoid series and mineralization. Econ Geol 75th Anniv Vol:458-484

Janssen A, Putnis A, Geisler T, Putnis CV (2010) The experimental replacement of ilmenite by rutile in HCl solutions. Mineral Mag 74(4):633-644

Jochum KP, Weis U, Stoll B, Kuzmin D, Yang Q, Raczek I, Jacob DE, Stracke A, Birbaum K, Frick DA, Günther D, Enzweiler J (2011) Determination of reference values for NIST SRM 610-617 glasses following ISO guidelines. Geostand Geoanal Res 35(4):397-429

Johnsen RL, Smith EI, Biek RF (2010) Subalkaline volcanism in the Black Rock Desert and Markagunt Plateau volcanic fields of south-central Utah. In: Carney SM, Tabet DE, Johnson CL (eds) Geology of South-Central Utah. Utah Geol Assoc Publ, 39:109-150

Johnson CM, Lipman PW (1988) Origin of metaluminous and alkaline volcanic rocks of the Latir volcanic field, northern Rio Grande rift, New Mexico. Contrib Mineral Petrol 100(1):107-128

Jones WR, Hernon RM, Moore SL (1967) General geology of Santa Rita quadrangle, Grant County, New Mexico. Geol Surv Prof Pap 555:144 pp

Jugo P, Candela P, Piccoli P (1999) Magmatic sulfides and Au:Cu ratios in porphyry deposits: an experimental study of copper and gold partitioning at 850 °C, 100 MPa in a haplogranitic melt–pyrrhotite–intermediate solid solution–gold metal assemblage, at gas saturation. Lithos 46(3):573-589

Jugo PJ, Wilke M, Botcharnikov RE (2010) Sulphur K-edge XANES analysis of natural and synthetic basaltic glasses: Implications for S speciation and S content as function of oxygen fugacity. Geochim Cosmochim Acta 74(20):5926-5938

Keith J, Shanks W (1988) Chemical evolution and volatile fugacities of the Pine Grove porphyry molybdenum and ash-flow tuff system, southwestern Utah. In: Taylor RP, Strong DF (eds) Recent advances in the geology of granite-related mineral deposits. Can Inst Min Met Spec Vol, 39:402-423

Keith JD, Shanks WC, Archibald DA, Farrar E (1986) Volcanic and intrusive history of the Pine Grove porphyry molybdenum system, southwestern Utah. Econ Geol 81(3):553-577

Keller J (1969) Origin of rhyolites by anatectic melting of granitic crustal rocks. B Volcanol 33(3):942-959

Keppler H (1993) Influence of fluorine on the enrichment of high field strength trace elements in granitic rocks. Contrib Mineral Petrol 114(4):479-488

Knott JR, Sarna-Wojcicki AM (2001) Stop C3 Late Pliocene tephrostratigraphy and geomorphic development of the Artists Drive structural block In: Machette MN, Johnson ML, Slate JL (eds) Quaternary and Late Pliocene Geology of the Death Valley Region: Recent Observations on Tectonics, Stratigraphy, and Lake Cycles. Guidebook for the 2001 Pacific Cell—Friends of the Pleistocene Fieldtrip:105-111

Lasky SG (1938) Geology and ore deposits of the Lordsburg mining district, Hidalgo County, New Mexico. US Geol Surv Bull 885:62 pp

Lattard D, Sauerzapf U, Käsemann M (2005) New calibration data for the Fe-Ti oxide thermo-oxybarometers from experiments in the Fe-Ti-O system at 1 bar, 1,000-1,300°C and a large range of oxygen fugacities. Contrib Mineral Petrol 149(6):735-754

Lehmann B (1990) Metallogeny of tin (Lecture Notes in Earth Sciences 32):211 pp

Lepage LD (2003) ILMAT: an Excel worksheet for ilmenite–magnetite geothermometry and geobarometry. Comput Geosci 29(5):673-678

Lindsley DH, Frost BR (1992) Equilibria among Fe-Ti oxides, pyroxenes, olivine, and quartz; Part I, Theory. Am Mineral 77(9-10):987-1003

Linnen RL, Pichavant M, Holtz F (1996) The combined effects of fO$_2$ and melt composition on SnO$_2$ solubility and tin diffusivity in haplogranitic melts. Geochim Cosmochim Acta 60(24):4965-4976

Lipman PW, Mehnert HH, Naeser CW (1986) Evolution of the Latir Volcanic Field, Northern New Mexico, and Its Relation to the Rio Grande Rift, as Indicated by Potassium-Argon and Fission Track Dating J Geophys Res 91(B6):6329-6345

Lowenstern JB, Bacon CR, Calk LC, Hervig RL, Aines RD (1994) Major-element, trace-element, and volatile concentrations in silicate melt inclusions from the tuff of Pine Grove, Wah Wah Mountains, Utah. US Geological Survey Open-File Report 94-242:20 pp

Mallmann G, O'Neill HSC (2009) The crystal/melt partitioning of V during mantle melting as a function of oxygen fugacity compared with some other elements (Al, P, Ca, Sc, Ti, Cr, Fe, Ga, Y, Zr and Nb). J Petrol 50(9):1765-1794

Mercer CN, Hofstra AH, Todorov TI, Roberge J, Burgisser A, Adams DT, Cosca M (2015) Pre-Eruptive Conditions of the Hideaway Park Topaz Rhyolite: Insights into Metal Source and Evolution of Magma Parental to the Henderson Porphyry Molybdenum Deposit, Colorado. J Petrol 56(4):645-679

Mutschler F, Ernst D, Gaskill D, Billings P (1981) Igneous rocks of the Elk Mountains and vicinity, Colorado-chemistry and related ore deposits. Western Slope Colorado: New Mexico Geological Society 32nd Field Conference Guide Book:317-324

Obradovich J, D, Mutschler F, E, Bryant B (1969) Potassium-argon ages bearing on the igneous and tectonic history of the Elk Mountains and Vicinity, Colorado: a preliminary report. Geol Soc Am Bull 80(9):1749-1756

Ogoh K, Toyoda S, Ikeda S, Ikeya M, Goff F (1993) Cooling history of the Valles caldera, New Mexico using ESR dating method. Appl Radiat Isot 44(1):233-237

Peiffert C, Cuney M, Nguyen-Trung C (1994) Uranium in granitic magmas: Part 1. Experimental determination of uranium solubility and fluid-melt partition coefficients in the uranium oxide-haplogranite-H$_2$O-Na$_2$CO$_3$ system at 720–770° C, 2 kbar. Geochim Cosmochim Acta 58(11):2495-2507

Phillips W, Poths J, Goff F, Reneau S, McDonald E (1997) Ne-21 surface exposure ages from the Banco Bonito obsidian flow, Valles caldera, New Mexico, USA. Geological Society of America, Abstracts with Programs 29(6):A-419

Pierce KL, Fosberg M, Scott WE, Lewis GC, Colman SM (1982) Loess deposits of southeastern Idaho: Age and correlation of the upper two loess units. Idaho Bur Mines Geol Bull 26:717-725

Poletski SJ (2010) The Nomlaki Tuff eruption: chemical correlation of a widespread Pliocene stratigraphic marker. MSc thesis. California State University

Putirka KD (2008) Thermometers and Barometers for Volcanic Systems. Rev Mineral Geochem 69(1):61-120

Putirka, K. (2016) Rates and styles of planetary cooling on Earth, Moon, Mars, and Vesta, using new models for oxygen fugacity, ferric-ferrous ratios, olivine-liquid Fe-Mg exchange, and mantle potential temperature. Am. Mineral. 101:819-840.

Ridolfi F, Renzulli A, Puerini M (2009) Stability and chemical equilibrium of amphibole in calc-alkaline magmas: an overview, new thermobarometric formulations and application to subduction-related volcanoes. Contrib Mineral Petrol 160(1):45-66

Righter K, Leeman WP, Hervig RL (2006a) Partitioning of Ni, Co and V between spinel-structured oxides and silicate melts: Importance of spinel composition. Chem Geol 227(1-2):1-25

Righter K, Sutton SR, Newville M, Le L, Schwandt CS, Uchida H, Lavina B, Downs RT (2006b) An experimental study of the oxidation state of vanadium in spinel and basaltic melt with implications for the origin of planetary basalt. Am Mineral 91(10):1643-1656

Rose AW, Baltosser WW (1966) The porphyry copper deposit at Santa Rita, New Mexico. In: Titley SR, Hicks CL (eds) Geology of the Porphyry Copper Deposits in Southwestern North America. University of Arizona, Tucson:205–220

Sarna-Wojcicki AM, Bowman H, Meyer CE, Russell P, Woodward M, McCoy G, Rowe Jr J, Baedecker P, Asaro F, Michael H (1984) Chemical analyses, correlations, and ages of upper Pliocene and Pleistocene ash layers of east-central and southern California. Geol Surv Prof Pap 1293:40 pp

Seghedi I (2011) Permian rhyolitic volcanism, changing from subaqueous to subaerial in post-Variscan intra-continental Sirinia Basin (SW Romania–Eastern Europe). J Volcanol Geotherm Res 201(1-4):312-324

Smith P, York D, Chen Y, Evensen N (1996) Single crystal 40Ar-39Ar dating of a Late Quaternary paroxysm on Kos, Greece: Concordance of terrestrial and marine ages. Geophys Res Lett 23(21):3047-3050

Steven TA (1989) Geologic map of the Crystal Peak caldera, west-central Utah. US Geol Surv Misc Inv Ser Map I-2002

Stormer JC (1983) The effects of recalculation on estimates of temperature and oxygen fugacity from analyses of multicomponent iron-titanium oxides. Am Mineral 68(5-6):586-594

Taylor JR, Wall VJ (1992) The behavior of tin in granitoid magmas. Econ Geol 87(2):403-420

Thorman C, Drewes H (1978) Cretaceous–early Tertiary history of the northern Pyramid Mountains, southwestern New Mexico. In: Callender JF, Wilt J, Clemons RE, James HL (eds), New Mexico Geological Society 29th Annual Fall Field Conference Guidebook:215-218

Turley C, Nash W (1980) Petrology of late Tertiary and Quaternary volcanism in western Juab and Millard Counties, Utah. Utah Geol Min Surv Spec Stud 52:1-33

Varga RJ, Bailey RA, Suemnicht GA (1990) Evidence for 600 year-old basalt and magma mixing at Inyo Craters Volcanic Chain, Long Valley Caldera, California. J Geophys Res 95(B13):21441-21450

Watson EB, Harrison TM (1983) Zircon saturation revisited: temperature and composition effects in a variety of crustal magma types. Earth Planet Sci Lett 64(2):295-304

Wones D (1981) Mafic silicates as indicators of intensive variables in granitic magmas. Mining Geol 31(4):191-212

Wones D, Eugster H (1965) Stability of biotite–experiment theory and application. Am Mineral 50(9):1228-1272

Wörner G, Harmon R, Davidson J, Moorbath S, Turner D, McMillan N, Nyes C, Lopez-Escobar L, Moreno H (1988) The Nevados de Payachata volcanic region (18 S/69 W, N. Chile). Bull Volcanol 50(5):287-303

Xirouchakis D, Lindsley DH, Frost BR (2001) Assemblages with titanite ($CaTiOSiO_4$), Ca-Mg-Fe olivine and pyroxenes, Fe-Mg-Ti oxides, and quartz: Part II. Application. Am Mineral 86(2-3):254-264

Yang Q-C, Jochum KP, Stoll B, Weis U, Kuzmin D, Wiedenbeck M, Traub H, Andreae MO (2012) BAM-S005 type A and B: New silicate reference glasses for microanalysis. Geostand Geoanal Res 36(3):301-313

Zajacz Z, Halter WE, Pettke T, Guillong M (2008) Determination of fluid/melt partition coefficients by LA-ICPMS analysis of co-existing fluid and silicate melt inclusions: Controls on element partitioning. Geochim Cosmochim Acta 72(8):2169-2197

Supplementary Table 7.S1/1: Extended table of the thermometry and oxybarometry results.

Sample name	mineralogy	ASI[1] based on	n mgt	n ilm	n MI/mx	Rb/Sr and Cs/Ba scatter	matrix vs MI comp. diff.	inclusions in qtz MI	feldspars	opq	others	inclusions in fsp MI	feldspars	opq	others	Nb	Y
Most reliable samples																	
Oravita hyalodacite mx	plag($An_{49}Ab_{48}Or_{03}$), qtz, bio, amph, mgt (34.9 % usp), ilm (90% ilm), zirc	0.96 ± 0.01 mx	6	5	9	small	-	-	-	-	-	xx	-	mgt	zi, ol?	12	27
Mount Rano vitrophyre mx	plag, px, mgt (39.3 % usp), ilm (89% ilm), zirc	1.01 ± 0.01 mx	4	3	5	small	-	-	-	-	-	-	-	-	-	4	49
Parinacota mx	qtz, $Kfsp(Or_{74}Ab_{22}An_{04})$, plag, bio, px, mgt (10.0 % usp) & mgt (16.9 % usp), ilm (74% ilm) & ilm (55% ilm), tit, zirc	0.99 ± 0.00 mx	6	4	3	small	small	gl	-	-	-	gl	$Kfsp(Or_{74}Ab_{22}An_{04})$ host $Plag(An_{25}Ab_{69}Or_{06})$	-	-	9	2
Parinacota vitrophyre incl	qtz, $Kfsp(Or_{74}Ab_{22}An_{04})$, plag, bio, px, mgt (10.0 % usp) & mgt (16.9 % usp), ilm (74% ilm) & ilm (55% ilm), tit, zirc	0.99 ± 0.04 MI	-	-	6	small/ medium with 2 outliers	small	gl	-	-	-	gl	$Kfsp(Or_{74}Ab_{22}An_{04})$ host $Plag(An_{25}Ab_{69}Or_{06})$	-	-	9	2
Hideaway Park incl	qtz, Kfsp $(Or_{60}Ab_{38}An_{02})$, plag, bio, mgt, ilm, ap, zirc, tit	1.04 ± 0.02 xxMI	2	6	small	-	xx	-	mgt (12.7% usp) ilm (82%ilm)	ap		$Kfsp(Or_{60}Ab_{38}An_{02})$ host plag($An_{20}Ab_{72}Or_{08}$)	mgt (12.4 % usp)	-	168	42
Hideaway Park mx literature	qtz, Kfsp $(Or_{60}Ab_{38}An_{02})$, plag, bio, mgt, ilm, ap, zirc, tit	1.04 ± 0.02 xxMI	-	-	-	-	xx	-	mgt (12.7% usp) ilm (82%ilm)	-		$Kfsp(Or_{60}Ab_{38}An_{02})$ host plag($An_{20}Ab_{72}Or_{08}$)	mgt (12.4 % usp)	-		
Cottonwood tuff mx	qtz, plag, bio, amph, px, mgt (19.0 % usp), ilm (81 % ilm), po, zirc, ap	1.01 ± 0.02 mx	5	2	3	small	big	?	plag($An_{71}Ab_{28}Or_{01}$)	mgt (19.8 % usp)	po	-	-	-	-	15	12
Cottonwood tuff incl	qtz, plag, bio, amph, px, mgt (19.0 % usp), ilm (81 % ilm), po, zirc, ap	0.98 ± 0.03 MI	4	-	7	small	big	?	plag($An_{71}Ab_{28}Or_{01}$)	mgt (19.8 % usp)	po	-	-	-	-	16	14

melt / matrix (ppm)			T zirc (°C)[2]			T two-fsp (°C)[3]	T mgt-ilm (°C)[4]			log$f$O$_2$ via mgt-ilm (ΔFMQ)[5]			log$f$O$_2$ via V-partitioning (ΔFMQ)[6]				References
Y+Nb	Rb	Zr	WH 83 (utilized ASI)	Boe 13	Ger 16	Putirka 08 (based on)	based on	G & E (08)	A & L (Ilmat)	based on	G & E (08)	A & L (Ilmat)	based on	temp	ASI	fO$_2$ (ΔFMQ)	
39	196	98±6 mx	748±7 (mx 0.96)			-	mp	798±57	814±41	mp	0.44 ±0.34	0.55 ±0.33	mx+ mgt mp	T zirc matrix	0.96 ±0.01	0.06±0.16	
53	81	247±9 mx	829±4 (mx 1.01)			-	mp	863±12	851±10	mp	0.46 ±0.08	0.58 ±0.06	mx+ mgt mp	T zirc matrix	0.97 ±0.04	0.76±0.13	
11	241	68±1 mx	723±11 (mx 0.99)	661±3	556±3	753±40, 726±11 (fsp in fsp)	mp	711±22, 723±84	837±72	mp	2.16 ±0.16	2.53 ±0.11	mx+ mgt mp	T zirc matrix	0.99 ±0.00	1.71±0.43	Hora et al., 2013
11	251	67±7 MI	718±9 (MI 0.99)	660±12	531±25	753±40, 726±11 (fsp in fsp)							MI+ mgt mp	T zirc MI	0.99 ±0.00	1.78±0.18	Hora et al., 2013
210	779	100±2 MI	756±11 (MI 1.04)	706±3	618±3	737±9 (fsp in fsp)	mgt& ilm incl. in qtz	666±7	779±7	mgt&ilm incl. In qtz	1.23 ±0.09	2.14 ±0.17	MI+ mgt incl in qtz	T zirc	1.05 ±0.02	1.72±0.18	
						733±9 (fsp pc)	mp lit	730±50		mp lit	0.36 ±0.5						Mercer et al., 2015
27	369	90±5 MI	745±26 (mx 1.01)	692±8	582±17	-	mp	769±47	817±30	mp	1.63 ±0.26	1.77 ±0.26	mx+ mgt mp	T zirc	1.01 ±0.02	1.83±0.11	
30	239	101±11 MI	751±11 (MI 0.98)	698±14	602±26	-							MI+ mgt incl in qtz	T zirc	0.98 ±0.03	1.20±0.31	

Supplementary Table 7.S1/2: Extended table of the thermometry and oxybarometry results.

Sample name	mineralogy	ASI[1] based on	n mgt	n ilm	n MI/mx	Rb/Sr and Cs/Ba scatter	matrix vs MI comp. diff.	incl. qtz MI	incl. qtz feldspars	incl. qtz opq	incl. qtz others	incl. fsp MI	incl. fsp feldspars	incl. fsp opq	incl. fsp others	melt/matrix Nb (ppm)	melt/matrix Y (ppm)
Medium reliable samples																	
Lordsburg granodiorite mx	qtz, plag, Kfsp, bio, amph, mgt (19.6 % usp), ilm (64% ilm), tit, zirc, all	0.98? mx	2	3	1	one measurement	-	-	-	-	-	-	-	-	-	11	28
Smelter Knolls rhyolite mx	qtz, plag($An_{44}Ab_{53}Or_{03}$), Kfsp, bio, mgt (11 % usp), ilm (73% ilm), zirc, tit, fl, all	0.96 WR, 1.01 mx	4	1	1	one measurement	small compared to qtz MI, big compared to Fsp MI	gl & xx	-	mgt (7.6 % usp)	-	gl	-	mgt (9.0 % usp) ilm (68 %ilm)	-	6	3
Smelter Knolls rhyolite Fsp incl	qtz, plag($An_{44}Ab_{53}Or_{03}$), Kfsp, bio, mgt (11 % usp), ilm (73% ilm), zirc, tit, fl, all	1.06 ± 0.06 glMI in Fsp	3	1	2	big	big	gl & xx	-	mgt (7.6 % usp)	-	gl	-	mgt (9.0 % usp) ilm (68 %ilm)	-	30	39
Smelter Knolls qtz incl	qtz, plag($An_{44}Ab_{53}Or_{03}$), Kfsp, bio, mgt (11 % usp), ilm (73% ilm), zirc, tit, fl, all	1.07 ± 0.04 gl/xx MI in qtz	1	-	4	medium/big	small compared to mx	gl & xx	-	mgt (7.6 % usp)	-	gl	-	mgt (9.0 % usp) ilm (68 %ilm)	-	28	28
Banco Bonito vitrophyre mx	qtz, plag, Kfsp, bio, px, mgt (16.8 % usp), ilm (70% ilm), zirc, ap	1.02 ± 0.03 mx	4	1	12	small	big	gl & xx	-	-	-	-	-	-	-	41	22
Banco Bonito incl	qtz, plag, Kfsp, bio, px, mgt (16.8 % usp), ilm (70% ilm), zirc, ap	0.97 ± 0.03 gl/xx MI in qtz	-	-	4	big	big	gl & xx	-	-	-	-	-	-	-		
Santa Rita rhyodacite (SR9) incl	qtz, plag, Kfsp, amph, bio, mgt, ilm, zirc, ap, anhy, tit	1.02 ± 0.02 xxMI, 1.03 ± 0.03 WR	3	-	6	small	-	xx	plag($An_{47}Ab_{50}Or_{03}$)	mgt (7.7 % usp)	-	-	-	-	-	10	8
Santa Rita rhyodacite (SR15) incl	qtz, plag, Kfsp, amph, bio, mgt (16.4 % usp), ilm (72% ilm), zirc, ap, anhy, tit	1.03 ± 0.02 mx	1		3	small (Cs/Ba big) + 1 different	big	gl & xx	Kfsp($Or_{70}Ab_{25}An_{04}$) plag($An_{44}Ab_{53}Or_{03}$)	mgt (7.4 % usp) ilm (70 % ilm)	-	-	-	-	-	10	10

melt / matrix (ppm)			T zirc (°C)[2]			T two-fsp (°C)[3]	T mgt-ilm (°C)[4]			log fO₂ via mgt-ilm (ΔFMQ)[5]			log fO₂ via V-partitioning (ΔFMQ)[6]				References
Y+Nb	Rb	Zr	WH 83 (utilized ASI)	Boe 13	Ger 16	Putirka 08 (based on)	based on	G & E (08)	A & L (Ilmat)	based on	G & E (08)	A & L (Ilmat)	based on	temp	ASI	fO₂ (ΔFMQ)	
40	172	-	-	-	-	-	mp	723±30	841±22	mp	2.33±0.11	2.76±0.10	mx+mgt mp	T zirc	0.98	2.40±0.11	
9	236	48 mx	692 (mx 1.01)	609±9	407±25	630-685 (fsp pc)	mp	714±26	789±10	mp	2.26±0.08	2.62±0.12	mx+mgt mp	T zirc		1.1±0.2	Christiansen et al, 1986; Turley & Nash, 1981
69	734	29±4 MI in Fsp	666±4 (MI 1.06)			630-685 (fsp pc)	mgt&ilm incl in Fsp	632±4	792±2	mgt&ilm incl in Fsp	2.28±0.02	2.85±0.02	MI+mgt incl in Fsp	T zirc	1.06±0.06	2.5±0.4	Christiansen et al, 1986; Turley & Nash, 1981
56	314	33±6 MI in Q	671±9 (MI 1.07)	604±2	404±7	630-685 (fsp pc)	no ilm in qtz			no ilm in qtz			MI+mgt incl in qtz	T zirc	1.07±0.04	1.1±0.5	Christiansen et al, 1986; Turley & Nash, 1981
62	175	103±3 mx	755±4 (mx 1.02)			-	mp	802±18	844±7	mp	2.09±0.04	2.29±0.06	mx+mgt mp	T zirc MI	1.02±0.03	2.11±0.20	
		98±8 MI	744±10 (MI 0.97)			-	-	-	-	-	-	-	-	-	-	-	
18	167	77±2 MI	725±3 (MI 1.02)	667±4	519±7	832±12 (Kfsp (AVG from SR15) & plag in Q)	-	-	-	-	-	-	MI+mgt incl in Qtz	T zirc	1.02±0.02	2.22±0.10	
20	377	63±9 MI	710±10 (MI 1.03)	702±17	594±26	838±16 (Kfsp & plag in Q)	mgt&ilm incl in qtz	600	772	mgt&ilm incl in qtz	2.31	2.77	MI+mgt incl in qtz	T zirc	1.03±0.02	2.23±0.65	Audétat &Pettke, 2006

Supplementary Table 7.S1/3: Extended table of the thermometry and oxybarometry results.

Sample name	mineralogy	ASI[1] based on	n mgt	n ilm	n MI/mx	Rb/Sr and Cs/Ba scatter	matrix vs MI comp. diff.	inclusions in qtz MI	feldspars	opq	others	inclusions in fsp MI	feldspars	opq	others	melt / matrix (ppm) Nb	Y
Santa Rita rhyodacite (SR15) mx	qtz, plag, Kfsp, amph, bio, mgt (16.4 % usp), ilm (72% ilm), zirc, ap, anhy, tit	1.03 ± 0.02 glMI in qtz 1.00 xxMI in qtz	1	2	small	big	gl & xx	Kfsp(Or$_{70}$Ab$_{25}$An$_{04}$) plag(An$_{44}$Ab$_{53}$Or$_{03}$)	mgt (7.4 % usp) ilm (70 % ilm)	-	-	-	-	-	-	11	8
Santa Rita rhyodacite SR15) mx literature	qtz, plag, Kfsp, amph, bio, mgt (16.4 % usp), ilm (72% ilm), zirc, ap, anhy, tit	-	-	-		-	gl & xx	Kfsp(Or$_{70}$Ab$_{25}$An$_{04}$) Plag(An$_{44}$Ab$_{53}$Or$_{03}$)	mgt (7.4 % usp) ilm (70 % ilm)	-	-	-	-	-	-		
The Dyke incl	qtz, Kfsp(Or$_{74}$Ab$_{22}$An$_{04}$), plag(An$_{52}$Ab$_{45}$Or$_{02}$), amph, bio, mgt (9.1 % usp), ilm (64% ilm), zirc	1.10 ± 0.04 xxMI	-	12	small (Cs/Ba big)	-	xx	plag(An$_{51}$Ab$_{43}$Or$_{06}$)	mgt (6.6 % usp)	-	-	Kfsp(Or$_{74}$Ab$_{22}$An$_{04}$) host plag(An$_{45}$Ab$_{52}$Or$_{03}$)	mgt (8.7 % usp)		18	8
The Dyke mx	qtz, Kfsp(Or$_{74}$Ab$_{22}$An$_{04}$), plag(An$_{52}$Ab$_{45}$Or$_{02}$), amph, bio, mgt (9.1 % usp), ilm (64% ilm), zirc	1.10 ± 0.04 xxMI	4	-	not usable	-	xx	plag(An$_{51}$Ab$_{43}$Or$_{06}$)	mgt (6.6 % usp)	-	-	Kfsp(Or$_{74}$Ab$_{22}$An$_{04}$) host plag(An$_{45}$Ab$_{52}$Or$_{03}$)	mgt (8.7 % usp)	-	-	-
Nomlaki Tuff mx	plag, amph, px, mgt (17.5 % usp), ilm (72% ilm)	1.09 ± 0.07 mx	4	6	small/ medium	-	-	-	-	-	-	-	-	-	6	14
Amalia tuff incl	qtz, plag(An$_{07}$Ab$_{69}$Or$_{25}$), Kfsp (Or$_{39}$Ab$_{58}$An$_{03}$) & Kfsp (Or$_{45}$Ab$_{54}$An$_{01}$), mgt (25.7 % usp), ilm (47 % ilm), ti, zi, ap	0.87 ± 0.04 xx/gl MI	1	13	small/ medium	-	gl & xx	Kfsp(Or$_{46}$Ab$_{53}$An$_{00}$)	mgt (13.5 % usp)	-	-	Kfsp(Or$_{4,}$ (12.7 % usp)	mgt	-	58	71
Amalia tuff mx	qtz, plag(An$_{07}$Ab$_{69}$Or$_{25}$), Kfsp (Or$_{39}$Ab$_{58}$An$_{03}$) & Kfsp (Or$_{45}$Ab$_{54}$An$_{01}$), mgt (25.7 % usp), ilm (47 % ilm), ti, zi, ap	0.87 ± 0.04 xx/gl MI	1	-	-	-	gl & xx	Kfsp(Or$_{46}$Ab$_{53}$An$_{00}$)	mgt (13.5 % usp)	-	-	Kfsp(Or$_{4,}$ (12.7 % usp)	mgt	-	-	-
Kos granite enclave	qtz, plag, Kfsp, bio, mgt (7.5 % usp), ilm (86% ilm), zi, ap, mon	1.13 ± 0.03 gl MI	3 + 1	6	3	3 small + 1 different	-									22	14

melt / matrix (ppm)			T zirc (°C)[2]			T two-fsp (°C)[3]	T mgt-ilm (°C)[4]			logƒO₂ via mgt-ilm (ΔFMQ)[5]			logƒO₂ via V-partitioning (ΔFMQ)[6]				References
Y+Nb	Rb	Zr	WH 83 (utilized ASI)	Boe 13	Ger 16	Putirka 08 (based on)	based on	G & E (08)	A & L (Ilmat)	based on	G & E (08)	A & L (Ilmat)	based on	temp	ASI	ƒO₂ (ΔFMQ)	
19	88	110±27 mx	755±17 (mx 1.03)			-	mp	770	834	mp	1.98	2.2	mx+ mgt mp	T zirc	1.03 ±0.02	2.52±0.33	Audétat &Pettke, 2006
		59±8 MI	740±10			-	mp	-	730±60	mp	-	2.26 ±0.30	-	-	-	-	Audétat &Pettke, 2006
26	227	78±7 MI	734±8 (MI 1.10)	680± 10	537 ±21	785±43 (fsp in fsp)	mgt incl. In qtz &ilm mp	631± 5	790±1	mgt incl. In qtz &ilm mp	2.33± 0.04	2.95 ±0.01	MI+ mgt incl. in Qtz	T zirc	1.10 ±0.04	2.30±0.33	
-	-	not usable	-	-	-	-	mp	723± 76	807±3	mp	2.29± 0.03	2.77 ±0.02	MI+ mp	T zirc	1.10 ±0.03	2.25±0.32	
20	99	142±1 6 mx	791±12 (mx 1.09)			-	mp	809± 3	850±1	mp	1.95± 0.01	2.07 ±0.01	mx+ mgt mp	T zirc matrix	1.09 ±0.07	2.78±0.21	
129	172	532±1 9 MI	888±8 (MI 0.86)	852± 12	876 ±12	676±25 (fsp pc)	mgt & ilm in Fsp	767± 49	816±23	mgt & ilm in Fsp	1.57± 0.15	2.09 ±0.22	MI in qtz+m gt in qtz/Fs p	T fsp	0.86 ±0.0 4	1.46±0.71	
-	-												MI + mp	T fsp	0.86 ±0.0 4	1.58±0.96	
35	167		721±17 (MI 1.13)			717±31 (fsp pc)	mp	562± 36	722±20	mp	1.25± 0.20	2.27 ±0.11	MI+ mgt mp	T zirc matrix	1.13 ±0.0 3	2.49±0.10 1.58±0.06	

Supplementary Table 7.S1/4: Extended table of the thermometry and oxybarometry results.

Sample name	mineralogy	ASI[1] based on	n mgt	n ilm	n MI/mx	Rb/Sr and Cs/Ba scatter	matrix vs MI comp. diff.	inclusions in qtz MI	feldspars	opq	others	inclusions in fsp MI	feldspars	opq	others	melt / matrix (ppm) Nb	Y
Least reliable samples																	
Los Humeros vitrophyre mx	plag, mgt (44.8 % usp), ilm (91% ilm), px, zirc, ol	0.98 ± 0.03 mx	2	4		small	-	-	-	-	-	-	-	-	-	19	26
Glass Creek Dome vitrophyre mx	qtz, plag, Kfsp, mgt (38.2 % usp), ilm (85% ilm), ap, zirc, all	0.97 ± 0.02 mx	1	3		small/ medium	-	-	-	-	-	-	-	-	-	19	20
Glass Creek Flow vitrophyre mx	qtz, plag, Kfsp, mgt (43.4 % usp), ilm (88% ilm), ap, zirc, all	1.01 ± 0.01 mx	5	4		small/ medium	-	-	-	-	-	-	-	-	-	18	22
Mono #12 vitrophyre mx	qtz, plag, Kfsp, mgt (38.1 % usp), ilm (87% ilm), ap, zirc, all	$\underline{0.92}$, 0.98 ± 0.02 mx	6	3	4	small	-	-	-	-	-	-	-	-	-	18	22
Tunnel Spring Tuff (Crystal Peak) incl	qtz, $Kfsp(Or_{76}Ab_{22}An_{02})$, bio, mgt (8.4 % usp), ilm (59% ilm)	1.07 ± 0.01 gl MI	2	3		one measu rement	-	gl	-	ilm (84 % ilm)	-	-	$Kfsp(Or_{76}Ab_{22}An_{02})$ host plag($An_{40}Ab_{57}Or_{03}$)	ilm (49 % ilm) mgt (8.7 % usp)	-	-	35	37
Tunnel Spring Tuff (Crystal Peak) mx	qtz, $Kfsp(Or_{76}Ab_{22}An_{02})$, bio, mgt (8.4 % usp), ilm (59% ilm)		7	3	-	small/ medium	-	gl	-	ilm (84 % ilm)	-	-	$Kfsp(Or_{76}Ab_{22}An_{02})$ host plag($An_{40}Ab_{57}Or_{03}$)	ilm (49 % ilm) mgt (8.7 % usp)	-	-	-	-
Samples with temperature constraint only																	
Blackfoot lava field vitrophyre mx	$Kfsp(Or_{63}Ab_{35}An_{02})$, $plag(An_{21}Ab_{72}Or_{07})$	1.07 ± 0.03 mx	2				-	-	-	-	-	-	-	-	-		
Pine Grove tuff	qtz, Kfsp host $(Or_{64}Ab_{35}An_{02})$	0.99 ± 0.05 glMI	-	-	6	small	-	gl	-	-	-	-	Kfsp host	-	-		

abbreviations: ASI – alumina saturation index; ΔFMQ – relative to the fayalite-magnetite-quartz buffer; incl – inclusion; MI – melt inclusion; mp – microphenocryst; pc – phenocryst; opq – opaque; all – allanite; anhy – anhydrite; ap – apatite; bio – biotite; fl – fluorite; fsp – feldspar; ilm – ilmenite; Kfsp – potassic feldspar; mgt – magnetite; mon – monazite; ol – olivine; plag – plagioclase; po – pyrrhotite; px – pyroxene; qtz – quartz; tit – titanite; xe – xenothime; zirc – zircon

[1] ASI – alumina saturation index <u>underlined</u> literature data; mx – matrix; glMI – glassy melt inclusion; xxMI – crystallized melt inclusion

[2] zircon saturation temperature based on Watson and Harrison (1983), Boehnke et al. (2013) or Gervasoni et al. (2016)

[3] two-feldspar temperature based on equation 27b of Putirka (2008)

[4] magnetite-ilmenite tempearature based on Ghiorso and Evans (2008), or Andersen and Lindsley (1985) in ILMAT of Lepage (2003)

melt / matrix (ppm)			T zirc (°C)[2]			T two-fsp (°C)[3]	T mgt-ilm (°C)[4]			log fO$_2$ via mgt-ilm (ΔFMQ)[5]			log fO$_2$ via V-partitioning (ΔFMQ)[6]				References
Y+Nb	Rb	Zr	WH 83 (ASI)	Boe 13	Ger 16	Putirka 08 (based on)	based on	G & E (08)	A & L (Ilmat)	based on	G & E (08)	A & L (Ilmat)	based on	temp	ASI	fO$_2$ (ΔFMQ)	
45	159 mx	303±9 mx	841±6 (mx 0.98)			-	mp	847±28	838±23	mp	-0.02±0.13	0.12 ±0.13	mx+ mgt mp	T zirc matrix	0.98 ±0.03	0.59±0.12	
39	148	303±56 mx	839±18 (mx 0.97)			-	mp	941±140	895±3	mp	0.75±0.38	0.97 ±0.01	mx+ mgt mp	T zirc matrix	0.97 ±0.03	-0.07±0.83	Bray, 2014
40	138	410±26 mx	868±9 (mx 1.01)			905±48 (fsp pc)	mp	928±30	902±23	mp	0.73±0.14	0.69 ±0.11	mx+ mgt mp	T zirc matrix	1.01 ±0.01	1.33±0.14	
40	178	138±12 mx	773±10 (mx 0.98)			-	mp	876±44	861±33	mp	0.69±0.22	0.74 ±0.11	mx+ mgt mp	T zirc matrix	0.98 ±0.02	1.39±0.07	Bray, 2014
73	260 MI	27±4 MI	662±11 (MI 1.07)	601±13	402 ±31	757±49 (fsp in fsp)	mgt in fsp&ilm incl. in fsp&qtz	658±35	802±57	mgt in fsp&ilm incl. in fsp&qtz	2.08±0.22	2.53 ±0.46	MI+ mgt incl. in plag/k fsp	T zirc	1.07 ±0.01	2.10±0.38	
-	-						mp	630±3	802±23	mp	2.27±0.22	2.98 ±0.05	MI+ mp	T zirc	1.07 ±0.01	1.07±0.34	
						719±19 (fsp pc)	mp	745±4	775±6	mp	0.37±0.02	0.67 ±0.05	-	-	-	-	
		51 MI	713±6 (MI 1.13) 697±13 (MI 1.0)	660±8	528 ±18	694±14 (fsp in fsp)	-	-	-	-	-	-	-	-	-	-	Audétat et al., 2011

[5] log fO$_2$ relative to the fayalite-magnetite-quartz buffer, based on Ghiorso and Evans (2008) or Andersen and Lindsley (1985) in ILMAT of Lepage (2003)

[6] log fO$_2$ relative to the fayalite-magnetite-quartz buffer, based on Arato and Audetat (2016)

Table 7.S2 Comparison of Fe-Ti oxide compositions obtained by LA-ICP-MS (LA) versus electron microprobe (EPMA)

Sample	Banco Bonito				Mt Rano				Los Humeros			
Mineral	mgt	mgt	ilm	ilm	mgt	mgt	ilm	ilm	mgt	mgt	ilm	ilm
Method	LA	EPMA	LA	EPMA	LA	EPMA	LA	EPMA	LA	EPMA	LA	EPMA
n	5	5	1	4	4	7	3	4	2	7	2	6
SiO_2 (wt%)	0 (0)	0.1 (0)	0	1.8 (3.4)	0 (0)	0.1 (0)	0 (0)	0 (0)	0 (0)	0.1 (0)	0 (0)	0 (0)
TiO_2 (wt%)	6.0 (0.7)	5.7 (0.4)	36.8	36.5 (1.4)	13.3 (0.2)	13.9 (0.1)	47.5 (0.2)	49.0 (0.4)	15.4 (1.4)	16.3 (0.4)	48.8 (0.4)	49.1 (0.5)
Al_2O_3 (wt%)	2.0 (0.3)	1.8 (0.1)	0.3	0.5 (0.6)	1.9 (0.1)	1.7 (0.1)	0.1 (0)	0.1 (0)	1.5 (0)	1.5 (0)	0.1 (0.1)	0.1 (0)
FeO_{tot} (wt%)	83.9 (0.9)	84.1 (0.8)	56.1	54.4 (1.4)	78.5 (0.1)	78.2 (0.7)	48.2 (0.2)	46.9 (0.3)	76.9 (1)	76.1 (0.9)	47.1 (0.2)	46.5 (0.3)
MnO (wt%)	0.7 (0.1)	0.8 (0.1)	0.9	0.7 (0.1)	0.8 (0)	0.9 (0)	1.2 (0)	1.4 (0.1)	0.6 (0)	0.6 (0)	0.8 (0)	0.9 (0.1)
MgO (wt%)	1.5 (0.2)	1.8 (0.2)	2.4	2.5 (0.2)	1 (0)	1.1 (0)	1.8 (0)	1.9 (0.1)	1.3 (0.1)	1.3 (0)	2.1 (0.1)	2.2 (0.1)
CaO (wt%)	0 (0)	0 (0)	0	0.1 (0)	0 (0)	0 (0)	0 (0)	0 (0)	0 (0)	0 (0)	0 (0)	0 (0)
Cr_2O_3 (wt%)	0.1 (0.1)	0.1 (0.1)	0	0 (0)	0 (0)	0 (0)	0 (0)	0 (0)	0 (0)	0 (0)	0 (0)	0 (0)
ZnO (wt%)	0.1 (0)	0.1 (0)	0	0 (0)	0.2 (0)	0.2 (0)	0.1 (0)	0.1 (0)	0.2 (0)	0.1 (0)	0.1 (0)	0.1 (0)
V_2O_3 (wt%)	0.3 (0)	0.3 (0)	0.1	0.4 (0)	0.2 (0)	0.3 (0)	0 (0)	0.4 (0)	0.3 (0)	0.4 (0)	0.1 (0)	0.4 (0)
Nb_2O_3 (wt%)	0 (0)	0 (0)	0.2	0.1 (0)	0 (0)	0 (0)	0 (0)	0 (0)	0 (0)	0 (0)	0.1 (0)	0.1 (0)

Numbers in parentheses correspond to 1 sigma standard deviations of the reported averages.

Only magnetite-ilmenite populations are listed that passed the Mg/Mn test of Bacon and Hirschmann (1988) if combined with each other.

n= number of analyses

Supplementary Table 7.S3/1: LA-ICP-MS analyses of melt inclusions (MI) and rock matrix, corresponding melt composition parameters and calculated zircon saturation temperatures

				Melt inclusion composition								
Analysis	Sample name[1]	Sample type	B µg/g	Na$_2$O[2] meas wt%	Na$_2$O[3]$_c$ orr wt%	MgO wt%	Al$_2$O$_3$ wt%	SiO$_2$ wt%[4]	K$_2$O wt%	CaO wt%	TiO$_2$ wt%	V µg/g
Oravita hyalodacite												
16Au24k05	Oravita glassy matrix	matrix	37	4.0	N/A	0.06	12.1	77.8	4.3	0.7	0.09	0.6
16Au24k06	Oravita glassy matrix	matrix	39	3.9	N/A	0.06	12.2	77.7	4.4	0.7	0.09	0.6
16Au24k07	Oravita glassy matrix	matrix	39	3.9	N/A	0.06	12.1	77.7	4.5	0.8	0.09	0.6
16Au24k08	Oravita glassy matrix	matrix	44	3.9	N/A	0.06	12.2	77.7	4.4	0.7	0.09	0.7
16Au24k09	Oravita glassy matrix	matrix	45	4.1	N/A	0.07	12.3	77.5	4.3	0.8	0.09	0.7
16Au24k10	Oravita coarser matrix	matrix	36	4.3	N/A	0.07	12.7	77.1	4.0	1.0	0.09	0.7
16Au24k11	Oravita coarser matrix	matrix	32	4.6	N/A	0.06	13.5	75.8	3.6	1.5	0.08	0.7
16Au24k12	Oravita coarser matrix	matrix	44	4.2	N/A	0.06	12.1	77.8	4.1	0.7	0.09	0.6
16Au24k13	Oravita coarser matrix	matrix	44	4.1	N/A	0.08	12.1	77.8	4.2	0.7	0.10	1.1
Mount Rano vitrophyre												
15Se11c12	Mt Rano A matrix	matrix	48	4.7	N/A	0.18	14.1	74.2	3.7	1.2	0.22	1.5
15Se11c13	Mt Rano A matrix	matrix	54	4.6	N/A	0.16	13.3	75.4	3.6	1.1	0.20	1.3
15Se11c14	Mt Rano B matrix	matrix	51	4.7	N/A	0.17	13.9	74.6	3.6	1.1	0.21	1.4
15Se11c15	Mt Rano C matrix	matrix	47	4.7	N/A	0.17	14.0	74.4	3.6	1.2	0.21	1.3
15Se11c16	Mt Rano C matrix	matrix	48	4.7	N/A	0.17	14.1	74.2	3.6	1.2	0.21	1.5
Parinacota vitrophyre												
16Au05k12	PC matrix 50 µm	matrix	77	3.6	N/A	0.05	12.2	77.9	4.9	0.6	0.08	2.9
16Au05k13	PC matrix 50 µm	matrix	82	3.7	N/A	0.05	12.3	77.8	5.0	0.6	0.08	3.0
16Au05k14	PC matrix 50 µm	matrix	76	3.7	N/A	0.05	12.2	78.0	4.9	0.5	0.09	3.1
16Au05j07	PC qtz D exp gl MI1 30 µm	MI in qtz	69	4.4	N/A	0.06	13.7	74.9	5.4	0.7	0.09	3.5
16Au05j08	PC qtz D exp gl MI2 40 µm (sh	MI in qtz	94	3.5	N/A	0.05	13.4	76.4	5.4	0.6	0.09	2.8
16Au05j09	PC qtz D exp gl MI2 40 µm	MI in qtz	90	3.5	N/A	0.05	12.6	77.5	5.2	0.6	0.08	2.6
16Au05j10	PC qtz D exp gl MI3 40 µm +q	MI in qtz	81	4.6	N/A	0.06	14.1	74.2	5.5	0.8	0.10	3.2
16Au05j13	PC qtz F exp gl MI 40 µm	MI in qtz	141	4.4	N/A	0.07	13.5	75.3	5.4	0.5	0.08	3.5
16Au05j11	PC Kfsp E exp gl MI 40 µm 9	MI in Kfsp	139	3.3	N/A	0.04	13.0	76.8	5.6	0.6	0.07	1.4
16Au05i13	PC Kfsp A exp MI gl 40 µm 9	MI in Kfsp	138	3.2	N/A	0.04	12.5	77.5	5.7	0.5	0.07	2.1
16Au05i15	PC Kfsp A exp MI gl 40 µm	MI in Kfsp	81	3.5	N/A	0.05	12.5	77.5	5.1	0.6	0.08	2.9
Hideaway Park tuff												
15De09j05	WP qtz1 xxMI1 70 µm **	MI in qtz	37	1.3	4.0	0.03	**13.2**	76.8	4.5	0.5	0.09	0.3
15De09j06	WP qtz1 xxMI2 40 µm ***	MI in qtz	33	0.4	3.9	0.03	**13.2**	76.8	4.7	0.6	0.07	0.4
15De09j07	WP qtz1 xxMI3 60 µm ***	MI in qtz	35	1.2	3.9	0.03	**13.2**	76.8	4.7	0.5	0.10	0.3
15De10b05	WP qtz2 xxMI1 60 µm ***	MI in qtz	31	0.9	4.1	0.03	**13.2**	76.5	4.8	0.4	0.09	0.4
15De10b06	WP qtz2 xxMI2 60 µm ***	MI in qtz	32	1.1	3.8	0.03	**13.2**	76.2	5.1	0.7	0.10	0.3
15De10b07	WP qtz3 xxMI 70 µm **	MI in qtz	44	2.8	4.1	0.03	**13.2**	76.7	4.6	0.4	0.09	0.3
Cottonwood tuff												
15Se10h11	Cw C matrix 50µm	matrix	68	2.7	N/A	0.21	12.9	75.7	6.5	0.9	0.15	6.9
15Se10h12	Cw B matrix 50µm	matrix	62	2.4	N/A	0.20	12.8	76.0	6.5	0.8	0.15	5.2
15Se10h13	Cw A matrix 50µm	matrix	63	2.6	N/A	0.17	12.6	76.4	6.7	0.5	0.15	5.1
15Se10h09	Cw C xxMI in plag 35µm	MI in plag	79	3.7	3.1	0.13	**12.8**	77.0	3.2	2.8	0.15	5.2
15Se10h10	Cw C xxMI in plag 50µm (deep	MI in plag	68	4.7	3.2	0.12	**12.8**	76.6	4.0	2.2	0.13	7.6
15De09f11	Cw qtz3 MI1 35 µm ***	MI in qtz	72	0.7	3.1	0.11	**12.8**	76.5	5.4	1.2	0.14	2.4
15De09f12	Cw qtz3 MI2 45 µm ***	MI in qtz	91	1.9	3.6	0.12	**12.8**	75.8	5.7	1.0	0.11	3.5
15De09g05	Cw qtz 6 MI1 40 µm	MI in qtz	96	0.9	3.4	0.11	**12.8**	76.4	5.3	1.0	0.09	5.3
15De09g06	Cw qtz 6 MI2 30 µm rim	MI in qtz	92	0.3	2.8	0.14	**12.8**	76.4	5.6	1.2	0.08	2.9
15De09g07	Cw qtz 7 MI 35 µm	MI in qtz	62	1.0	3.0	0.11	**12.8**	76.6	5.4	1.1	0.13	2.3
15De09g10	Cw qtz 10 MI1 40 µm	MI in qtz	66	0.8	3.2	0.10	**12.8**	76.9	5.1	1.0	0.14	2.9
15De09g11	Cw qtz 10 MI2 50 µm	MI in qtz	77	1.0	3.2	0.10	**12.8**	76.7	5.3	1.0	0.12	3.5
Lordsburg rhyolite												
15De09d05	Lord2 qtz1 MI1 30 µm *** rim	MI in qtz	16	0.9	4.0	0.07	**14.0**	75.9	4.6	0.8	0.06	1.7
15De09d06	Lord2 qtz1 MI2 35 µm **(*) rim	MI in qtz	14	1.0	4.6	0.07	**14.0**	76.5	3.4	0.8	0.05	1.1
15De09d10	Lord2 qtz2 gl MI1 25 µm ***	MI in qtz	9	1.0	4.3	0.08	**14.0**	76.0	4.3	1.0	0.06	1.1
15De09d11	Lord2 qtz2 gl MI2 20 µm ***	MI in qtz	(23)	0.4	4.0	0.05	**14.0**	76.4	4.0	1.1	0.06	0.8
15De09e05	Lord2 qtz3 gl MI 55 µm ***	MI in qtz	10	1.5	4.2	0.06	**14.0**	76.2	4.1	1.0	0.06	0.8
15De09e09	Lord2 qtz5 large exp gl MI ***	MI in qtz	13	4.3		0.05	14.0	75.8	4.5	0.8	0.05	1.0
15De09e10	Lord2 qtz4 xx MI1 35 µm ***	MI in qtz	12	2.5	4.5	0.08	**14.0**	75.6	4.2	1.1	0.03	0.6
Lordsburg granodiorite												
16Au05b15	Lord3 matrix 70 µm 7 Hz movir	matrix	8	3.7	N/A	0.49	15.1	72.6	4.9	2.2	0.16	6.7
Smelter Knolls rhyolite												
15De10c09	Sk qtz2 xx MI 60 µm **(*)	MI in qtz	45	1.2	4.0	0.06	**13.1**	77.5	3.9	0.8	0.05	0.2
15De10c10	Sk qtz2 gl MI 60 µm ***	MI in qtz	59	0.6	4.0	0.05	**13.1**	77.5	3.8	0.9	0.04	0.1
15De14i05	Sk qtz1 xx MI1 55 µm	MI in qtz	42	1.5	4.0	0.06	**13.1**	77.3	4.0	0.9	0.06	0.2

								Melt inclusion composition										melt comp. param.			T_{zirc}
Cr	MnO	FeO	Zn	Rb	Sr	Y	Zr	Nb	Mo	Cs	Ba	Ce	Hf	Th	U	total	M^5	A/NK^6	A/CNK^7	T_{zirc}^8
µg/g	wt%	wt%	µg/g	µg/g	µg/g	µg/g	µg/g	µg/g	µg/g	µg/g	µg/g	µg/g	µg/g	µg/g	µg/g	wt%				(°C)
(9)	0.03	0.8	29	200	49	26	102	12	2	8	626	73	3	19	6	**100**	1.42	1.08	0.97	753
(9)	0.03	0.9	32	200	51	28	103	12	2	8	636	74	3	19	6	**100**	1.42	1.08	0.97	753
(8)	0.03	0.8	30	198	49	27	100	12	2	7	635	73	4	19	6	**100**	1.44	1.08	0.96	750
(9)	0.03	0.9	34	202	48	27	102	12	2	8	634	74	3	19	6	**100**	1.40	1.09	0.98	754
(9)	0.03	0.9	30	198	49	28	103	12	2	8	640	76	4	20	6	**100**	1.43	1.09	0.97	753
(9)	0.02	0.8	31	195	66	26	96	12	2	7	638	72	3	18	6	**100**	1.46	1.11	0.96	745
(10)	0.02	0.8	26	168	115	24	84	10	2	7	589	66	3	16	5	**100**	1.48	1.18	0.96	733
(9)	0.03	0.9	28	202	49	28	97	12	2	8	649	77	4	19	6	**100**	1.44	1.06	0.96	747
(10)	0.03	0.9	29	200	49	27	99	13	2	8	649	73	3	18	6	**100**	1.43	1.07	0.96	749
(6)	0.08	1.7	61	82	96	50	253	5	n.a.	5	549	n.a.	n.a.	7	2	**100**	1.43	1.21	1.01	831
(5)	0.07	1.6	58	81	88	47	234	4	n.a.	5	508	n.a.	n.a.	6	2	**100**	1.45	1.16	0.99	823
(4)	0.08	1.7	64	82	95	47	240	5	n.a.	5	545	n.a.	n.a.	6	2	**100**	1.43	1.19	1.01	827
(5)	0.08	1.6	56	80	96	49	254	4	n.a.	5	535	n.a.	n.a.	6	2	**100**	1.44	1.20	1.01	831
(5)	0.08	1.7	58	81	96	50	256	5	n.a.	5	537	n.a.	n.a.	7	2	**100**	1.41	1.22	1.03	834
(9)	0.03	0.5	26	240	67	2	68	9	4	14	192	37	3	32	9	**100**	1.40	1.08	0.98	722
(9)	0.03	0.5	27	243	65	2	68	9	4	13	203	37	3	32	10	**100**	1.39	1.08	0.99	722
(9)	0.03	0.5	26	241	66	2	69	9	3	14	200	36	3	31	10	**100**	1.39	1.07	0.99	724
(16)	0.03	0.6	31	226	98	2	62	9	3	12	160	31	3	32	8	**100**	1.52	1.05	0.95	707
(15)	0.03	0.6	21	238	60	2	69	9	4	14	147	39	2	34	10	**100**	1.33	1.15	1.05	727
(13)	0.03	0.5	22	237	54	2	63	8	3	14	130	35	3	31	9	**100**	1.36	1.11	1.01	718
(12)	0.03	0.6	33	226	114	3	79	8	4	11	264	40	3	32	8	**100**	1.55	1.05	0.94	724
(17)	0.04	0.7	29	311	46	2	59	13	6	22	49	36	3	32	14	**100**	1.47	1.04	0.97	706
(14)	0.05	0.5	27	325	7	2	65	13	4	23	1	34	4	31	14	**100**	1.35	1.12	1.03	721
(14)	0.04	0.5	23	356	8	2	62	12	4	23	2	31	3	29	14	**100**	1.36	1.09	1.02	717
(13)	0.04	0.5	29	269	35	2	67	9	3	15	40	36	4	33	10	**100**	1.36	1.11	1.01	723
(6)	0.11	0.7	52	740	1	43	97	162	17	17	1	n.a.	6	58	31	100	1.32	1.14	1.05	755
(21)	0.10	0.6	50	755	1	30	101	143	16	16	1	n.a.	6	51	30	100	1.34	1.15	1.04	757
(6)	0.11	0.7	54	758	1	42	97	164	16	17	1	n.a.	7	59	30	100	1.31	1.15	1.06	756
(11)	0.10	0.7	48	736	2	43	102	151	15	16	1	n.a.	6	61	29	100	1.36	1.10	1.03	757
(8)	0.12	0.8	54	830	1	45	102	178	17	17	1	n.a.	6	63	31	100	1.38	1.12	1.02	755
(3)	0.13	0.7	50	856	1	52	101	210	18	22	1	n.a.	7	64	38	100	1.33	1.12	1.05	757
(5)	0.04	1.0	28	366	78	13	85	15	n.a.	11	561	n.a.	n.a.	51	14	**100**	1.43	1.13	0.99	738
(6)	0.05	1.1	27	373	54	14	91	16	n.a.	11	609	n.a.	n.a.	50	12	**100**	1.36	1.16	1.03	747
(5)	0.03	0.8	24	369	28	10	94	15	n.a.	17	195	n.a.	n.a.	50	12	**100**	1.37	1.10	1.02	749
(14)	0.05	0.8	22	130	294	30	118	20	n.a.	9	176	n.a.	n.a.	52	17	100	1.47	1.50	0.94	761
(10)	0.04	0.9	21	164	250	30	124	17	n.a.	9	173	n.a.	n.a.	68	16	100	1.48	1.34	0.94	764
(17)	0.04	0.8	28	238	121	10	98	15	6	10	617	n.a.	3	70	15	100	1.43	1.16	0.98	749
(11)	0.04	0.8	26	250	108	16	101	16	6	12	446	n.a.	5	68	17	100	1.54	1.06	0.92	743
(16)	0.04	0.9	28	246	106	17	87	16	7	13	406	n.a.	4	68	19	100	1.43	1.13	0.98	739
(32)	0.04	0.9	32	245	85	17	88	17	8	14	145	n.a.	4	64	16	100	1.41	1.19	0.99	741
(16)	0.04	0.8	26	239	127	11	103	14	5	11	713	n.a.	5	62	13	100	1.39	1.18	1.00	755
(14)	0.03	0.7	25	218	133	7	121	15	5	9	791	n.a.	4	54	13	100	1.37	1.19	1.01	770
(15)	0.03	0.7	26	235	105	22	105	18	6	11	427	n.a.	4	64	15	100	1.41	1.15	0.99	756
(47)	0.07	0.5	46	187	97	24	32	12	1	2	561	n.a.	2	5	3	100	1.01	1.21	1.07	596
(23)	0.06	0.5	49	158	108	18	33	11	1	3	271	n.a.	3	4	2	100	0.98	1.25	1.10	598
(56)	0.04	0.4	32	156	122	32	35	12	1	3	397	n.a.	2	5	2	100	1.02	1.21	1.05	599
(66)	0.04	0.4	40	151	126	34	36	13	(1)	3	362	n.a.	(2)	6	2	100	0.94	1.29	1.09	559
(5)	0.05	0.4	37	167	132	28	71	12	1	3	324	n.a.	3	5	2	100	1.34	1.22	1.05	729
(10)	0.04	0.4	32	215	115	24	41	12	1	4	307	n.a.	2	7	3	**100**	1.38	1.16	1.03	685
(19)	0.06	0.5	47	163	112	38	37	7	1	4	324	n.a.	2	4	2	100	1.42	1.17	1.01	676
(9)	0.03	0.8	21	178	361	7	142	12	0	7	1550	30	4	3	1	**100**	1.51	1.33	0.98	774
(7)	0.08	0.5	47	192	65	32	30	27	1	8	115	n.a.	2	4	6	100	1.30	1.20	1.06	669
(6)	0.09	0.5	57	686	45	30	25	32	2	10	51	n.a.	2	4	7	100	1.31	1.21	1.05	655
(5)	0.08	0.5	48	193	91	32	34	26	2	8	230	n.a.	24	2	5	100	1.34	1.19	1.03	675

Supplementary Table 7.S3/2: LA-ICP-MS analyses of melt inclusions (MI) and rock matrix, corresponding melt composition parameters and calculated zircon saturation temperatures

Analysis	Sample name[1]	Sample type	B µg/g	Na$_2$O[2] meas wt%	Na$_2$O[3]$_c$ orr wt%	MgO wt%	Al$_2$O$_3$ wt%	SiO$_2$ wt%[4]	K$_2$O wt%	CaO wt%	TiO$_2$ wt%	V µg/g
Smelter Knolls rhyolite												
15De14i06	Sk qtz1 xx MI2 50 µm	MI in qtz	38	1.7	4.0	0.06	**13.1**	77.9	3.9	0.4	0.06	0.2
15De10c11	Sk Fsp1 exp.gl MI (+host)	MI in fsp	48	4.8	4.0	0.07	13.1	77.1	4.3	0.9	0.06	1.0
15De10c13	Sk Fsp2 exp.gl MI (+host)	MI in fsp	69	4.6	4.0	0.06	13.0	77.3	4.5	0.2	0.05	0.6
16Au05h08	Sk matrix 70 µm 7 Hz moving	matrix	23	3.4		1.24	13.8	73.7	5.2	1.3	0.02	0.3
Amalia Tuff												
15De10b08	Am qtz1 xxMI1 70 µm ***	MI in qtz	11	1.5	5.2	0.04	**11.8**	76.7	4.3	0.2	0.13	0.7
15De10b09	Am qtz1 xxMI2 80 µm **(*)	MI in qtz	11	2.7	4.8	0.04	**11.8**	77.2	4.3	0.2	0.13	0.7
15De10b10	Am qtz2 xxMI1 55 µm ***	MI in qtz	10	0.9	5.3	0.04	**11.8**	76.7	4.3	0.3	0.13	0.6
15De10b11	Am qtz2 xxMI2 30 µm ***	MI in qtz	10	0.7	5.0	0.04	**11.8**	76.9	4.3	0.4	0.12	0.7
15De10b12	Am qtz2 xxMI3 40 µm ***	MI in qtz	10	0.6	5.2	0.04	**11.8**	76.6	4.3	0.4	0.14	0.6
15De10b13	Am qtz3 xxMI1 40 µm ***	MI in qtz	9	0.9	5.1	0.04	**11.8**	76.8	4.3	0.3	0.13	0.6
15De10b14	Am qtz3 xxMI2 30 µm ***	MI in qtz	12	0.7	5.2	0.04	**11.8**	76.4	4.5	0.4	0.14	0.6
15De10b15	Am qtz4 xxMI 35 µm **	MI in qtz	9	2.3	5.5	0.04	**11.8**	76.6	4.2	0.2	0.14	0.6
15De10b16	Am qtz5 exp. +/- glMI 40 µm *ʼ	MI in qtz	14	4.7	5.0	0.03	**11.8**	76.8	4.8	(0.1)	0.13	0.6
15De10c05	Am qtz5 exp. glMI 40 µm ***	MI in qtz	14	4.7	4.8	0.03	**11.8**	76.8	4.8	0.1	0.13	0.7
15De10c06	Am qtz5 xx MI 45 µm ***	MI in qtz	15	0.5	5.5	0.04	**11.8**	75.6	4.7	0.5	0.14	0.9
15De10c07	Am qtz6 xx MI 55 µm **(*)	MI in qtz	13	2.0	5.6	0.04	**11.8**	76.2	4.4	0.2	0.14	0.7
15De10c08	Am qtz6 exp. gl MI 40 µm ***	MI in qtz	13	4.5	4.8	0.02	**11.8**	77.5	4.6	(0.1)	0.12	0.4
Banco Bonito vitrophyre												
15Se10b14	BB matrix 1 50 µm	matrix	14	3.6	N/A	0.13	13.3	76.4	4.7	0.8	0.18	4.7
15Se10b15	BB matrix 2 50 µm	matrix	12	3.7	N/A	0.14	13.7	75.9	4.7	0.9	0.19	5.3
15Se10b16	BB matrix 3 50 µm	matrix	12	3.7	N/A	0.14	13.2	76.3	4.7	0.8	0.19	5.5
15Se10b17	BB matrix 4 50 µm	matrix	13	3.7	N/A	0.15	13.5	75.9	4.8	0.9	0.19	5.5
15De14i07	BB qtz1 unexp. gl MI1 40 µm	MI in qtz	18	2.8	4.2	0.06	**13.4**	75.6	5.3	0.5	0.08	0.4
15De14i08	BB qtz2 unexp. xx MI1 35 µm ª	MI in qtz	12	2.0	4.6	0.06	**13.4**	75.6	4.9	0.6	0.12	2.0
15De14i09	BB qtz2 large exp. gl MI1 35 µr	MI in qtz	21	5.0	4.9	0.05	**13.4**	75.1	5.2	0.5	0.10	1.5
15De14i10	BB qtz3 ± gl MI1 30 µm ***	MI in qtz	17	2.1	4.4	0.09	**13.4**	75.8	4.6	0.7	0.11	0.8
Santa Rita rhyodacite (SR15)												
16Au05h04	SR15 matrix 70 µm 7 Hz movin	matrix	2	5.4	N/A	0.41	15.6	72.6	4.3	1.0	0.21	13.2
16Au05h05	SR15 matrix 70 µm 7 Hz movin	matrix	(2)	5.4	N/A	0.25	14.8	74.6	4.0	0.6	0.04	5.1
15De14i11	SR15 qtz1 xxMI 65 µm **(*) [9]	MI in qtz	31	1.9	4.7	2.72	**16.5**	71.1	1.4	1.4	0.08	11.9
15De14i12	SR15 qtz2 xxMI 50 µm ***	MI in qtz	16	1.5	4.9	0.08	**16.5**	70.7	5.7	1.2	0.10	2.8
15De14i13	SR15 qtz3 large exp gl MI 30 µr	MI in qtz	22	4.7	5.2	0.00	**16.5**	72.1	4.7	1.2	0.06	1.9
15De14i14	SR15 qtz4 exp gl MI 20 µm	MI in qtz	33	4.1	4.8	(0.00)	**16.5**	71.7	5.6	1.1	0.07	1.9
Santa Rita rhyodacite (SR9)												
15De16l07	SR9 qtz3 outer growth zone MI	MI in qtz	20	2.0	5.0	0.08	**16.5**	71.2	5.3	1.1	0.10	4.7
15De16l08	SR9 qtz3 outer growth zone MI	MI in qtz	27	0.7	5.0	0.07	**16.5**	71.1	5.3	1.3	0.08	3.9
15De16l09	SR9 qtz3 outer growth zone MI	MI in qtz	22	0.8	5.0	0.08	**16.5**	71.1	5.0	1.4	0.10	4.2
15De16l10	SR9 qtz3 middle growth zone M	MI in qtz	20	0.5	5.0	0.16	**16.5**	70.5	5.2	1.6	0.14	5.4
15De16l11	SR9 qtz3 core MI1 30 µm **	MI in qtz	20	0.5	5.0	0.09	**16.5**	71.3	4.9	1.4	0.10	3.7
15De16l12	SR9 qtz3 core MI2 40 µm **	MI in qtz	15	0.8	5.0	0.10	**16.5**	71.1	4.9	1.4	0.10	4.2
The Dyke												
15De10g06	Dk qtz1 xx MI1 60 µm ***	MI in qtz	44	0.7	3.9	0.07	**16.3**	71.7	5.4	1.8	0.12	2.3
15De10g07	Dk qtz1 xx MI2 80 µm ** + hos	MI in qtz	49	1.5	4.0	0.08	**16.3**	71.7	5.6	1.6	0.12	2.6
15De10g09	Dk qtz2 xx MI1 50 µm ***	MI in qtz	76	0.8	3.5	0.08	**16.3**	72.1	5.8	1.5	0.09	2.9
15De10g10	Dk qtz2 xx MI2 50 µm **	MI in qtz	74	1.2	3.3	0.08	**16.3**	72.4	5.5	1.5	0.09	2.9
15De10g11	Dk qtz2 xx MI3 40 µm **	MI in qtz	28	0.7	3.7	0.19	**16.3**	71.8	4.1	2.1	0.19	6.1
15De10g12	Dk qtz2 xx MI4 30 µm **	MI in qtz	62	0.7	3.7	0.10	**16.3**	72.3	5.1	1.5	0.13	3.9
15De10g13	Dk qtz3 xx MI1 35 µm ***	MI in qtz	67	0.6	3.7	0.09	**16.3**	71.4	6.1	1.4	0.10	3.5
15De10g14	Dk qtz3 xx MI2 50 µm ***	MI in qtz	88	0.6	3.8	0.08	**16.3**	71.4	6.1	1.5	0.08	3.0
The Dyke												
15De10g15	Dk qtz4 xx MI1 30 µm **(*)	MI in qtz	79	1.0	3.7	0.09	**16.3**	71.9	5.8	1.5	0.09	3.2
15De10g16	Dk qtz4 xx MI2 40 µm ***	MI in qtz	66	0.6	3.7	0.08	**16.3**	71.7	5.9	1.4	0.10	3.5
15De10h05	Dk qtz5 xx MI1 30 µm **	MI in qtz	73	1.3	3.5	0.08	**16.3**	72.2	5.6	1.4	0.09	2.8
15De10h06	Dk qtz5 xx MI2 60 µm ***	MI in qtz	71	0.7	3.6	0.08	**16.3**	71.9	5.9	1.4	0.08	3.1
Nomlaki tuff												
15Se10b04	Chalk Mt A matrix 1 50µm	matrix	66	3.6	N/A	0.08	13.9	76.1	4.1	1.1	0.23	8.9
15Se10b05	Chalk Mt A matrix 2 50µm	matrix	58	3.4	N/A	0.08	14.1	76.0	4.4	0.9	0.22	8.5
15Se10b06	Chalk Mt B matrix 1 50µm	matrix	45	3.9	N/A	0.09	12.7	77.5	3.3	1.1	0.27	11.8
15Se10b07	Chalk Mt B matrix 2 50µm	matrix	49	3.3	N/A	0.05	12.2	77.5	5.1	0.7	0.22	9.0
15Se10b08	Chalk Mt C matrix 1 50µm	matrix	24	4.5	N/A	0.03	13.2	77.3	2.6	1.2	0.22	10.9

| Melt inclusion composition | | | | | | | | | | | | | | | | | melt comp. param. | | | T_{zirc} |
| Cr | MnO | FeO | Zn | Rb | Sr | Y | Zr | Nb | Mo | Cs | Ba | Ce | Hf | Th | U | total | M^5 | A/NK^6 | A/CNK[7] | T_{zirc}[8] |
µg/g	wt%	wt%	µg/g	µg/g	µg/g	µg/g	µg/g	µg/g	µg/g	µg/g	µg/g	µg/g	µg/g	µg/g	µg/g	wt%				(°C)
(5)	0.08	0.5	50	186	80	20	29	25	1	7	262	n.a.	20	2	4	100	1.22	1.20	1.13	670
(5)	0.06	0.5	49	543	27	40	34	23	1	16	97	n.a.	2	12	7	**100**	1.37	1.16	1.02	674
(8)	0.29	0.6	28	921	(0)	38	26	38	2	226	(1)	n.a.	2	8	10	**100**	1.25	1.13	1.11	662
(9)	0.03	1.2	39	236	75	3	48	6	0	3	224	n.a.	12	3	3	**100**	1.45	1.22	1.01	692
(4)	0.14	1.4	181	167	0	75	548	61	7	3	1	n.a.	17	25	10	100	1.26	0.90	0.87	799
(2)	0.14	1.4	168	168	0	74	547	60	5	3	1	n.a.	17	23	10	100	1.31	0.94	0.91	860
(9)	0.13	1.4	167	162	1	71	530	56	6	3	1	n.a.	17	22	9	100	1.23	0.89	0.86	757
(22)	0.13	1.3	151	164	0	65	505	49	6	3	1	n.a.	15	20	9	100	1.20	0.92	0.87	743
(14)	0.13	1.4	173	164	0	72	567	58	6	3	(1)	n.a.	18	24	10	100	1.21	0.90	0.86	727
(11)	0.14	1.4	166	163	1	73	558	59	5	3	1	n.a.	16	24	10	100	1.21	0.91	0.87	767
(25)	0.13	1.5	163	163	0	69	520	54	6	3	(2)	n.a.	14	21	10	100	1.24	0.88	0.84	734
(10)	0.14	1.4	178	164	1	76	538	60	7	3	1	n.a.	17	23	10	100	1.35	0.87	0.85	828
(6)	0.12	1.5	182	193	0	70	526	56	7	3	1	n.a.	15	22	9	100	1.57	0.88	0.89	888
(5)	0.12	1.5	172	190	0	70	526	59	7	3	1	n.a.	15	22	9	100	1.58	0.90	0.89	892
(23)	0.15	1.6	188	184	1	71	544	63	8	3	1	n.a.	17	23	10	100	1.82	0.83	0.79	874
(10)	0.14	1.5	163	169	1	69	521	59	7	3	1	n.a.	15	25	9	100	1.73	0.84	0.82	877
(7)	0.09	1.1	152	182	1	66	501	57	7	3	1	n.a.	14	21	9	100	1.53	0.91	0.91	891
(6)	0.04	0.8	24	175	102	22	100	40	n.a.	5	569	n.a.	n.a.	25	7	**100**	1.32	1.20	1.06	758
(6)	0.04	0.8	23	177	109	23	107	41	n.a.	5	612	n.a.	n.a.	25	7	**100**	1.32	1.22	1.07	763
(6)	0.04	0.8	25	175	105	21	102	41	n.a.	5	601	n.a.	n.a.	24	7	**100**	1.35	1.18	1.04	757
(6)	0.04	0.8	24	172	110	21	102	41	n.a.	5	597	n.a.	n.a.	24	7	**100**	1.35	1.19	1.05	758
(7)	0.05	0.7	30	253	15	53	97	66	7	8	43	64	5	35	11	100	1.44	1.07	0.99	747
(13)	0.04	0.7	24	206	30	31	101	43	5	5	158	75	5	25	7	100	1.49	1.04	0.96	747
(4)	0.06	0.7	24	352	6	27	87	53	7	14	10	61	4	31	9	100	1.56	0.98	0.92	730
(46)	0.04	0.8	24	149	40	41	105	50	7	6	116	77	5	27	8	100	1.44	1.09	0.99	754
(8)	0.01	0.5	8	94	849	12	128	14	0	1	1790	43	5	10	3	**100**	1.49	1.15	1.01	767
(11)	0.00	0.3	5	82	824	4	90	8	0	1	1666	22	3	10	3	**100**	1.40	1.12	1.04	743
(8)	0.10	1.9	124	188	142	5	58	8	0	8	169	15	2	7	2	100	1.09	1.77	1.40	729
(15)	0.07	0.7	29	190	242	15	70	12	1	5	1218	29	3	8	5	100	1.54	1.16	1.00	715
(22)	0.02	0.2	(7)	540	304	8	66	9	1	7	689	24	3	13	6	100	1.45	1.21	1.04	717
(34)	0.03	0.2	(14)	400	249	8	53	8	1	29	445	21	3	11	6	100	1.47	1.19	1.04	698
(34)	0.06	0.7	26	177	324	8	74	9	2	6	754	46	3	25	9	100	1.47	1.19	1.04	724
(26)	0.06	0.7	27	167	270	7	81	10	2	5	707	36	4	21	8	100	1.50	1.19	1.02	728
(23)	0.06	0.8	24	166	342	8	79	11	2	5	697	36	3	22	8	100	1.49	1.22	1.03	727
(29)	0.06	0.8	26	173	339	8	77	12	3	6	1089	46	4	21	8	100	1.57	1.20	0.99	721
(33)	0.05	0.7	19	157	353	9	76	10	2	5	924	43	4	21	7	100	1.48	1.23	1.03	725
(12)	0.05	0.8	25	163	413	8	78	9	2	4	1690	37	3	21	7	100	1.48	1.23	1.03	727
(5)	0.05	0.7	36	205	317	10	78	13	2	7	550	n.a.	3	18	7	100	1.43	1.33	1.05	731
(4)	0.05	0.7	35	219	265	12	82	14	3	7	445	n.a.	3	18	8	100	1.43	1.29	1.06	735
(16)	0.05	0.7	33	233	286	6	76	18	4	8	256	n.a.	4	17	10	100	1.34	1.36	1.11	734
(9)	0.05	0.7	35	231	295	7	84	17	3	9	308	n.a.	4	19	10	100	1.30	1.42	1.14	745
(19)	0.11	1.5	71	136	808	7	65	31	3	2	1320	n.a.	3	8	4	100	1.31	1.56	1.14	724
(19)	0.06	0.8	39	214	307	11	81	20	4	12	728	n.a.	4	28	11	100	1.30	1.41	1.15	742
(14)	0.06	0.8	40	239	288	8	85	17	3	6	615	n.a.	4	18	9	100	1.41	1.29	1.07	738
(9)	0.06	0.7	36	264	214	5	68	16	4	9	154	n.a.	3	21	13	100	1.45	1.26	1.05	718
(20)	0.06	0.7	36	243	280	7	87	17	4	9	556	n.a.	4	18	11	100	1.37	1.33	1.09	742
(14)	0.06	0.8	31	241	269	9	79	19	4	8	507	n.a.	3	21	10	100	1.39	1.31	1.09	735
(12)	0.05	0.7	34	244	262	6	76	15	4	10	305	n.a.	3	21	12	100	1.32	1.37	1.13	735
(7)	0.06	0.7	38	249	236	5	69	16	4	9	231	n.a.	3	18	11	100	1.35	1.33	1.11	726
(7)	0.01	0.9	38	115	97	14	140	6	n.a.	5	939	n.a.	n.a.	12	4	**100**	1.25	1.35	1.13	792
6	0.02	1.0	39	121	94	14	142	6	n.a.	9	972	n.a.	n.a.	12	5	**100**	1.18	1.37	1.19	798
9	0.02	1.2	46	88	107	17	170	8	n.a.	7	976	n.a.	n.a.	13	6	**100**	1.30	1.28	1.06	805
5	0.01	0.9	29	140	76	13	129	7	n.a.	6	1067	n.a.	n.a.	12	5	**100**	1.39	1.11	0.99	774
7	0.01	1.0	17	64	124	12	125	6	n.a.	3	1057	n.a.	n.a.	11	4	**100**	1.29	1.30	1.07	779

Supplementary Table 7.S3/3: LA-ICP-MS analyses of melt inclusions (MI) and rock matrix, corresponding melt composition parameters and calculated zircon saturation temperatures

Analysis	Sample name[1]	Sample type	B µg/g	Na$_2$O[2] meas wt%	Na$_2$O$_c$[3] corr wt%	MgO wt%	Al$_2$O$_3$ wt%	SiO$_2$ wt%[4]	K$_2$O wt%	CaO wt%	TiO$_2$ wt%	V µg/g
Nomlaki tuff												
15Se10b09	Chalk Mt C matrix 2 50µm	matrix	21	4.3	N/A	0.03	13.2	77.6	2.5	1.2	0.13	10.3
Kos granite enclave												
15Se10b10	KS-A gl MI in qtz 35µm	MI in qtz	41	0.6	3.5	0.07	**12.7**	78.4	4.0	0.7	0.13	1.6
15Se10b11	KS-A gl MI in qtz 30µm	MI in qtz	50	1.2	3.5	0.09	**12.7**	79.0	3.5	0.7	0.11	1.2
15Se10b12	KS-A gl MI in qtz 35µm	MI in qtz	39	2.0	3.8	0.09	**12.7**	78.6	3.7	0.6	0.09	1.4
15Se10b13	KS-A gl MI in qtz 35µm	MI in qtz	68	2.0	3.8	0.07	**12.7**	78.6	3.6	0.7	0.10	0.7
Los Humeros vitrophyre												
15Se11c08	117450-58 matrix	matrix	32	4.8	N/A	0.16	14.7	72.4	5.3	0.8	0.22	2.5
15Se11c09	117450-58 matrix	matrix	36	4.9	N/A	0.15	14.5	72.6	5.3	0.8	0.21	2.4
15Se11c10	117450-58 matrix	matrix	31	4.8	N/A	0.16	15.2	72.0	5.2	0.7	0.23	2.5
15Se11c11	117450-58 matrix	matrix	35	4.9	N/A	0.16	14.9	72.1	5.3	0.8	0.22	2.4
Glass Creek Dome vitrophyre												
15Se10g15	Inyo1 A matrix 50µm*	matrix	29	4.3	N/A	0.07	13.8	73.5	5.4	0.8	0.12	0.2
15Se10g16	Inyo1 A matrix 50µm*	matrix	28	4.7	N/A	0.09	14.4	73.0	5.1	1.1	0.14	0.4
15Se10g17	Inyo1 B matrix 50µm ***	matrix	29	4.6	N/A	0.18	15.0	71.8	5.2	1.2	0.24	1.4
15Se10h04	Inyo1 B matrix 50µm	matrix	28	4.7	N/A	0.19	15.6	71.0	5.3	1.2	0.24	1.5
Glass Creek Flow vitrophyre												
15Se10g10	Inyo4 A matrix 50µm	matrix	22	4.5	N/A	0.29	16.1	68.8	6.0	1.1	0.34	5.3
15Se10g11	Inyo4 A matrix 50µm	matrix	21	4.5	N/A	0.30	16.1	68.7	6.0	1.1	0.33	5.1
15Se10g12	Inyo4 B matrix 50µm	matrix	22	4.7	N/A	0.44	16.4	68.2	5.7	1.4	0.31	5.4
15Se10g13	Inyo4 B matrix 50µm	matrix	25	4.5	N/A	0.23	16.5	68.5	6.1	1.1	0.33	4.8
Mono #12 vitrophyre												
15Se10h05	Mono2 A matrix 50µm	matrix	44	3.9	N/A	0.23	14.2	74.0	4.7	1.5	0.24	6.8
15Se10h06	Mono2 B matrix 50µm	matrix	41	3.8	N/A	0.38	14.1	73.6	4.8	1.6	0.25	8.5
15Se10h07	Mono2 C matrix 50µm	matrix	40	4.4	N/A	0.22	14.9	72.7	4.3	2.0	0.28	7.6
15Se10h08	Mono2 D matrix 50µm	matrix	39	3.8	N/A	0.26	14.3	73.7	4.9	1.5	0.27	7.6
Tunnel Spring Tuff												
15De16k05	Cryst2 transp grainmt qtz2 xxM	MI in qtz	44	1.1	2.8	0.05	**12.7**	80.2	3.7	0.8	0.05	0.2
15De16k06	Cryst2 transp grainmt exp gl MI	MI in qtz	47	2.9	N/A	0.08	12.6	78.9	5.0	1.0	0.05	0.3
15De16k07	Cryst2 transp grainmt qtz3 ±gl M	MI in qtz	56	0.9	3.1	0.07	**12.7**	79.1	4.5	1.0	0.03	0.3
15De16k08	Cryst2 transp grainmt qtz4 exp g	MI in qtz	65	3.3	N/A	0.05	12.8	78.4	4.8	0.6	0.04	0.3
Blackfoot Lava Field												
16No18n05	Blackfoot gl matrix 40µm	matrix	34	4.0	N/A	0.02	13.5	76.1	5.0	0.5	0.05	(0.3)
16No18n06	Blackfoot gl matrix 70µm	matrix	35	4.0	N/A	0.02	14.1	75.4	5.0	0.6	0.06	(0.1)
16No18n07	Blackfoot gl matrix 80µm	matrix	37	3.9	N/A	0.02	13.9	76.0	4.8	0.5	0.05	(0.1)
Pine Grove tuff												
16Au05b09	Pine8 pheno A exp gl MI 30 µm	MI in qtz	56	4.7	0.0	0.01	**13.6**	75.2	4.5	0.8	0.01	(0.9)
16Au05b12	Pine8 pheno D large gl MI 80 µ	MI in qtz	51	4.4	N/A	0.01	**13.6**	76.3	4.3	0.5	0.01	(0.1)
15De09b11	Pine8 qtz1 +-exp.gl MI >70 µm	MI in qtz	51	4.0	N/A	0.01	**13.6**	74.9	6.2	0.4	0.01	(0.1)

Bold values served as internal standard; red values in parentheses denote detection limits. n.a. – not analyzed; N/A – not applicable

The number of stars behind the sample name refer to the quality of the LA-ICP-MS analysis; three stars means perfect ablation; one star means partial decrepitation and thus potential loss of part of the inclusion content. (exp) means that the inclusion was slightly exposed.

[1] gl. MI – glassy melt inclusion; xxMI – crystallized melt inclusion; size in µm refers to diameter of the melt inclusion or of the pit size used for matrix analysis

[2] actually measured Na$_2$O content.

[3] estimated original Na$_2$O content before diffusional loss of Na. N/A means that the actually measured content was considered trustworthy.

[4] The SiO$_2$ content of the crystallized and/or unexposed inclusions was calculated by difference assuming a total of 100 wt % major element oxides (volatile-free).

[5] melt composition parameter of Watson and Harrison (1983).

[6] molar Al$_2$O$_3$/(Na$_2$O+K$_2$O).

[7] molar Al$_2$O$_3$/(Na2O+K2O+CaO).

[8] zircon saturation temperature according to Watson and Harrison (1983) based on the Zr concentration mesured in the melt inclusion or in the matrix.

[9] this analysis is considered an outlier and thus was not used in the calculation of averages

						Melt inclusion composition											melt comp. param.			T_{zirc}
Cr μg/g	MnO wt%	FeO wt%	Zn μg/g	Rb μg/g	Sr μg/g	Y μg/g	Zr μg/g	Nb μg/g	Mo μg/g	Cs μg/g	Ba μg/g	Ce μg/g	Hf μg/g	Th μg/g	U μg/g	total wt%	M[5]	A/NK[6]	A/CNK[7]	T_{zirc}[8] (°C)
(5)	0.01	1.1	15	65	120	14	148	3	n.a.	3	1042	n.a.	n.a.	12	5	100	1.25	1.35	1.10	796
(43)	0.08	0.4	(35)	168	29	13	46	23	n.a.	6	464	n.a.	n.a.	13	6	100	1.21	1.25	1.12	704
(28)	0.08	0.5	(23)	144	36	14	55	21	n.a.	5	690	n.a.	n.a.	14	5	100	1.14	1.33	1.18	723
(16)	0.09	0.5	17	189	36	13	52	22	n.a.	7	586	n.a.	n.a.	14	6	100	1.21	1.23	1.12	713
(19)	0.21	0.3	(16)	340	5	22	78	36	n.a.	90	22	n.a.	n.a.	21	11	100	1.22	1.25	1.11	744
(6)	0.04	1.6	44	158	36	24	296	19	n.a.	6	656	n.a.	n.a.	20	6	100	1.54	1.07	0.97	838
(6)	0.04	1.6	45	162	35	29	295	19	n.a.	6	631	n.a.	n.a.	19	6	100	1.58	1.05	0.94	834
(8)	0.04	1.6	46	157	35	25	310	19	n.a.	6	669	n.a.	n.a.	20	6	100	1.47	1.12	1.03	848
(6)	0.04	1.6	43	159	36	26	312	19	n.a.	6	661	n.a.	n.a.	21	6	100	1.53	1.08	0.98	843
(6)	0.06	1.6	60	161	49	21	250	19	n.a.	4	534	n.a.	n.a.	18	6	100	1.51	1.07	0.97	824
(6)	0.06	1.5	54	147	128	19	263	17	n.a.	4	851	n.a.	n.a.	15	5	100	1.56	1.09	0.95	824
(6)	0.06	1.9	65	142	138	19	336	20	n.a.	3	1068	n.a.	n.a.	14	5	100	1.54	1.14	0.98	850
(7)	0.06	1.7	59	142	115	22	365	19	n.a.	3	1011	n.a.	n.a.	15	5	100	1.52	1.16	1.00	859
(6)	0.06	2.1	54	144	108	22	416	19	n.a.	4	1085	n.a.	n.a.	17	4	100	1.54	1.17	1.01	871
(5)	0.06	2.1	59	138	99	24	425	18	n.a.	3	1187	n.a.	n.a.	18	4	100	1.56	1.16	1.01	872
(6)	0.06	2.1	54	125	211	20	372	17	n.a.	3	1652	n.a.	n.a.	15	4	100	1.59	1.17	0.99	855
(5)	0.06	2.0	53	144	98	23	428	19	n.a.	4	1111	n.a.	n.a.	17	4	100	1.53	1.17	1.03	874
(7)	0.03	1.1	32	173	138	20	142	18	n.a.	5	291	n.a.	n.a.	15	4	100	1.45	1.24	1.00	778
(8)	0.04	1.4	39	179	134	23	141	18	n.a.	5	315	n.a.	n.a.	15	5	100	1.49	1.23	0.98	775
(8)	0.03	1.1	31	157	206	20	121	18	n.a.	5	357	n.a.	n.a.	13	4	100	1.55	1.26	0.96	758
(8)	0.04	1.2	33	203	146	25	147	20	n.a.	5	305	n.a.	n.a.	16	5	100	1.46	1.24	1.00	780
(13)	0.07	0.5	40	174	69	32	28	25	1	9	112	19	1	4	5	100	1.05	1.47	1.26	678
(9)	0.07	0.5	39	285	71	30	29	27	2	9	136	18	2	4	6	100	1.29	1.24	1.06	666
(8)	0.07	0.4	36	231	80	56	30	42	1	12	87	28	2	16	12	100	1.26	1.27	1.08	670
(8)	0.10	0.5	44	264	25	25	22	37	1	14	20	17	2	5	9	100	1.26	1.20	1.08	649
(10)	0.05	0.8	50	510	1	134	120	86	3	20	0	39	7	43	33	100	1.36	1.12	1.04	770
(3)	0.05	0.8	51	507	1	140	125	88	3	20	0	40	7	46	34	100	1.33	1.17	1.08	776
(3)	0.05	0.8	48	485	1	136	122	85	3	19	1	39	7	45	32	100	1.29	1.19	1.10	777
(0)	0.37	0.8	75	547	0	83	57	57	2	18	(2)	28	5	24	17	100	1.30	1.09	0.97	685
(4)	0.14	0.7	78	475	0	83	56	52	2	15	(0)	24	5	25	15	100	1.34	1.14	1.05	711
(2)	0.11	0.7	85	625	0	84	51	63	2	19	(0)	4	20	20	0	100	1.48	1.02	0.97	694

Supplementary Table 7.S4/1: LA-ICP-MS analyses of minerals

Analysis	Sample name	Sample type	Mineral	µg/g / wt%	B	Na / Na$_2$O	Mg / MgO	Al / Al$_2$O$_3$	Si / SiO$_2$	K / K$_2$O	Ca / CaO	Ti / TiO$_2$	V	Cr / Cr$_2$O$_3$
Oravita hyalodacite														
16Au24j05	Oravita mgt	phenocryst	magnetite		(23)	(0.0)	0.4	1.5	(0.8)	(0.0)	(1.0)	13.1	1990	0.1
16Au24j07	Oravita mgt	phenocryst	magnetite		(46)	(0.0)	0.3	1.5	(1.5)	(0.1)	(2.0)	10.5	2112	0.0
16Au24j08	Oravita mgt	phenocryst	magnetite		(50)	0.0	0.4	1.5	(1.7)	(0.1)	(2.2)	11.4	2104	0.0
16Au24j09	Oravita mgt	phenocryst	magnetite		(46)	0.0	0.3	1.6	(1.6)	(0.1)	(2.1)	11.4	2036	0.0
16Au24j13	Oravita mgt	phenocryst	magnetite		(70)	(0.0)	0.4	1.4	(2.4)	(0.2)	(3.2)	12.8	1958	0.0
16Au24j14	Oravita mgt	phenocryst	magnetite		(96)	0.0	0.2	1.4	(3.3)	(0.2)	(4.3)	11.9	1949	0.0
16Au24j15	Oravita mgt	phenocryst	magnetite		(56)	(0.0)	0.3	1.4	(2.4)	(0.2)	(3.5)	10.5	2051	0.0
16Au24k14	Oravita Fsp	phenocryst	plagioclase		(7)	6.9	0.0	23.1	61.7	1.3	6.7	0.0	(1)	(0.0)
16Au24k15	Oravita Fsp	phenocryst	plagioclase		(7)	7.5	0.0	23.2	61.9	0.6	6.6	0.0	(0)	(0.0)
16Au24k16	Oravita Fsp	phenocryst	plagioclase		(7)	7.4	0.0	23.5	61.6	0.5	6.7	0.0	(1)	(0.0)
16Au24k17	Oravita Fsp	phenocryst	plagioclase		(7)	7.3	0.0	23.3	61.6	0.4	7.1	0.0	(1)	(0.0)
Mount Rano vitrophyre														
15Se11h05	Mt Rano A mgt	phenocryst	magnetite		(36)	(0.0)	1.0	2.0	(1.1)	(0.1)	(1.5)	13.0	1518	(0.0)
15Se11h08	Mt Rano A mgt	phenocryst	magnetite		(32)	(0.0)	0.9	1.8	(0.9)	(0.1)	(1.3)	13.4	1185	(0.0)
15Se11g16	Mt Rano C mgt	phenocryst	magnetite		(17)	0.0	1.0	1.8	(0.8)	(0.1)	(1.2)	13.3	1184	(0.0)
15Se11g17	Mt Rano C mgt	phenocryst	magnetite		(19)	(0.0)	1.0	1.9	(0.9)	(0.1)	(1.3)	13.5	1217	(0.0)
15Se11h07	Mt Rano A ilm	phenocryst	ilmenite		(34)	0.0	1.8	0.1	(1.0)	(0.1)	(1.4)	47.3	258	(0.0)
15Se11h06	Mt Rano A ilm	phenocryst	ilmenite		(32)	0.0	1.8	0.1	(1.0)	(0.1)	(1.3)	47.4	268	(0.0)
15Se11h04	Mt Rano C ilm	phenocryst	ilmenite		(39)	(0.0)	1.8	0.1	(1.8)	(0.1)	(2.7)	47.7	265	(0.0)
Parinacota vitrophyre														
16Au05k05	Pc G mgt 20 um	phenocryst	magnetite		(24)	x	0.8	1.7	(0.8)	(0.1)	(1.3)	6.1	2857	0.1
16Au05k07	Pc G mgt 20 um	phenocryst	magnetite		(26)	x	1.0	2.3	x	x	(1.3)	5.4	1932	(0.0)
16Au05k08	Pc H mgt 20 um	phenocryst	magnetite		(22)	(0.0)	0.5	0.8	(0.7)	(0.0)	(1.0)	3.5	1712	0.0
16Au05k09	Pc H mgt 20 um	phenocryst	magnetite		(24)	(0.0)	0.5	0.9	(0.7)	(0.1)	(1.2)	3.5	1636	0.0
16Au05k10	Pc I mgt 20 um	phenocryst	magnetite		(24)	(0.0)	0.6	0.8	(0.8)	(0.1)	(1.2)	3.5	2037	(0.0)
16Au05k11	Pc I mgt 20 um	phenocryst	magnetite		(19)	(0.0)	0.6	0.9	(0.6)	(0.0)	(0.9)	3.7	2025	0.0
16Au05l05	Pc ilm attached to tit	phenocryst	ilmenite		(34)	x	0.7	0.2	(1.5)	(0.1)	(2.0)	28.6	1907	0.0
16Au05l07	Pc ilm micropheno + glass	phenocryst	ilmenite		(36)	(0.0)	1.5	0.7	x	(0.1)	(1.6)	39.4	943	(0.0)
16Au05k06	Pc G ilm 20 um	phenocryst	ilmenite		(22)	x	1.3	0.2	(0.8)	(0.0)	(1.2)	39.1	891	(0.0)
16Au05l04	Pc ilm incl in hbl	incl. in hbl	ilmenite		(19)	(0.0)	1.3	0.1	(0.8)	(0.1)	(1.1)	39.5	799	0.0
16Au05i12	Pc Kfsp A Kfsp 40 um	phenocryst	K-feldspar		(7)	3.6	0.0	18.9	65.7	11.5	0.2	0.0	(0)	(0.0)
16Au05i14	Pc Kfsp A Kfsp 40 um	phenocryst	K-feldspar		(4)	3.5	0.0	18.5	66.2	11.5	0.2	0.0	(0)	(0.0)
16Au05i17	Pc Kfsp A Kfsp	phenocryst	K-feldspar		(4)	3.4	0.0	18.5	66.3	11.4	0.2	0.0	(0)	(0.0)
16Au05j04	Pc Kfsp B kfsp incl	incl in Kfsp	K-feldspar		(6)	3.3	0.0	19.1	65.3	11.9	0.3	0.0	(0)	(0.0)
16Au05j05	Pc Kfsp B kfsp	phenocryst	K-feldspar		(6)	3.3	0.0	19.3	65.2	11.8	0.3	0.0	(0)	(0.0)
16Au05j06	Pc Kfsp C	phenocryst	K-feldspar		(6)	3.3	0.0	19.6	65.0	11.6	0.3	0.0	(0)	(0.0)
16Au05j12	Pc Kfsp E Kfsp 40 um	phenocryst	K-feldspar		(9)	3.4	(0.0)	19.1	65.5	11.8	0.2	0.0	(1)	(0.0)
16Au05i11	Pc A plag incl 40 um	incl in Kfsp	plagioclase		(8)	9.2	0.0	20.8	65.7	1.3	2.8	0.0	(0)	(0.0)
16Au05i16	Pc A plag incl 40 um	incl in Kfsp	plagioclase		(7)	9.1	0.0	21.0	65.3	1.3	3.1	0.0	(1)	(0.0)
Hideaway Park tuff														
15De10d05	WP qtz1 mgt with melt 20	incl in qtz	magnetite		(15)	(0.0)	0.2	(0.0)	(0.3)	x	(0.4)	4.4	187	(0.0)
15De16k12	WP grainmt qtz5 exp mgt	incl in qtz	magnetite		(18)	(0.0)	0.1	1.0	(0.7)	(0.1)	(0.7)	4.9	247	(0.0)
16Au05d10	WP Kfsp C mgt incl 20 um	incl in Kfsp	magnetite		(50)	(0.0)	0.2	(0.0)	x	(0.1)	(2.1)	4.5	212	(0.0)
16Au05d11	WP Kfsp C mgt incl 15 um	incl in Kfsp	magnetite		(86)	(0.0)	0.2	(0.0)	x	(0.2)	(3.7)	4.7	191	(0.0)
15De10d06	WP qtz2 ilm incl 30 um	incl in qtz	ilmenite		(19)	(0.0)	0.5	0.2	(1.0)	x	(1.2)	41.1	46	(0.0)
15De10d07	WP qtz3 ilm incl 35 um	incl in qtz	ilmenite		(5)	(0.0)	0.3	(0.0)	(0.2)	x	(0.3)	43.3	47	(0.0)
15De10d08	WP qtz4 ilm incl 20 um (c	incl in qtz	ilmenite		(22)	(0.0)	0.8	0.3	(1.5)	(0.1)	(2.0)	44.4	102	(0.0)
15De10d09	WP qtz4 exp ilm 30 um	incl in qtz	ilmenite		(9)	(0.0)	0.5	(0.0)	x	(0.0)	(0.4)	43.4	41	(0.0)
15De16k11	WP grainmt qtz5 exp ilm	incl in qtz	ilmenite		(28)	x	0.2	0.1	(1.3)	(0.1)	(1.1)	42.6	55	(0.0)
16Au05c05	WP Fsp A Kfsp host 40 um	phenocryst	K-feldspar		(4)	4.3	(0.0)	19.2	65.6	10.6	0.2	0.0	(0)	(0.0)
16Au05c07	WP Fsp B Kfsp host 40 um	phenocryst	K-feldspar		(6)	4.3	(0.0)	19.3	65.5	10.5	0.3	0.0	(0)	(0.0)
16Au05c09	WP Fsp B Kfsp host 40 um	phenocryst	K-feldspar		(6)	4.4	(0.0)	19.3	65.6	10.4	0.2	0.0	(0)	(0.0)
16Au05c11	WP Fsp B Kfsp host 40 um	phenocryst	K-feldspar		(6)	4.4	(0.0)	19.3	65.6	10.4	0.3	0.0	(0)	(0.0)
16Au05d09	WP Kfsp C host	phenocryst	K-feldspar		(10)	4.4	(0.0)	18.7	66.5	10.1	0.3	0.0	(1)	(0.0)
16Au05b17	Winter Park Fsp A kfsp ho	phenocryst	K-feldspar		(5)	4.4	(0.0)	18.4	66.7	10.2	0.2	0.0	(0)	(0.0)
16Au05c04	WP Fsp A plag incl 30 um	incl in Kfsp	plagioclase		(8)	9.3	(0.0)	21.8	64.9	1.3	2.6	0.0	(1)	(0.0)
16Au05c06	WP Fsp B plag incl 30 um	incl in Kfsp	plagioclase		(10)	9.4	0.0	20.9	65.7	1.5	2.3	0.0	(1)	(0.0)
16Au05c08	WP Fsp B plag incl 30 um	incl in Kfsp	plagioclase		(10)	9.3	0.0	21.2	65.5	1.4	2.4	0.0	(1)	(0.0)
16Au05c10	WP Fsp B plag incl 30 um	incl in Kfsp	plagioclase		(11)	9.4	(0.0)	20.9	65.7	1.6	2.3	0.0	(1)	(0.0)
16Au05b16	WP Fsp A plag incl	incl in Kfsp	plagioclase		(5)	9.4	0.0	20.5	66.4	1.4	2.3	0.0	(0)	(0.0)
Cottonwood tuff														
15Se10k04	Cw B small mgt	phenocryst	magnetite		(28)	(0.0)	0.3	1.5	(1.1)	(0.1)	(1.7)	5.9	2881	0.1

Mn	Fe			Zn	Rb	Sr	Y	Zr	Nb	Mo	Cs	Ba	Ce	Hf	Th	U	total	Or	Ab	An
MnO	FeO$_{tot}$	Fe$_2$O$_3$[1]	FeO[1]														wt%	mol%	mol%	mol%
0.5	79.8	41.8	42.2	1333	(1)	(1)	(1)	23	59	27	(0)	(2)	(0)	(1)	(0)	(0)	100			
0.4	82.1	46.8	40.0	1598	(2)	2	9	14	21	31	(1)	(5)	25	(2)	(1)	(1)	100			
0.4	81.2	44.9	40.8	1776	(2)	3	24	21	40	32	(1)	(5)	50	(2)	(1)	(1)	100			
0.5	81.2	44.9	40.8	1692	(2)	(1)	(1)	6	21	29	(1)	(5)	(1)	(2)	(1)	(1)	100			
0.5	80.1	42.4	41.9	1476	(3)	(2)	(2)	12	50	30	(1)	(8)	(1)	(4)	(1)	(1)	100			
0.4	81.1	44.1	41.4	1776	(4)	(3)	(2)	21	73	37	(1)	(10)	(2)	(5)	(2)	(2)	100			
0.4	82.2	46.9	40.0	1506	(4)	(2)	(1)	19	47	28	(1)	(8)	(1)	(4)	(1)	(1)	100			
0.0	0.2	N/A	N/A	7	14	540	0	1	(0)	(0)	1	419	17	(0)	(0)	(0)	100	6	45	49
0.0	0.2	N/A	N/A	8	1	554	0	(0)	(0)	(0)	(0)	435	16	(0)	(0)	(0)	100	2	50	48
0.0	0.2	N/A	N/A	8	1	544	1	(0)	(0)	(0)	(0)	425	18	(0)	(0)	(0)	100	2	49	49
0.0	0.2	N/A	N/A	6	1	526	0	(0)	(0)	(0)	(0)	373	19	(0)	(0)	(0)	100	2	47	51
0.8	78.6	41.8	40.9	0	1	0	0	50	0	n.a.	0	1	n.a.	n.a.	0	0	100			
0.8	78.5	41.2	41.4	0	0	0	0	57	0	n.a.	0	0	n.a.	n.a.	0	0	100			
0.8	78.5	41.4	41.2	0	0	2	10	54	0	n.a.	0	1	n.a.	n.a.	0	0	100			
0.8	78.4	41.0	41.5	0	0	0	0	55	0	n.a.	0	0	n.a.	n.a.	0	0	100			
1.2	48.4	11.4	38.1	0	0	1	3	380	0	n.a.	0	1	n.a.	n.a.	0	0	100			
1.2	48.2	11.1	38.2	0	0	0	5	372	0	n.a.	0	1	n.a.	n.a.	0	0	100			
1.3	47.9	10.6	38.4	0	0	0	3	370	0	n.a.	0	0	n.a.	n.a.	0	0	100			
0.8	84.3	55.1	34.8	1650	(1)	x	(1)	6	3	2	(0)	(6)	x	(2)	(1)	(1)	100			
0.8	84.5	56.2	34.0	1634	x	x	(1)	6	3	(1)	(1)	x	(1)	(2)	(0)	(0)	100			
0.8	87.8	61.2	32.7	1463	(1)	(1)	(1)	3	3	2	(0)	(4)	(0)	(2)	(0)	(0)	100			
0.8	87.8	61.3	32.6	1435	(1)	(1)	(1)	2	2	2	(0)	(4)	(0)	(2)	(0)	(0)	100			
0.8	87.7	61.2	32.6	1387	(2)	(1)	(1)	2	2	2	(0)	(3)	(1)	(2)	(0)	(0)	100			
0.8	87.5	60.8	32.8	1384	(2)	x	(1)	2	3	2	(0)	(2)	(1)	(1)	(0)	(0)	100			
0.4	65.2	45.7	24.0	387	(2)	(1)	(1)	157	139	10	(1)	(5)	(1)	5	(1)	(1)	100			
1.4	54.2	25.4	31.3	493	(2)	x	(1)	248	387	x	(1)	x	x	6	x	x	100			
1.3	55.2	26.3	31.5	541	(1)	x	(1)	88	451	5	(0)	(5)	x	4	1	(0)	100			
1.4	54.9	25.7	31.8	636	(1)	(1)	(0)	67	397	x	(1)	(3)	(0)	3	(0)	(0)	100			
(0.0)	0.1	N/A	N/A	(3)	219	254	(0)	(0)	(0)	(0)	0	902	1	(0)	(0)	(0)	100	67	31	2
(0.0)	0.1	N/A	N/A	(4)	194	361	(0)	(0)	(0)	(0)	0	738	1	(0)	(0)	(0)	100	67	31	2
(0.0)	0.1	N/A	N/A	(4)	215	213	(0)	(0)	(0)	(0)	0	451	1	(0)	(0)	(0)	100	67	31	2
(0.0)	0.1	N/A	N/A	(4)	161	774	(0)	(0)	(0)	(0)	0	5463	1	(0)	(0)	(0)	100	68	29	3
(0.0)	0.1	N/A	N/A	(4)	161	764	(0)	(0)	(0)	(0)	0	6331	0	(0)	(0)	(0)	100	68	29	3
(0.0)	0.1	N/A	N/A	(3)	166	795	0	(0)	(0)	(0)	0	7306	1	(0)	(0)	(0)	100	68	30	3
(0.0)	0.1	N/A	N/A	(4)	206	209	(0)	(0)	(0)	(0)	0	155	1	(0)	(0)	(0)	100	69	30	2
0.0	0.2	N/A	N/A	4	4	255	(0)	(0)	(0)	(0)	(0)	31	4	(0)	(0)	(0)	100	6	70	24
0.0	0.2	N/A	N/A	(7)	4	260	(0)	(0)	(0)	(0)	(0)	27	4	(1)	(0)	(0)	100	6	68	25
2.5	86.6	60.6	32.0	1901	x	(0)	(0)	(1)	104	20	x	(2)	n.a.	(1)	(0)	x	100			
2.1	85.8	58.4	33.2	1769	(2)	(1)	1	12	82	14	(0)	(5)	n.a.	(2)	(1)	(1)	100			
2.4	86.6	60.3	32.3	1633	x	(1)	(2)	4	75	10	(1)	(5)	(1)	(3)	(1)	(1)	100			
2.4	86.3	59.9	32.4	2097	(6)	(3)	(3)	6	99	12	x	(9)	x	(6)	(1)	(2)	100			
6.4	48.0	20.5	29.5	879	17	(1)	30	92	13099	20	(1)	(4)	n.a.	x	x	x	100			
6.1	47.0	16.5	32.1	750	x	x	3	91	11986	18	x	x	n.a.	x	x	x	100			
4.3	47.6	15.0	34.1	1085	x	(2)	12	118	7735	9	x	(9)	n.a.	(5)	13	(1)	100			
7.1	45.5	16.2	30.9	841	x	(1)	3	57	13776	16	x	(3)	n.a.	x	(0)	x	100			
6.3	47.5	17.9	31.4	1011	(2)	(2)	(1)	110	10092	17	(1)	(8)	(1)	4	(1)	(1)	100			
0.0	0.1	N/A	N/A	(5)	507	11	(0)	(0)	(0)	(0)	0	26	3	(0)	(0)	(0)	100	61	37	2
0.0	0.1	N/A	N/A	(3)	505	11	(0)	0	(0)	(0)	0	23	3	(0)	(0)	(0)	100	60	38	2
0.0	0.1	N/A	N/A	(3)	492	11	(0)	(0)	(0)	(0)	0	21	3	(0)	(0)	(0)	100	60	38	2
(0.0)	0.1	N/A	N/A	(3)	491	11	(0)	(0)	(0)	(0)	0	21	3	(0)	(0)	(0)	100	59	38	3
0.0	0.1	N/A	N/A	(7)	461	11	(0)	(0)	(0)	(0)	0	18	3	(1)	(0)	(8)	100	59	39	2
(0.0)	0.1	N/A	N/A	(4)	499	12	(0)	(0)	(0)	(0)	0	29	3	(0)	(0)	(0)	100	59	39	2
0.0	0.2	N/A	N/A	(8)	14	14	(0)	1	(0)	(1)	(0)	(2)	10	(1)	0	(0)	100	7	71	22
0.0	0.2	N/A	N/A	(5)	14	12	(0)	(0)	(0)	(0)	(0)	(2)	10	(1)	(0)	(0)	100	8	73	20
0.0	0.2	N/A	N/A	(5)	15	12	(0)	(0)	(0)	(0)	(0)	(2)	10	(1)	(0)	(0)	100	7	72	21
0.0	0.2	N/A	N/A	(6)	15	12	(0)	(0)	(0)	(0)	(0)	(2)	10	(1)	(0)	(0)	100	8	73	19
0.0	0.1	N/A	N/A	(4)	13	13	0	(0)	(0)	(0)	(0)	1	10	(0)	(0)	(0)	100	7	73	20
0.5	85.6	55.6	35.6	1213	0	1	0	4	15	n.a.	0	1	n.a.	n.a.	0	0	100			

Supplementary Table 7.S4/2: LA-ICP-MS analyses of minerals

Analysis	Sample name	Sample type	Mineral	µg/g wt% B	Na Na₂O	Mg MgO	Al Al₂O₃	Si SiO₂	K K₂O	Ca CaO	Ti TiO₂	V	Cr Cr₂O₃
Cottonwood tuff													
15Se10k05	Cw B big mgt rim	phenocryst	magnetite	(26)	(0.0)	0.5	2.1	(1.0)	(0.1)	(1.6)	7.2	3140	0.1
15Se10k06	Cw B big mgt core	phenocryst	magnetite	(26)	(0.0)	0.5	2.1	(1.0)	(0.1)	(1.6)	6.4	3048	0.2
15Se10k08	Cw B big spongy mgt rim	phenocryst	magnetite	(24)	(0.0)	0.5	1.8	(1.0)	(0.1)	(1.5)	5.9	3156	0.1
15Se10k09	Cw B small mgt in fsp /qtz incl in fsp/qtz	magnetite	(30)	0.0	0.6	1.7	(2.2)	(0.2)	(4.1)	5.3	3079	(0.0)
15Se10k10	Cw B mgt	phenocryst	magnetite	(13)	(0.0)	0.3	2.0	(0.9)	(0.1)	(1.7)	6.4	3125	0.2
15De09f13	Cw qtz3 mgt incl (+ melt) incl in qtz	magnetite	(12)	(0.0)	0.7	0.8	(0.6)	(0.0)	x	6.8	3172	0.2
15De09f14	Cw qtz4 mgt incl 10 um incl in qtz	magnetite	(120)	(0.0)	0.8	(0.0)	(4.2)	(0.3)	x	7.3	2851	0.1
15De09f16	Cw qtz5 mgt incl qtz 35 u incl in qtz	magnetite	(6)	(0.0)	1.0	2.3	(0.3)	x	(0.4)	6.8	2969	0.1
15Se10k07	Cw B small ilm	phenocryst	ilmenite	(24)	(0.0)	1.1	0.2	(1.0)	(0.1)	(1.5)	40.5	1670	0.0
15Se10k11	Cw A ilm	phenocryst	ilmenite	(55)	(0.0)	1.1	0.1	(2.3)	(0.1)	(3.8)	45.5	602	(0.0)
15De09f08	Cw qtz1 exp plag incl30 u incl in qtz	plagioclase	(6)	5.3	0.0	25.9	58.2	0.4	9.9	0.0	(0)	(0.0)
15De09f09	Cw qtz1 plag incl20 um incl in qtz	plagioclase	(18)	4.9	0.0	29.2	53.3	0.5	11.8	x	(1)	(0.0)
15De09g08	Cw qtz 8 plag incl 30 um incl in qtz	plagioclase	(8)	4.9	0.0	29.2	53.5	0.4	11.8	x	(1)	(0.0)
15De09g09	Cw qtz 8 plag incl	incl in qtz	plagioclase	(11)	4.7	0.0	29.2	53.5	0.3	12.0	(0.0)	(1)	(0.0)
Lordsburg rhyolite													
15De09d07	Ld2 qtz1 mgt incl 10 um c incl in qtz	magnetite	(43)	(0.0)	0.2	1.6	(3.0)	x	(3.1)	2.6	743	(0.0)
15De09d08	Ld2 qtz1 mgt incl 5 um ri incl in qtz	magnetite	(106)	(0.0)	0.2	2.5	(7.5)	(0.5)	(7.3)	1.9	868	(0.1)
15De09d12	Ld2 qtz2 mgt incl 17 um incl in qtz	magnetite	(31)	(0.0)	0.2	0.8	(1.6)	(0.1)	(1.7)	2.6	831	(0.0)
15De09d13	Ld2 qtz2 mgt incl 40 um incl in qtz	magnetite	(10)	(0.0)	0.2	0.7	(0.5)	(0.0)	(0.5)	2.6	852	(0.0)
15De09e08	Ld2 qtz3 mgt incl 25 um (incl in qtz	magnetite	(15)	(0.0)	0.2	1.5	(0.6)	x	(0.6)	2.0	801	(0.0)
15De09e13	Ld2 qtz4 mgt incl 15 um incl in qtz	magnetite	(18)	(0.0)	0.2	0.8	(1.3)	(0.1)	(1.2)	2.6	740	(0.0)
15De09i08	Ld2 ilm groß	phenocryst	ilmenite	(13)	x	0.3	0.3	(0.5)	(0.0)	(0.5)	26.2	753	(0.0)
15De09i09	Ld2 ilm klein	phenocryst	ilmenite	(43)	x	0.5	0.2	(1.5)	(0.1)	(1.5)	35.7	674	(0.0)
15De09i10	Ld2 ilm groß	phenocryst	ilmenite	(41)	x	0.4	0.2	(1.5)	(0.1)	(1.5)	29.3	790	(0.0)
15De09d14	Ld2 qtz2 exp Kfsp 40 um incl in qtz	K-feldspar	(2)	2.1	0.0	**17.0**	68.6	11.7	0.2	0.0	4	(0.0)
15De09d15	Ld2 qtz2 Kfsp incl 40 um incl in qtz	K-feldspar	(4)	2.4	(0.0)	**18.6**	67.7	10.9	0.2	x	(0)	(0.0)
15De09d16	Ld2 qtz2 very deep Kfsp 3 incl in qtz	K-feldspar	(8)	2.7	0.0	**18.6**	67.2	11.1	0.3	(0.0)	(1)	(0.0)
15De09e15	Ld2 qtz2 Kfsp incl 40 um incl in qtz	K-feldspar	(4)	2.5	(0.0)	**18.6**	66.8	11.9	0.2	x	(0)	(0.0)
15De09d09	Ld2 qtz1 plag incl 20 um incl in qtz	plagioclase	(17)	8.0	(0.0)	**23.5**	62.9	0.9	4.6	(0.0)	(1)	(0.0)
15De09e06	Ld2 qtz3 plag incl 25 um incl in qtz	plagioclase	(10)	8.1	0.0	**23.5**	62.9	0.9	4.6	x	(1)	(0.0)
15De09e07	Ld2 qtz3 plag incl 30 um incl in qtz	plagioclase	(7)	8.0	0.0	**23.7**	62.2	1.1	5.0	x	(1)	(0.0)
15De09e16	Ld2 qtz2 plag incl 20 um incl in qtz	plagioclase	(10)	7.6	(0.0)	**22.6**	63.7	2.2	3.8	x	(1)	(0.0)
Lordsburg granodiorite													
15De09i11	Ld3 Mgt	phenocryst	magnetite	(15)	x	0.2	2.0	x	x	(0.5)	3.7	814	(0.0)
15De09i14	Ld3 Mgt	phenocryst	magnetite	x	x	0.3	3.3	x	x	x	3.7	1004	(0.0)
15De09i15	Ld3 Mgt	phenocryst	magnetite	x	x	0.4	5.7	x	x	(0.7)	3.8	1391	(0.0)
15De09i16	Ld3 Mgt	phenocryst	magnetite	x	x	0.2	3.0	x	x	(0.5)	3.7	1154	(0.0)
15De09h05	Ld3 Mgt 15 um	phenocryst	magnetite	(25)	(0.0)	0.2	1.5	(1.4)	(0.1)	(1.3)	3.4	1506	0.0
15De09h06	Ld3 Mgt 15 um	phenocryst	magnetite	(42)	x	0.3	1.5	(1.6)	(0.1)	(1.5)	3.2	1414	0.0
15De09h07	Ld3 Mgt 20 um	phenocryst	magnetite	(11)	(0.0)	0.2	1.7	(0.7)	(0.1)	(0.7)	3.9	1661	(0.0)
15De09h08	Ld3 Mgt 15 um	phenocryst	magnetite	(23)	(0.0)	0.2	1.4	(1.0)	(0.1)	(1.1)	2.9	1239	0.0
15De09h09	Ld3 Mgt 15 um	phenocryst	magnetite	(20)	x	0.1	1.7	(1.1)	(0.1)	x	3.1	1290	(0.0)
15De09h10	Ld3 Mgt 20 um	phenocryst	magnetite	(24)	x	0.3	2.5	x	x	(0.7)	3.2	1394	0.0
15Se09h11	Ld3 Mgt 15 um	phenocryst	magnetite	(26)	x	0.2	1.3	(1.2)	(0.1)	(1.1)	3.0	1110	0.0
15De09h13	Ld3 Mgt	phenocryst	magnetite	(21)	(0.0)	0.3	1.8	(1.1)	(0.1)	(1.4)	3.3	1351	(0.0)
15De09h14	Ld3 Mgt	phenocryst	magnetite	(17)	x	0.2	2.0	x	x	x	3.2	1240	(0.0)
15De09i05	Ld3 ilm	phenocryst	ilmenite	(24)	(0.0)	0.6	0.3	(0.9)	(0.1)	(1.0)	28.3	1228	(0.0)
15De09i06	Ld3 ilm	phenocryst	ilmenite	(48)	x	0.3	0.3	(1.9)	(0.1)	(2.0)	34.2	1282	(0.0)
15De09i07	Ld3 ilm	phenocryst	ilmenite	(42)	x	0.2	0.4	x	(0.1)	(1.8)	30.1	1175	(0.0)
15De09i12	Ld3 ilm	phenocryst	ilmenite	(18)	x	0.4	0.3	(0.5)	(0.0)	(0.5)	25.6	905	(0.0)
15De09i13	Ld3 ilm	phenocryst	ilmenite	(20)	(0.0)	0.4	0.3	x	(0.0)	(0.6)	25.6	873	(0.0)
15De09h12	Ld3 ilm 20 um	phenocryst	ilmenite	(13)	x	0.3	0.4	(0.9)	(0.1)	x	34.6	1179	0.0
15De09h15	Ld3 ilm	phenocryst	ilmenite	(38)	x	0.4	0.4	x	x	(1.7)	31.1	1095	0.0
15De09h16	Ld3 ilm	phenocryst	ilmenite	(33)	(0.0)	0.2	0.3	(2.1)	(0.1)	(2.0)	34.0	1171	(0.0)
Smelter Knolls rhyolite													
15De10e07	SK exp attached mgt mx 2 phenocryst	magnetite	(26)	(0.0)	0.2	8.1	(0.9)	(0.1)	(1.4)	3.1	702	0.0
15De10e08	SK exp attached mgt mx 2 phenocryst	magnetite	(28)	(0.0)	0.2	8.0	(1.0)	(0.1)	(1.5)	2.9	630	(0.0)
15De10d14	SK biotite1 exp mgt 20 un incl in bt	magnetite	(24)	0.0	0.2	6.3	(0.8)	(0.1)	(0.9)	2.8	546	(0.0)
15De10d15	SK biotite1 exp mgt 20 un incl in bt	magnetite	(25)	x	0.1	7.2	(0.9)	(0.1)	(0.9)	2.5	475	(0.0)
15De10c15	SK Fsp3 mgt incl	incl in fsp	magnetite	(5)	(0.0)	0.2	(0.0)	(0.4)	(0.0)	(0.4)	3.1	448	(0.0)
15De10c16	SK Fsp4 mgt incl	incl in fsp	magnetite	(13)	(0.0)	0.2	(0.0)	(0.5)	(0.0)	(0.6)	3.3	319	0.0
15De10e09	SK Fsp3 mgt incl 30 um	incl in fsp	magnetite	(5)	(0.0)	0.2	(0.0)	(0.2)	(0.0)	(0.3)	3.3	441	0.0

Mn	Fe			Zn	Rb	Sr	Y	Zr	Nb	Mo	Cs	Ba	Ce	Hf	Th	U	total	Or	Ab	An
MnO	FeO$_{tot}$	Fe$_2$O$_3$[1]	FeO[1]														wt%	mol%	mol%	mol%
0.4	83.9	52.2	36.9	1159	0	0	0	36	90	n.a.	0	0	n.a.	n.a.	0	0	100			
0.5	84.5	53.9	36.0	1114	0	0	0	25	33	n.a.	0	0	n.a.	n.a.	0	0	100			
0.5	85.2	55.3	35.4	905	0	1	1	5	11	n.a.	0	0	n.a.	n.a.	0	0	100			
0.7	85.5	56.7	34.5	1067	2	4	7	8	14	n.a.	0	0	n.a.	n.a.	2	0	100			
0.4	84.7	53.8	36.3	1018	0	0	0	5	12	n.a.	0	0	n.a.	n.a.	0	0	100			
0.6	84.9	54.7	35.6	1048	(2)	(1)	15	24	21	7	(0)	x	n.a.	(1)	x	x	100			
0.7	85.1	54.9	35.7	1685	(6)	x	56	14	20	11	(3)	(24)	n.a.	(11)	(3)	(3)	100			
0.5	83.3	53.0	35.6	1027	x	x	1	15	12	6	(0)	x	n.a.	(1)	x	(0)	100			
0.8	54.6	23.4	33.5	423	0	1	0	286	937	n.a.	0	1	n.a.		0	3	100			
1.1	50.4	14.0	37.8	546	0	1	2	868	1381	n.a.	0	5	n.a.		1	3	100			
0.0	0.3	N/A	N/A	13	1	1150	0	(0)	(0)	(0)	(0)	283	n.a.	(0)	(0)	(0)	100			
0.0	0.3	N/A	N/A	12	6	1106	x	x	x	x	x	274	n.a.	(1)	x	x	100			
0.0	0.3	N/A	N/A	(12)	4	1239	(0)	(1)	(0)	(1)	(0)	262	n.a.	(1)	x	(0)	100			
0.0	0.3	N/A	N/A	(11)	(1)	1162	1	(1)	(1)	(0)	(0)	226	n.a.	(1)	(0)	(0)	100			
0.7	88.3	62.1	32.4	1908	x	x	(3)	(4)	(3)	(2)	(2)	(12)	n.a.	(7)	(3)	(2)	100			
0.6	88.2	62.3	32.1	1807	(16)	x	(6)	(12)	(5)	(9)	(3)	(41)	n.a.	(19)	(5)	(5)	100			
0.7	89.0	62.9	32.3	2261	(3)	(1)	13	727	3	(2)	(1)	(9)	n.a.	x	x	x	100			
0.7	89.1	63.2	32.2	2195	(1)	(0)	(0)	(1)	2	(1)	(0)	(3)	n.a.	(1)	(0)	(0)	100			
0.7	88.7	63.2	31.8	2247	(1)	(1)	2	7	(1)	(1)	(0)	(5)	n.a.	(2)	(0)	(1)	100			
0.7	89.0	63.0	32.3	2237	(3)	(2)	15	228	2	(1)	(1)	(7)	n.a.	x	x	x	100			
0.5	67.5	50.1	22.4	536	(0)	x	1	51	381	3	(0)	(3)	n.a.	(1)	0	(0)	100			
0.4	59.8	32.2	30.8	317	(2)	(2)	2	59	476	3	(1)	(9)	n.a.	(4)	(1)	(1)	100			
0.6	64.7	44.2	25.0	490	(1)	x	2	66	479	3	(1)	(9)	n.a.	(4)	(1)	(1)	100			
0.0	0.4	N/A	N/A	10	150	625	(0)	0	(0)	(0)	0	11814	n.a.	(0)	(0)	(0)	100	77	21	2
0.0	0.0	N/A	N/A	(5)	141	802	1	(0)	0	(0)	(0)	13111	n.a.	(0)	(0)	(0)	100	73	25	2
0.0	0.1	N/A	N/A	10	152	665	1	x	0	(0)	0	11790	n.a.	(1)	(0)	(0)	100	71	26	4
0.0	0.0	N/A	N/A	(5)	157	651	(0)	(0)	(0)	(0)	(0)	4481	n.a.	(0)	(0)	(0)	100	74	23	2
0.0	0.1	N/A	N/A	(17)	5	1085	1	(1)	(1)	(1)	(1)	209	n.a.	(2)	(1)	(1)	100	4	58	37
0.0	0.1	N/A	N/A	(11)	5	732	2	(1)	(1)	(1)	(0)	119	n.a.	(2)	(0)	(0)	100	4	59	37
0.0	0.1	N/A	N/A	(10)	13	738	2	(1)	(0)	(1)	(0)	168	n.a.	(1)	(0)	(0)	100	5	56	39
0.0	0.1	N/A	N/A	(13)	44	1098	(0)	(1)	(1)	(1)	(0)	718	n.a.	(1)	(0)	(0)	100	11	58	32
0.8	86.8	59.4	33.3	3981	x	x	2	19	28	168	x	x	n.a.	(2)	x	x	100			
0.8	85.4	57.9	33.3	4257	x	x	7	11	26	145	x	x	n.a.	(2)	x	x	100			
0.5	83.6	54.9	34.2	2557	x	x	4	14	37	127	x	x	n.a.	(2)	4	3	100			
0.8	85.8	58.2	33.4	3947	x	x	4	14	22	148	x	x	n.a.	(1)	7	2	100			
1.4	86.7	60.4	32.4	2908	(2)	(2)	(2)	(3)	6	(1)	(1)	(7)	n.a.	(3)	(1)	(1)	100			
1.4	86.8	60.9	32.0	3054	(3)	(2)	x	5	5	(3)	(1)	(7)	n.a.	(5)	(1)	(1)	100			
1.1	86.6	59.3	33.3	2303	(1)	(1)	(0)	6	4	(0)	(0)	(3)	n.a.	(2)	(1)	(1)	100			
1.1	87.8	61.7	32.3	2255	(2)	(2)	(1)	(2)	5	(1)	(1)	(6)	n.a.	(3)	(1)	(1)	100			
1.1	87.4	60.8	32.6	2787	x	x	x	x	3	(1)	(1)	(8)	n.a.	(3)	(1)	(1)	100			
1.3	86.2	59.8	32.4	2202	x	x	x	11	5	(1)	x	x	n.a.	(2)	(1)	(1)	100			
1.4	87.4	61.6	31.9	2921	(2)	x	x	x	4	(1)	(1)	(6)	n.a.	9	(1)	(1)	100			
1.3	86.8	60.5	32.4	2478	x	x	x	x	5	(1)	x	(8)	n.a.	(3)	(1)	(1)	100			
1.1	87.0	60.2	32.8	2549	x	x	x	x	4	(1)	x	(6)	n.a.	(2)	x	(1)	100			
1.4	64.5	46.3	22.9	297	(1)	3	x	157	264	(1)	(1)	(4)	n.a.	5	x	x	100			
0.6	60.9	34.8	29.6	67	(3)	18	x	190	190	(2)	(1)	(8)	n.a.	6	x	x	100			
0.4	64.4	42.4	26.2	28	(2)	9	x	204	189	(2)	(1)	(7)	n.a.	6	x	x	100			
0.7	67.6	51.4	21.4	708	(1)	(1)	(0)	51	317	1	(0)	(4)	n.a.	x	(0)	(0)	100			
0.9	67.4	51.2	21.3	798	(1)	2	x	x	306	2	(0)	(4)	n.a.	x	x	x	100			
0.5	60.6	33.8	30.2	74	x	x	25	185	199	(1)	(1)	x	n.a.	x	x	x	100			
0.6	63.2	40.7	26.6	125	x	x	2	246	177	(1)	(1)	x	n.a.	(5)	(1)	(1)	100			
0.4	61.3	35.0	29.8	63	(5)	x	x	x	174	(2)	(1)	(9)	n.a.	(4)	(1)	(2)	100			
2.9	80.0	53.4	32.0	2102	(2)	(1)	x	x	24	3	(1)	(4)	n.a.	x	x	x	100			
2.7	80.5	54.0	31.9	1974	(2)	(1)	x	x	23	2	(1)	(5)	n.a.	x	x	x	100			
2.1	82.7	56.2	32.2	2086	(2)	(1)	(1)	(1)	32	3	(1)	(5)	n.a.	(3)	(0)	(1)	100			
2.6	81.7	55.7	31.5	1605	(2)	(1)	(1)	(2)	27	3	(1)	(5)	n.a.	(3)	(0)	3	100			
1.1	88.9	62.9	32.3	2621	x	x	(0)	1	18	1	(0)	x	n.a.	(1)	(0)	(0)	100			
1.0	88.9	62.6	32.6	2629	x	(1)	(1)	1	15	2	(1)	(2)	n.a.	(1)	(0)	(0)	100			
1.1	88.8	62.7	32.4	2749	(0)	x	(0)	(0)	(0)	(0)	(0)	(1)	n.a.	(1)	(0)	(0)	100			

Supplementary Table 7.S4/3: LA-ICP-MS analyses of minerals

Analysis	Sample name	Sample type	Mineral	µg/g wt% B	Na Na$_2$O	Mg MgO	Al Al$_2$O$_3$	Si SiO$_2$	K K$_2$O	Ca CaO	Ti TiO$_2$	V	Cr Cr$_2$O$_3$
Smelter Knolls rhyolite													
15De10e16	SK qtz3 mgt incl 20 um	incl in qtz	magnetite	(10)	(0.0)	0.2	(0.0)	(0.6)	(0.1)	(0.6)	2.7	864	0.0
15De10e06	SK exp ilm matrix6 20um	phenocryst	ilmenite	(17)	(0.0)	0.2	0.4	(0.6)	(0.0)	(0.9)	38.5	297	(0.0)
15De10e05	SK Fsp5 exp ilm incl *	incl in fsp	ilmenite	(27)	x	0.3	0.5	(0.8)	(0.1)	(1.1)	36.1	404	(0.0)
15De10d16	SK Fsp5 exp ilm incl ***	incl in fsp	ilmenite	(12)	0.0	0.4	0.4	(0.9)	(0.1)	(0.8)	34.9	391	(0.0)
15De10e11	SK Fsp7 Kfsp host	phenocryst	K-feldspar	(3)	3.0	0.0	18.7	66.5	11.6	0.2	0.0	(0)	(0.0)
15De10e13	SK Fsp8 Kfsp host	phenocryst	K-feldspar	(2)	2.8	0.0	18.9	66.1	12.0	0.2	0.0	(0)	(0.0)
15De10e15	SK Fsp9 Kfsp host	phenocryst	K-feldspar	(1)	2.6	0.0	19.2	65.8	12.2	0.2	0.0	(0)	(0.0)
15De10e10	SK Fsp7 plag incl	incl in Kfsp	plagioclase	(2)	8.7	(0.0)	21.5	65.2	0.8	3.8	0.0	(0)	(0.0)
15De10e12	SK Fsp8 plag incl	incl in Kfsp	plagioclase	(3)	8.3	0.0	21.8	64.9	0.9	4.1	0.0	(0)	(0.0)
15De10e14	SK Fsp9 plag incl	incl in Kfsp	plagioclase	(1)	8.3	0.0	22.1	64.6	0.9	4.0	0.0	(0)	(0.0)
Amalia Tuff													
16Au05g04	Am grainmt mgt	phenocryst	magnetite	(14)	x	3.1	3.4	(0.4)	(0.0)	(0.7)	11.1	1665	0.0
16Au05g05	Am grainmt mgt	phenocryst	magnetite	(9)	x	0.0	0.1	(0.2)	(0.0)	(0.5)	14.0	216	(0.0)
16Au05g06	Am grainmt mgt	phenocryst	magnetite	(9)	x	0.0	0.1	(0.2)	(0.0)	(0.5)	11.3	194	(0.0)
16Au05g07	Am grainmt mgt	phenocryst	magnetite	(10)	(0.0)	0.5	1.5	(0.3)	(0.0)	(0.5)	7.4	931	0.0
16Au05g08	Am grainmt mgt	phenocryst	magnetite	(9)	x	1.2	1.4	x	(0.0)	(0.5)	6.9	873	(0.0)
16Au05g09	Am grainmt mgt	phenocryst	magnetite	(11)	(0.0)	0.3	0.8	(0.3)	(0.0)	(0.6)	7.1	789	(0.0)
16Au05g11	Am grainmt mgt	phenocryst	magnetite	(11)	x	1.3	1.5	(0.3)	(0.0)	(0.6)	7.3	981	(0.0)
16Au05g12	Am grainmt mgt	phenocryst	magnetite	(8)	x	0.3	0.1	x	x	x	6.6	112	(0.0)
16Au05g13	Am grainmt mgt	phenocryst	magnetite	(8)	x	0.2	0.1	x	x	x	6.0	80	(0.0)
15De10d10	Am Fsp1 exp mgt 20 um r	incl in fsp	magnetite	(23)	x	0.5	0.4	x	(0.1)	(0.9)	5.3	288	(0.0)
15De10d11	Am Fsp2 exp mgt 20 um r	incl in fsp	magnetite	(16)	0.0	0.4	0.4	(0.5)	(0.0)	(0.7)	5.2	827	(0.0)
15De10d12	Am Fsp3 exp mgt 20 um r	incl in fsp	magnetite	(16)	(0.0)	0.2	0.2	(0.9)	(0.1)	(1.0)	4.4	150	(0.0)
15De10d13	Am qtz7 exp mgt 20 um n	incl in qtz	magnetite	(12)	0.0	0.4	0.1	(0.7)	(0.0)	(0.8)	5.3	300	(0.0)
16Au05d04	Am Kfsp C exp mgt incl1	incl in Kfsp	magnetite	(20)	(0.0)	0.5	0.9	(0.8)	(0.1)	(1.1)	7.0	1082	0.0
16Au05d05	Am Kfsp C exp mgt incl2	incl in Kfsp	magnetite	(23)	x	0.4	0.9	(0.9)	(0.1)	(1.2)	7.1	1079	0.0
16Au05g10	Am Körnerpreparat ilm	phenocryst	ilmenite	(13)	x	0.1	1.5	x	(0.0)	(0.7)	27.8	47	(0.0)
16Au05d06	Am Kfsp D exp ilm incl 2	incl in Kfsp	ilmenite	(61)	(0.0)	0.7	1.7	x	x	(4.2)	40.7	294	(0.0)
15De10f07	Am Fsp3 Kfsp 40 um	phenocryst	K-feldspar	(2)	6.1	0.0	16.6	69.3	7.4	0.1	0.0	(0)	(0.0)
15De10f08	Am Fsp4 Kfsp 40 um	phenocryst	K-feldspar	(2)	6.1	0.0	16.0	70.2	7.2	0.1	0.0	(0)	(0.0)
16Au05d07	Am Kfsp D Kfsp host 40 u	phenocryst	K-feldspar	(4)	6.7	0.0	19.0	66.7	6.9	0.3	0.0	(0)	(0.0)
16Au05c13	Am KfspA Kfsp host 40 u	phenocryst	K-feldspar	(4)	6.1	0.0	18.9	66.4	8.1	0.1	0.0	(0)	(0.0)
16Au05c15	Am KfspB Kfsp host 40 u	phenocryst	K-feldspar	(3)	5.9	0.0	19.3	66.1	8.1	0.1	0.0	(0)	(0.0)
15De10f05	Am qtz8 Kfsp 40 um	incl in qtz	K-feldspar	x	5.8	0.0	15.9	68.9	7.5	0.0	0.0	(0)	(0.0)
16Au05c12	Am KfspA Kfsp incl 40 u	incl in Kfsp	K-feldspar	(4)	6.2	0.0	18.6	66.5	8.2	0.1	0.0	(0)	(0.0)
16Au05c14	Am KfspB Kfsp incl 30 u	incl in Kfsp	K-feldspar	(5)	6.2	0.0	18.9	66.5	7.8	0.1	0.0	(1)	(0.0)
15De10f06	Am Fsp2 plag host 40 um	phenocryst	plagioclase	(2)	7.9	0.0	17.6	69.3	4.3	0.7	0.0	(0)	(0.0)
Banco Bonito vitrophyre													
15Se10d12	BB A mgt1	phenocryst	magnetite	(31)	0.0	1.8	2.4	(1.1)	(0.1)	(1.8)	7.0	1977	0.0
15Se10d13	BB A mgt2	phenocryst	magnetite	(35)	0.0	1.4	1.8	(1.3)	(0.1)	(2.1)	5.5	1796	0.2
15Se10d15	BB B mgt3	phenocryst	magnetite	(33)	(0.0)	1.5	1.9	(2.2)	(0.1)	(3.2)	6.1	2244	0.0
15Se10d16	BB B mgt4	phenocryst	magnetite	(41)	(0.0)	1.4	1.8	(2.8)	(0.1)	(3.9)	5.9	1737	0.1
15Se10d17	BB B mgt5	phenocryst	magnetite	(35)	(0.0)	1.2	1.9	(2.4)	(0.1)	(3.4)	5.3	1641	0.1
15Se10d14	BB A ilm1	phenocryst	ilmenite	(62)	0.0	2.4	0.3	(2.3)	(0.2)	(3.7)	36.8	810	0.0
Santa Rita rhyodacite (SR15)													
15De14j09	SR15 exp mgt in matrix 2(	phenocryst	magnetite	(10)	(0.0)	0.5	1.6	(0.5)	(0.0)	(0.5)	5.7	2040	(0.0)
15De14j13	SR15 exp mgt in matrix 2(	phenocryst	magnetite	(8)	x	0.3	1.7	(0.7)	(0.0)	(0.6)	5.5	2035	0.0
15De14i15	SR15 qtz1 mgt incl 30 um	incl in qtz	magnetite	(6)	(0.0)	0.3	(0.0)	(0.4)	x	(0.4)	3.3	1582	0.0
15De14i16	SR15 qtz5 mgt incl 20 um	incl in qtz	magnetite	(13)	x	0.2	0.9	(0.9)	x	(0.9)	2.2	1326	0.0
15De14j05	SR15 qtz5 exp mgt incl 7(	incl in qtz	magnetite	(14)	(0.0)	0.4	0.7	(0.7)	(0.0)	(0.6)	2.6	1753	0.0
15De14j06	SR15 qtz5 exp mgt incl in	incl in qtz	magnetite	(18)	(0.0)	0.3	0.9	(0.9)	(0.1)	(0.8)	2.1	2128	0.0
15De14j14	SR15 qtz6 mgt incl 20 um	incl in qtz	magnetite	(33)	x	0.4	1.1	(1.6)	(0.1)	(1.8)	2.8	1582	0.0
15De14j10	SR15 exp ilm in matrix 20	phenocryst	ilmenite	(5)	x	1.2	0.2	(0.4)	(0.0)	(0.4)	37.0	1103	0.0
15De14j11	SR15 attached ??? Grain a	phenocryst	ilmenite	(5)	x	0.4	0.1	(0.4)	(0.0)	(0.3)	38.6	1141	0.0
15De14j07	SR15 qtz5 exp ilm incl in	incl in qtz	ilmenite	(16)	(0.0)	0.6	0.1	(0.8)	(0.1)	(0.7)	36.4	839	0.0
15De14j08	SR15 qtz5 exp ilm incl in	incl in qtz	ilmenite	(25)	(0.0)	0.6	0.1	(1.2)	(0.1)	(1.1)	36.9	960	0.0
15De14k05	SR15 qtz5 Kfsp incl 30 ur	incl in qtz	K-feldspar	(14)	2.8	0.0	**19.1**	65.7	11.8	0.5	0.0	(1)	(0.0)
15De14k06	SR15 qtz5 Kfsp incl 30 ur	incl in qtz	K-feldspar	(9)	3.0	0.0	**19.1**	65.5	11.7	0.5	(0.0)	(1)	(0.0)
15De14j15	SR15 qtz6 Kfsp incl 20 ur	incl in qtz	K-feldspar	(24)	2.7	(0.0)	**18.9**	66.4	11.9	0.3	0.0	(2)	(0.0)
15De14k07	SR15 qtz3 plag incl 30 ur	incl in qtz	plagioclase	(10)	7.3	0.0	**24.4**	62.0	0.7	5.5	0.0	(1)	(0.0)
Santa Rita rhyodacite (SR9)													
15De16l05	SR9 qtz2 mgt incl 15 um	incl in qtz	magnetite	(30)	(0.0)	0.4	(0.0)	(1.5)	(0.1)	x	2.5	1940	0.0

Mn	Fe			Zn	Rb	Sr	Y	Zr	Nb	Mo	Cs	Ba	Ce	Hf	Th	U	total	Or	Ab	An
MnO	FeO$_{tot}$	Fe$_2$O$_3$[1]	FeO[1]														wt%	mol%	mol%	mol%
1.1	89.3	63.7	32.0	1936	(2)	(1)	(1)	(1)	x	x	(1)	(3)	n.a.	(1)	(0)	x	**100**			
3.8	54.1	26.3	30.4	171	(1)	(1)	(1)	69	2248	3	(0)	0	n.a.	5	(0)	2	**100**			
3.1	56.5	30.8	28.7	645	(2)	x	x	x	2227	3	(1)	(4)	n.a.	x	3	0	**100**			
2.0	58.5	33.3	28.6	667	11	3	(1)	54	2084	3	2	(6)	n.a.	(2)	6	2	**100**			
0.0	0.0	N/A	N/A	(4)	260	301	(0)	(0)	(0)	(0)	0	1256	n.a.	(0)	(0)	(0)	**100**	71	27	2
0.0	0.0	N/A	N/A	(3)	260	242	(0)	(0)	(0)	(0)	0	768	n.a.	(0)	(0)	(0)	**100**	72	26	2
0.0	0.0	N/A	N/A	(1)	257	237	(0)	(0)	0	(0)	0	780	n.a.	(0)	(0)	(0)	**100**	74	24	2
0.0	0.0	N/A	N/A	(4)	2	269	1	(0)	(0)	(0)	(0)	19	n.a.	(0)	(0)	(0)	**100**	4	65	31
0.0	0.0	N/A	N/A	(3)	3	235	1	0	1	(0)	(0)	15	n.a.	(0)	(0)	1	**100**	4	62	34
0.0	0.1	N/A	N/A	2	3	305	1	(0)	0	(0)	(0)	29	n.a.	(0)	(0)	(0)	**100**	4	62	33
0.5	77.0	45.1	36.5	906	(1)	(1)	(0)	30	8	0	(0)	(2)	(0)	x	(0)	(0)	**100**			
6.2	73.8	41.7	36.3	12795	(0)	(0)	(0)	20	1022	11	(0)	(1)	(0)	x	(0)	(0)	**100**			
5.5	77.2	46.9	35.0	8457	(0)	(0)	(0)	27	986	8	(0)	(1)	(0)	x	(0)	(0)	**100**			
2.2	79.4	84.7	3.2	3371	(0)	(0)	(0)	29	46	2	(0)	(1)	(0)	x	(0)	(0)	**100**			
1.2	83.5	54.6	34.3	2204	(0)	x	x	24	17	2	(0)	(1)	x	x	(0)	(0)	**100**			
3.7	87.9	67.9	26.8	5952	(0)	(0)	(0)	13	89	3	(0)	(2)	(0)	(1)	(0)	(0)	**100**			
1.4	82.6	53.7	34.3	2562	(0)	(0)	0	25	18	2	(0)	(2)	x	x	x	(0)	**100**			
1.2	85.9	56.4	35.2	2475	x	x	x	34	52	18	x	x	x	x	x	x	**100**			
1.2	83.2	88.5	3.6	2711	x	x	x	71	101	17	x	x	x	x	x	x	**100**			
3.6	83.7	58.5	31.1	5610	(1)	(1)	x	x	12	2	(0)	(4)	n.a.	(1)	(1)	(1)	**100**			
3.4	84.0	58.5	31.3	5394	(1)	(1)	(1)	6	7	2	(1)	(3)	n.a.	(2)	(0)	(0)	**100**			
4.2	84.3	60.3	30.0	5802	(2)	(1)	(0)	2	12	2	(1)	(5)	n.a.	(4)	(0)	(1)	**100**			
3.6	84.0	58.8	31.1	5910	(2)	(1)	(1)	(1)	4	1	(1)	(3)	n.a.	(2)	(1)	(0)	**100**			
1.9	83.8	54.6	34.7	2547	(2)	(0)	(1)	2	6	3	(1)	(3)	(0)	(1)	(0)	(0)	**100**			
2.0	83.5	54.2	34.8	3094	(2)	(1)	(1)	4	7	2	(1)	(3)	(0)	(2)	(0)	(0)	**100**			
0.9	90.3	67.1	29.8	4465	(0)	x	x	143	373	193	(0)	x	x	x	(0)	(0)	**100**			
4.1	50.3	21.3	31.1	1260	x	(2)	2	433	710	9	(2)	(13)	16	16	(2)	(2)	**100**			
0.0	0.5	N/A	N/A	2	64	10	(0)	(0)	(0)	(0)	(0)	13	n.a.	(0)	(0)	(0)	**100**	44	55	1
0.0	0.5	N/A	N/A	3	63	6	(0)	(0)	(0)	(0)	(0)	17	n.a.	(0)	(0)	(0)	**100**	44	56	1
(0.0)	0.3	N/A	N/A	1	44	67	(0)	(0)	(0)	(0)	(0)	504	n.a.	3	(0)	(0)	**100**	39	58	3
(0.0)	0.4	N/A	N/A	(4)	56	16	(0)	(0)	(0)	(0)	(0)	54	n.a.	0	(0)	(0)	**100**	46	53	1
0.0	0.5	N/A	N/A	(4)	56	12	(0)	(0)	(0)	(0)	(0)	21	n.a.	0	(0)	(0)	**100**	47	52	1
0.0	1.8	N/A	N/A	63	373	1	x	x	x	x	x	7	n.a.	x	x	x	**100**	46	53	0
(0.0)	0.5	N/A	N/A	(4)	60	14	(0)	(0)	(0)	(0)	(0)	19	n.a.	0	(0)	(0)	**100**	47	53	0
(0.0)	0.5	N/A	N/A	(5)	70	13	(0)	(0)	(0)	(0)	(0)	18	n.a.	(0)	(0)	(0)	**100**	45	54	1
0.0	0.2	N/A	N/A	2	25	95	(0)	(0)	(0)	(0)	(0)	833	n.a.	(0)	(0)	(0)	**100**	25	69	7
0.6	82.4	53.3	34.4	0	1	2	0	9	0	n.a.	0	7	n.a.	n.a.	0	0	**100**			
0.8	84.4	56.6	33.5	0	0	0	0	7	0	n.a.	0	0	n.a.	n.a.	0	0	**100**			
0.7	83.8	55.4	33.9	0	0	0	0	7	0	n.a.	0	0	n.a.	n.a.	0	0	**100**			
0.8	84.0	55.8	33.7	0	0	0	0	9	0	n.a.	0	0	n.a.	n.a.	0	0	**100**			
0.6	84.8	56.9	33.6	0	0	0	0	9	0	n.a.	0	0	n.a.	n.a.	0	0	**100**			
0.9	56.1	31.4	27.9	0	0	0	0	166	0	n.a.	0	1	n.a.	n.a.	0	0	**100**			
1.2	84.9	56.1	34.4	1329	(1)	2	x	x	9	(1)	(1)	x	x	(1)	x	x	**100**			
1.2	85.1	56.2	34.5	1861	(1)	x	(1)	x	8	(1)	(1)	(2)	x	(1)	(0)	(0)	**100**			
0.9	88.9	62.5	32.7	983	(1)	(1)	(0)	(1)	2	(1)	(0)	x	(0)	(1)	(0)	(0)	**100**			
0.9	89.2	63.5	32.0	1125	x	x	(1)	(2)	2	(1)	(1)	(4)	x	(3)	(1)	(1)	**100**			
0.9	88.6	63.1	31.9	1014	(2)	(1)	(1)	x	3	(1)	(1)	(4)	(1)	(1)	(0)	(0)	**100**			
0.7	89.1	63.7	31.8	1148	(2)	(1)	(1)	(1)	1	(2)	(1)	(5)	(1)	(1)	(0)	(0)	**100**			
1.0	88.2	62.4	32.1	1100	x	x	(2)	(3)	3	(2)	(1)	(11)	(1)	(3)	(1)	x	**100**			
1.5	56.9	30.4	29.6	318	(1)	(0)	x	349	325	(1)	(0)	(2)	x	8	(0)	(0)	**100**			
1.4	56.6	26.6	32.7	65	(1)	x	x	327	362	(1)	(0)	x	x	11	(0)	(0)	**100**			
1.8	57.8	31.0	29.9	528	(2)	(1)	x	50	259	(1)	(1)	(4)	x	x	(0)	(0)	**100**			
1.6	57.6	30.0	30.5	449	(3)	(2)	x	42	297	(2)	(1)	(7)	x	x	x	(1)	**100**			
0.0	0.1	N/A	N/A	(15)	143	1240	(1)	x	(1)	(1)	(0)	9063	x	(2)	(1)	(1)	100	70	25	5
0.0	0.1	N/A	N/A	33	159	1001	(0)	x	(1)	(1)	3	6600	x	(1)	x	x	100	68	26	5
0.0	0.1	N/A	N/A	(23)	156	1204	(1)	(1)	(2)	(1)	(1)	15776	(1)	(2)	(1)	(1)	100	72	24	3
0.0	0.1	N/A	N/A	(10)	4	2271	(0)	(1)	(0)	(1)	(1)	260	4	(1)	(0)	(0)	100	3	53	44
0.9	89.5	64.1	31.8	754	(3)	x	x	1994	(2)	(2)	(1)	(6)	x	x	x	x	**100**			

Supplementary Table 7.S4/4: LA-ICP-MS analyses of minerals

Analysis	Sample name	Sample type	Mineral	µg/g wt% B	Na Na₂O	Mg MgO	Al Al₂O₃	Si SiO₂	K K₂O	Ca CaO	Ti TiO₂	V	Cr Cr₂O₃
Santa Rita rhyodacite (SR9)													
15De16l06	SR9 qtz2 mgt incl 5 um	incl in qtz	magnetite	(130)	(0.0)	0.5	0.2	(6.4)	(0.4)	(5.3)	3.3	1875	(0.1)
15De16l13	SR9 qtz3 rim exp mgt 20	incl in qtz	magnetite	(9)	0.0	0.0	1.1	(0.5)	(0.0)	(0.5)	2.4	1937	0.0
15De14l05	SR9 qtz1 exp plag 1 20 ur	incl in qtz	plagioclase	(10)	7.6	0.0	**24.7**	61.0	0.5	6.0	0.0	(1)	(0.0)
15De14l06	SR9 qtz1 exp plag 2 20 ur	incl in qtz	plagioclase	(4)	7.5	0.0	**25.2**	59.7	0.5	6.9	0.0	(0)	(0.0)
15De14l07	SR9 qtz1 plag incl 3 20 ur	incl in qtz	plagioclase	(56)	8.0	0.0	**25.3**	58.0	0.8	7.7	0.0	(5)	(0.0)
15De14l08	SR9 qtz1 plag incl 4 30 ur	incl in qtz	plagioclase	(6)	7.4	0.0	**24.8**	60.2	0.9	6.6	0.0	(1)	(0.0)
15De14l09	SR9 qtz1 plag incl 5 30 ur	incl in qtz	plagioclase	(7)	7.5	0.0	**24.7**	60.8	0.7	6.1	0.0	(1)	(0.0)
15De14l10	SR9 qtz1 plag incl 6 20 ur	incl in qtz	plagioclase	(18)	7.2	0.0	**24.7**	60.9	0.9	6.0	0.0	(2)	(0.0)
15De14l11	SR9 qtz1 plag incl 7 30 ur	incl in qtz	plagioclase	(7)	7.9	0.0	**24.1**	61.5	0.9	5.5	0.0	(1)	(0.0)
The Dyke													
15De10j06	Dk matrix mgt1 20 um	phenocryst	magnetite	(24)	(0.0)	0.6	1.1	(0.7)	(0.1)	(0.8)	3.2	1849	0.0
15De10j07	Dk matrix mgt2 20 um	phenocryst	magnetite	(21)	0.0	0.8	1.3	(0.6)	(0.1)	(0.7)	4.3	1937	0.0
15De10j08	Dk matrix mgt3 20 um	phenocryst	magnetite	(25)	0.0	0.8	1.1	(0.7)	(0.1)	(0.8)	3.6	1762	0.0
15De10j10	Dk matrix mgt4 20 um	phenocryst	magnetite	(24)	0.0	0.3	1.1	(0.7)	(0.0)	(0.6)	3.9	1856	0.0
15De10j11	Dk matrix mgt5 20 um	phenocryst	magnetite	(26)	(0.0)	0.9	1.1	(0.8)	(0.1)	(0.7)	3.3	1779	0.0
15De10j12	Dk matrix mgt6 20 um	phenocryst	magnetite	(25)	(0.0)	1.0	1.1	(0.8)	(0.1)	(0.7)	3.4	1756	0.0
15De10h07	Dk qtz5 exp mgt in embay	incl in qtz	magnetite	(20)	(0.0)	0.4	1.1	(0.7)	(0.0)	(0.8)	2.9	1847	0.0
15De10h13	Dk exp mgt incl 20 um	incl in Kfsp	magnetite	(15)	(0.0)	1.1	(0.0)	(1.0)	(0.1)	x	2.6	1010	(0.0)
15De10h14	Dk mgt incl 13 um deep	incl in Kfsp	magnetite	(47)	(0.0)	0.4	(0.0)	(2.1)	(0.2)	(2.4)	3.0	1735	0.0
15De10j05	Dk matrix ilm1 20 um	phenocryst	ilmenite	(24)	(0.0)	1.4	0.1	(0.7)	(0.1)	(0.8)	34.3	1041	0.0
15De10j09	Dk matrix ilm2 20 um	phenocryst	ilmenite	(46)	(0.0)	1.2	0.1	(1.4)	(0.1)	(1.2)	34.1	861	(0.0)
15De10j13	Dk matrix ilm4 20 um	phenocryst	ilmenite	(21)	0.0	1.6	0.1	(0.7)	(0.0)	(0.7)	35.3	998	(0.0)
15De10j14	Dk matrix ilm5 20 um	phenocryst	ilmenite	(18)	0.0	1.4	0.1	(0.6)	(0.0)	(0.6)	34.6	967	(0.0)
15De10j15	Dk matrix ilm6 20 um	phenocryst	ilmenite	(17)	0.0	1.3	0.1	(0.6)	(0.0)	(0.6)	34.6	982	(0.0)
15De10i06	Dk Kfsp host	phenocryst	K-feldspar	(2)	2.4	0.0	20.0	64.9	12.3	0.4	0.0	(0)	(0.0)
15De10i08	Dk Kfsp host	phenocryst	K-feldspar	(2)	2.4	0.0	19.8	65.0	12.4	0.4	0.0	(0)	(0.0)
15De10h16	Dk Kfsp host	phenocryst	K-feldspar	(3)	2.4	0.0	19.8	65.5	11.9	0.4	0.0	(0)	(0.0)
15De10h08	Dk Fsp1 plag 40 um	phenocryst	plagioclase	(3)	7.1	0.0	23.6	62.2	0.6	6.3	0.0	(0)	(0.0)
15De10h09	Dk Fsp2 plag host 30 um	phenocryst	plagioclase	(5)	6.8	0.0	23.4	62.0	0.5	7.1	0.0	(0)	(0.0)
15De10h12	Dk Fsp3 plag 40 um	phenocryst	plagioclase	(2)	7.5	0.0	23.1	62.7	0.7	5.9	0.0	(0)	(0.0)
15De10i05	Dk Kfsp host plag incl	incl in Kfsp	plagioclase	(4)	6.7	0.0	25.2	60.2	0.6	7.0	0.0	(0)	(0.0)
15De10i07	Dk Kfsp host plag incl	incl in Kfsp	plagioclase	(2)	9.0	0.0	22.8	64.0	0.6	3.7	0.0	(0)	(0.0)
15De10h15	Dk Kfsp host plag incl	incl in Kfsp	plagioclase	(3)	7.2	0.0	24.2	61.2	0.7	6.5	0.0	(0)	(0.0)
15De10g08	Dk qtz1 plag incl in qtz 20	incl in qtz	plagioclase	9	6.8	0.0	**25.4**	58.6	1.4	7.3	0.0	(1)	(0.0)
Nomlaki tuff													
15Se10d04	Chalk Mt A mgt1	phenocryst	magnetite	(19)	(0.0)	0.9	1.7	(1.1)	(0.1)	(1.8)	5.9	2595	0.0
15Se10d06	Chalk Mt A mgt2	phenocryst	magnetite	(20)	(0.0)	0.8	1.7	(1.2)	(0.1)	(1.9)	6.1	2691	(0.0)
15Se10d08	Chalk Mt A mgt3	phenocryst	magnetite	(32)	(0.0)	0.5	2.5	(1.2)	(0.1)	(1.9)	6.3	2701	0.0
15Se10d09	Chalk Mt B mgt4	phenocryst	magnetite	(26)	0.0	0.7	2.0	(1.0)	(0.1)	(1.5)	6.4	2725	0.0
15Se10d05	Chalk Mt A ilm1	phenocryst	ilmenite	(19)	0.0	0.9	0.2	(1.1)	(0.1)	(1.8)	38.6	1273	(0.0)
15Se10d07	Chalk Mt A ilm2	phenocryst	ilmenite	(19)	0.0	1.0	0.3	(1.1)	(0.1)	(1.8)	38.9	1270	(0.0)
15Se10d10	Chalk Mt B ilm3	phenocryst	ilmenite	(27)	0.0	0.8	0.3	(1.0)	(0.1)	(1.6)	37.3	1426	(0.0)
15Se10d11	Chalk Mt C ilm4	phenocryst	ilmenite	(21)	0.0	0.8	0.5	(1.2)	(0.1)	(1.6)	36.8	1685	(0.0)
Kos granite enclave													
15Se10e05	KS C mgt	phenocryst	magnetite	(12)	(0.0)	0.2	2.6	(1.1)	(0.1)	(1.6)	3.0	0	(0.0)
15Se10e08	KS B mgt	phenocryst	magnetite	(19)	0.0	0.2	2.5	(1.2)	(0.1)	(1.9)	2.5	0	(0.0)
15Se10e09	KS A large mgt rim	phenocryst	magnetite	(16)	(0.0)	0.2	2.5	(1.2)	(0.1)	(1.5)	2.4	0	(0.0)
15Se10e10	KS A large mgt core	phenocryst	magnetite	(17)	(0.0)	0.2	2.5	(1.2)	(0.1)	(1.5)	2.3	0	(0.0)
15Se10e11	KS A attached smaller mg	phenocryst	magnetite	(16)	(0.0)	0.2	2.4	(1.1)	(0.1)	(1.5)	2.3	0	(0.0)
15Se10e12	KS A attached smaller mg	phenocryst	magnetite	(15)	(0.0)	0.2	2.4	(1.1)	(0.1)	(1.4)	2.4	0	(0.0)
15Se10e04	KS C ilm	phenocryst	ilmenite	(15)	(0.0)	0.6	0.1	(1.4)	(0.1)	(2.0)	44.9	0	(0.0)
15Se10e06	KS B ilm	phenocryst	ilmenite	(17)	(0.0)	0.6	0.1	(1.0)	(0.1)	(1.6)	46.1	0	(0.0)
15Se10e07	KS B ilm	phenocryst	ilmenite	(18)	0.0	0.6	0.1	(1.2)	(0.1)	(1.8)	44.1	0	(0.0)
16Au05e05	KS grain B Kfsp 40 um	phenocryst	K-feldspar	(4)	3.8	0.0	19.2	65.3	11.5	0.2	0.0	(0)	(0.0)
16Au05e07	KS grain B kfsp 40 um	phenocryst	K-feldspar	(5)	3.6	0.0	19.2	65.6	11.5	0.0	0.0	(0)	(0.0)
16Au05e12	KS grain D Kfsp 40 um	phenocryst	K-feldspar	(3)	3.7	0.0	19.1	66.0	11.1	0.2	0.0	(0)	(0.0)
16Au05e13	KS grain E Kfsp 40 um	phenocryst	K-feldspar	(6)	3.8	0.0	19.4	65.2	11.4	0.2	0.0	(0)	(0.0)
16Au05e15	KS grain E Kfsp 40 um	phenocryst	K-feldspar	(6)	3.8	0.0	19.2	65.2	11.5	0.1	0.0	(0)	(0.0)
16Au05e04	KS grain A plag 2 40 um	phenocryst	plagioclase	(3)	9.1	0.0	22.4	64.1	0.6	3.8	0.0	(0)	(0.0)
16Au05e08	KS grain C plag 40 um	phenocryst	plagioclase	(4)	8.6	0.0	23.0	63.3	0.6	4.4	0.0	(0)	(0.0)
16Au05e09	KS grain C plag 40 um	phenocryst	plagioclase	(4)	9.2	0.0	22.1	64.4	0.7	3.5	0.0	(0)	(0.0)
16Au05e10	KS grain D plag 40 um	phenocryst	plagioclase	(5)	9.1	0.0	21.8	64.8	0.7	3.4	0.0	(0)	(0.0)

Mn	Fe			Zn	Rb	Sr	Y	Zr	Nb	Mo	Cs	Ba	Ce	Hf	Th	U	total	Or	Ab	An
MnO	FeO$_{tot}$	Fe$_2$O$_3$[1]	FeO[1]														wt%	mol%	mol%	mol%
0.8	88.6	62.3	32.5	818	(14)	(13)	x	4112	(8)	(7)	(6)	(26)	(5)	x	x	x	100			
1.0	88.8	62.8	32.3	895	(1)	(0)	(1)	1	2	1	(0)	(3)	(0)	(1)	(0)	(0)	100			
0.0	0.2	N/A	N/A	(17)	1	3148	(0)	(1)	(1)	(1)	(0)	777	6	(2)	(1)	(0)	100			
0.0	0.2	N/A	N/A	(7)	1	3295	(0)	(0)	(0)	(0)	(0)	442	10	(1)	(0)	(0)	100			
0.0	0.2	N/A	N/A	(99)	4	3050	(2)	(7)	(4)	(4)	(2)	520	9	(11)	(3)	(3)	100			
0.0	0.2	N/A	N/A	(11)	9	2963	(0)	(1)	(1)	(0)	(0)	895	9	(1)	x	(0)	100			
0.0	0.2	N/A	N/A	(6)	7	2299	x	x	(1)	(0)	(0)	402	8	(1)	x	x	100			
0.0	0.2	N/A	N/A	(15)	12	2228	(1)	x	(2)	(1)	(1)	316	6	(2)	x	x	100			
0.0	0.2	N/A	N/A	(6)	7	2430	(0)	x	(1)	(0)	(0)	416	6	(1)	x	x	100			
1.1	87.4	61.5	32.0	1295	(1)	x	x	x	9	2	(1)	(4)	n.a.	(2)	1	(0)	100			
1.5	85.7	59.4	32.3	1566	(1)	x	x	x	29	2	(1)	(4)	n.a.	(2)	4	(0)	100			
1.4	86.5	60.9	31.8	1351	(1)	x	x	x	30	2	(1)	7	n.a.	(2)	2	(0)	100			
1.3	86.8	59.9	32.9	1699	(1)	x	x	x	26	4	(0)	x	n.a.	(2)	x	x	100			
1.3	86.8	61.5	31.5	1237	(1)	(1)	(0)	x	18	1	(1)	(3)	n.a.	(2)	(1)	(1)	100			
1.4	86.5	61.3	31.3	1350	(1)	(0)	(0)	x	26	1	(0)	(3)	n.a.	(2)	(1)	(1)	100			
1.0	88.0	62.1	32.1	1273	(2)	(1)	(1)	3	4	(1)	(0)	(3)	n.a.	(2)	(1)	(0)	100			
0.8	88.8	64.3	30.9	1199	(2)	(1)	11	(1)	(2)	2	(0)	(4)	n.a.	(3)	(1)	(1)	100			
0.8	89.1	63.1	32.3	1337	(4)	(2)	(1)	(3)	5	3	x	(13)	n.a.	(5)	(2)	(2)	100			
2.0	58.3	35.6	26.2	365	(1)	(1)	(1)	205	572	4	(1)	(4)	n.a.	6	(1)	(0)	100			
2.9	57.9	36.0	25.5	281	(2)	x	x	306	600	4	(1)	(5)	n.a.	10	(1)	(1)	100			
1.9	57.4	33.9	26.9	321	(2)	(1)	x	169	683	5	(0)	(4)	n.a.	5	(0)	(1)	100			
2.4	57.6	35.0	26.1	322	(1)	x	x	183	581	3	(0)	(4)	n.a.	4	(0)	(0)	100			
2.1	58.2	34.9	26.7	352	(1)	(0)	x	163	627	4	(0)	(3)	n.a.	1	(0)	(0)	100			
0.0	0.1	N/A	N/A	(3)	165	2063	(0)	(0)	(0)	(0)	0	11777	n.a.	(0)	(0)	(0)	100	74	22	4
0.0	0.1	N/A	N/A	(3)	178	1708	(0)	(0)	(0)	(0)	0	10239	n.a.	(0)	(0)	(0)	100	74	22	4
0.0	0.1	N/A	N/A	(3)	159	1925	(0)	(0)	(0)	(0)	0	11777	n.a.	(0)	(0)	(0)	100	73	22	4
0.0	0.2	N/A	N/A	5	1	1753	(0)	(0)	(0)	(0)	(0)	297	n.a.	(0)	(0)	(0)	100	3	49	48
0.0	0.2	N/A	N/A	10	1	1716	(0)	(0)	(0)	(0)	(0)	312	n.a.	(0)	(0)	(0)	100	2	45	52
0.0	0.2	N/A	N/A	7	1	1673	(0)	(0)	(0)	(0)	(0)	211	n.a.	(0)	(0)	(0)	100	3	52	45
0.0	0.2	N/A	N/A	9	1	1813	(0)	(0)	(0)	(0)	(0)	152	n.a.	(1)	(0)	(0)	100	3	45	52
0.0	0.1	N/A	N/A	5	5	1730	(0)	(0)	(0)	(0)	0	124	n.a.	(0)	(0)	(0)	100	3	67	30
0.0	0.2	N/A	N/A	6	2	1663	0	0	(0)	(0)	(0)	181	n.a.	(0)	(0)	(0)	100	3	49	48
0.0	0.3	N/A	N/A	12	33	1505	1	5	3	(1)	1	159	n.a.	(1)	1	1	100	6	43	51
0.5	84.8	55.7	34.7	0	0	0	0	13	0	n.a.	0	0	n.a.	n.a.	0	0	100			
0.5	84.9	55.3	35.1	0	0	0	0	13	0	n.a.	0	0	n.a.	n.a.	0	0	100			
0.5	84.3	53.7	36.0	0	0	0	0	11	0	n.a.	0	1	n.a.	n.a.	0	0	100			
0.5	84.3	54.2	35.6	0	0	1	0	14	0	n.a.	0	1	n.a.	n.a.	0	0	100			
0.6	56.7	26.8	32.5	0	0	3	7	232	0	n.a.	0	0	n.a.	n.a.	0	2	100			
0.6	56.4	26.4	32.6	0	0	2	3	242	0	n.a.	0	0	n.a.	n.a.	0	1	100			
0.7	57.7	29.2	31.5	0	0	0	0	289	0	n.a.	0	1	n.a.	n.a.	0	1	100			
0.6	58.0	30.0	31.0	0	1	2	0	291	0	n.a.	0	5	n.a.	n.a.	0	0	100			
2.3	85.6	60.1	31.5	0	0	0	0	1	0	n.a.	0	0	n.a.	n.a.	0	0	100			
2.1	86.3	61.1	31.3	0	0	0	0	1	0	n.a.	0	1	n.a.	n.a.	0	0	100			
2.0	86.6	61.4	31.3	0	0	0	0	0	0	n.a.	0	0	n.a.	n.a.	0	0	100			
2.0	86.6	61.5	31.3	0	0	0	0	0	0	n.a.	0	0	n.a.	n.a.	0	0	100			
1.9	86.7	61.6	31.3	0	0	0	0	0	0	n.a.	0	0	n.a.	n.a.	0	0	100			
2.0	86.6	61.4	31.3	0	0	0	0	0	0	n.a.	0	0	n.a.	n.a.	0	0	100			
6.5	44.9	13.6	32.7	0	0	0	0	31	2	n.a.	0	0	n.a.	n.a.	0	1	100			
6.3	44.3	11.5	34.0	0	0	0	0	38	1	n.a.	0	2	n.a.	n.a.	0	1	100			
6.4	45.7	15.1	32.1	0	0	0	0	62	2	n.a.	0	0	n.a.	n.a.	0	0	100			
0.0	0.0	N/A	N/A	(4)	270	57	(0)	(0)	(0)	(0)	2	558	1	(0)	(0)	(0)	100	65	33	2
0.0	0.0	N/A	N/A	(4)	279	56	(0)	(0)	(0)	(0)	4	967	2	(0)	(0)	(0)	100	67	32	0
0.0	0.0	N/A	N/A	(4)	254	58	(0)	(0)	(0)	(0)	6	479	2	(0)	(0)	(0)	100	65	33	2
0.0	0.0	N/A	N/A	(4)	260	60	(0)	(0)	(0)	(0)	2	189	2	(0)	(0)	(0)	100	65	33	1
0.0	0.0	N/A	N/A	(4)	256	62	(0)	(0)	(0)	(0)	1	413	2	(0)	(0)	(0)	100	66	33	1
0.0	0.0	N/A	N/A	(5)	2	578	0	(0)	(0)	(0)	(0)	787	10	(0)	(0)	(0)	100	3	66	30
0.0	0.1	N/A	N/A	(3)	1	670	(0)	(0)	(0)	(0)	(0)	760	11	(0)	(0)	(0)	100	3	62	35
0.0	0.1	N/A	N/A	(4)	2	493	(0)	(0)	(0)	(0)	(0)	734	8	(0)	(0)	(0)	100	3	68	28
0.0	0.1	N/A	N/A	(4)	2	494	(0)	(0)	(0)	(0)	(0)	804	9	(0)	(0)	(0)	100	4	68	28

Supplementary Table 7.S4/5: LA-ICP-MS analyses of minerals

Analysis	Sample name	Sample type	Mineral	µg/g wt%	B	Na Na₂O	Mg MgO	Al Al₂O₃	Si SiO₂	K K₂O	Ca CaO	Ti TiO₂	V	Cr Cr₂O₃
Kos granite enclave														
16Au05e11	KS grain D plag 40 um	phenocryst	plagioclase		(5)	9.4	0.0	22.1	64.4	0.7	3.3	0.0	(0)	(0.0)
16Au05e14	KS grain E plag 40 um	phenocryst	plagioclase		(6)	10.0	(0.0)	20.5	67.0	1.0	1.5	0.0	(0)	(0.0)
16Au05e06	KS grain B plag in qtz 30	incl in qtz	plagioclase		(7)	10.2	(0.0)	20.8	66.0	0.8	2.2	0.0	(1)	(0.0)
Los Humeros vitrophyre														
15Se11i04	117450-58 large mgt	phenocryst	magnetite		(15)	0.0	1.2	1.6	(0.9)	(0.1)	(1.4)	16.4	0	(0.0)
15Se11i06	117450-58 small mgt	phenocryst	magnetite		(39)	0.0	1.3	1.5	(2.3)	(0.2)	(3.5)	14.4	0	(0.0)
15Se11i07	117450-58 small ilm	phenocryst	ilmenite		(39)	(0.0)	2.0	0.1	(2.2)	(0.2)	(3.5)	49.1	0	(0.0)
15Se11i05	117450-58 ilm	phenocryst	ilmenite		(35)	0.0	2.2	0.2	(2.0)	(0.2)	(3.2)	48.5	0	(0.0)
Glass Creek Dome vitrophyre														
15Se10j04	Inyo1 A mgt	phenocryst	magnetite		(30)	(0.0)	2.5	3.5	(1.0)	(0.1)	(1.4)	12.9	1121	(0.0)
15Se10j05	Inyo1 A mgt	phenocryst	magnetite		(33)	(0.0)	2.2	3.5	(1.1)	(0.1)	(1.5)	12.5	1110	(0.0)
15Se10j06	Inyo1 B ilm	phenocryst	ilmenite		(32)	0.0	0.9	0.1	(1.1)	(0.1)	(1.5)	44.6	481	(0.0)
Glass Creek Flow vitrophyre														
15Se10i10	Inyo-4 A mgt	phenocryst	magnetite		(30)	(0.0)	1.4	2.3	(0.9)	(0.1)	(1.7)	13.1	0	0.0
15Se10i12	Inyo-4 A mgt	phenocryst	magnetite		(31)	(0.0)	1.6	3.0	(0.9)	(0.1)	(1.8)	15.1	0	(0.0)
15Se10i14	Inyo-4 A mgt	phenocryst	magnetite		(33)	0.0	1.8	3.1	(1.0)	(0.1)	(1.9)	13.9	0	(0.0)
15Se10i16	Inyo-4 A mgt	phenocryst	magnetite		(33)	(0.0)	1.6	2.6	(1.0)	(0.1)	(1.9)	14.1	0	(0.0)
15Se10i17	Inyo-4 A mgt	phenocryst	magnetite		(32)	(0.0)	1.4	2.6	(1.0)	(0.1)	(1.8)	14.6	0	(0.0)
15Se10i11	Inyo-4 A ilm	phenocryst	ilmenite		(30)	(0.0)	2.6	0.3	(0.9)	(0.1)	(1.7)	47.2	0	(0.0)
15Se10i13	Inyo-4 A ilm	phenocryst	ilmenite		(29)	(0.0)	2.7	0.3	(0.9)	(0.1)	(1.7)	45.6	0	(0.0)
15Se10i15	Inyo-4 A ilm	phenocryst	ilmenite		(32)	(0.0)	2.7	0.3	(1.0)	(0.1)	(1.8)	46.6	0	(0.0)
16Au05f05	Inyo-4 grain D Kfsp 40 un	phenocryst	K-feldspar		(5)	3.8	0.0	19.3	65.3	11.3	0.3	0.0	(0)	(0.0)
16Au05f07	Inyo-4 grain F Kfsp 40 un	phenocryst	K-feldspar		(6)	4.0	0.0	20.1	64.8	10.4	0.6	0.0	(0)	(0.0)
16Au05e16	Inyo-4 grain A plag 40 um	phenocryst	plagioclase		(5)	6.1	0.0	26.1	58.6	0.6	8.3	0.0	(0)	(0.0)
16Au05e17	Inyo-4 grain A plag 40 um	phenocryst	plagioclase		(5)	6.0	0.0	26.2	58.2	0.6	8.7	0.0	(0)	(0.0)
16Au05f04	Inyo-4 grain D plag 40 um	phenocryst	plagioclase		(5)	6.5	0.0	25.4	59.3	0.8	7.7	0.0	(0)	(0.0)
16Au05f06	Inyo-4 grain E plag 40 um	phenocryst	plagioclase		(6)	8.3	0.0	22.4	63.8	1.5	3.9	0.0	(0)	(0.0)
Mono #12 vitrophyre														
15Se10j09	Mono2 A mgt	phenocryst	magnetite		(21)	0.0	1.0	2.0	(0.9)	(0.1)	(1.7)	12.1	1	0.1
15Se10j11	Mono2 B mgt	phenocryst	magnetite		(32)	(0.0)	1.0	1.9	(1.3)	(0.1)	(1.7)	11.9	1	0.1
15Se10j13	Mono2 C mgt	phenocryst	magnetite		(11)	(0.0)	1.2	2.2	(1.0)	(0.1)	(1.7)	13.3	1	0.1
15Se10j14	Mono2 C mgt	phenocryst	magnetite		(12)	(0.0)	1.2	2.4	(1.1)	(0.1)	(1.8)	13.0	1	0.1
15Se10j15	Mono2 C mgt	phenocryst	magnetite		(14)	(0.0)	1.5	3.1	(1.2)	(0.1)	(2.0)	13.1	1	0.1
15Se10j16	Mono2 C mgt	phenocryst	magnetite		(13)	(0.0)	1.0	1.8	(1.2)	(0.1)	(1.9)	12.4	1	0.1
15Se10j17	Mono2 C mgt	phenocryst	magnetite		(13)	0.0	1.1	2.5	(1.1)	(0.1)	(1.8)	12.5	1	0.1
15Se10j07	Mono2 A ilm*	phenocryst	ilmenite		(25)	x	1.9	0.9	x	x	(2.0)	47.2	0	(0.0)
15Se10j08	Mono2 A ilm*	phenocryst	ilmenite		(27)	0.0	4.9	0.5	(1.2)	(0.1)	(2.2)	45.5	0	0.0
15Se10j10	Mono2 B ilm	phenocryst	ilmenite		(27)	(0.0)	1.7	0.2	(1.1)	(0.1)	(1.4)	45.6	0	0.0
15Se10j12	Mono2 B ilm	phenocryst	ilmenite		(27)	0.0	1.8	0.2	(1.1)	(0.1)	(1.4)	46.6	0	0.0
Tunnel Spring Tuff														
15De16i07	Cryst2 grainmt mgt2 20 u	phenocryst	magnetite		(25)	(0.0)	0.2	2.1	(1.5)	(0.1)	(1.5)	3.0	594	(0.0)
15De16i08	Cryst2 grainmt mgt3 20 u	phenocryst	magnetite		(22)	(0.0)	0.2	2.2	(1.0)	(0.1)	(1.1)	2.8	840	(0.0)
15De16i09	Cryst2 grainmt mgt4 20 u	phenocryst	magnetite		(18)	(0.0)	0.2	2.2	(1.0)	(0.1)	(1.2)	2.8	835	(0.0)
15De16i10	Cryst2 grainmt mgt5 20 u	phenocryst	magnetite		(45)	(0.0)	0.2	2.1	(1.1)	(0.1)	(1.4)	2.7	777	0.0
15De16i11	Cryst2 grainmt mgt6 20 u	phenocryst	magnetite		(26)	(0.0)	0.2	2.1	(1.2)	(0.1)	(1.1)	2.7	855	(0.0)
15De16i12	Cryst2 grainmt mgt7 20 u	phenocryst	magnetite		(19)	(0.0)	0.2	2.1	(1.3)	(0.1)	(1.1)	2.7	782	0.0
15De16i13	Cryst2 grainmt mgt8 20 u	phenocryst	magnetite		(29)	(0.0)	0.2	2.1	(1.5)	(0.1)	(2.0)	2.8	766	0.0
15De16j07	Cryst2 grainmt mgt2 20 u	phenocryst	magnetite		(12)	(0.0)	1.3	1.5	(0.8)	(0.1)	(0.8)	7.2	1019	(0.0)
15De16i16	Cryst2 grainmt mgt9 20 u	incl in Kfsp	magnetite		(12)	(0.0)	0.2	2.7	(0.8)	(0.0)	(0.8)	2.9	343	0.0
16Au05d14	Cryst2 Kfsp B exp mgt inc	incl in Kfsp	magnetite		(44)	x	0.2	4.4	x	x	(1.5)	3.2	190	(0.0)
16Au05d13	Cryst2 plag A exp mgt inc	incl in plag	magnetite		(28)	(0.0)	0.3	1.8	(0.8)	(0.1)	(1.2)	3.8	1627	0.0
15De14h06	Cryst2 fsp1 exp mgt 14 un	incl in fsp	magnetite		(23)	(0.0)	0.2	2.5	(1.1)	(0.1)	(1.2)	3.1	260	(0.0)
15De14h08	Cryst2 fsp1 unexp. Mgt ne	incl in fsp	magnetite		(23)	(0.0)	0.2	2.5	(1.1)	(0.1)	(1.2)	3.1	261	(0.0)
15De16i05	Cryst2 grainmt ilm 120 u	phenocryst	ilmenite		(9)	(0.0)	0.2	0.3	(0.5)	(0.0)	(0.5)	25.8	661	(0.0)
15De16i06	Cryst2 grainmt ilm reactio	phenocryst	ilmenite		(26)	(0.0)	0.4	0.2	(1.0)	(0.1)	(0.9)	34.0	431	(0.0)
15De16i14	Cryst2 grainmt ilm2 20 u	phenocryst	ilmenite		(16)	(0.0)	0.4	0.2	(0.9)	(0.1)	(1.1)	32.8	465	(0.0)
15De16j05	Cryst2 grainmt ilm3 20 un	phenocryst	ilmenite		(19)	(0.0)	0.4	0.2	(0.5)	(0.0)	(0.5)	35.4	192	(0.0)
15De16j08	Cryst2 opq grainmt alterie	phenocryst	ilmenite		(9)	x	0.0	0.9	(0.5)	(0.0)	(0.5)	24.3	37	(0.0)
15De14h05	Cryst2 qtz1 exp ilm 20 un	incl in qtz	ilmenite		(15)	x	0.3	0.9	x	x	(0.6)	43.8	78	(0.0)
16Au05d12	Cryst2 plag A exp ilm incl	incl in plag	ilmenite		(25)	(0.0)	0.2	0.4	(0.7)	(0.1)	(1.0)	25.5	973	0.0
15De16j10	Cryst2 grainmt Kfsp2 hos	phenocryst	K-feldspar		(3)	2.4	0.0	18.6	66.1	12.6	0.2	0.0	(0)	(0.0)
15De16j12	Cryst2 grainmt Kfsp3 hos	phenocryst	K-feldspar		(4)	2.3	0.0	19.5	65.3	12.6	0.2	0.0	(0)	(0.0)

Mn	Fe			Zn	Rb	Sr	Y	Zr	Nb	Mo	Cs	Ba	Ce	Hf	Th	U	total	Or	Ab	An
MnO	FeO$_{tot}$	Fe$_2$O$_3$[1]	FeO[1]														wt%	mol%	mol%	mol%
0.0	0.0	N/A	N/A	(4)	2	544	(0)	(0)	(0)	(0)	(0)	1084	8	(0)	(0)	(0)	100	4	70	27
0.0	0.0	N/A	N/A	(4)	5	40	0	(0)	(0)	(0)	(0)	23	9	(0)	(0)	(0)	100	5	81	13
0.0	0.0	N/A	N/A	(6)	3	51	1	(0)	(0)	(0)	(0)	31	7	(1)	(0)	(0)	100	4	78	18
0.6	76.3	35.9	44.0	0	0	0	0	80	0	n.a.	0	1	n.a.	n.a.	0	0	100			
0.6	77.6	39.7	41.9	0	0	2	14	58	0	n.a.	0	4	n.a.	n.a.	1	0	100			
0.8	47.0	8.2	39.6	0	1	2	6	421	0	n.a.	0	0	n.a.	n.a.	0	0	100			
0.8	47.2	9.2	38.9	0	2	4	28	452	0	n.a.	0	5	n.a.	n.a.	1	1	100			
0.5	76.2	41.1	39.2	974	0	0	0	61	13	n.a.	0	0	n.a.	n.a.	0	0	100			
0.5	76.8	41.8	39.2	1208	0	1	0	68	13	n.a.	0	0	n.a.	n.a.	0	0	100			
1.3	51.2	15.6	37.2	473	0	7	17	87	1209	n.a.	0	3	n.a.	n.a.	1	0	100			
0.6	78.1	41.5	40.7	0	0	0	0	86	0	n.a.	0	0	n.a.	n.a.	0	0	100			
0.6	75.5	36.9	42.3	0	0	0	0	98	0	n.a.	0	0	n.a.	n.a.	0	0	100			
0.5	76.3	39.1	41.1	0	0	0	0	93	0	n.a.	0	0	n.a.	n.a.	0	0	100			
0.6	76.7	39.2	41.5	0	0	0	0	108	0	n.a.	0	0	n.a.	n.a.	0	0	100			
0.6	76.6	38.3	42.2	0	0	1	3	116	0	n.a.	0	0	n.a.	n.a.	0	0	100			
0.8	47.8	12.0	37.1	0	0	0	2	715	0	n.a.	0	0	n.a.	n.a.	0	0	100			
0.6	49.2	15.1	35.6	0	0	0	3	670	0	n.a.	0	1	n.a.	n.a.	0	0	100			
0.7	48.0	13.0	36.3	0	0	0	2	751	0	n.a.	0	1	n.a.	n.a.	0	0	100			
0.0	0.1	N/A	N/A	(4)	116	255	(0)	(0)	(0)	(0)	(0)	1639	1	(0)	(0)	(0)	100	65	33	3
0.0	0.1	N/A	N/A	(4)	91	754	0	(0)	(0)	(0)	(0)	12089	5	(0)	(0)	(0)	100	60	35	5
0.0	0.3	N/A	N/A	6	1	1596	0	(0)	(0)	(0)	(0)	758	11	(0)	(0)	0	100	3	39	59
0.0	0.3	N/A	N/A	4	1	1503	0	(0)	(0)	(0)	(0)	706	10	(0)	(0)	(0)	100	3	37	60
0.0	0.3	N/A	N/A	8	1	1523	0	x	(0)	x	(0)	937	13	(0)	(0)	(0)	100	4	42	55
0.0	0.2	N/A	N/A	6	2	491	(0)	(0)	(0)	(0)	(0)	381	18	(0)	(0)	(0)	100	7	61	31
0.6	79.0	43.1	40.2	0	0	1	0	26	0	n.a.	0	5	n.a.	n.a.	0	0	100			
0.5	79.4	43.5	40.3	0	1	0	0	28	0	n.a.	0	1	n.a.	n.a.	0	0	100			
0.6	77.8	40.6	41.2	0	0	0	0	32	0	n.a.	0	0	n.a.	n.a.	0	0	100			
0.6	77.7	40.9	40.9	0	0	0	0	28	0	n.a.	0	0	n.a.	n.a.	0	0	100			
0.6	76.8	40.1	40.7	0	0	0	0	21	0	n.a.	0	0	n.a.	n.a.	0	0	100			
0.6	79.0	42.7	40.6	0	0	0	0	34	0	n.a.	0	0	n.a.	n.a.	0	0	100			
0.6	78.3	41.6	40.8	0	0	0	0	25	0	n.a.	0	1	n.a.	n.a.	0	0	100			
0.8	47.8	10.6	38.3	0	11	4	12	384	0	n.a.	1	8	n.a.	n.a.	2	1	100			
0.4	46.8	16.7	31.7	0	0	0	0	242	0	n.a.	0	6	n.a.	n.a.	0	0	100			
0.6	50.1	14.3	37.3	0	0	0	4	438	0	n.a.	0	0	n.a.	n.a.	0	1	100			
0.8	49.1	12.4	38.0	0	1	2	6	330	0	n.a.	0	1	n.a.	n.a.	0	0	100			
1.1	87.1	60.7	32.5	2020	(3)	(1)	(1)	(3)	22	(1)	(1)	(7)	(1)	(4)	(1)	(2)	100			
1.2	87.1	61.0	32.2	2417	(2)	(2)	(1)	(2)	11	(1)	(1)	(6)	(1)	(3)	(1)	(1)	100			
1.2	87.1	61.0	32.2	2459	(2)	(1)	(1)	(2)	10	(1)	(1)	(7)	(1)	(2)	(1)	(1)	100			
1.1	87.4	61.3	32.2	2087	(3)	(1)	(1)	(2)	9	(2)	(1)	(6)	(1)	(4)	(1)	(1)	100			
1.1	87.3	61.2	32.2	2083	(2)	(2)	(1)	(2)	9	(1)	(1)	(7)	(1)	(2)	(1)	(1)	100			
1.1	87.3	61.3	32.2	2065	(3)	(1)	(1)	(2)	10	(2)	(1)	(7)	(1)	(2)	(1)	(1)	100			
1.1	87.3	61.1	32.3	2091	(2)	(1)	(2)	(2)	10	(2)	(1)	(10)	(1)	(4)	(1)	(1)	100			
1.2	83.0	53.9	34.4	2177	(2)	(1)	(1)	23	18	(2)	(0)	(5)	(1)	(2)	(1)	(1)	100			
1.1	86.7	60.2	32.5	2433	(2)	(1)	x	x	18	1	(1)	(3)	(0)	x	(1)	3	100			
1.0	85.0	57.6	33.1	2577	x	x	(1)	(2)	19	(2)	(1)	x	x	(2)	(1)	(1)	100			
0.7	87.0	59.3	33.7	1408	(2)	(1)	x	(2)	3	1	(0)	(3)	x	(2)	(1)	(0)	100			
1.0	86.8	60.0	32.8	2999	(2)	(1)	(1)	(2)	12	2	(1)	(5)	(1)	(3)	(1)	(1)	100			
1.0	86.8	60.0	32.8	2980	(2)	(1)	(1)	(2)	12	2	(1)	(5)	(1)	(3)	(1)	(1)	100			
0.6	67.7	50.6	22.2	346	(1)	(1)	(1)	55	943	3	(0)	(2)	(0)	4	(1)	(1)	100			
1.6	59.9	35.2	28.1	599	(2)	(1)	(1)	54	1760	3	(1)	(4)	(1)	4	(1)	(1)	100			
1.4	61.0	37.4	27.3	587	(1)	(1)	(1)	49	1828	2	(1)	(6)	(1)	5	(1)	(1)	100			
1.6	58.7	32.7	29.3	532	(2)	(2)	(2)	76	1757	3	(2)	(4)	(2)	(3)	(2)	x	100			
0.9	68.0	52.8	20.5	3260	(2)	x	x	217	414	148	(0)	(3)	x	6	1	(0)	100			
2.3	50.6	15.8	36.5	890	x	x	x	77	3237	2	(1)	x	x	x	x	x	100			
0.6	67.9	51.1	21.9	402	(1)	(1)	x	69	297	4	(0)	(3)	x	3	(0)	1	100			
0.0	0.0	N/A	N/A	(3)	252	249	(0)	(0)	(0)	(0)	0	755	1	(0)	(0)	(0)	100	76	22	2
0.0	0.0	N/A	N/A	1	216	799	(0)	(0)	(0)	(0)	0	7650	1	(0)	(0)	(0)	100	76	21	2

Supplementary Table 7.S4/6: LA-ICP-MS analyses of minerals

Analysis	Sample name	Sample type	Mineral	µg/g wt%	B	Na	Mg	Al	Si	K	Ca	Ti	V	Cr
						Na$_2$O	MgO	Al$_2$O$_3$	SiO$_2$	K$_2$O	CaO	TiO$_2$		Cr$_2$O$_3$
Tunnel Spring Tuff														
15De16j14	Cryst2 grainmt Kfsp4 host	phenocryst	K-feldspar		(3)	2.4	0.0	19.3	65.9	12.2	0.2	0.0	(0)	(0.0)
15De16j16	Cryst2 grainmt Kfsp5 host	phenocryst	K-feldspar		(4)	2.4	0.0	18.8	65.9	12.6	0.2	0.0	(0)	(0.0)
16Au05d15	Cryst2 Kfsp B host 40 um	phenocryst	K-feldspar		(16)	2.5	0.0	19.1	65.6	12.5	0.3	0.0	(1)	(0.0)
15De14h07	Cryst2 fsp1 kfsp host 30 u	phenocryst	K-feldspar		(5)	2.4	0.0	18.7	65.8	12.9	0.2	0.0	(0)	(0.0)
16Au05d16	Cryst2 plag A host	phenocryst	plagioclase		(16)	6.4	0.0	26.2	58.6	0.4	8.2	0.0	(1)	(0.0)
15De16j09	Cryst2 grainmt plag incl	incl in Kfsp	plagioclase		(3)	8.6	0.0	21.9	64.5	0.8	4.2	0.0	(0)	(0.0)
15De16j11	Cryst2 grainmt plag incl	incl in Kfsp	plagioclase		(6)	7.2	0.0	25.2	59.8	0.5	7.1	0.0	(0)	(0.0)
15De16j13	Cryst2 grainmt plag incl	incl in Kfsp	plagioclase		(4)	8.4	0.0	22.2	64.3	0.7	4.3	0.0	(0)	(0.0)
15De16j15	Cryst2 grainmt plag incl	incl in Kfsp	plagioclase		(4)	8.2	0.0	22.2	64.1	0.7	4.7	0.0	(0)	(0.0)
Blackfoot Lava Field														
MP 114	mgt microprobe 1	phenocryst	Magnetite	n.a.	n.a.	n.a.	0.1	0.8	0.1	n.a.	n.a.	9.4	0	n.a.
MP 115	mgt microprobe 2	phenocryst	Magnetite	n.a.	n.a.	n.a.	0.1	0.8	0.1	n.a.	n.a.	9.7	0	n.a.
MP 111	ilm microprobe 1	phenocryst	Ilmenite	n.a.	n.a.	n.a.	0.4	0.1	0.5	n.a.	n.a.	46.3	0	n.a.
MP 112	ilm microprobe 2	phenocryst	Ilmenite	n.a.	n.a.	n.a.	0.4	0.0	0.1	n.a.	n.a.	46.4	0	n.a.
16Au05f08	Bf grain A Kfsp1 40 um	phenocryst	K-feldspar		(5)	4.1	(0.0)	19.1	65.3	11.1	0.3	0.0	(0)	(0.0)
16Au05f09	Bf grain A Kfsp2 40 um	phenocryst	K-feldspar		(5)	4.0	(0.0)	19.1	65.5	10.9	0.2	0.0	(0)	(0.0)
16Au05f10	Bf grain A Kfsp3 40 um	phenocryst	K-feldspar		(5)	4.0	(0.0)	19.3	65.0	11.5	0.2	0.0	(0)	(0.0)
16Au05f13	Bf grain B Kfsp1 40 um	phenocryst	K-feldspar		(5)	4.1	(0.0)	18.7	65.9	11.1	0.2	0.0	(0)	(0.0)
16Au05f15	Bf grain B Kfsp2 40 um	phenocryst	K-feldspar		(5)	4.0	(0.0)	19.1	65.5	11.1	0.2	0.0	(0)	(0.0)
16Au05f16	Bf grain B Kfsp3 40 um	phenocryst	K-feldspar		(5)	4.1	(0.0)	19.1	65.3	11.2	0.1	0.0	(0)	(0.0)
16Au05f18	Bf grain C Kfsp 40 um	phenocryst	K-feldspar		(6)	4.0	(0.0)	18.8	65.6	11.2	0.2	0.0	(0)	(0.0)
16Au05f11	Bf grain A plag1 40 um	phenocryst	plagioclase		(6)	9.3	0.0	21.4	65.3	1.3	2.7	0.0	(0)	(0.0)
16Au05f12	Bf grain A plag2 40 um	phenocryst	plagioclase		(6)	9.3	0.0	21.4	65.3	1.4	2.4	0.0	(0)	(0.0)
16Au05f14	Bf grain B plag2 40 um	phenocryst	plagioclase		(5)	9.3	(0.0)	21.3	65.4	1.3	2.5	0.0	(0)	(0.0)
16Au05f17	Bf grain B plag3 40 um	phenocryst	plagioclase		(5)	9.4	0.0	20.6	66.3	1.5	2.1	0.0	(0)	(0.0)
Pine Grove tuff														
15De09b13	Pn8 Fsp1 Kfsp host 40 um	phenocryst	K-feldspar		(3)	3.9	(0.0)	18.9	66.0	11.0	0.1	0.0	(0)	(0.0)
15De09b15	Pn8 Fsp2 Kfsp host 40 um	phenocryst	K-feldspar		(2)	3.9	0.0	18.9	66.2	10.8	0.2	0.0	(0)	(0.0)
15De09b17	Pn8 Fsp3 Kfsp host 40 um	phenocryst	K-feldspar		(2)	3.9	(0.0)	18.8	66.1	11.0	0.2	0.0	(0)	(0.0)
15De09c05	Pn8 Fsp4 Kfsp host 40 um	phenocryst	K-feldspar		(3)	3.9	(0.0)	18.8	66.4	10.8	0.2	0.0	(0)	(0.0)
15De09b12	Pn8 Fsp1 exp.plag. incl 40	incl in Kfsp	plagioclase		(3)	9.7	(0.0)	20.7	66.4	1.3	1.9	0.0	(0)	(0.0)
15De09b14	Pn8 Fsp2 exp.plag. incl 40	incl in Kfsp	plagioclase		(2)	9.5	0.0	21.0	66.3	1.1	2.0	0.0	(0)	(0.0)
15De09b16	Pn8 Fsp3 exp.plag. incl 40	incl in Kfsp	plagioclase		(2)	9.6	(0.0)	20.5	66.5	1.1	2.4	0.0	(0)	(0.0)
15De09c04	Pn8 Fsp4 exp. Plag incl 40	incl in Kfsp	plagioclase		(3)	9.7	0.0	20.5	66.7	1.1	2.0	0.0	(0)	(0.0)

underlined values are reported in wt% oxides

bold values have been used as internal standard (commonly the sum of all measured major elements)

The SiO$_2$ content of the crystallized and/or unexposed inclusions was calculated by difference assuming a total of 100 wt % major element oxides (volatile-free).

red values in parentheses denote detection limits

n.a. – not analyzed

N/A – not applicable

 x – cannot be calculated due to signal interference from co-ablated host or matrix, or due to surface contamination arising from analysis of other phases nearby

um refers to the size (in micrometer) of the inclusion

grainmt=grain mount

[1] recalculated based on the method of Stormer (1983)

| Mn | Fe | | | Zn | Rb | Sr | Y | Zr | Nb | Mo | Cs | Ba | Ce | Hf | Th | U | total | Or | Ab | An |
MnO	FeO$_{tot}$	Fe$_2$O$_3$[1]	FeO[1]														wt%	mol%	mol%	mol%
0.0	0.0	N/A	N/A	(3)	201	732	(0)	(0)	(0)	(0)	0	8455	1	(0)	(0)	(0)	100	75	22	2
0.0	0.0	N/A	N/A	(5)	214	445	(0)	(0)	(0)	(0)	0	1881	1	(0)	(0)	(0)	100	76	22	2
0.0	0.0	N/A	N/A	(9)	215	565	(0)	(1)	(0)	(1)	0	4825	1	(1)	(0)	(19)	100	75	23	3
0.0	0.0	N/A	N/A	(5)	232	359	(0)	(0)	(0)	(0)	0	1720	1	(1)	(0)	(0)	100	77	21	2
0.0	0.1	N/A	N/A	(9)	(1)	1217	0	(1)	(0)	(1)	(0)	228	10	(1)	(0)	(12)	100	2	41	58
0.0	0.1	N/A	N/A	(3)	2	428	1	(0)	(0)	(0)	(0)	47	12	(0)	(0)	(0)	100	4	62	34
0.0	0.1	N/A	N/A	5	1	1289	1	(0)	(0)	(0)	(0)	252	16	(1)	(0)	(0)	100	2	47	51
0.0	0.1	N/A	N/A	(3)	1	707	1	(0)	(0)	(0)	(0)	135	13	(0)	(0)	(0)	100	4	61	35
0.0	0.1	N/A	N/A	(5)	2	581	1	(0)	(0)	(0)	(0)	70	12	(0)	(0)	(0)	100	3	59	37
1.1	84.1	50.3	38.8	0	n.a.	n.a.	n.a.	n.a.	0	n.a.	n.a.	n.a.	n.a.	n.a.	n.a.	n.a.	100			
1.1	83.8	49.7	39.1	0	n.a.	n.a.	n.a.	n.a.	0	n.a.	n.a.	n.a.	n.a.	n.a.	n.a.	n.a.	100			
2.7	46.8	9.0	38.7	0	n.a.	n.a.	n.a.	n.a.	1	n.a.	n.a.	n.a.	n.a.	n.a.	n.a.	n.a.	100			
2.6	47.1	9.6	38.5	0	n.a.	n.a.	n.a.	n.a.	1	n.a.	n.a.	n.a.	n.a.	n.a.	n.a.	n.a.	100			
0.0	0.1	N/A	N/A	(4)	321	5	(0)	(0)	(0)	(0)	0	10	1	(0)	(0)	(0)	100	62	35	2
0.0	0.1	N/A	N/A	(3)	297	5	(0)	(0)	(0)	(0)	0	16	1	(0)	(0)	(0)	100	63	35	2
0.0	0.1	N/A	N/A	(4)	348	4	(0)	(0)	(0)	(0)	0	3	1	(0)	(0)	(0)	100	64	34	2
0.0	0.1	N/A	N/A	(4)	330	3	(0)	(0)	(0)	(0)	0	5	1	(0)	(0)	(0)	100	63	35	2
0.0	0.1	N/A	N/A	(4)	333	3	(0)	(0)	(0)	(0)	0	3	1	(0)	(0)	(0)	100	63	35	2
0.0	0.1	N/A	N/A	(4)	329	5	0	(0)	(0)	(0)	0	10	1	(0)	(0)	(0)	100	64	35	1
0.0	0.1	N/A	N/A	(4)	319	5	(0)	(0)	(0)	(0)	0	5	1	(0)	(0)	(0)	100	63	35	2
0.0	0.1	N/A	N/A	7	7	5	0	(0)	(0)	(0)	(0)	(1)	4	(0)	(0)	(0)	100	6	71	23
0.0	0.1	N/A	N/A	6	7	6	0	(0)	(0)	(0)	(0)	(1)	4	(0)	(0)	(0)	100	7	72	21
0.0	0.1	N/A	N/A	7	6	3	0	(0)	(0)	(0)	(0)	1	4	(0)	(0)	(0)	100	7	72	21
0.0	0.1	N/A	N/A	4	9	3	0	(0)	0	(0)	(0)	0	2	(0)	(0)	(0)	100	8	74	18
0.0	0.0	N/A	N/A	(3)	403	2	(0)	(0)	(0)	(0)	0	5	n.a.	(0)	(0)	(0)	100	64	35	1
0.0	0.0	N/A	N/A	(4)	387	2	(0)	(0)	(0)	(0)	0	6	n.a.	(0)	(0)	(0)	100	64	35	2
0.0	0.0	N/A	N/A	(3)	373	2	(0)	(0)	(0)	(0)	0	2	n.a.	(0)	(0)	(0)	100	64	34	2
0.0	0.0	N/A	N/A	(2)	402	2	(0)	(0)	(0)	(0)	0	6	n.a.	(0)	(0)	(0)	100	64	35	2
0.0	0.1	N/A	N/A	(3)	9	2	0	(0)	(0)	(0)	(0)	(1)	n.a.	(0)	(0)	(0)	100	7	77	17
0.0	0.1	N/A	N/A	(3)	10	2	0	0	(0)	(0)	0	(1)	n.a.	(0)	(0)	0	100	6	76	18
0.0	0.1	N/A	N/A	(3)	6	3	1	(0)	(0)	(0)	(0)	(1)	n.a.	(0)	(0)	(0)	100	5	74	20
0.0	0.1	N/A	N/A	3	8	2	0	(0)	(0)	(0)	(0)	1	n.a.	(0)	(0)	0	100	6	76	18

8   FeTiMM – a new oxybarometer for mafic to felsic magmas

R. Arató[1]* and A. Audétat[1]*

Abstract

The oxidation state of magmas is a key parameter that is notoriously difficult to reconstruct. The most common approach is via magnetite–ilmenite oxybarometry. However, many natural magmas do not contain ilmenite, preventing application of this technique. Here we present a new method that allows fO_2 to be reconstructed based on the partitioning of Fe and Ti between magnetite and silicate melt. The new method, which we call FeTiMM, is applicable to both ilmenite-free and ilmenite-bearing samples, and even to slowly-cooled intrusive rocks such as granites. FeTiMM was calibrated on 109 experiments covering a wide range of oxygen fugacities, temperatures, pressures and silicate melts ranging from basaltic to rhyolitic composition, and returned fO_2 values that agree within 0.5 log units with independently constrained fO_2 values in all but five cases. A first test on 19 natural samples of dacitic to rhyolitic compositions was equally successful. FeTiMM thus opens the door for numerous new applications in various disciplines of Earth Sciences, including the fields of volcanology, igneous petrology, experimental geochemistry and ore geology.

8.1   Introduction

Oxygen fugacity is an important thermodynamic parameter in magmatic systems because it exerts a first-order control on phase equilibria as well as on mineral–melt and fluid–melt partition coefficients. The most commonly used and most reliable way to reconstruct magmatic fO2 is via magnetite–ilmenite oxybarometry (e.g., Buddington and Lindsley, 1964; Carmichael, 1967; Stormer, 1983; Andersen and Lindsley, 1988; Ghiorso and Sack, 1991; Lattard et al., 2005; Ghiorso and Evans, 2008). Alternative approaches are based on (i) the Fe2+/Fe3+ ratio of whole-rocks (Kress and Carmichael, 1989; Putirka, 2016), (ii) mineral reactions involving olivine, pyroxene, and/or sphene (Frost and Lindsley, 1992; Lindsley and Frost, 1992; Andersen et al., 1993; Xirouchakis et al., 2001), (iii) biotite, K-feldspar and magnetite (Wones and Eugster,

[1] Bayerisches Geoinstitut, Universität Bayreuth, 95440 Bayreuth, Germany
*Corresponding authors (email: robert.arato@uni-bayreuth.de; andreas.audetat@uni-bayreuth.de)

1965; Wones, 1981) , (iv) zircon Ce (and Eu) anomaly (Ballard et al., 2002; Trail et al., 2012; Smythe and Brenan, 2016), and (v) single-amphibole oxybarometry (Ridolfi et al., 2010). However, despite these various approaches, reconstruction of magmatic fO2 in igneous rocks remains difficult, particularly in the case of intrusives, because during slow cooling Fe-Ti-oxide minerals usually get either reset or altered. Furthermore, many magmas do not contain ilmenite but only magnetite (Frost and Lindsley, 1991), precluding the application of magnetite–ilmenite oxybarometry.

8.2 Calibration of the FeTiMM oxybarometer

The aim of this study was to develop an oxybarometer that is based on element partitioning between a mineral and silicate melt, such that it can be applied to samples in which these phases occur as inclusions within phenocrysts and thus were protected from re-equilibration and alteration during slow cooling. Iron partitioning between magnetite and melt is a promising candidate because magnetite is a common mineral and because magnetite solubility in silicic melts has been shown to depend on fO_2 (Gaillard *et al.*, 2001). However, magnetite solubility (and thus Fe partitioning between magnetite and silicate melt) depends also strongly on temperature and melt composition. At constant fO_2 and T, magnetite solubility increases by a factor of up to 6 as the alumina saturation index (ASI; defined as the molar $Al_2O_3/(Na_2O+K_2O+CaO)$ ratio) decreases from 1.0 to 0.6. Magnetite solubility is thus not suitable as oxybarometer unless T and ASI can be extremely well constrained, which is commonly difficult in natural samples (Arató and Audétat, 2017a). However, we noticed that the effect of ASI on magnetite solubility is similar to that on TiO_2 solubility (Kularatne and Audétat, 2014), with the latter being independent on fO_2. Hence, the effect of melt composition may be diminished by dividing the mgt–melt partition coefficient of Fe ($D_{Fe}^{mgt/melt}$) by that of Ti ($D_{Ti}^{mgt/melt}$).

We tested this idea first on a set of 50 own experiments conducted in the system magnetite–H_2O–rhyolite melt at various oxygen fugacities, temperatures, pressures, melt ASI's, and magnetite compositions (Arató and Audétat, 2017b; Table 8.S1). The results (Fig. 8.S1) revealed that the melt composition effect indeed gets greatly reduced in this way, and that the Fe–Ti exchange coefficient between magnetite and silicate melt, $D_{Fe-Ti}^{mgt/melt}$ = $(D_{FeOtot}^{mgt/melt})/(D_{TiO_2}^{mgt/melt})$, depends most strongly on fO_2, with the effect of temperature

becoming negligible. In a second step we extended the dataset by 59 experiments from 14 different studies performed at 750-1100 °C, 0.1-700 MPa, oxygen fugacities of -1.3 to +5.5 log units relative to the fayalite-magnetite-quartz buffer (ΔFMQ-1.3 to ΔFMQ+5.5), with melt compositions of 48-79 wt% SiO_2 and ASI=0.3-1.3, and magnetite compositions of 0.01-28 wt% TiO_2. These 59 experiments were left after screening 33 experimental studies with a total of >1600 experiments (Table 8.S2) for the following criteria: (i) fO_2 was controlled experimentally, (ii) magnetite coexists with ilmenite in at least some of the experiments, (iii) compositional data for magnetite, silicate melt, ±ilmenite are available, (iv) the reported average compositions of magnetite and ilmenite represent equilibrium pairs (Bacon and Hirschmann, 1988), and (v) the average compositions of magnetite and silicate melt pass a similar test that we developed to check for magnetite–melt equilibrium (Fig. 8.S2). In this second step, we focused on ilmenite-saturated experiments to be able to independently constrain fO_2 values via magnetite–ilmenite oxybarometry. In nine cases, the reported experimental fO_2 values deviated by more than 1.0 log unit fO_2 from the values obtained via magnetite–ilmenite oxybarometry (Ghiorso and Evans, 2008; Fig. 8.S3), suggesting problems with the control of experimental fO_2 (Matjuschkin *et al.*, 2015). We thus relied on the fO_2 values calculated via magnetite–ilmenite oxybarometry for all 59 ilmenite-saturated experiments. To account for the large range of melt compositions, it was necessary to include MgO in the melt compositional parameter. Based on the extended dataset of 109 experiments we developed a model (which we hereinafter call FeTiMM) that allows fO_2 to be calculated as a function of $D_{Fe–Ti}^{mgt/melt}$ (with FeO_{tot} and TiO_2 measured in weight percent, and the melt composition reported dry) and the melt compositional parameter AMCNK = molar $Al_2O_3/(CaO+Na_2O+K_2O+MgO)$:

$$\Delta FMQ = (\log(D_{FeOtot}^{mgt/melt}/D_{TiO2}^{mgt/melt}) + 0.137*AMCNK+0.102)/(0.288*AMCNK+0.054) \quad (Eq.\ 8.1)$$

The rationale behind this equation is depicted in Figure 8.1. The overall uncertainty of the FeTiMM model, calculated from the errors of the fits in Figures 8.1b, c propagated into equation 8.1 (see Supplementary Information) increases from ±0.2-0.3 log units fO_2 at ≤ΔFMQ+1.5, to ±0.3-0.5 log units fO_2 at ΔFMQ+4.5 (data S1). The performance of FeTiMM on the 59 ilmenite-saturated experiments is shown in Figure 8.2. As explained above, we relied on fO_2 values calculated via magnetite–ilmenite oxybarometry (Ghiorso and Evans, 2008) for this test. The uncertainty of the latter model was not explicitly stated (Ghiorso and Evans, 2008), but based on

their Figure 27 it can be estimated at ca. ±0.3 log units at reducing conditions (ΔFMQ-1 to ΔFMQ+1) to ca. ±0.5 log units at strongly oxidizing conditions (ΔFMQ+4.5; not considering a group of outliers), *i.e.*, similar to the uncertainty associated with our model. Within these errors, 63 out of the 109 experiments show perfect agreement between the two methods and all but five experiments return fO_2 values that agree within ≤0.5 log units. No correlations are evident between the degree of correspondence and fO_2, temperature, melt SiO_2 content, ASI, or magnetite composition (Fig. 8.S4), suggesting that FeTiMM works equally well over the entire range of the investigated P-T-X conditions. It should be mentioned that any misfit can result from various sources including (i) analytical errors, (ii) experimental problems, as well as (iii) weaknesses in either model.
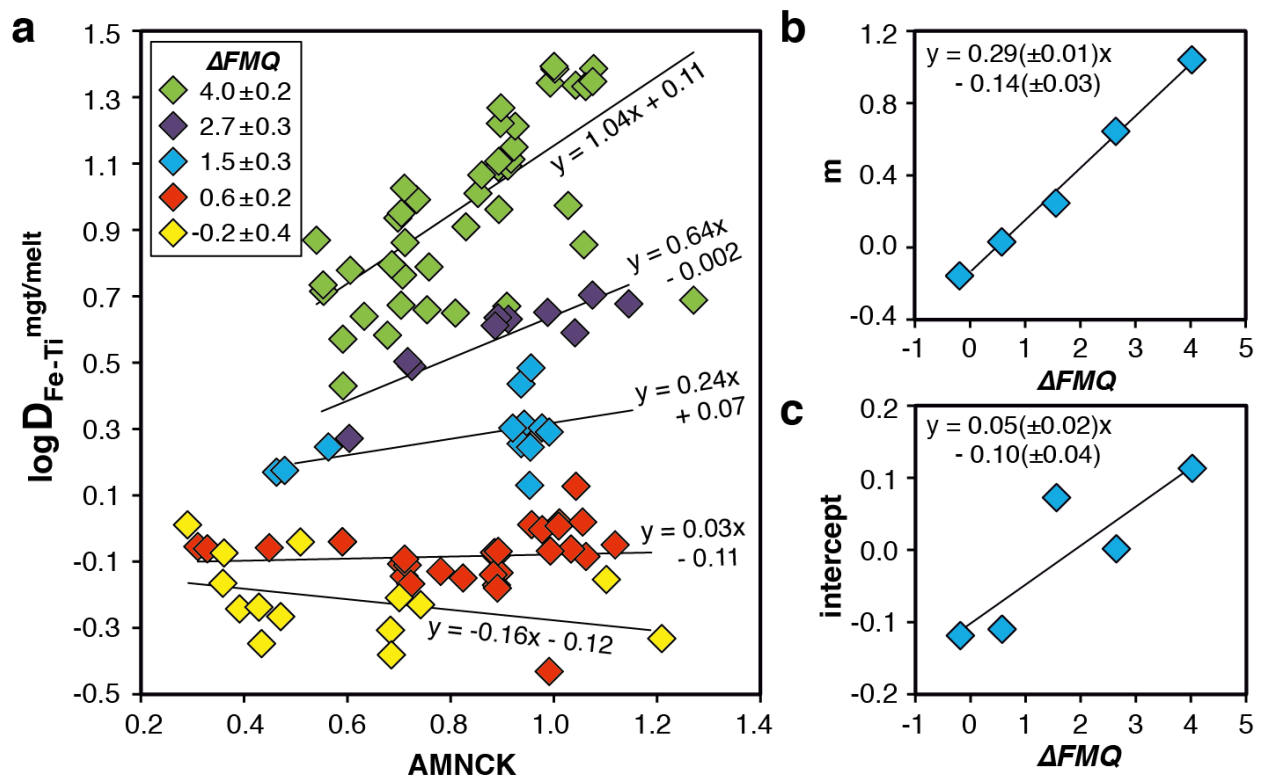
Fig. 8.1 Development of the FeTiMM model. (**a**) 109 experimental data points (59 ilmenite-saturated; 50 ilmenite-undersaturated) were split into five groups of similar oxygen fugacity, through which linear regressions were fit. $D_{Fe-Ti}^{mgt/melt} = (D_{FeOtot}^{mgt/melt})/(D_{TiO2}^{mgt/melt})$; A/MCNK = molar $Al_2O_3/(MgO+CaO+Na_2O+K_2O)$. (**b-c**) Variation of the slopes and intercepts of the linear fits in (**a**) as a function of oxygen fugacity expressed in log units deviation from the fayalite-magnetite-quartz (FMQ) buffer.
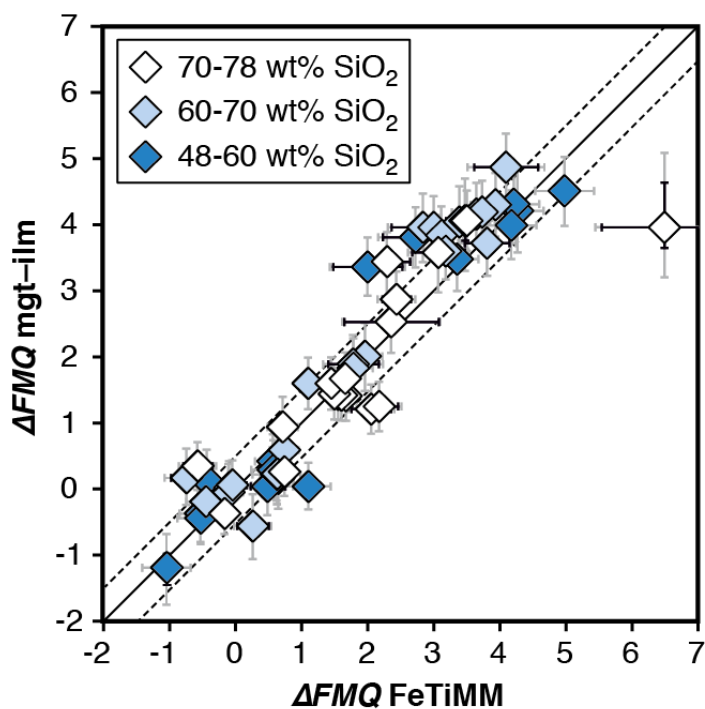
Fig. 8.2 Performance of FeTiMM in ilmenite-saturated magmas. Oxygen fugacities (expressed in log units relative to the FMQ buffer) obtained via FeTiMM are compared with ones obtained via magnetite–ilmenite oxybarometry using the model of (2). The data are divided into three groups of contrasting melt SiO_2. Black error bars (in most cases smaller than symbol size) denote the analytical error, whereas the grey error bars denote the overall error that includes both the analytical scatter and the error inherent to the model. Details about the calculation of errors are provided in the supplementary information.

8.3 Test on additional ilmenite-undersaturated experiments

As discussed above, equation 8.1 was derived from a database that comprises 50 ilmenite-undersaturated, rhyolitic experiments, plus 59 ilmenite-saturated, basaltic to rhyolitic experiments. It remains to be tested whether FeTiMM works also for ilmenite-undersaturated intermediate to mafic magmas. However, in ilmenite-undersaturated experiments fO_2 cannot be independently constrained via magnetite–ilmenite thermobarometry, which forces us to rely on reported experimental fO_2 values even if the test with the ilmenite-saturated experiments (Fig. 8.S3) revealed that these values are not always reliable. To reduce the chance of including erroneous fO_2 reference values, we restricted our choice of ilmenite-undersaturated experiments to studies which comprised both ilmenite-undersaturated and ilmenite-saturated experiments, and which in the latter case showed good agreement between the reported experimental and magnetite–ilmenite-based fO_2 values. This approach returned 27 data points from 5 different studies (Table 8.S1), excluding 22 data points that did not pass the Mn/Mg magnetite–melt equilibrium test mentioned above. The performance of FeTiMM on these 27 literature-based experiments plus 50 own ilmenite-undersaturated experiments is shown in Figure 8.3. The data in Figure 8.3 show a larger scatter than those in Figure 8.2, which is likely due to errors in the reported experimental fO_2 values (cf. Fig. 8.S3). Nevertheless, within the error quoted for FeTiMM, 7 of the 27 experiments return fO_2 values that agree between the two methods and all but 5 experiments show a correspondence within

0.5 log units. Again, no correlations are evident between the degree of fO$_2$ correspondence and other key variables (Fig. 8.S5), suggesting that FeTiMM works equally well for mafic as for silicic rocks.

In summary, the results in Figures 8.2 and 8.3 suggest that FeTiMM provides reliable fO$_2$ estimates for both ilmenite-saturated and ilmenite-undersaturated magmas over the entire range of basaltic to rhyolitic compositions. It should be mentioned that none of the investigated melt compositions plot in the alkaline field (Macdonald and Katsura, 1964) in the total alkali vs. SiO$_2$ (TAS) diagram (Le Maitre *et al.*, 1989), so the performance of FeTiMM in highly alkaline magmas is not known yet. However, 102 out of the 136 data points plotted in Figures 8.2 and 8.3 are peralkaline according to molar Al$_2$O$_3$/(Na$_2$O+K$_2$O+CaO) (=A/CNK), with 17 melts having A/CNK values <0.7.
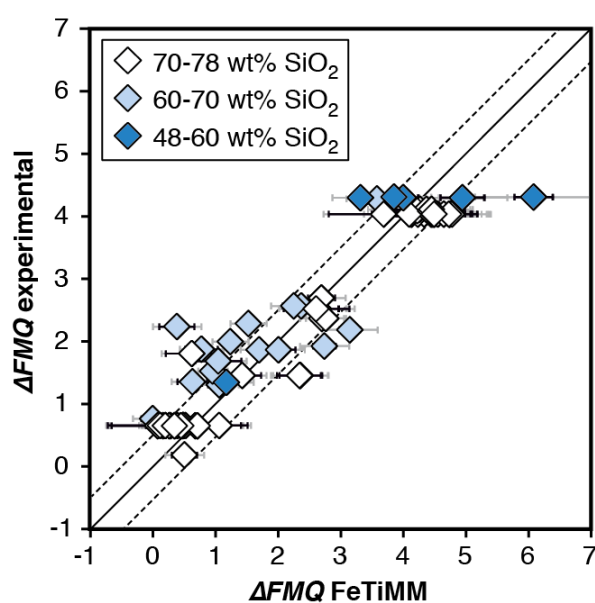
Fig. 8.3 Performance of FeTiMM in ilmenite-undersaturated magmas. Due to the lack of ilmenite, one has to rely on the reported experimentally imposed fO$_2$ values, which are associated with considerable (but unknown) uncertainty. Correspondingly, error bars in y-axis direction cannot be displayed. See Figure 8.2 for abbreviations and the meaning of the black and grey error bars in x-axis direction.
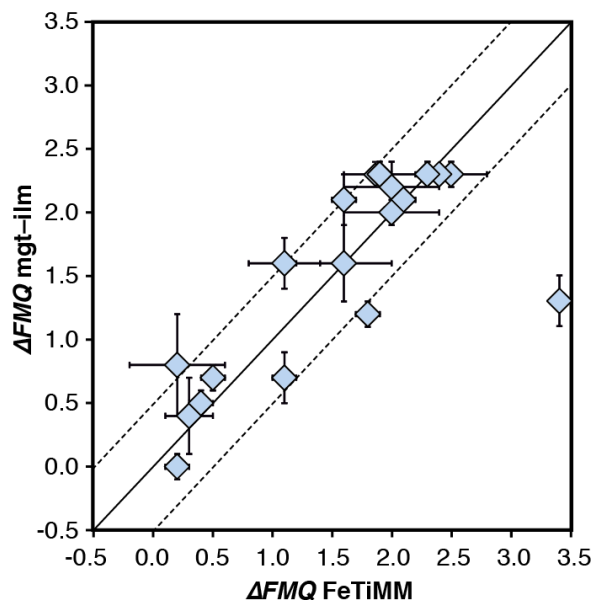
Fig. 8.4 Application of FeTiMM to a set of 19 natural, ilmenite-saturated samples of rhyolitic to dacitic composition (12). Oxygen fugacities (reported in log units relative to the fayalite–magnetite–quartz buffer) obtained via FeTiMM agree within 0.5 log units with those obtained via magnetite–ilmenite oxybarometry (2) in all but one case. Error bars denote 1σ standard deviation of the fO$_2$ values obtained from several magnetite–melt pairs.

8.4 Application to natural samples

The results of a first application of FeTiMM to 19 natural samples of rhyolitic to dacitic composition are shown in Figure 8.4. Details on the samples and analytical methods can be found in Arató and Audétat (2017a). All samples were ilmenite-saturated, such that fO$_2$ could be independently constrained via magnetite–ilmenite oxybarometry. Coexistence of analyzed magnetite, ilmenite and silicate melt was verified by means of the Mg/Mn magnetite–ilmenite

partitioning test (Bacon and Hirschmann, 1988) plus our own Mn/Mg magnetite–melt partitioning test described in the Supplementary Information. In all but one sample, FeTiMM returned fO$_2$ values that agree within 0.5 log units with those obtained via magnetite–ilmenite oxybarometry (Fig. 8.4).

One of the main advantages of FeTiMM is that it can be applied to magmas that do not contain ilmenite, which is true for many igneous rocks of mafic to felsic composition, particularly for those that are alkali-rich (Lindsley and Frost, 1992). Another major advantage of the method is that it can be applied to slowly-cooled and/or altered rocks if magnetite and silicate melt are present as inclusions within phenocrysts (preferably quartz) and are analyzed as entities by LA-ICP-MS, thereby effectively reversing compositional heterogeneities that developed within the inclusions during slow cooling. The sole disadvantage of FeTiMM is that it requires knowledge of the silicate melt composition. This can be readily accomplished in rapidly-quenched, volcanic samples with glassy matrix, but it is a bit more difficult in holocrystalline, porphyritic samples (for fresh samples selective analysis of the matrix suffices), and can be challenging in holocrystalline, coarse-grained samples. In the latter samples, both magnetite and silicate melt need to be analyzed as inclusions within phenocrysts, with the quantification of melt compositions requiring re-homogenization experiments and/or constraints from whole-rock data (Audétat and Lowenstern, 2014; Arató and Audétat, 2017a).

8.5 Acknowledgments

8.6 References

Andersen, D.J., Lindsley, D.H. (1988) Internally consistent solution models for Fe-Mg-Mn-Ti oxides: Fe-Ti oxides. *American Mineralogist* 73, 714-726.

Andersen, D.J., Lindsley, D.H., Davidson, P.M. (1993) QUILF: A pascal program to assess equilibria among Fe–Mg–Mn–Ti oxides, pyroxenes, olivine, and quartz. *Computers & Geosciences* 19, 1333-1350.

Arató, R., Audétat, A. (2017a) Vanadium magnetite–melt oxybarometry of natural, silicic magmas: a comparison of various oxybarometers and thermometers. *Contributions to Mineralogy and Petrology* 172.

Arató, R., Audétat, A. (2017b) Experimental calibration of a new oxybarometer for silicic magmas based on vanadium partitioning between magnetite and silicate melt. *Geochimica et Cosmochimica Acta* 209, 284-295.

Audétat, A., Lowenstern, J.B. (2014) Melt inclusions. In Geochemistry of mineral deposits (ed. S. D. Scott). *Treatise on Geochemistry 2nd ed.* 13, 143-173.

Bacon, C.R., Hirschmann, M.M. (1988) Mg/Mn partitioning as a test for equilibrium between coexisting Fe-Ti oxides. *American Mineralogist* 73, 57-61.

Ballard, J.R., Palin, M.J., Campbell, I.H. (2002) Relative oxidation states of magmas inferred from Ce(IV)/Ce(III) in zircon: application to porphyry copper deposits of northern Chile. *Contributions to Mineralogy and Petrology* 144, 347-364.

Buddington, A., Lindsley, D. (1964) Iron-titanium oxide minerals and synthetic equivalents. *Journal of Petrology* 5, 310-357.

Carmichael, I.S.E. (1967) The iron-titanium oxides of salic volcanic rocks and their associated ferromagnesian silicates. *Contributions to Mineralogy and Petrology* 14, 36-64.

Frost, B., Lindsley, D.H. (1991) Occurrence of iron-titanium oxides in igneous rocks. *Reviews in Mineralogy and Geochemistry* 25, 433-468.

Frost, B.R., Lindsley, D. (1992) Equilibria among Fe-Ti oxides, pyroxenes, olivine, and quartz: Part II. Application. *American Mineralogist* 77, 1004-1004.

Gaillard, F., Scaillet, B., Pichavant, M., Bény, J.-M. (2001) The effect of water and fO$_2$ on the ferric–ferrous ratio of silicic melts. *Chemical Geology* 174, 255-273.

Ghiorso, M.S., Evans, B.W. (2008) Thermodynamics of rhombohedral oxide solid solutions and a revision of the Fe-Ti two-oxide geothermometer and oxygen-barometer. *American Journal of Science* 308, 957-1039.

Ghiorso, M.S., Sack, O. (1991) Fe-Ti oxide geothermometry: thermodynamic formulation and the estimation of intensive variables in silicic magmas. *Contributions to Mineralogy and Petrology* 108, 485-510.

Kress, V.C., Carmichael, I.S. (1989) The lime-iron-silicate melt system: Redox and volume systematics. *Geochimica et Cosmochimica Acta* 53, 2883-2892.

Kularatne, K., Audétat, A. (2014) Rutile solubility in hydrous rhyolite melts at 750–900°C and 2kbar, with application to titanium-in-quartz (TitaniQ) thermobarometry. *Geochimica et Cosmochimica Acta* 125, 196-209.

Lattard, D., Sauerzapf, U., Käsemann, M. (2005) New calibration data for the Fe-Ti oxide thermo-oxybarometers from experiments in the Fe-Ti-O system at 1 bar, 1,000-1,300°C and a large range of oxygen fugacities. *Contributions to Mineralogy and Petrology* 149, 735-754.

Le Maitre, R.W.B., Dudek, P., Keller, A., Lameyre, J., Le Bas, J., Sabine, M., Schmid, P., Sorensen, R., Streckeisen, H., Woolley, A. (1989) *A classification of igneous rocks and glossary of terms: Recommendations of the International Union of Geological Sciences, Subcommission on the Systematics of Igneous Rocks*. International Union of Geological Sciences.

Lindsley, D.H., Frost, B.R. (1992) Equilibria among Fe-Ti oxides, pyroxenes, olivine, and quartz; Part I, Theory. *American Mineralogist* 77, 987-1003.

MacDonald, G.A., Katsura, T. (1964) Chemical composition of Hawaiian lavas. *Journal of Petrology* 5, 82-133.

Matjuschkin, V., Brooker, R.A., Tattitch, B., Blundy, J.D., Stamper, C.C. (2015) Control and monitoring of oxygen fugacity in piston cylinder experiments. *Contributions to Mineralogy and Petrology* 169, 9.

Putirka, K. (2016) Rates and styles of planetary cooling on Earth, Moon, Mars, and Vesta, using new models for oxygen fugacity, ferric-ferrous ratios, olivine-liquid Fe-Mg exchange, and mantle potential temperature. *American Mineralogist* 101, 819-840.

Ridolfi, F., Renzulli, A., Puerini, M. (2010) Stability and chemical equilibrium of amphibole in calc-alkaline magmas: an overview, new thermobarometric formulations and application to subduction-related volcanoes. *Contributions to Mineralogy and Petrology* 160, 45-66.

Sisson, T.W., Ratajeski, K., Hankins, W.B., Glazner, A.F. (2004) Voluminous granitic magmas from common basaltic sources. *Contributions to Mineralogy and Petrology* 148, 635-661.

Smythe, D.J., Brenan, J.M. (2016) Magmatic oxygen fugacity estimated using zircon-melt partitioning of cerium. *Earth and Planetary Science Letters* 453, 260-266.

Stormer, J.C. (1983) The effects of recalculation on estimates of temperature and oxygen fugacity from analyses of multicomponent iron-titanium oxides. *American Mineralogist* 68, 586-594.

Trail, D., Bruce Watson, E., Tailby, N.D. (2012) Ce and Eu anomalies in zircon as proxies for the oxidation state of magmas. *Geochimica et Cosmochimica Acta* 97, 70-87.

Wones, D. (1981) Mafic silicates as indicators of intensive variables in granitic magmas. *Mining Geology* 31, 191-212.

Wones, D., Eugster, H. (1965) Stability of biotite–experiment theory and application. *American Mineralogist* 50, 1228-1272.

Xirouchakis, D., Lindsley, D.H., Frost, B.R. (2001) Assemblages with titanite ($CaTiOSiO_4$), Ca-Mg-Fe olivine and pyroxenes, Fe-Mg-Ti oxides, and quartz: Part II. Application. *American Mineralogist* 86, 254-264.

8.7 Supplementary information

The Supplementary Information includes:

> ➢ Details on the Mn/Mg equilibrium test
>
> ➢ Details on the estimation of uncertainty
>
> ➢ Figures 8.S1 to 8.S5
>
> ➢ Tables 8.S1 and 8.S2
>
> ➢ Supplementary Information References

Mn/Mg test to check for equilibrium between magnetite and silicate melt

To be able to check for equilibrium between a given magnetite–silicate melt pair a new test was developed. Accidentally, this test is based on the same two elements (Mn, Mg) as the equilibrium test between magnetite and ilmenite (Bacon and Hirschmann, 1988), although the rationale behind is quite different. We seeked for two elements whose magnetite–melt partition coefficients depend in a similar manner on melt composition, but whose absolute concentrations in the silicate melt vary strongly during magma differentiation. With this approach, melts that do not coexist with a given magnetite composition should be easily identifiable. We thus use the Mn–Mg exchange coefficient $D_{Mn-Mg}^{mgt/melt}$ = $(D_{MnO}^{mgt/melt})/(D_{MgO}^{mgt/melt})$, with MnO and MgO given in weight percent. A plot of $D_{Mn-Mg}^{mgt/melt}$ versus MnO/MgO ratio in the silicate melt for 356 magnetite–melt pairs with melts ranging from basaltic composition (48 wt% SiO_2) to high-silica rhyolitic composition (79 wt% SiO_2) is shown in Figure 8.S2. It turns out that 95% of the data points with reported Mn and Mg concentrations display a $D_{Mn-Mg}^{mgt/melt}$ value between 1 and 4, with the remaining 5% apparently representing outliers because no correlation between magnitude of mismatch and the MnO/MgO ratio in the silicate melt (Fig. 8.S2) or other parameters (Table 8.S1) is evident.

Estimation of the uncertainty of FeTiMM

We assume that f is an *n*-dimensional differentiable function and $X_1, X_2, ..., X_n$ are independent variables with $\sigma_1, \sigma_2, ..., \sigma_n$ standard deviations. Therefore, the overall uncertainty can be estimated from the first-order linear estimate of $f(X_1, X_2, ..., X_n)$:

$$\sigma_{X_1, X_2, ..., X_n} \approx \sqrt{\sum_{i=1}^{n} \left(\frac{\partial f}{\partial x_i} (EX_1, EX_2, ..., EX_n) \right)^2 \sigma_i^2}, \qquad (8.S1)$$

where $\frac{\partial f}{\partial x_i}$ is the *i*-th partial derivative of the function *f*. If the expected values (EX_i) of the variables (in our case chemical analyses) are unknown, one can replace the expected values by the variables themselves:

$$D(f(X_1, X_2, \dots, X_n)) \approx \sqrt{\sum_{i=1}^{n} \left(\frac{\partial f}{\partial x_i}(X_1, X_2, \dots, X_n)\right)^2 \sigma_i^2}. \qquad (8.S2)$$

Our function has the following form:

$$\Delta FMQ\left(FeO_{tot\ mgt}, FeO_{tot\ melt}, TiO_{2\ mgt}, TiO_{2\ melt}, Al_2O_3, Denom, a, b, c, d\right)$$
$$= \frac{\log_{10}(D) - b \cdot AMCNK + d}{a \cdot AMCNK + c}$$

, where

$$D\left(FeO_{tot\ mgt}, FeO_{tot\ melt}, TiO_{2\ mgt}, TiO_{2\ melt}\right) = \frac{\dfrac{FeO_{tot\ mgt}}{FeO_{tot\ melt}}}{\dfrac{TiO_{2\ mgt}}{TiO_{2\ melt}}} = \frac{FeO_{tot\ mgt} \cdot TiO_{2\ melt}}{FeO_{tot\ melt} \cdot TiO_{2\ mgt}}$$

and $AMCNK(Al_2O_3, Denom) = \frac{Al_2O_3}{Denom}$.

The variables CaO, Na₂O, K₂O, and MgO appear only as a sum in the equation (i.e. as CaO+Na₂O+K₂O+MgO) and their variances are independent, therefore they can be treated as a single variable in the calculation of the partial derivatives – named "Denom" – the variance of which is the sum of the individual elements' variances:

$$Denom = CaO + Na2O + K2O + MgO, \sigma_{Denom}^2 = \sigma_{CaO}^2 + \sigma_{Na2O}^2 + \sigma_{K2O}^2 + \sigma_{MgO}^2$$

It is important to note that Al₂O₃, CaO, Na₂O, K₂O, and MgO (as well as their standard deviations) refer to molar abundances, whereas FeO$_{tot\ mgt}$, FeO$_{tot\ melt}$, TiO$_{2\ mgt}$ and TiO$_{2\ melt}$ are given in weight percent.

The partial derivatives used for the propagation of uncertainty are the following:

a) For the analytical uncertainty:

$$\frac{\partial \Delta FMQ}{\partial FeO_{tot\ mgt}} = \frac{1}{FeO_{tot\ mgt} \cdot \ln(10) \cdot (a \cdot AMCNK + c)}$$

$$\frac{\partial \Delta FMQ}{\partial FeO_{tot\ melt}} = \frac{-1}{FeO_{tot\ melt} \cdot \ln(10) \cdot (a \cdot AMCNK + c)}$$

$$\frac{\partial \Delta FMQ}{\partial TiO_{2\ mgt}} = \frac{1}{TiO_{2\ mgt} \cdot \ln(10) \cdot (a \cdot AMCNK + c)}$$

$$\frac{\partial \Delta FMQ}{\partial TiO_{2\ melt}} = \frac{-1}{TiO_{2\ melt} \cdot \ln(10) \cdot (a \cdot AMCNK + c)}$$

$$\frac{\partial \Delta FMQ}{\partial AMCNK} = \frac{-(log_{10}(D) - b \cdot AMCNK + d) \cdot a - b \cdot (a \cdot AMCNK + c)}{(a \cdot AMCNK + c)^2}$$

$$\frac{\partial \Delta FMQ}{\partial Al_2O_3} = \frac{1}{Denom} \cdot \frac{\partial \Delta FMQ}{\partial AMCNK}$$

$$\frac{\partial \Delta FMQ}{\partial Denom} = \frac{-Al_2O_3}{Denom^2} \cdot \frac{\partial \Delta FMQ}{\partial AMCNK}$$

b) For the uncertainty inherent to the model:

$$\frac{\partial \Delta FMQ}{\partial a} = -\frac{log_{10}(D) - b \cdot AMCNK + d}{(a \cdot AMCNK + c)^2} AMCNK$$

$$\frac{\partial \Delta FMQ}{\partial b} = -\frac{AMCNK}{a \cdot AMCNK + c}$$

$$\frac{\partial \Delta FMQ}{\partial c} = -\frac{log_{10}(D) - b \cdot AMCNK + d}{(a \cdot AMCNK + c)^2}$$

$$\frac{\partial \Delta FMQ}{\partial d} = \frac{1}{a \cdot AMCNK + c}$$

From the individual partial derivatives and variances (σ_i^2) of $FeO_{tot\ mgt}$, $FeO_{tot\ melt}$, $TiO_{2\ mgt}$, $TiO_{2\ melt}$, Al_2O_3, Denom, a, b, c and d the overall uncertainty can be estimated according to Equation 8.S2. For the estimation of the propagated analytical uncertainty only the partial derivatives and variances of $FeO_{tot\ mgt}$, $FeO_{tot\ melt}$, $TiO_{2\ mgt}$, $TiO_{2\ melt}$, Al_2O_3 and Denom have to be considered.
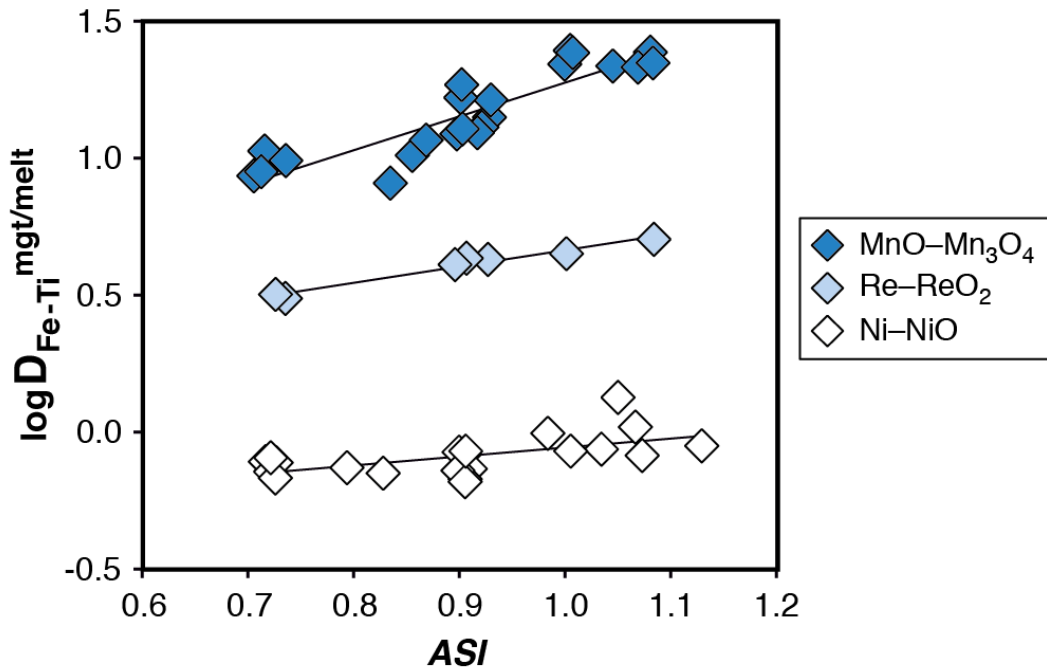
Fig 8.S1 Dependence of the Fe–Ti exchange coefficient between magnetite and rhyolitic melt on fO_2 and melt alumina saturation index. $D_{Fe-Ti}^{mgt/melt}$ refers to $(D_{FeOtot}^{mgt/melt})/(D_{TiO2}^{mgt/melt})$, whereas ASI refers to molar $Al_2O_3/(CaO + Na_2O + K_2O)$. The dataset comprises magnetite–melt pairs from 50 different experiments performed at three different oxygen fugacity buffers, temperatures of 800-1000°C, pressures of 100-500 MPa, with melt ASI values of 0.71-1.12, and magnetite compositions of 0.2-14 wt% TiO_2 (Arató and Audétat, 2017).
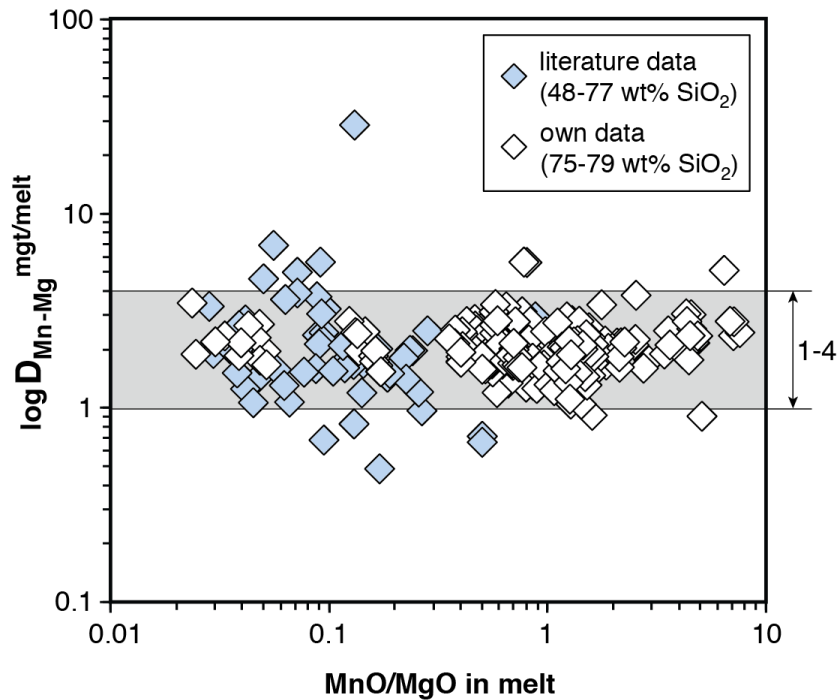
Fig. 8.S2 Variance of the Mn–Mg exchange coefficient between magnetite and silicate melt as a function of the MnO/MgO weight ratio in the silicate melt. $D_{Mn-Mg}^{mgt/melt}$ refers to $(D_{MnO}^{mgt/melt})/(D_{MgO}^{mgt/melt})$, with MnO and MgO given in weight percent. The data set comprises the 296 magnetite–rhyolite pairs from own experiments, plus the data points shown in Figure 2. The shaded envelope, which encompasses $D_{Mn-Mg}^{mgt/melt}$ values of 1-4, comprises 95% of all data points.
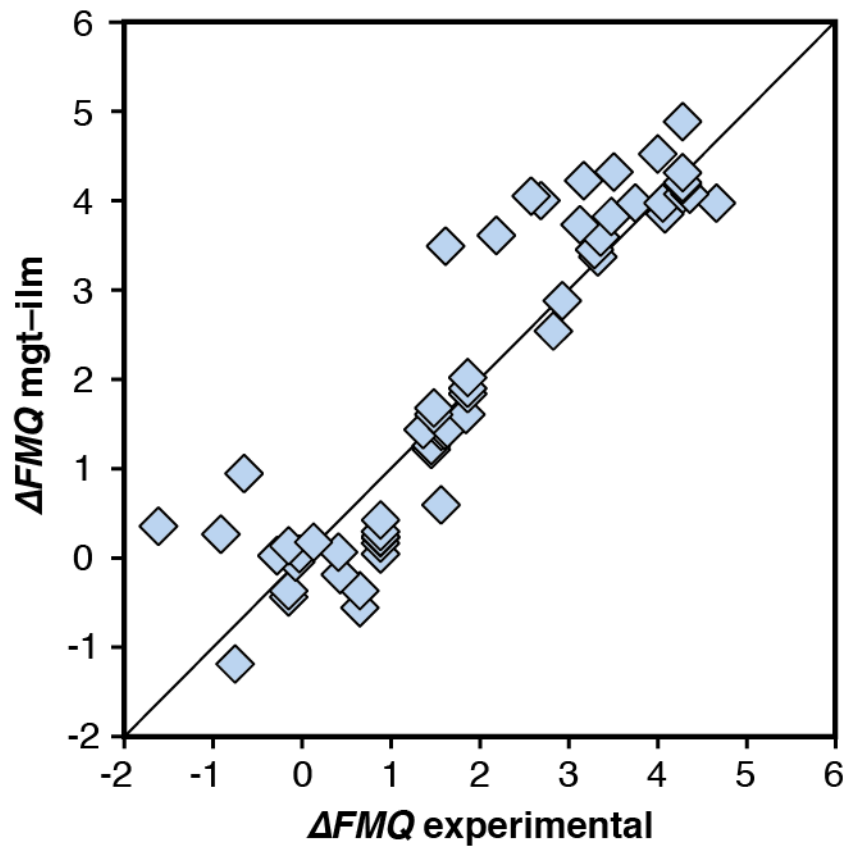
Fig. 8.S3 Comparison of reported experimental fO_2 values with fO_2 values obtained via magnetite–ilmenite (Ghiorso and Evans, 2008) for 59 ilmenite-bearing experiments taken from the literature. Oxygen fugacities are reported in log units relative to the fayalite-magnetite-quartz (FMQ) buffer.
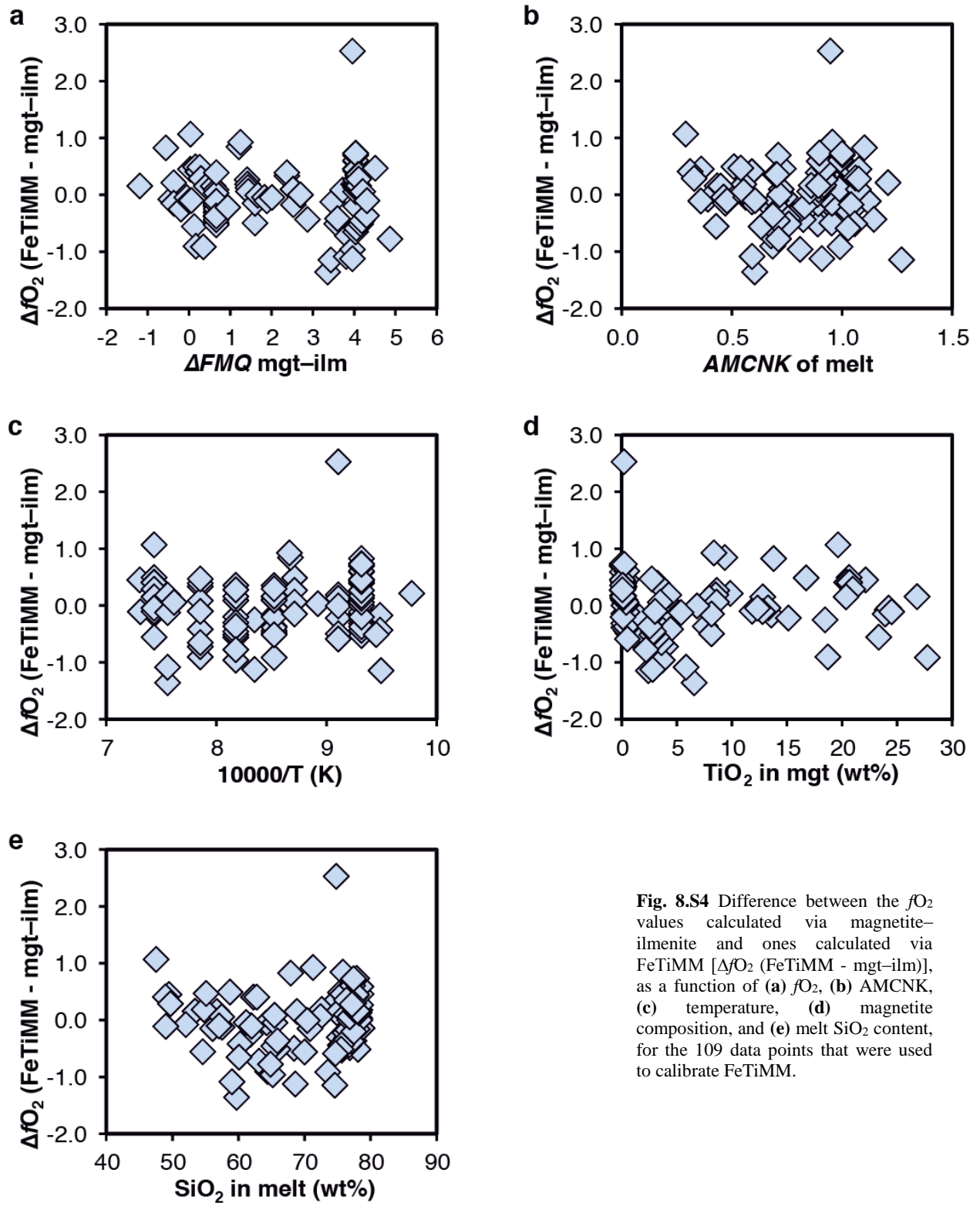
Fig. 8.S4 Difference between the fO_2 values calculated via magnetite–ilmenite and ones calculated via FeTiMM [ΔfO_2 (FeTiMM - mgt–ilm)], as a function of (**a**) fO_2, (**b**) AMCNK, (**c**) temperature, (**d**) magnetite composition, and (**e**) melt SiO_2 content, for the 109 data points that were used to calibrate FeTiMM.
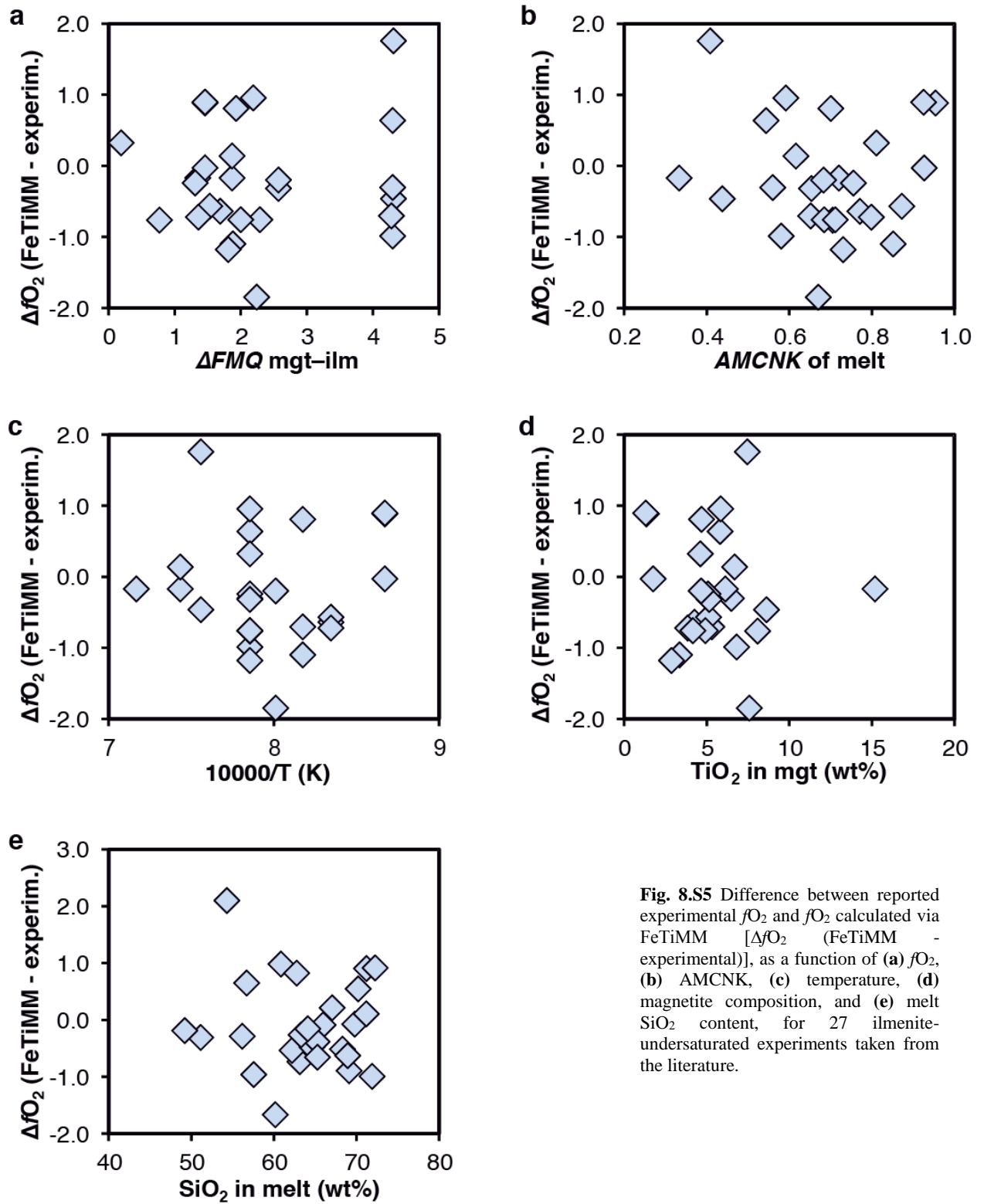
Fig. 8.S5 Difference between reported experimental fO_2 and fO_2 calculated via FeTiMM [ΔfO_2 (FeTiMM - experimental)], as a function of (**a**) fO_2, (**b**) AMCNK, (**c**) temperature, (**d**) magnetite composition, and (**e**) melt SiO_2 content, for 27 ilmenite-undersaturated experiments taken from the literature.

Supplementary Table 8.S.1/1a: Dataset used for the calibration and testing of the FeTiMM oxybarometer.

Own experiments (ilmenite-undersaturated) — **Chemical composition**

melt

Reference	Run:	n:	SiO2	TiO2	Al2O3	FeO	MnO	MgO	CaO
this study	RA-V03-0.8	7	77.28(0.29)	0.005(0.000	9.52(0.19)	3.86(0.05)	0.02(0.00)	0.03(0.00)	0.24(0.00)
this study	RA-V03-1.0	7	78.51(0.30)	0.008(0.002	11.29(0.23)	1.44(0.02)	0.01(0.00)	0.02(0.00)	0.16(0.01)
this study	RA-V03-1.1	7	77.85(0.13)	0.007(0.001	13.04(0.08)	0.54(0.01)	0.02(0.00)	0.01(0.00)	0.13(0.02)
this study	RA-V04-0.8	7	76.36(0.10)	0.006(0.003	9.73(0.08)	4.40(0.02)	0.08(0.00)	0.07(0.00)	0.15(0.00)
this study	RA-V05-Arm	7	77.44(0.19)	0.04(0.00)	12.68(0.21)	0.67(0.00)	0.02(0.00)	0.01(0.00)	0.47(0.01)
this study	RA-V05-Chi	6	76.84(0.10)	0.09(0.00)	11.36(0.15)	2.31(0.03)	0.02(0.00)	0.00(0.00)	0.21(0.00)
this study	RA-V05-NZ	7	75.75(0.10)	0.14(0.00)	10.56(0.06)	3.42(0.04)	0.03(0.00)	0.00(0.00)	0.24(0.00)
this study	RA-V06-NZ	5	75.63(0.34)	0.02(0.00)	10.47(0.18)	3.76(0.10)	0.12(0.00)	0.01(0.00)	0.24(0.00)
this study	RA-V07-0.8	5	77.48(0.09)	0.01(0.00)	10.80(0.13)	2.34(0.01)	0.01(0.00)	0.02(0.00)	0.16(0.00)
this study	RA-V07-1.0	5	78.56(0.43)	0.01(0.00)	11.52(0.21)	1.19(0.01)	0.01(0.00)	0.01(0.00)	0.16(0.01)
this study	RA-V07-1.1	6	77.77(0.15)	0.01(0.00)	12.77(0.17)	0.55(0.00)	0.01(0.00)	0.00(0.00)	0.13(0.02)
this study	RA-V08-AgP	5	78.28(0.16)	0.03(0.00)	11.44(0.12)	1.47(0.00)	0.01(0.00)	0.01(0.00)	0.16(0.01)
this study	RA-V08-AuP	6	78.38(0.28)	0.01(0.00)	11.28(0.15)	1.48(0.03)	0.01(0.00)	0.02(0.00)	0.16(0.01)
this study	RA-V08-Pt	5	78.53(0.09)	0.01(0.00)	11.22(0.10)	1.46(0.00)	0.01(0.00)	0.01(0.00)	0.16(0.01)
this study	RA-V09-Bol	6	77.29(0.69)	0.06(0.00)	12.87(0.43)	0.64(0.01)	0.00(0.00)	0.02(0.00)	0.16(0.01)
this study	RA-V09-norm	6	77.88(0.21)	0.01(0.00)	11.35(0.06)	1.50(0.05)	0.01(0.00)	0.01(0.00)	0.16(0.01)
this study	RA-V09-V-mgt	6	77.53(0.29)	0.02(0.00)	12.79(0.16)	0.64(0.01)	0.00(0)	0.01(0.00)	0.16(0.02)
this study	RA-V10-0.8	7	76.73(0.20)	0.01(0.00)	9.70(0.12)	4.10(0.02)	0.05(0.00)	0.07(0.00)	0.15(0.00)
this study	RA-V10-1.0	6	77.98(0.19)	0.006(0.001	11.35(0.14)	1.72(0.02)	0.04(0.00)	0.06(0.00)	0.16(0.01)
this study	RA-V11-0.8	6	76.86(0.10)	0.02(0.00)	9.78(0.10)	3.65(0.02)	0.03(0.00)	0.06(0.00)	0.15(0.00)
this study	RA-V11-1.0	7	78.39(0.10)	0.02(0.00)	11.28(0.06)	1.42(0.01)	0.02(0.00)	0.04(0.00)	0.16(0.01)
this study	RA-V13-12	4	77.40(0.18)	0.34(0.00)	11.00(0.13)	2.57(0.02)	0.00(0.00)	0.07(0.00)	0.16(0.01)
this study	RA-V13-6	3	77.48(0.19)	0.16(0.00)	11.05(0.15)	2.67(0.04)	0.01(0.00)	0.07(0.00)	0.16(0.01)
this study	RA-V13-R	6	76.86(0.20)	0.01(0.00)	11.15(0.17)	2.86(0.02)	0.05(0.00)	0.08(0.00)	0.16(0.01)
this study	RA-V15-1.2	5	77.21(0.30)	0.005(0.001	13.02(0.22)	1.36(0.02)	0.05(0.00)	0.03(0.00)	0.13(0.02)
this study	RA-V15-Arm	6	77.17(0.34)	0.01(0.00)	12.68(0.33)	1.18(0.00)	0.07(0.00)	0.04(0.00)	0.47(0.01)
this study	RA-V15-Chi	6	76.75(0.31)	0.02(0.00)	11.04(0.27)	2.66(0.04)	0.08(0.00)	0.01(0.00)	0.21(0.00)
this study	RA-V17-0.8	6	75.41(0.16)	0.01(0.00)	9.57(0.09)	5.30(0.04)	0.06(0.00)	0.07(0.00)	0.15(0.00)
this study	RA-V17-1.0	6	76.98(0.11)	0.003(0.000	11.03(0.09)	2.95(0.04)	0.05(0.00)	0.07(0.00)	0.16(0.01)
this study	RA-V17-1.1	6	76.14(0.19)	0.007(0.001	12.68(0.14)	2.36(0.03)	0.04(0.00)	0.04(0.00)	0.13(0.02)
this study	RA-V18-0.8	6	76.60(0.19)	0.04(0.00)	9.57(0.16)	4.20(0.03)	0.03(0.00)	0.05(0.00)	0.15(0.00)
this study	RA-V18-1.0	6	77.70(0.18)	0.02(0.00)	11.03(0.06)	1.93(0.07)	0.02(0.00)	0.04(0.00)	0.16(0.01)
this study	RA-V18-1.1	6	77.42(0.15)	0.02(0.00)	12.79(0.16)	0.96(0.01)	0.02(0.00)	0.02(0.00)	0.13(0.02)
this study	RA-V19-0.8	6	75.27(0.11)	0.02(0.00)	9.45(0.07)	5.61(0.02)	0.06(0.00)	0.07(0.00)	0.15(0.00)
this study	RA-V19-1.0	6	76.85(0.05)	0.01(0.00)	11.11(0.12)	3.04(0.01)	0.04(0.00)	0.07(0.00)	0.16(0.01)
this study	RA-V19-1.1	6	76.50(0.18)	0.00(0.00)	12.58(0.12)	2.49(0.02)	0.05(0.00)	0.04(0.00)	0.13(0.02)
this study	RA-V21-6	6	76.60(0.14)	0.44(0.01)	11.16(0.06)	3.08(0.02)	0.01(0.00)	0.07(0.00)	0.16(0.01)
this study	RA-V21-rein	6	76.64(0.20)	0.03(0.00)	11.24(0.09)	3.16(0.04)	0.04(0.00)	0.07(0.00)	0.16(0.01)
this study	RA-V25-0.8	7	76.29(0.16)	0.03(0.00)	9.77(0.09)	4.36(0.11)	0.03(0.00)	0.06(0.00)	0.15(0.00)
this study	RA-V25-1.0	7	77.75(0.19)	0.01(0.00)	12.07(0.10)	1.48(0.02)	0.02(0.00)	0.05(0.00)	0.16(0.01)
this study	RA-V25-1.1	7	77.32(0.21)	0.01(0.00)	12.92(0.13)	1.26(0.01)	0.03(0.00)	0.03(0.00)	0.13(0.02)
this study	RA-V28	6	78.24(0.31)	0.01(0.00)	11.66(0.21)	1.33(0.01)	0.01(0)	0.02(0.00)	0.16(0.01)
this study	RA-V29-0.8	7	76.38(0.22)	0.03(0.00)	9.66(0.09)	4.43(0.03)	0.03(0.00)	0.05(0.00)	0.15(0.00)
this study	RA-V29-1.0	7	78.02(0.21)	0.03(0.01)	11.21(0.18)	1.97(0.03)	0.02(0)	0.04(0.00)	0.16(0.01)
this study	RA-V29-1.1	6	77.17(0.56)	0.01(0.00)	13.00(0.19)	1.09(0.02)	0.02(0.00)	0.02(0.00)	0.13(0.02)
this study	RA-V30 A	7	77.15(0.15)	0.008(0.001	10.56(0.10)	3.04(0.04)	0.04(0.00)	0.07(0.00)	0.15(0.00)
this study	RA-V30 B	3	77.29(1.17)	0.002(0.000	12.95(0.70)	0.97(0.01)	0.03(0.00)	0.02(0.00)	0.13(0.02)
this study	RA-V31 A	10	78.11(0.15)	0.01(0.00)	10.76(0.07)	2.69(0.02)	0.05(0.00)	0.07(0.00)	0.16(0.01)
this study	RA-V31 B	6	78.37(0.27)	0.005(0.001	11.40(0.15)	1.98(0.02)	0.05(0.00)	0.03(0.00)	0.16(0.02)
this study	RA-V37 A	5	78.72(0.53)	0.001(0.000	11.87(0.36)	1.27(0.03)	0.06(0.00)	#DIV/0!	0.13(0.02)

Values with "<" signs denote detection limits. Values in brackets refer to standard deviation.

Chemical composition

melt				magnetite									
Na2O	K2O	P2O5	Total	n:	SiO2	TiO2	Al2O3	MgO	CaO	MnO	FeO	Cr2O3	Tot
5.29(0.05)	3.99(0.02)		100.02	7	<1.11	0.01(0.00)	2.47(1.72)	0.36(0.03)		0.74(0.01)	99.2(0.01)	0.02(0.01)	100
4.67(0.04)	3.87(0.03)		99.85	7	<1.30	0.04(0.00)	2.23(3.29)	0.49(0.08)		0.70(0.00)	99(0(0.72)	0.02(0.00)	100
4.61(0.05)	3.92(0.02)		100.03	7	<5.42	0.05(0.01)	1.45(1.56)	0.11(0.02)		0.60(0.03)	99.3(0.02)	0.02(0.03)	100
5.36(0.03)	3.98(0.02)		100.18	7	<1.14	0.19(0.08)	0.41(0.45)	0.12(0.02)		0.38(0.01)	99.4(0.08)	0.03(0.01)	100
4.18(0.03)	4.62(0.04)		99.71	7	<6.98	0.24(0.04)	0.76(0.81)	0.24(0.03)		0.87(0.01)	98.8(0.06)	<0.0	100
4.95(0.05)	4.41(0.02)		100.02	6	<1.26	0.39(0.03)	0.89(0.99)	0.12(0.01)		0.93(0.00)	98.6(0.04)	0.00(0.00)	100
5.55(0.03)	4.44(0.01)		99.94	7	<0.89	0.42(0.03)	0.25(0.35)	0.08(0.00)		0.96(0.00)	98.6(0.07)	0.00(0.00)	100
5.54(0.06)	4.53(0.10)		100.36	5	<3.10	1.08(0.11)	0.53(0.85)	0.03(0.00)		0.60(0.00)	98.3(0.11)	<0.0	100
4.95(0.07)	4.12(0.06)		99.77	5	<3.58	0.10(0.06)	1.10(1.46)	0.41(0.02)		0.70(0.05)	99.1(0.05)	0.05(0.05)	100
4.80(0.15)	3.88(0.11)		100.01	5	<5.52	0.07(0.02)	0.34(0.83)	0.49(0.07)		0.68(0.01)	99(0(0.83)	0.05(0.01)	100
4.61(0.07)	4.04(0.09)		99.81	6	<6.26	0.11(0.02)	1.27(1.28)	0.15(0.01)		0.63(0.05)	99.2(0.02)	0.04(0.05)	100
4.74(0.06)	3.99(0.03)		100.01	5	<3.50	0.18(0.02)	0.78(0.94)	0.38(0.01)		0.63(0.01)	99.2(0.08)	0.03(0.01)	100
4.85(0.07)	3.96(0.04)		100.01	6	<5.93	0.07(0.03)	0.61(1.00)	0.44(0.07)		0.63(0.05)	99.3(0.03)	0.00(0.00)	100
4.77(0.02)	3.97(0.01)		100.01	5	<4.34	0.05(0.02)	0.29(0.35)	0.41(0.04)		0.65(0.02)	99.2(0.03)	0.04(0.02)	100
4.90(0.19)	4.18(0.07)		100.00	6	<7.95	0.46(0.04)	3.46(3.33)	0.50(0.09)		0.05(0.03)	99.4(0.04)	<0.0	100
4.85(0.04)	3.96(0.09)		99.61	6	<5.07	0.03(0.01)	1.75(2.49)	0.41(0.04)		0.64(0.04)	99.3(0.02)	0.00(0.04)	100
4.86(0.12)	4.10(0.07)		99.98	6	<5.59	0.14(0.01)	1.20(1.44)	0.36(0.08)		0.02(0.13)	99.8(0.01)	0.08(0.13)	100
5.39(0.04)	3.97(0.03)		100.21	7	<4.36	0.39(0.07)	0.53(1.45)	0.10(0.08)		0.25(0.02)	99.3(0.08)	0.06(0.02)	100
4.85(0.03)	3.92(0.04)		100.13	6	<5.48	0.45(0.09)	3.26(1.51)	0.25(0.02)		0.38(0.01)	99.1(0.09)	0.07(0.01)	100
5.40(0.05)	4.00(0.04)		99.83	6	<2.36	0.20(0.01)	0.76(1.03)	0.27(0.03)		0.50(0.01)	99.2(0.01)	0.03(0.01)	100
4.85(0.03)	3.96(0.04)		100.02	7	<5.30	0.39(0.04)	1.26(2.02)	0.46(0.03)		0.54(0.04)	99(0(0.05)	0.06(0.04)	100
4.68(0.06)	3.90(0.02)		100.17	4	<7.12	13.5(0.61)	2.31(1.95)	0.41(0.06)		0.12(0.03)	86.2(0.61)	0.08(0.03)	100
4.64(0.02)	3.89(0.02)		100.17	3	<3.50	7.57(0.39)	0.67(1.20)	0.33(0.02)		0.10(0.01)	92.3(0.39)	0.09(0.01)	100
4.74(0.01)	3.89(0.01)		99.82	6	<2.74	0.56(0.07)	0.48(1.05)	0.21(0.01)		0.26(0.01)	99.1(0.07)	0.04(0.01)	100
4.37(0.03)	3.79(0.04)		100.01	5	<13.0	0.47(0.14)	8.06(2.63)	0.07(0.09)		0.27(0.06)	99.2(0.13)	<0.0	100
4.15(0.08)	4.67(0.09)		100.48	6	<6.01	1.37(0.20)	4.34(2.03)	0.24(0.04)		0.70(0.01)	97.9(0.27)	<0.0	100
4.94(0.04)	4.47(0.05)		100.21	6	<7.30	1.26(0.20)	2.04(2.15)	0.06(0.03)		0.59(0.00)	98.1(0.21)	<0.0	100
5.33(0.04)	3.92(0.02)		99.87	6	<4.18	0.40(0.05)	1.28(1.86)	0.11(0.03)		0.23(0.01)	99.3(0.05)	0.05(0.01)	100
4.76(0.05)	3.82(0.02)		99.86	6	<4.43	0.18(0.01)	2.63(2.73)	0.21(0.05)		0.28(0.01)	99.5(0.02)	0.04(0.01)	100
4.47(0.03)	3.90(0.03)		99.81	6	<4.40	0.39(0.03)	4.59(2.88)	0.10(0.02)		0.20(0.01)	99.3(0.02)	0.05(0.01)	100
5.42(0.04)	4.05(0.01)		99.99	6	<2.98	0.12(0.01)	0.56(1.21)	0.53(0.08)		0.63(0.01)	99.2(0.01)	0.04(0.01)	100
4.88(0.07)	4.01(0.05)		99.67	6	<3.49	0.11(0.03)	2.06(0.70)	0.52(0.04)		0.56(0.02)	99.3(0.03)	0.05(0.02)	100
4.53(0.04)	3.94(0.02)		99.75	6	<2.51	0.14(0.02)	3.55(0.59)	0.23(0.03)		0.43(0.01)	99.4(0.01)	0.03(0.01)	100
5.27(0.04)	3.93(0.04)		99.89	6	<5.09	0.65(0.06)	1.86(1.21)	0.19(0.02)		0.23(0.03)	99.1(0.05)	0.07(0.03)	100
4.77(0.02)	3.83(0.02)		99.93	6	<4.33	0.55(0.10)	2.24(1.30)	0.25(0.03)		0.28(0.04)	99.1(0.10)	0.10(0.04)	100
4.46(0.04)	3.89(0.02)		100.19	6	<3.94	0.23(0.06)	5.12(0.36)	0.11(0.03)		0.27(0.01)	99.4(0.06)	0.03(0.01)	100
4.76(0.07)	3.85(0.01)		100.01	6	<1.65	3.24(0.09)	0.85(0.54)	0.40(0.02)		0.11(0.02)	96.6(0.09)	0.08(0.02)	100
4.69(0.02)	3.81(0.03)		99.72	6	<6.46	0.22(0.02)	1.10(1.05)	0.35(0.05)		0.33(0.06)	99.4(0.03)	0.03(0.06)	100
5.29(0.04)	3.99(0.04)		99.87	7	<8.69	0.28(0.05)	2.21(3.15)	0.32(0.05)		0.36(0.07)	99.3(0.05)	0.03(0.07)	100
4.61(0.05)	3.89(0.05)		99.92	7	<6.05	0.21(0.06)	2.82(1.60)	0.38(0.05)		0.37(0.04)	99.4(0.05)	0.05(0.04)	100
4.52(0.05)	3.93(0.05)		100.05	7	<7.44	0.16(0.02)	4.53(1.82)	0.15(0.03)		0.32(0.01)	99.5(0.02)	0.05(0.01)	100
4.93(0.10)	3.98(0.04)		100.22	6	<3.28	0.09(0.02)	0.30(0.36)	0.72(0.07)		0.64(0.00)	99.2(0.02)	0.03(0.00)	100
5.43(0.07)	4.01(0.05)		100.05	7	<3.03	0.07(0.01)	0.51(0.47)	0.55(0.03)		0.65(0.01)	99.2(0.02)	0.03(0.01)	100
4.80(0.08)	3.9(0.03)		100.02	7	<3.50	0.13(0.04)	1.90(1.26)	0.74(0.06)		0.57(0.00)	99.2(0.04)	0.03(0.00)	100
4.54(0.04)	3.96(0.04)		99.87	6	<3.08	0.05(0.01)	4.13(1.47)	0.29(0.02)		0.44(0.01)	99.4(0.02)	0.03(0.01)	100
5.40(0.04)	3.73(0.06)		100.20	7	<4.02	0.37(0.06)	2.42(2.44)	0.22(0.05)		0.32(0.02)	99.2(0.05)	0.05(0.02)	100
4.66(0.33)	4.08(0.16)		100.17	3	<4.75	0.18(0.03)	0.94(0.92)	0.15(0.03)		0.36(0.00)	99.4(0.06)	0.03(0.00)	100
4.57(0.05)	3.77(0.05)		100.21	10	<4.65	0.82(0.34)	0.65(0.83)	0.22(0.03)		0.29(0.04)	98.8(0.37)	0.02(0.04)	100
4.46(0.05)	3.74(0.07)		100.24	6	<4.56	0.29(0.06)	3.94(0.63)	0.11(0.02)		0.32(0.01)	99.3(0.07)	0.04(0.01)	100
4.34(0.08)	3.78(0.09)		100.21	5	<7.87	0.17(0.04)	11.3(9.59)	#DIV/0!		0.42(0)	99.3(0.07)	#DIV/0!	100

Supplementary Table 8.S.1/1b: Dataset used for the calibration and testing of the FeTiMM oxybarometer.

Own experiments(ilmenite-undersaturated). | **Experimental conditions** | | | | **Calculated values**

Reference	Run:	T	10000_T	p (bar)	dFMQ experim.	AMCNK	DFe mgt-melt	DTi mgt-melt
this study	RA-V03-0.8	800	9.32	2000	4.04	0.71	25.70	2.44
this study	RA-V03-1.0	800	9.32	2000	4.04	0.92	68.75	4.77
this study	RA-V03-1.1	800	9.32	2000	4.04	1.08	182.33	7.52
this study	RA-V04-0.8	800	9.32	2000	0.66	0.72	22.58	28.98
this study	RA-V05-Arm	800	9.32	2000	4.04	1.00	145.92	5.88
this study	RA-V05-Chi	800	9.32	2000	4.04	0.85	42.69	4.18
this study	RA-V05-NZ	800	9.32	2000	4.04	0.73	28.79	2.94
this study	RA-V06-NZ	800	9.32	2000	0.66	0.72	26.14	38.51
this study	RA-V07-0.8	800	9.32	2000	4.04	0.83	42.32	5.78
this study	RA-V07-1.0	800	9.32	2000	4.04	0.93	83.22	5.31
this study	RA-V07-1.1	800	9.32	2000	4.04	1.04	178.81	8.23
this study	RA-V08-AgP	800	9.32	2000	4.04	0.92	67.28	5.12
this study	RA-V08-AuP	800	9.32	2000	4.04	0.89	66.98	5.83
this study	RA-V08-Pt	800	9.32	2000	4.04	0.90	67.81	4.32
this study	RA-V09-Bol	800	9.32	2000	4.04	0.99	154.50	7.03
this study	RA-V09-norm	800	9.32	2000	4.04	0.90	65.95	3.66
this study	RA-V09-V-mgt	800	9.32	2000	4.04	1.00	155.06	6.41
this study	RA-V10-0.8	800	9.32	2000	0.66	0.71	24.22	30.27
this study	RA-V10-1.0	800	9.32	2000	0.66	0.89	57.41	67.81
this study	RA-V11-0.8	800	9.32	2000	2.70	0.72	27.19	8.55
this study	RA-V11-1.0	800	9.32	2000	2.70	0.89	69.38	17.00
this study	RA-V13-12	900	8.52	2000	0.66	0.89	33.50	39.62
this study	RA-V13-6	900	8.52	2000	0.66	0.89	34.46	46.91
this study	RA-V13-R	900	8.52	2000	0.66	0.89	34.60	51.25
this study	RA-V15-1.2	800	9.32	2000	0.66	1.12	72.72	82.78
this study	RA-V15-Arm	800	9.32	2000	0.66	0.99	82.29	96.97
this study	RA-V15-Chi	800	9.32	2000	0.66	0.82	36.84	52.49
this study	RA-V17-0.8	900	8.52	2000	0.66	0.71	18.72	26.18
this study	RA-V17-1.0	900	8.52	2000	0.66	0.88	33.72	46.68
this study	RA-V17-1.1	900	8.52	2000	0.66	1.06	41.98	50.85
this study	RA-V18-0.8	900	8.52	2000	4.09	0.70	23.61	2.75
this study	RA-V18-1.0	900	8.52	2000	4.09	0.86	51.25	4.52
this study	RA-V18-1.1	900	8.52	2000	4.09	1.06	103.34	4.82
this study	RA-V19-0.8	950	8.18	1000	0.66	0.71	17.65	22.62
this study	RA-V19-1.0	950	8.18	1000	0.66	0.89	32.51	39.52
this study	RA-V19-1.1	950	8.18	1000	0.66	1.06	39.82	38.82
this study	RA-V21-6	1000	7.85	1500	2.37	0.89	31.31	7.25
this study	RA-V21-rein	1000	7.85	2000	2.37	0.91	31.38	7.38
this study	RA-V25-0.8	900	8.52	2000	2.52	0.72	22.76	7.45
this study	RA-V25-1.0	900	8.52	2000	2.52	0.99	67.10	15.07
this study	RA-V25-1.1	900	8.52	2000	2.52	1.07	78.46	15.21
this study	RA-V28	800	9.32	1000	4.04	0.91	74.25	6.18
this study	RA-V29-0.8	950	8.18	1000	4.11	0.70	22.36	2.53
this study	RA-V29-1.0	950	8.18	1000	4.11	0.89	50.29	3.96
this study	RA-V29-1.1	950	8.18	1000	4.11	1.08	90.63	4.15
this study	RA-V30 A	800	9.32	1000	0.66	0.78	32.58	44.11
this study	RA-V30 B	800	9.32	1000	0.66	1.04	102.08	75.24
this study	RA-V31 A	900	8.52	1000	0.66	0.89	36.67	57.83
this study	RA-V31 B	850	8.92	3000	0.66	0.98	50.09	50.87
this study	RA-V37 A	800	9.32	5000	0.66	1.03	77.98	91.39

AMCNK refers to molar $Al_2O_3/(CaO+MgO+Na_2O+K_2O)$, whereas logD to $log(DFeO_{tot}^{mgt/melt}/DTiO_2^{mgt/melt})$.

Calculated values				Errors		
					FeTiMM error	
DFe/DTi				Propag.	"model"	Propag.
mgt/melt	log D	FeTiMM	Mn/Mg	anal. error	error	total error
10.55	1.03	4.73	2.68	0.34	0.37	0.51
14.40	1.15	4.30	2.14	0.37	0.30	0.48
24.26	1.39	4.49	2.14	0.27	0.29	0.40
0.78	-0.11	0.34	2.43	1.05	0.19	1.06
24.80	1.39	4.76	2.11	0.32	0.32	0.46
10.22	1.01	4.09	2.34	0.17	0.30	0.34
9.78	0.99	4.49	2.49	0.17	0.34	0.38
0.68	-0.17	0.13	2.89	0.22	0.19	0.29
7.33	0.91	3.83	2.41	0.87	0.28	0.91
15.66	1.21	4.49	2.05	0.55	0.31	0.63
21.73	1.34	4.46	1.94	0.39	0.30	0.49
13.14	1.11	4.21	2.20	0.34	0.30	0.45
11.49	1.09	4.21	2.15	0.63	0.29	0.69
15.69	1.22	4.62	2.35	0.62	0.32	0.70
21.98	1.34	4.64	2.11	0.16	0.31	0.35
18.00	1.27	4.77	2.29	0.45	0.33	0.56
24.20	1.38	4.73	2.27	0.22	0.32	0.39
0.80	-0.09	0.41	3.14	0.36	0.19	0.41
0.85	-0.07	0.50	2.44	0.36	0.16	0.40
3.18	0.50	2.69	2.87	0.17	0.24	0.29
4.08	0.61	2.70	2.50	0.21	0.22	0.31
0.85	-0.07	0.49	2.37	0.08	0.16	0.18
0.73	-0.13	0.29	2.11	0.09	0.16	0.19
0.68	-0.17	0.17	1.94	0.26	0.17	0.31
0.88	-0.05	0.55	2.52	0.43	0.15	0.46
0.85	-0.07	0.50	1.93	0.23	0.15	0.28
0.70	-0.15	0.22	1.85	0.27	0.17	0.32
0.71	-0.14	0.21	2.53	0.26	0.19	0.32
0.72	-0.14	0.27	1.85	0.18	0.17	0.25
0.83	-0.08	0.45	1.68	0.19	0.15	0.24
8.57	0.94	4.44	2.03	0.23	0.35	0.41
11.35	1.07	4.25	2.00	0.44	0.30	0.53
21.46	1.33	4.38	1.70	0.27	0.29	0.39
0.78	-0.11	0.35	1.48	0.22	0.19	0.29
0.82	-0.08	0.45	1.76	0.32	0.16	0.36
1.03	0.02	0.74	1.60	0.36	0.15	0.39
4.32	0.64	2.76	1.70	0.05	0.22	0.23
4.25	0.63	2.70	1.54	0.16	0.22	0.27
3.06	0.49	2.62	1.98	0.35	0.23	0.42
4.45	0.65	2.62	1.94	0.52	0.21	0.56
5.16	0.70	2.62	2.02	0.33	0.20	0.39
12.02	1.09	4.16	2.30	0.47	0.29	0.55
8.82	0.95	4.46	1.91	0.35	0.35	0.49
12.71	1.11	4.27	1.77	0.71	0.30	0.77
21.84	1.35	4.38	1.45	0.29	0.29	0.40
0.74	-0.13	0.28	2.51	0.32	0.18	0.36
1.36	0.13	1.05	1.85	0.45	0.15	0.48
0.63	-0.18	0.14	1.83	0.73	0.17	0.75
0.98	0.00	0.69	2.05	0.38	0.16	0.41
0.85	-0.06	0.52	#####	0.39	0.15	0.41

Supplementary Table 8.S.1/2a: Dataset used for the calibration and testing of the FeTiMM oxybarometer

Ilmenite-undersaturated experiments taken from the literature.

			Chemical composition melt						
Reference	Run:	n:	SiO2	TiO2	Al2O3	FeO	MnO	MgO	CaO
Andujar et al, 2016	usc32	5	60.18(0.59)	0.98(0.15)	16.75(0.33)	7.58(0.21)	0.28(0.15)	2.2(0.06)	5.74(0.12)
Andujar et al, 2016	usc52	3	69.11(0.97)	0.62(0.11)	15.42(0.38)	3.36(0.01)	0.07(0.04)	0.78(0.04)	3.04(0.46)
Andujar et al, 2016	usc57b	2	64.1(0.34)	1.05(0.06)	16.22(0.25)	4.67(0.32)	0.28(0.14)	2.09(0.09)	5.02(0.03)
Andujar et al, 2016	usc62	11	60.87(0.13)	1.15(0.08)	16.41(0.14)	5.85(0.06)	0.2(0.21)	2.77(0.08)	6.55(0.21)
Andujar et al, 2016	usc65	4	65.97(0.44)	0.94(0.07)	15.36(0.79)	5.08(0.4)	0.19(0.14)	1.27(0.07)	3.74(0.34)
Andujar et al, 2016	usc66	3	70.21(0.57)	0.85(0.11)	13.38(0.2)	4.62(0.11)	0.09(0.1)	0.63(0.07)	2.3(0.14)
Andujar et al, 2016	usc70	3	62.2(0.43)	1.3(0.09)	15.38(0.05)	8.09(0.59)	0.09(0.12)	1.72(0.03)	4.69(0.08)
Andujar et al, 2016	usc72	4	63.3(0.33)	1.08(0.09)	16.06(0.14)	5.16(0.11)	0.23(0.08)	1.87(0.03)	5.65(0.4)
Andujar et al, 2016	usc73	4	65.28(0.31)	0.94(0.04)	15.3(0.2)	4.92(0.09)	0.2(0.07)	1.51(0.09)	4.45(0.2)
Andujar et al, 2016	usc74	2	68.94(0.65)	0.81(0.03)	13.96(0.53)	4.16(0.24)	0.1(0.06)	1.32(0.03)	3.29(0.26)
Andujar et al, 2016	usc75	3	71.91(0.33)	0.48(0.09)	13.27(0.61)	2.87(0.47)	0.07(0.01)	0.74(0.01)	2.55(0.22)
Andujar et al, 2016	usc77	3	62.76(0.53)	1.11(0.04)	17.26(0.22)	4.69(0.44)	0.12(0.1)	2.17(0.07)	5.72(0.2)
Andujar et al, 2016	usc82	10	64.62(0.76)	0.61(0.13)	17.25(0.32)	4.26(0.36)	0.17(0.07)	1.17(0.06)	5.57(0.07)
Andujar et al, 2016	usc83	1	65.23()	0.78()	16.93()	5.12()	0.22()	0.66()	4.43()
Andujar et al, 2016	usc84	9	68.32(0.42)	0.54(0.05)	15.38(0.24)	3.85(0.46)	0.11(0.09)	0.85(0.1)	3.52(0.12)
Berndt et al, 2005	36	4	57.57(0.55)	1.07(0.01)	18.04(0.41)	6.82(0.42)	0.12(0.04)	3.88(0.28)	8.05(0.14)
Berndt et al, 2005	37	3	56.17(0.83)	1.05(0.11)	18.79(0.33)	6.5(0.27)	0.13(0.14)	4.47(0.07)	8.76(0.29)
Berndt et al, 2005	41	2	51.13(0.33)	0.98(0.05)	18.17(0.1)	8.62(0.46)	0.24(0.14)	6.03(0.04)	12.1(0.08)
Berndt et al, 2005	49	4	63.16(0.96)	0.7(0.06)	16.75(0.5)	5.31(0.38)	0.12(0.13)	2.52(0.3)	6.43(0.33)
Berndt et al, 2005	94	3	54.32(0.64)	1.49(0.14)	16.36(0.52)	7.46(0.46)	0.15(0.06)	5.88(0.15)	10.7(0.21)
Berndt et al, 2005	99	3	56.7(0.2)	1.42(0.08)	18.42(0.64)	5.82(0.89)	0.14(0.05)	4.21(0.07)	9.3(0.15)
Brugger and Hammer, 2010	15-3	10	72.27(0.86)	0.35(0.08)	13.91(0.41)	1.31(0.1)	0.14(0.02)	0.34(0.01)	0.92(0.14)
Brugger and Hammer, 2010	18-1	6	71.21(1.38)	0.39(0.08)	14.26(0.16)	1.36(0.24)	0.12(0.01)	0.3(0.02)	1.28(0.05)
Brugger and Hammer, 2010	22-2	11	71.2(0.83)	0.38(0.08)	15.05(0.22)	1.76(0.12)	0.15(0.01)	0.42(0.07)	1.31(0.26)
Toplis et al, 1994	Fe-121	5	69.8(0.36)	1.81(0.07)	11.73(0.25)	6.13(0.26)		0.92(0.04)	3.95(0.07)
Toplis et al, 1994	Fe-122	10	67.07(0.77)	2.21(0.28)	11.51(0.23)	6.7(0.34)		1.35(0.07)	4.66(0.21)
Toplis et al, 1995	41	12	49.2(0.4)	3.7(0.16)	11.72(0.18)	15.2(0.32)		4.85(0.07)	9.62(0.07)

Values in brackets refer to standard deviation.

Supplementary Table 8.S.1/2b: Dataset used for the calibration and testing of the FeTiMM oxybarometer.

Ilmenite-undersaturated experiments taken from the literature.

			Experimental conditions				Calculated values		
Reference	Run:	T	10000_T	p (bar)	dFMQ experim.		AMCNK	DFe mgt-melt	DTi mgt-melt
Andujar et al, 2016	usc32	975	8.01	2000	2.24		0.67	9.81	12.27
Andujar et al, 2016	usc52	950	8.18	2000	1.88		0.85	23.33	22.52
Andujar et al, 2016	usc57b	975	8.01	1000	2.57		0.68	16.34	6.51
Andujar et al, 2016	usc62	1000	7.85	2000	2.19		0.59	13.10	3.92
Andujar et al, 2016	usc65	1000	7.85	2000	1.31		0.76	14.04	11.56
Andujar et al, 2016	usc66	1000	7.85	2000	0.19		0.81	14.96	17.41
Andujar et al, 2016	usc70	1000	7.85	4000	0.77		0.71	8.18	12.88
Andujar et al, 2016	usc72	1000	7.85	1000	2.57		0.65	14.47	6.39
Andujar et al, 2016	usc73	1000	7.85	1000	2.29		0.68	15.17	9.82
Andujar et al, 2016	usc74	1000	7.85	1000	2		0.71	17.23	13.00
Andujar et al, 2016	usc75	1000	7.85	1000	1.81		0.73	25.11	27.25
Andujar et al, 2016	usc77	950	8.18	4000	1.93		0.70	16.42	5.15
Andujar et al, 2016	usc82	925	8.35	4000	1.69		0.77	18.00	14.89
Andujar et al, 2016	usc83	925	8.35	4000	1.53		0.87	15.08	12.77
Andujar et al, 2016	usc84	925	8.35	4000	1.36		0.80	19.96	21.39
Berndt et al, 2005	36	1000	7.85	2050	4.3		0.58	10.90	3.06
Berndt et al, 2005	37	1000	7.85	2050	4.3		0.56	11.43	2.37
Berndt et al, 2005	41	1050	7.56	2020	4.31		0.44	8.58	2.52
Berndt et al, 2005	49	950	8.18	2030	4.28		0.65	14.63	3.10
Berndt et al, 2005	94	1050	7.56	2040	4.31		0.41	10.13	1.32
Berndt et al, 2005	99	1000	7.85	2040	4.3		0.54	12.61	1.72
Brugger and Hammer, 2010	15-3	880	8.67	260	1.46		0.93	61.90	18.40
Brugger and Hammer, 2010	18-1	880	8.67	680	1.46		0.95	59.05	17.08
Brugger and Hammer, 2010	22-2	880	8.67	50	1.46		0.93	42.98	25.26
Toplis et al, 1994	Fe-121	1072	7.43	1	1.87		0.72	12.53	7.14
Toplis et al, 1994	Fe-122	1072	7.43	1	1.87		0.62	11.34	5.96
Toplis et al, 1995	41	1122	7.17	1	1.35		0.33	4.57	4.27

Chemical composition

melt Na2O	K2O	P2O5	Total	n:	SiO2	TiO2	Al2O3	MgO	CaO	MnO	FeO	Cr2O3	Tot
4.46(0.27)	1.52(0.03)	0.32(0.02)	99.69	3	0.23(0.17)	12.0(0.15)	3.7(0.13)	3.07(0.2)	0.15(0.0	0.48(0.07)	74.3(0.55)		94
4.76(0.21)	2.56(0.25)	0.28(0.1)	99.72	1			3.35()	2.9()	0.2()	0.77()	78.4()		100
4.56(0.41)	1.69(0.04)	0.32(0.04)	99.68	2	0.16(0.16)	6.84(6.83)	3.49(3.93)	4.16(0.53)	0.15(0.0	0.66(0.53)	76.3()		92
4.45(0.14)	1.38(0.05)	0.37(0.07)	99.63	2	0.11(0.05)	4.51(0.19)	3.17(0.1)	4.11(0.12)	0.14(0.0	0.62(0.12)	76.6(0.71)		89
4.72(0.06)	2.36(0.07)	0.38(0.11)	99.63	2	0.31(0.16)	10.8(0.03)	2.93(0.06)	2.98(0.13)	0.21(0.0	0.56(0.13)	71.3(0.79)		89
4.24(0.12)	3.46(0.06)	0.22(0.08)	99.78	1			2.86()	2.01()	0.45()	0.57()	69.1()		93
4.09(0.34)	2.04(0.08)	0.4(0.04)	99.60	2	0.27(0.03)	16.7(0.3)	3.74(0.07)	2.53(0.06)	0.23(0.0	0.38(0.06)	66.1(0.78)		90
4.7(0.23)	1.69(0.05)	0.25(0.03)	99.74	2	0.17(0)	6.9((0.27)	3.95(0.02)	4.04(0.14)	0.15(0.0	0.64(0.14)	74.6(1.08)		91
5.08(0.25)	1.92(0.15)	0.41(0.09)	99.60	1			3.33()	3.49()	0.15()	0.53()	74.6()		92
4.77(0.31)	2.26(0.06)	0.4(0.15)	99.61	1			2.94()	2.9()	0.34	0.49()	71.6(0)		90
5.39(0.09)	2.58(0.14)	0.14(0.01)	99.86	1			2.57()	2.45()	0.21	0.35()	72.0(0.1)		92
4.37(0.2)	1.44(0.11)	0.37(0.07)	99.64	2	0.15(0.05)	5.72(0.18)	3.13(0.01)	3.52(0.08)	0.11(0.0	0.58(0.08)	77.0(0.44)		90
4.55(0.82)	1.66(0.07)	0.15(0.11)	99.86	3	0.25(0.08)	9.08(0.38)	3.28(0.27)	2.01(0.15)	0.16(0.0	0.59(0.15)	76.6(0.74)		92
4.78()	1.67()	0.17()	99.82	3	0.24(0.06)	9.96(0.19)	3.39(0.07)	1.69(0.08)	0.1(0.0	0.61(0.08)	77.1(1.15)		93
5.01(0.08)	2.27(0.12)	0.17(0.15)	99.85	5	0.26(0.13)	11.5(0.19)	3.31(0.12)	1.75(0.1)	0.19(0.0	0.59(0.1)	76.8()		95
3.84(0.23)	0.29(0.04)	0.33(0.17)	100.01	2	0.22(0.08)	3.27(0.07)	6.06(0.07)	6.96(0.02)	0.41(0.0	0.38(0.02)	74.3(1)		92
3.74(0.67)	0.14(0.09)	0.24(0.02)	99.99	2	0.25(0.16)	2.49(0.06)	7.13(0.04)	7.84(0.04)	0.4(0.1	0.38(0.04)	74.2(1)		93
2.43(0.18)	0.07(0.01)	0.15(0.09)	100.01	2	0.49(0.2)	2.47(0.02)	7.2(0.74)	7.49(0.06)	0.45(0.0	0.38(0.06)	73.9(1)		92
4.45(0.66)	0.29(0.1)	0.25(0.25)	99.98	4	0.28(0.03)	2.17(0.12)	4.94(0.01)	6.22(0.05)	0.37(0.0	0.38(0.05)	77.7(1)		92
3.31(0.2)	0.17(0.04)	0.13(0.06)	100.01	2	0.18(0.01)	1.96(0.04)	4.85(0.14)	8.53(0.02)	0.32(0.0	0.41(0.02)	75.5(1)		92
3.67(0.41)	0.24(0.06)	0.08(0.03)	100.00	3	0.22(0.04)	2.44(0.04)	5.91(0.02)	8.46(0.11)	0.43(0.0	0.56(0.11)	73.3(1)		91
5.3(0.12)	3.49(0.06)	0.07(0.03)	98.03	1			2.11()	2.37()	0.01()	1.52()	81.0()		94
5.15(0.25)	3.13(0.04)	0.06(0.02)	97.20	1			2.28()	2.59()	0.04()	1.87()	80.3()		94
5.34(0.37)	3.7(0.2)	0.06(0.05)	99.31	1			3.54()	2.31()	0.03()	1.13()	75.6()		93
2.93(0.27)	1.81(0.08)	0.05(0.05)	99.08	7	0.11(0.05)	12.9(0.26)	1.72(0.08)	2.44()	0.16		76.8(0.96)		94
3.07(0.41)	1.61(0.06)	0.39(0.16)	98.18	7	0.11(0.05)	13.1(0.51)	1.74(0.05)	2.76()	0.09		75.9(0.89)		94
2.9(0.08)	0.57(0.03)		97.76	7	0.55(0.02)	15.8(0.19)	3.98(0.05)	4.74()	0.53		69.5(0.39)		95

Errors

FeTiMM error

DFe/DTi mgt/melt	log D	FeTiMM	Mn/Mg	Propag. anal. error	"model" error	Propag. total error
0.80	-0.10	0.39	1.23	0.27	0.19	0.34
1.04	0.02	0.78	2.96	0.26	0.17	0.31
2.51	0.40	2.37	1.18		0.23	
3.34	0.52	3.14	2.09	0.16	0.29	0.33
1.21	0.08	1.07	1.26	0.18	0.18	0.25
0.86	-0.07	0.51	1.99	0.20	0.17	0.26
0.63	-0.20	0.01	2.87	0.17	0.19	0.26
2.26	0.35	2.25	1.29	0.17	0.23	0.28
1.55	0.19	1.53	1.15	0.08	0.20	0.21
1.33	0.12	1.24	2.23	0.12	0.19	0.22
0.92	-0.04	0.63	1.51	0.41	0.18	0.45
3.19	0.50	2.74	2.98	0.18	0.24	0.30
1.21	0.08	1.05	2.02	0.37	0.18	0.41
1.18	0.07	0.96	1.08	0.03	0.17	0.17
0.93	-0.03	0.64	2.61	0.23	0.17	0.29
3.57	0.55	3.31	1.77	0.13	0.30	0.33
4.82	0.68	3.99	1.67	0.23	0.35	0.42
3.41	0.53	3.84	1.27	0.18	0.38	0.42
4.72	0.67	3.57	1.28	0.23	0.30	0.38
7.70	0.89	6.07	1.88	0.29	0.60	0.67
7.34	0.87	4.93	1.99	0.34	0.43	0.55
3.36	0.53	2.35	1.56	0.33	0.20	0.38
3.46	0.54	2.34	1.81	0.36	0.20	0.41
1.70	0.23	1.43	1.37	0.30	0.17	0.34
1.75	0.24	1.70	#####	0.11	0.20	0.22
1.90	0.28	2.01	#####	0.27	0.22	0.35
1.07	0.03	1.18	#####	0.14	0.29	0.32

Supplementary Table 8.S.1/3a: Dataset used for the calibration and testing of the FeTiMM oxybarometer.

Ilmenite-saturated experiments taken from the literature.	Chemical composition melt							
Reference	Run:	n:	SiO2	TiO2	Al2O3	FeO	MnO	MgO	CaO
Andujar et al, 2016	usc28	4	61.91(0.45)	0.94(0.11)	16.1(0.11)	7.58(0.27)	0.1(0.08)	1.59(0.05)	5.06(0.11)
Andujar et al, 2016	usc29	1	64.44()	0.83()	14.72()	6.9()	0.27()	1.43()	4.21()
Andujar et al, 2016	usc87	10	61.81(0.51)	0.84(0.09)	16.53(0.13)	6.74(0.22)	0.15(0.1)	1.63(0.03)	5.7(0.11)
Berndt et al, 2005	96	5	59.03(0.71)	1.19(0.26)	17.96(2.23)	5.74(0.74)	0.23(0.22)	3.7(0.32)	7.72(0.77)
Berndt et al, 2005	98	4	59.73(1.23)	0.9(0.23)	17.92(1.08)	5.56(0.53)	0.09(0.02)	3.19(0.31)	7.58(0.42)
Berndt et al, 2005	102	5	63.13(0.96)	1.05(0.08)	16.18(0.56)	5.43(0.42)	0.08(0.06)	1.7(0.25)	5.59(0.55)
Berndt et al, 2005	103	3	64.87(0.13)	0.82(0.23)	17.18(0.25)	3.92(0.26)	0.2(0)	2.61(0.1)	6(0.14)
Berndt et al, 2005	104	5	65.88(0.85)	0.84(0.09)	15.94(0.42)	4.11(0.16)	0.07(0.07)	1.81(0.26)	5.85(0.25)
Berndt et al, 2005	105	2	65.98(1.18)	0.78(0.09)	16.79(0.06)	3.7(0.25)	0.13(0.13)	1.5(0.09)	5.42(0.1)
Berndt et al, 2005	106	3	70.02(1.13)	0.65(0.09)	13.08(1.05)	3.7(0.02)	0.05(0.06)	1.21(0.14)	4.13(0.36)
Berndt et al, 2005	111	4	65.36(1.21)	0.91(0.12)	16.32(0.94)	4.22(0.65)	0.18(0.05)	1.73(0.23)	6.03(0.45)
Blatter et al, 2013	2370	24	65.2(0.6)	0.73(0.08)	17.4(0.05)	3.54(0.36)	0.11()	1.92(0.39)	4.7(0.21)
Bolte et al, 2015	A18	10	76.12(0.42)	0.24(0.02)	12.43(0.32)	1.33(0.08)	0.05(0.01)	0.10(0.01)	0.67(0.04)
Bolte et al, 2015	F09	11	73.52(0.39)	0.32(0.04)	13.14(0.18)	2.25(0.20)	0.05(0.01)	0.16(0.09)	0.86(0.02)
Bolte et al, 2015	M14	14	75.45()	0.31()	12.80()	1.46()	0.04()	0.11()	0.67()
Brugger and Hammer, 2010	11-1	8	75.81(1.42)	0.36(0.07)	11.26(0.62)	1.2(0.13)	0.06(0.02)	0.06(0.01)	0.26(0.07)
Brugger and Hammer, 2010	16-2	10	71.3(0.35)	0.41(0.08)	13.52(0.16)	1.37(0.12)	0.09(0.04)	0.32(0.02)	0.94(0.09)
Freise et al, 2009	50	7	54.82(0.17)	1.89(0.04)	18.93(0.19)	6.02(0.22)	0.19(0.05)	4.23(0.08)	8.39(0.06)
Freise et al, 2009	51	5	55.12(0.21)	1.56(0.05)	19.06(0.13)	5.73(0.1)	0.18(0.05)	4.75(0.16)	9.34(0.19)
Freise et al, 2009	52	5	57.08(0.41)	1.23(0.07)	19.35(0.1)	5.03(0.26)	0.12(0.07)	3.43(0.09)	8.3(0.07)
Freise et al, 2009	53	2	60.09(0.09)	1.04(0.05)	19.07(0.35)	4.57(0.06)	0.17(0)	2.59(0.06)	6.36(0.21)
Freise et al, 2009	57	5	57.53(0.45)	1.62(0.08)	18.16(0.72)	5.78(0.16)	0.15(0.05)	3.63(0.29)	6.61(0.47)
Freise et al, 2009	58	2	60.25(0.87)	1.04(0.1)	19.5(0.76)	3.92(0.36)	0.06(0.01)	1.9(0.68)	5.62(0.51)
Freise et al, 2009	110	4	65.46(0.73)	0.78(0.12)	18.81(0.21)	1.6(0.29)	0.02(0.01)	0.42(0.11)	6.17(0.12)
Freise et al, 2009	114	6	57.47(0.52)	1.63(0.06)	17.74(0.48)	6.55(0.22)	0.12(0.09)	4.07(0.1)	8.48(0.21)
Gardner et al, 1995	G-8a-M	6	74.93()	0.21()	11.77()	1.1()	0.03()	0.18()	0.89()
Gardner et al, 1995	G-8b-M	6	74.14()	0.27()	11.82()	1.23()	0.03()	0.23()	1.03()
Gardner et al, 1995	G-10a-M	6	72.6()	0.28()	12.4()	1.31()	0.04()	0.26()	1.15()
Gardner et al, 1995	G-10b-M	6	72.44()	0.28()	12.33()	1.47()	0.02()	0.28()	1.25()
Gardner et al, 1995	G-15a-M	10	68.43()	0.28()	14.08()	2.06()	0.06()	0.52()	2.07()
Gardner et al, 1995	G-16a-M	8	70.41()	0.27()	13.41()	1.6()	0.05()	0.41()	1.68()
Gardner et al, 1995	G-16b-M	8	70.83()	0.31()	13.12()	1.75()	0.06()	0.42()	1.65()
Parat et al, 2008	2	9	68.87(0.26)	0.57(0.04)	16.4(0.19)	3.24(0.28)	0.07(0.09)	0.78(0.01)	3.29(0.1)
Pietranik et al, 2009	800/1/2	6	67.9(0.9)	0.2(0)	13.8(0.3)	1.5(0.3)	0(b.d.)	0.2(0.1)	2.1(0.2)
Scaillet and Evans, 1999	8	7	75.54(0.4)	0.17(0.05)	14.38(0.13)	1.04(0.15)	0.07(0.06)	0.38(0.13)	1.95(0.18)
Scaillet and Evans, 1999	51	7	75.6(0.79)	0.23(0.04)	14.64(0.21)	1.18(0.09)	0.03(0.03)	0.31(0.1)	1.84(0.1)
Scaillet and Evans, 1999	58	4	76.56(1.45)	0.21(0.12)	13.52(0.34)	1.2(0.12)	0.03(0.04)	0.34(0.11)	1.63(0.03)
Scaillet and Evans, 1999	69	7	74.61(0.48)	0.13(0.04)	16.38(0.18)	0.98(0.11)	0.07(0.06)	0.59(0.05)	1.97(0.17)
Sisson et al, 2005	1619	7	74.8(0.5)	0.2(0.1)	13.6(0.2)	1.06(0.12)	0.11(0.07)	0.47(0.22)	1.42(0.17)
Sisson et al, 2005	1652	3	74.7(0.5)	0.06(0.01)	14.1(0.6)	0.99(0.07)	0.07(0.03)	0.32(0.07)	1.34(0.2)
Sisson et al, 2005	1723	30	68.6(0.3)	0.35(0.12)	16.3(0.2)	2.2(0.11)	0.1(0.05)	0.85(0.04)	2.27(0.11)
Tomiya et al, 2010	C08-2	7	77.42()	0.07()	13.75()	1.22()	0.14()	0.16()	1.17()
Toplis et al, 1994	Fe-95	9	62.29(0.73)	2.52(0.17)	11.9(0.17)	9.34(0.32)		1.44(0.06)	5.22(0.26)
Toplis et al, 1994	Fe-96	8	58.71(0.25)	3.09(0.05)	11.49(0.09)	11.4(0.23)		1.87(0.06)	6.34(0.18)
Toplis et al, 1994	Fe-97	13	56.74(0.45)	3.28(0.12)	11.14(0.13)	12.9(0.29)		2.4(0.06)	6.99(0.15)
Toplis et al, 1994	Fe-98	13	48.94(0.62)	4.25(0.19)	9.7(0.08)	16.3(0.51)		3.78(0.08)	9.06(0.21)
Toplis et al, 1994	Fe-99	12	49.7(0.55)	4.21(0.14)	9.97(0.1)	16.1(0.39)		3.58(0.1)	8.79(0.2)
Toplis et al, 1994	Fe-100	9	47.56(0.25)	4.72(0.14)	9.61(0.08)	16.2(0.36)		4.23(0.08)	9.73(0.11)
Toplis et al, 1994	Fe-123	9	65.53(0.39)	2.05(0.1)	11.55(0.18)	7.22(0.26)		1.53(0.07)	5.16(0.14)
Toplis et al, 1994	Fe-124	20	62.01(2.57)	2.33(0.25)	11.31(0.27)	9.17(1.17)		2.45(0.37)	6.18(0.78)
Toplis et al, 1994	Fe-125	11	61.16(0.89)	2.45(0.14)	11.38(0.17)	9.23(0.31)		2.63(0.16)	6.43(0.27)
Toplis et al, 1994	Fe-131	11	56.09(0.41)	2.94(0.16)	11.27(0.12)	15.3(0.38)		2.04(0.05)	6.72(0.16)
Toplis et al, 1994	Fe-132	12	54.61(0.42)	3.26(0.11)	10.93(0.13)	16.4(0.28)		2.26(0.07)	7.2(0.12)
Toplis et al, 1994	Fe-133	11	52.02(0.37)	3.62(0.15)	10.54(0.14)	17.9(0.28)		2.68(0.08)	7.77(0.16)
Toplis et al, 1994	Fe-136	10	53.43(0.45)	3.22(0.12)	10.69(0.14)	17.4(0.66)		2.11(0.07)	6.92(0.17)
Toplis et al, 1995	Fe-21	9	49.01(0.85)	4.55(0.36)	11.59(0.09)	17.4(0.71)		4.23(0.25)	8.72(0.23)
Toplis et al, 1995	Fe-43	16	49.49(0.5)	4.65(0.4)	11.28(0.18)	16.7(0.5)		3.86(0.2)	8.6(0.11)
Toplis et al, 1995	Fe-52	15	64.27(0.4)	2.03(0.11)	12.08(0.12)	9.58(0.3)		1.23(0.09)	1.23(0.02)
Toplis et al, 1995	Fe-95	9	62.79(0.73)	2.52(0.17)	11.9(0.17)	9.34(0.32)		1.44(0.06)	5.22(0.26)

Chemical composition

melt					magnetite									
Na2O	K2O	P2O5	H$_2$O	Tot	n: SiO2	TiO2	Al2O3	MgO	CaO	MnO	FeO	Cr2O3	Tot
4.72(0.2)	1.83(0.1)	0.16(0.12)		100	1 0.94()	11.83()	6.29()	2.86()	0.15()	0.65()	58.94()		82
4.83()	2.09()	0.29()		100	2 1.58(0.16)	18.73(2.45)	3.43(0.98)	1.83(0.34)	0.21(0.03)	0.52(0.11)	64.66(2.62)		91
4.87(0.36)	1.55(0.06)	0.18(0.12)		100	1 0.46()	18.47()	4.21()	2.67()	0.18()	0.75()	73.06()		100
4.05(0.11)	0.27(0.11)	0.09(0.09)		100	2 0.43(0.01)	5.85(0.16)	4.34(0.03)	5.67(0.04)	0.45(0.07)	0.46(0.05)	75.83()		93
4.54(0.57)	0.34(0.21)	0.15(0)		100	3 0.12(0.01)	6.57(0.16)	3.87(0.03)	4.89(0.03)	0.3(0.04)	0.46(0.01)	75.85()		92
5.42(0.22)	0.46(0.01)	0.95(0.14)		100	1 0.14()	3.97()	3.37()	4.29()	0.36()	0.4()	78.51()		91
3.87(0.08)	0.24(0.04)	0.29(0)		100	2 0.39(0.21)	2.2(0.03)	4.56(0.09)	6.14(0.05)	0.29(0.38)	0.72(0.04)	76.46()		91
4.67(0.26)	0.3(0.02)	0.52(0.06)		100	2 2.38(0.61)	2.54(0.06)	4.17(1.07)	5.35(0.05)	0.73(0.47)	0.55(0.02)	77.56()		93
4.94(0.2)	0.34(0.11)	0.42(0.07)		100	3 0.21(0.11)	2.74(0.08)	3.13(0.55)	4.05(0.09)	0.38(0.46)	0.56(0.11)	79.75()		91
5.6(0.92)	0.82(0.02)	0.75(0.11)		100	1 0.97()	3.21()	3.93()	3.33()	0.95()	0.39()	79.59()		92
4.49(0.64)	0.33(0.08)	0.43(0.12)		100	2 0.87(0.32)	2.87(0.07)	4.39(0.25)	5.22(0.02)	0.72(0.16)	0.84(0.06)	77.22()		92
3.63(0.45)	1.96(0.09)	0.55(0.06)	5.70	100	3 0.34(0.03)	3.69(0.06)	5.14(0.06)	4.44(0.15)	0.25(0.09)	0.4()	79.86(0.05)	0.16(	95
2.71(0.17)	5.85(0.09)	0.05(0.00)	1.46	100	3	15.14(0.60)	(0.60)	1.06(0.08)		(0.00)	83.78(3.19)		100
3.10(0.18)	5.69(0.12)	0.07(0.01)	2.03	99	1	27.75()					72.25()		100
3.00()	5.73()	0.04()	1.12	100	1 ()	16.74(0.02)	(0.33)	1.98(0.02)	(0.05)	(0.00)	81.27(0.07)	0.00	100
3.83(0.35)	4.71(0.12)	0.03()		98	1 0.13()	9.37()	1.9()	0.83()	0.05()	1.28()	85.06()		99
4.96(0.13)	3.2(0.05)	0.01()		96	1 0.12()	8.37()	1.92()	2.38()	0.2()	1.67()	85.17()		100
3.93(0.14)	1.61(0.05)			100	4 0.47(0.23)	4.27(0.11)	9.11(0.07)	7.31(0.07)	0.38(0.1)	0.35(0.09)	70.51(0.49)		92
2.94(0.08)	1.33(0.1)			100	3 0.42(0.21)	2.74(0.05)	5.82(0.11)	8.02(0.09)	0.31(0.1)	0.46(0.06)	74.4(0.8)		92
4.01(0.17)	1.45(0.05)			100	5 0.17(0.07)	3.03(0.04)	6.97(0.14)	6.36(0.12)	0.25(0.08)	0.45(0.03)	74.32(0.64)		92
4.16(0.13)	1.96(0.12)			100	2 0.37(0.04)	3.62(0.17)	6.54(0.09)	5.4(0.17)	0.28(0.01)	0.38(0.06)	74.87(0.54)		92
4.33(0.06)	2.21(0.2)			100	2 0.37(0.09)	5.38(0.1)	7.85(0.18)	6.56(0.06)	0.38(0.03)	0.34(0.04)	71.36(0.63)		92
4.38(0.19)	3.34(0.62)			100	1 0.16()	4.43()	6.32()	5.57()	0.26()	0.38()	76.12()		93
5.29(0.34)	0.06(0.03)			99	4 0.72(0.3)	4.03(0.14)	6.19(0.24)	5.23(0.09)	0.47(0.07)	0.36(0.03)	75.67(0.87)		93
3.74(0.23)	0.19(0.02)			100	5 0.57(0.35)	3.5(0.04)	6.61(0.11)	6.4(0.15)	0.44(0.06)	0.36(0.05)	76.19(0.4)		94
4.47()	2.26()			96	6	7.96()	2.07()	1.28()		0.43()	81.44()	0.08(	93
4.42()	2.6()			96	3	8.63()	2.16()	1.41()		0.48()	81.02()	0.12(	94
4.45()	2.42()			95	6	8.53()	2.31()	1.46()		0.42()	80.22()	0.08(	93
4.55()	2.49()			95	6	8.61()	2.32()	1.47()		0.41()	81.35()	0.08(	94
4.6()	1.96()		5.70	94	6	8.16()	2.62()	1.53()		0.37()	80.94()	0.06(	94
4.94()	2.17()		4.70	95	5	6.83()	2.63()	1.62()		0.41()	81.17()	0.09(	93
4.49()	2.12()		0.00	95	4	8.16()	2.62()	1.53()		0.37()	80.94()	0.06(	94
3.63(0.34)	2.96(0.11)	0.15()	4.93	100	3 0.69(0.28)	12.8(0.04)	3.55(0.05)	1.78(0.1)	0.26(0.1)	0.34(0.08)	74.68(0.92)		94
2.8(0.4)	3.32(0.15)		0.00	92	4 0.8(0.5)	13.8(0.4)	3.2(0.3)	1.4(0.1)	0.3(0.1)	0.6(0.1)	72.5(1.8)		93
3.69(0.42)	2.78(0.18)		7.88	100	10	2.116(0.07)	2.33(0.08)	2.17(0.08)		0.57(0.1)	92.80(0.98)		100
3.49(0.3)	2.69(0.12)		7.66	100	5	3.743(0.03)	2.49(0.13)	1.89(0.13)		0.59(0.01)	91.27(1.33)		100
3.76(0.15)	2.75(0.08)		6.52	100	3	4.091(0.23)	2.72(0.2)	1.90(0.08)		0.39(0.05)	90.88(0.97)		100
3.75(0.18)	1.52(0.07)		8.15	100	2	2.428(0.15)	5.62(0.07)	2.15(0.24)		0.45(0.1)	89.34(1.34)		100
3.36(0.22)	4.68(0.17)	0.18(0.07)		100	2 0.6(0.2)	0.2(0.1)	2.7(0.4)	4.1(0.6)		1.9(0.7)	82.3(0.15)	0.2()	92
2.82(0.58)	5.39(0.26)	0.16(0.01)		100	4 0.3(0.2)	0.52(0.05)	6(0.22)	4.3(0.9)		1.7(0.37)	80.7(0.24)	0.07(	94
3.5(0.34)	5.45(0.1)	0.2(0.06)		100	13 0.4(0.2)	2.8(0.1)	4.8(0.1)	3.7(0.1)		0.7(0.02)	82.3(0.1)	0.03(	95
4.07()	1.98()	0.02()		100	3 0.58()	9.86()	3.24()	0.47()	0.06()	1.21()	79.98()		96
3.26(0.26)	1.53(0.07)	0.04(0.04)		98	7 0.11(0.04)	20.69(0.28)	1.88(0.08)	2.36(0.06)	0.16(0.06)		69.81(0.85)		95
2.98(0.6)	1.29(0.05)	0.51(0.16)		98	7 0.09(0.06)	20.64(0.15)	1.91(0.08)	2.46(0.09)	0.13(0.05)		69.3(0.68)		95
2.92(0.46)	1.15(0.08)	0.91(0.09)		98	7 0.12(0.06)	20.38(0.23)	2.07(0.09)	2.71(0.09)	0.25(0.09)		70.03(0.44)		96
2.69(0.14)	0.74(0.05)	2.74(0.17)		98	6 0.16(0.04)	20.42(0.39)	2.25(0.07)	3.09(0.06)	0.37(0.13)		69.04(0.42)		95
2.72(0.07)	0.77(0.04)	2.5(0.18)		98	3 0.07(0.05)	20.97(0.22)	2.18(0)	2.93(0.06)	0.15(0.03)		69.62(0.48)		96
2.45(0.09)	0.65(0.02)	3.41(0.28)		99	8 0.12(0.04)	19.64(0.19)	2.62(0.09)	3.56(0.08)	0.22(0.05)		69.08(0.49)		95
3.38(0.11)	1.56(0.08)	0.81(0.14)		99	8 0.1(0.03)	12.34(0.17)	1.86(0.06)	2.79(0.07)	0.09(0.06)		76.51(0.56)		94
2.96(0.18)	1.24(0.13)	1.23(0.36)		99	8 0.1(0.06)	12.79(0.33)	2.14(0.06)	3.26(0.1)	0.17(0.09)		75.27(0.79)		94
3.01(0.08)	1.2(0.07)	1.34(0.15)		99	8 0.1(0.07)	13.28(0.23)	2.13(0.07)	3.43(0.11)	0.15(0.09)		73.9(0.93)		93
3.17(0.19)	1.23(0.06)	0.05(0.08)		99	5 0.11(0.04)	23.93(0.19)	1.86(0.07)	2.3(0.11)	0.15(0.1)		67.49(0.24)		96
3.31(0.09)	1.14(0.06)	0.39(0.12)		100	8 0.09(0.04)	23.34(0.21)	1.92(0.07)	2.4(0.07)	0.17(0.06)		67.97(0.42)		96
3.03(0.09)	0.97(0.05)	0.75(0.14)		99	7 0.09(0.04)	24.11(0.24)	2.1(0.06)	2.56(0.08)	0.21(0.11)		68.15(0.41)		97
3.31(0.11)	1.18(0.06)	0.06(0.07)		98	8 0.1(0.04)	26.82(0.06)	2.01(0.07)	2.32(0.09)	0.3(0.14)		65.12(0.97)		97
2.95(0.08)	0.83(0.04)			99	11 0.12(0.04)	24.51(0.5)	3.13(0.15)	4.17(0.11)	0.47(0.07)		64.21(0.47)		97
3.03(0.09)	0.78(0.07)			98	12 0.14(0.04)	22.15(0.49)	3.24(0.15)	3.79(0.17)	0.44(0.07)		67.12(0.5)		97
4.31(0.07)	3.55(0.04)			98	14 0.17(0.07)	24.24(0.41)	1.88(0.09)	2.09(0.09)	0.32(0.08)		67.29(0.51)		96
3.26(0.26)	1.53(0.07)			98	7 0.11(0.04)	20.69(0.28)	1.88(0.08)	2.36(0.06)	0.16(0.06)		69.81(0.85)		95

Supplementary Table 8.S.1/3b: Dataset used for the calibration and testing of the FeTiMM oxybarometer.

Ilmenite-saturated experiments taken from the literature.			**Chemical composition** ilmenite								
Reference	Run:	n:	SiO2	TiO2	Al2O3	MgO	CaO	MnO	FeO	Cr2O3	Tot
Andujar et al, 2016	usc28	3	0.14(0.05)	49.84(0.14)	0.29(0.05)	3.65(0.1)	0.25(0.1)	0.48(0.09)	45.04(0.77)		100
Andujar et al, 2016	usc29	1	0.85(0.43)	48.83(0.35)	0.37(0.18)	3.02(0.08)	0.3(0.02)	0.59(0.13)	46.63(0.83)		101
Andujar et al, 2016	usc87	2	0.34(0.12)	46.4(0.02)	0.24(0.06)	3.19(0.13)	0.27(0.02)	0.57(0.27)	41.94(0.02)		93
Berndt et al, 2005	96	1	0.69()	22.51()	1.32()	3.67()	0.48()	0.25()	61.97()		91
Berndt et al, 2005	98	1	0.48()	24.9()	1.08()	3.33()	0.52()	0.22()	61.84()		92
Berndt et al, 2005	102	2	0.13()	20.92()	1.59()	2.79()	0.73()	0.2()	67.01()		94
Berndt et al, 2005	103	2	0.14()	14.72()	1.27()	2.44()	0.3()	0.14()	70.54()		90
Berndt et al, 2005	104	2	0.17()	17.31()	1.1()	2.79()	0.39()	0.23()	66.72()		89
Berndt et al, 2005	105	2	0.42()	17.81()	1.82()	3.06()	1.42()	0.17()	67.35()		92
Berndt et al, 2005	106	2	0.34()	18.59()	2.31()	2.78()	1.22()	0.17()	65.70()		91
Berndt et al, 2005	111	2	0.86()	18.62()	1.14()	3.25()	0.69()	0.35()	66.32()		91
Blatter et al, 2013	2370	6	0.18(0.07)	20.5(0.05)	1.35(0.01)	2.32(0.04)	0.25(0.09)	0.12(0.01)	68.09(0.1)	0.09	93
Bolte et al, 2015	A18	1		45.87()					54.12()		100
Bolte et al, 2015	F09	1		46.34()		1.119()			52.53()		100
Bolte et al, 2015	M14	1		48.74()		4.769()	0.621()		45.86()		100
Brugger and Hammer, 2010	11-1	1	0.06()	42.64()	0.16()	1.64()	0.05()	1.97()	46.27()		93
Brugger and Hammer, 2010	16-2	1	0.06()	44.87()	0.16()	4.32()	0.03()	2.48()	43.63()		96
Freise et al, 2009	50	4	0.12(0.04)	22.85(0.25)	1.91(0.08)	3.74(0.09)	0.29(0.06)	0.1(0.05)	62.53(0.5)		92
Freise et al, 2009	51	5	0.12(0.04)	18.27(0.16)	1.4(0.03)	3.8(0.09)	0.27(0.06)	0.16(0.05)	66.17(0.63)		90
Freise et al, 2009	52	5	0.09(0.07)	19.16(0.19)	1.66(0.18)	3(0.11)	0.31(0.04)	0.15(0.05)	65.56(0.61)		90
Freise et al, 2009	53	3	0.62(0.44)	20.82(0.39)	1.63(0.05)	2.93(0.06)	0.41(0.04)	0.15(0.05)	65.24(0.48)		92
Freise et al, 2009	57	3	0.3(0.34)	25.35(0.42)	1.71(0.16)	3.87(0.33)	0.38(0.13)	0.14(0.12)	60.01(0.55)		92
Freise et al, 2009	58	1	0.69()	23.2()	1.62()	3.29()	0.52()	0.15()	62.72()		92
Freise et al, 2009	110	4	0.17(0.12)	22.66(0.24)	1.48(0.08)	2.85(0.05)	0.4(0.04)	0.11(0.03)	65.41(0.87)		93
Freise et al, 2009	114	3	0.32(0.35)	20.45(0.95)	1.83(0.23)	3.24(0.07)	0.39(0.04)	0.14(0.02)	67.23(0.48)		94
Gardner et al, 1995	G-8a-M	5		43.25()	0.21()	2.41()		0.63()	49.31()	0.04	96
Gardner et al, 1995	G-8b-M	5		43.43()	0.2()	2.48()		0.6()	49.71()	0.02	96
Gardner et al, 1995	G-10a-M	9		43.04()	0.25()	2.61()		0.59()	49.15()	0.02	96
Gardner et al, 1995	G-10b-M	5		42.91()	0.24()	2.54()		0.58()	49.42()	0.04	96
Gardner et al, 1995	G-15a-M	3		41.76()	0.31()	2.51()		0.52()	50.44()	0.03	96
Gardner et al, 1995	G-16a-M	4		41.91()	0.27()	3.01()		0.57()	49.45()	0.03	95
Gardner et al, 1995	G-16b-M	5		41.76()	0.31()	2.51()		0.52()	50.44()	0.03	96
Parat et al, 2008	2	2	0.53(0.28)	47.18(0.04)	0.46(0.05)	3.03(0.1)	(0.1)	0.46(0.08)	46.82(0.92)		98
Pietranik et al, 2009	800/1/2	2	1.3(1.5)	48.9(0.5)	0.5(0.3)	2.3(0.4)	0.3(0.1)	0.7(0.2)	44.7(1)		99
Scaillet and Evans, 1999	8	7		19.76(0.7)	0.751(0.12)	1.229(0.26)		0.206(0.04)	78.04(2.69)		100
Scaillet and Evans, 1999	51	1		24.91()	0.615()	1.491()		0.345()	72.62()		100
Scaillet and Evans, 1999	58	1		26.73()	0.652()	1.408()		0.186()	71.01()		100
Scaillet and Evans, 1999	69	3		22.79(0.2)	1.123(0.01)	1.231(0.08)		0.140(0.12)	74.71(2.45)		100
Sisson et al, 2005	1619	9	0.4(0.2)	10.7(0.1)	1.2(0.4)	1.8(0.6)		0.7(0.7)	76.3(0.15)	0.2	92
Sisson et al, 2005	1652	5	0.3(0.3)	14.9(0.42)	1.2(0.6)	2(0.5)		0.54(0.12)	72.4(0.35)	0.03	92
Sisson et al, 2005	1723	18	0.3(0.2)	19.3(0.3)	1.3(0)	1.8(0)		0.22(0.02)	69.7(0.9)	0.02	93
Tomiya et al, 2010	C08-2	3	0.1()	49.45()	0.14()	0.93()	0.04()	2.24()	46.44()		99
Toplis et al, 1994	Fe-95	9	0.05(0.03)	47.28(0.57)	0.29(0.04)	2.96(0.12)	0.24(0.08)		46.29(0.38)		97
Toplis et al, 1994	Fe-96	7	0.08(0.09)	47.75(0.58)	0.31(0.05)	3.04(0.05)	0.26(0.1)		46.22(0.56)		98
Toplis et al, 1994	Fe-97	8	0.03(0.03)	47.35(0.37)	0.32(0.05)	3.34(0.09)	0.25(0.06)		46.79(0.43)		98
Toplis et al, 1994	Fe-98	6	0.03(0.03)	49.12(0.23)	0.35(0.03)	3.88(0.12)	0.2(0.05)		46.42(0.57)		100
Toplis et al, 1994	Fe-99	3	0.04(0.04)	48(0.48)	0.31(0.07)	3.8(0.02)	0.23(0.12)		45.9(0.79)		98
Toplis et al, 1994	Fe-100	7	0.02(0.02)	49.1(0.09)	0.33(0.03)	4.35(0.08)	0.17(0.08)		44.51(0.27)		99
Toplis et al, 1994	Fe-123	3	0.08(0.03)	32.2(0.45)	0.43(0.04)	2.31(0.02)	0.19(0.04)		58.17(0.77)		93
Toplis et al, 1994	Fe-124	1	0()	33.24()	0.52()	2.62()	0.19()		57.39()		94
Toplis et al, 1994	Fe-125	6	0.07(0.09)	33.71(0.39)	0.55(0.05)	2.74(0.07)	0.2(0.07)		56.11(0.32)		93
Toplis et al, 1994	Fe-131	5	0.07(0.04)	49.43(0.44)	0.25(0.04)	2.91(0.09)	0.2(0.05)		45.82(0.72)		99
Toplis et al, 1994	Fe-132	6	0.08(0.13)	47.15(0.7)	0.25(0.05)	2.99(0.1)	0.23(0.05)		45.48(0.44)		96
Toplis et al, 1994	Fe-133	6	0.06(0.02)	49.25(0.32)	0.27(0.04)	3.08(0.04)	0.23(0.03)		45.04(0.37)		98
Toplis et al, 1994	Fe-136	8	0.06(0.09)	50.71(0.47)	0.2(0.03)	2.76(0.06)	0.22(0.05)		44.85(0.7)		99
Toplis et al, 1995	Fe-21	5	0.02(0.02)	49.01(0.38)	0.46(0.05)	5.39(0.14)	0.57(0.08)		42.31(0.59)		98
Toplis et al, 1995	Fe-43	5	0.04(0.03)	48.83(0.45)	0.47(0.06)	5.08(0.12)	0.35(0.05)		42.95(0.52)		98
Toplis et al, 1995	Fe-52	5	0.02(0.01)	47.9(0.54)	0.43(0.07)	2.51(0.08)	0.3(0.05)		46.2(0.35)		97
Toplis et al, 1995	Fe-95	9	0.05(0.03)	47.28(0.57)	0.29(0.04)	2.96(0.12)	0.24(0.08)		46.29(0.38)		97

| | | | | | **Experimental conditions** | | | | | | | **Calculated values** | | | | | | | **Errors** | | |

Experimental conditions					Calculated values							Errors		
													FeTiMM error	
	10000_	p	dFMQ	dFMQ	AMC	DFemgt-	DTimgt-	DFe/DTim			Mn/	Propag.	"model"	Propag.
T	T	(bar)	experim.	mgt-ilm	NK	melt	melt	gt/melt	log D	FeTiMM	Mg	anal. err.	err.	total err.
1000	7.85	2000	0.42	0.06	0.70	7.78	12.59	0.62	-0.21	-0.04	3.61	0.21	0.33	0.29
1000	7.85	2000	0.14	0.17	0.69	9.37	22.57	0.42	-0.38	-0.74	1.50	0.24	0.34	0.33
925	8.35	4000	0.44	-0.19	0.68	10.84	21.99	0.49	-0.31	-0.44	3.05	0.19	0.32	0.29
1050	7.56	2040	3.48	3.81	0.59	13.21	4.92	2.69	0.43	2.72	1.31	0.50	0.43	0.56
1050	7.56	2040	3.33	3.36	0.60	13.64	7.30	1.87	0.27	2.00	3.33	0.52	0.42	0.57
1000	7.85	2040	4.08	3.84	0.68	14.46	3.78	3.82	0.58	3.11	1.98	0.19	0.44	0.33
950	8.18	2010	4.28	4.87	0.71	19.51	2.68	7.27	0.86	4.09	1.53	0.48	0.50	0.58
950	8.18	2010	4.28	4.30	0.69	18.87	3.02	6.24	0.80	3.93	2.66	0.20	0.47	0.38
950	8.18	2010	4.28	4.16	0.76	21.56	3.51	6.14	0.79	3.64	1.60	0.22	0.46	0.36
950	8.18	2010	4.28	4.06	0.63	21.51	4.94	4.36	0.64	3.50	2.83	0.26	0.46	0.40
950	8.18	2030	4.28	4.19	0.71	18.30	3.15	5.80	0.76	3.73	1.55	0.34	0.47	0.46
950	8.18	7000	3.75	3.96	0.81	22.54	5.05	4.46	0.65	3.00	1.57	0.23	0.44	0.33
825	9.11	2000	-0.64	0.94	1.01	62.71	61.68	1.02	0.01	0.72	0.00	0.17	0.37	0.23
900	8.52	5000	-1.60	0.35	0.99	32.10	86.68	0.37	-0.43	-0.57	####	0.22	0.36	0.28
875	8.71	2000	-0.90	0.26	1.01	55.58	53.54	1.04	0.02	0.74	0.00	0.00	0.35	0.15
880	8.67	50	1.46	1.21	0.94	70.88	26.03	2.72	0.44	2.05	1.54	0.30	0.37	0.35
881	8.66	680	1.46	1.25	0.96	62.17	20.41	3.05	0.48	2.17	2.49	0.28	0.38	0.34
1050	7.56	5000	2.69	3.99	0.55	11.71	2.26	5.18	0.71	4.17	1.07	0.10	0.45	0.38
1000	7.85	5000	4.00	4.51	0.54	12.98	1.76	7.39	0.87	4.97	1.51	0.09	0.48	0.44
1000	7.85	5000	3.51	4.31	0.61	14.78	2.46	6.00	0.78	4.21	2.02	0.15	0.48	0.38
1000	7.85	5000	2.58	4.04	0.70	16.38	3.48	4.71	0.67	3.39	1.07	0.12	0.45	0.30
1050	7.56	5000	1.62	3.48	0.59	12.35	3.32	3.72	0.57	3.35	1.25	0.12	0.42	0.32
1000	7.85	5000	2.19	3.60	0.75	19.42	4.26	4.56	0.66	3.18	2.16	0.21	0.43	0.34
1000	7.85	5000	3.13	3.72	0.89	47.29	5.17	9.15	0.96	3.80	1.45	0.33	0.43	0.43
1040	7.62	5000	3.17	4.21	0.55	11.63	2.15	5.42	0.73	4.26	1.91	0.11	0.47	0.39
825	9.11	1500	1.37	1.43	0.99	74.04	37.90	1.95	0.29	1.55	2.02	0.00	0.38	0.17
875	8.71	1500	1.57	1.41	0.94	65.87	31.96	2.06	0.31	1.67	2.61	0.00	0.38	0.17
825	9.11	1500	1.61	1.42	0.98	61.24	30.46	2.01	0.30	1.60	1.87	0.00	0.38	0.17
875	8.71	1500	1.64	1.44	0.94	55.34	30.75	1.80	0.26	1.50	3.90	0.00	0.39	0.17
825	9.11	2500	1.85	1.60	0.95	39.29	29.14	1.35	0.13	1.10	2.10	0.00	0.39	0.16
825	9.11	2500	1.49	1.67	0.92	50.73	25.30	2.01	0.30	1.66	2.08	0.00	0.40	0.17
875	8.71	2500	1.49	1.60	0.95	46.25	26.32	1.76	0.24	1.45	1.69	0.00	0.39	0.17
900	8.52	3980	1.57	0.59	0.96	23.05	22.46	1.03	0.01	0.74	2.13	0.15	0.37	0.22
800	9.32	2000	0.66	-0.56	1.10	48.33	69.00	0.70	-0.15	0.26	####	0.24	0.30	0.28
785	9.45	2212	3.36	3.58	1.06	89.23	12.45	7.17	0.86	3.07	1.44	0.40	0.43	0.46
781	9.49	2237	2.93	2.87	1.15	77.35	16.28	4.75	0.68	2.43	3.23	0.22	0.41	0.29
781	9.49	2237	2.83	2.53	1.04	75.73	19.48	3.89	0.59	2.35	2.37	0.71	0.41	0.74
780	9.50	3890	3.29	3.44	1.27	91.17	18.68	4.88	0.69	2.29	1.76	0.34	0.42	0.39
825	9.11	7000	4.66	3.96	0.95	77.64	1.00	77.64	1.89	6.48	1.98	0.95	0.45	1.04
825	9.11	7000	4.36	4.06	1.03	81.52	8.67	9.41	0.97	3.47	1.81	0.29	0.46	0.38
925	8.35	7000	4.06	3.96	0.91	37.41	8.00	4.68	0.67	2.83	1.61	0.48	0.44	0.53
750	9.77	1960	0.66	-0.37	1.21	65.56	140.86	0.47	-0.33	-0.16	2.94	0.00	0.31	0.15
1072	7.43	1	0.89	0.23	0.59	7.47	8.21	0.91	-0.04	0.63	####	0.15	0.35	0.26
1072	7.43	1	0.89	0.16	0.51	6.08	6.68	0.91	-0.04	0.65	####	0.06	0.34	0.23
1072	7.43	1	0.89	0.42	0.45	5.43	6.21	0.87	-0.06	0.57	####	0.11	0.36	0.27
1072	7.43	1	0.89	0.22	0.31	4.24	4.80	0.88	-0.05	0.62	####	0.18	0.34	0.36
1072	7.43	1	0.89	0.29	0.33	4.32	4.98	0.87	-0.06	0.57	####	0.13	0.36	0.33
1072	7.43	1	0.89	0.04	0.29	4.26	4.16	1.02	0.01	1.10	####	0.12	0.33	0.34
1072	7.43	1	1.87	2.01	0.56	10.60	6.02	1.76	0.25	1.96	####	0.13	0.41	0.26
1072	7.43	1	1.87	1.89	0.48	8.21	5.49	1.50	0.17	1.78	####	0.38	0.40	0.45
1072	7.43	1	1.87	1.83	0.46	8.01	5.42	1.48	0.17	1.78	####	0.16	0.40	0.30
1072	7.43	1	-0.14	-0.37	0.47	4.41	8.14	0.54	-0.27	-0.52	####	0.14	0.31	0.32
1072	7.43	1	-0.14	0.13	0.43	4.14	7.16	0.58	-0.24	-0.43	####	0.10	0.33	0.32
1072	7.43	1	-0.14	-0.44	0.39	3.81	6.66	0.57	-0.24	-0.52	####	0.12	0.31	0.35
1072	7.43	1	-0.74	-1.19	0.43	3.74	8.33	0.45	-0.35	-1.04	####	0.13	0.30	0.37
1095	7.31	1	-0.27	0.02	0.36	3.68	5.39	0.68	-0.17	-0.09	####	0.25	0.32	0.41
1096	7.30	1	-0.02	0.04	0.36	4.01	4.76	0.84	-0.07	0.49	####	0.26	0.33	0.39
1057	7.52	1	-0.06	-0.05	0.74	7.02	11.94	0.59	-0.23	-0.10	####	0.11	0.32	0.22
1072	7.43	1	0.89	0.23	0.59	7.47	8.21	0.91	-0.04	0.63	####	0.15	0.35	0.26

Table 8.S2 List of experimental studies that were screened for the five criteria discussed in the text. The number of experiments in each study is given in parenthesis

#	Full reference	number of experiments listed
1	Almeev, R.R., Bolte, T., Nash, B.P., Holtz, F., Erdmann, M., Cathey, H.E. (2012) High-temperature, low-H2O Silicic Magmas of the Yellowstone Hotspot: an Experimental Study of Rhyolite from the Bruneau-Jarbidge Eruptive Center, Central Snake River Plain, USA. *Journal of Petrology* 53, 1837-1866.	73
2	Andújar, J., Scaillet, B., Pichavant, M., Druitt, T.H. (2017) Generation Conditions of Dacite and Rhyodacite via the Crystallization of an Andesitic Magma. Implications for the Plumbing System at Santorini (Greece) and the Origin of Tholeiitic or Calc-alkaline Differentiation Trends in Arc Magmas. *Journal of Petrology* 57, 1887-1920.	90
3	Barclay, J., Carmichael, I. (2004) A hornblende basalt from western Mexico: water-saturated phase relations constrain a pressure–temperature window of eruptibility. *Journal of Petrology* 45, 485-506.	26
4	Berndt, J. (2004) An Experimental Investigation of the Influence of Water and Oxygen Fugacity on Differentiation of MORB at 200 MPa. *Journal of Petrology* 46, 135-167.	63
5	Blatter, D.L., Sisson, T.W., Hankins, W.B. (2013) Crystallization of oxidized, moderately hydrous arc basalt at mid- to lower-crustal pressures: implications for andesite genesis. *Contributions to Mineralogy and Petrology* 166, 861-886.	25
6	Bogaerts, M., Scaillet, B., Auwera, J.V. (2006) Phase Equilibria of the Lyngdal Granodiorite (Norway): Implications for the Origin of Metaluminous Ferroan Granitoids. *Journal of Petrology* 47, 2405-2431.	92
7	Bolte, T., Holtz, F., Almeev, R., Nash, B. (2015) The Blacktail Creek Tuff: an analytical and experimental study of rhyolites from the Heise volcanic field, Yellowstone hotspot system. *Contributions to Mineralogy and Petrology* 169, 15.	42
8	Botcharnikov, R.E., Almeev, R.R., Koepke, J., Holtz, F. (2008) Phase Relations and Liquid Lines of Descent in Hydrous Ferrobasalt--Implications for the Skaergaard Intrusion and Columbia River Flood Basalts. *Journal of Petrology* 49, 1687-1727.	87
9	Brugger, C.R., Hammer, J.E. (2010) Crystallization Kinetics in Continuous Decompression Experiments: Implications for Interpreting Natural Magma Ascent Processes. *Journal of Petrology* 51, 1941-1965.	45
10	Cadoux, A., Scaillet, B., Druitt, T.H., Deloule, E. (2014) Magma Storage Conditions of Large Plinian Eruptions of Santorini Volcano (Greece). *Journal of Petrology* 55, 1129-1171.	91
11	Carroll, M.R., Rutherford, M.J. (1987) The stability of igneous anhydrite: experimental results and implications for sulfur behavior in the 1982 El Chichon trachyandesite and other evolved magmas. *Journal of Petrology* 28, 781-801.	37
12	Di Carlo, I., Rotolo, S.G., Scaillet, B., Buccheri, V., Pichavant, M. (2010) Phase Equilibrium Constraints on Pre-eruptive Conditions of Recent Felsic Explosive Volcanism at Pantelleria Island, Italy. *Journal of Petrology* 51, 2245-2276.	62
13	Erdmann, S., Martel, C., Pichavant, M., Bourdier, J.L., Champallier, R., Komorowski, J.C., Cholik, N. (2016) Constraints from Phase Equilibrium	49

Experiments on Pre-eruptive Storage Conditions in Mixed Magma Systems: a Case Study on Crystal-rich Basaltic Andesites from Mount Merapi, Indonesia. *Journal of Petrology* 57, 535-560.

14 Feig, S.T., Koepke, J., Snow, J.E. (2010) Effect of oxygen fugacity and water on phase equilibria of a hydrous tholeiitic basalt. *Contributions to Mineralogy and Petrology* 160, 551-568.   92

15 Freise, M., Holtz, F., Nowak, M., Scoates, J.S., Strauss, H. (2009) Differentiation and crystallization conditions of basalts from the Kerguelen large igneous province: an experimental study. *Contributions to Mineralogy and Petrology* 158, 505.   94

16 Gardner, J., Rutherford, M., Carey, S., Sigurdsson, H. (1995) Experimental constraints on pre-eruptive water contents and changing magma storage prior to explosive eruptions of Mount St Helens volcano. *Bulletin of Volcanology* 57, 1-17.   22

17 Grove, T.L., Elkins-Tanton, L.T., Parman, S.W., Chatterjee, N., Müntener, O., Gaetani, G.A. (2003) Fractional crystallization and mantle-melting controls on calc-alkaline differentiation trends. *Contributions to Mineralogy and Petrology* 145, 515-533.   26

18 Hamada, M., Fujii, T. (2007) Experimental constraints on the effects of pressure and H_2O on the fractional crystallization of high-Mg island arc basalt. *Contributions to Mineralogy and Petrology* 155, 767-790.   79

19 Krawczynski, M.J., Grove, T.L., Behrens, H. (2012) Amphibole stability in primitive arc magmas: effects of temperature, H_2O content, and oxygen fugacity. *Contributions to Mineralogy and Petrology* 164, 317-339.   25

20 Martel, C., Pichavant, M., Holtz, F., Scaillet, B., Bourdier, J.L., Traineau, H. (1999) Effects of $f O_2$ and H_2O on andesite phase relations between 2 and 4 kbar. Journal of Geophysical Research: *Solid Earth* 104, 29453-29470.   85

21 Mercer, C.N., Johnston, A.D. (2007) Experimental studies of the P–T–H_2O near-liquidus phase relations of basaltic andesite from North Sister Volcano, High Oregon Cascades: constraints on lower-crustal mineral assemblages. *Contributions to Mineralogy and Petrology* 155, 571-592.   50

22 Moore, G., Carmichael, I. (1998) The hydrous phase equilibria (to 3 kbar) of an andesite and basaltic andesite from western Mexico: constraints on water content and conditions of phenocryst growth. *Contributions to Mineralogy and Petrology* 130, 304-319.   48

23 Nandedkar, R.H., Ulmer, P., Müntener, O. (2014) Fractional crystallization of primitive, hydrous arc magmas: an experimental study at 0.7 GPa. *Contributions to Mineralogy and Petrology* 167, 1015.   17

24 Parat, F., Holtz, F., Feig, S. (2008) Pre-eruptive Conditions of the Huerto Andesite (Fish Canyon System, San Juan Volcanic Field, Colorado): Influence of Volatiles (C-O-H-S) on Phase Equilibria and Mineral Composition. *Journal of Petrology* 49, 911-935.   32

25 Parat, F., Streck, M.J., Holtz, F., Almeev, R. (2014) Experimental study into the petrogenesis of crystal-rich basaltic to andesitic magmas at Arenal volcano. *Contributions to Mineralogy and Petrology* 168.   20

26 Pichavant, M., Macdonald, R. (2007) Crystallization of primitive basaltic magmas at crustal pressures and genesis of the calc-alkaline igneous suite: experimental evidence from St Vincent, Lesser Antilles arc. *Contributions to Mineralogy and Petrology* 154, 535-558.   21

27	Pietranik, A., Holtz, F., Koepke, J., Puziewicz, J. (2009) Crystallization of quartz dioritic magmas at 2 and 1 kbar: experimental results. *Mineralogy and Petrology* 97, 1.	22
28	Prouteau, G., Scaillet, B. (2003) Experimental constraints on the origin of the 1991 Pinatubo dacite. *Journal of Petrology* 44, 2203-2241.	31
29	Scaillet, B., Evans, B.W. (1999) The 15 June 1991 eruption of Mount Pinatubo. I. Phase equilibria and pre-eruption P–T–fO2–fH2O conditions of the dacite magma. *Journal of Petrology* 40, 381-411.	57
30	Sisson, T.W., Ratajeski, K., Hankins, W.B., Glazner, A.F. (2004) Voluminous granitic magmas from common basaltic sources. *Contributions to Mineralogy and Petrology* 148, 635-661.	49
31	Tomiya, A., Takahashi, E., Furukawa, N., Suzuki, T. (2010) Depth and Evolution of a Silicic Magma Chamber: Melting Experiments on a Low-K Rhyolite from Usu Volcano, Japan. *Journal of Petrology* 51, 1333-1354.	20
32	Toplis, M., Carroll, M. (1995) An experimental study of the influence of oxygen fugacity on Fe-Ti oxide stability, phase relations, and mineral—melt equilibria in ferro-basaltic systems. *Journal of Petrology* 36, 1137-1170.	12
33	Toplis, M.J., Dingwell, D.B., Libourel, G. (1994) The effect of phosphorus on the iron redox ratio, viscosity, and density of an evolved ferro-basalt. *Contributions to Mineralogy and Petrology* 117, 293-304.	42

<div align="right">total number of experiments   1626</div>

Supplementary Information References

Bacon, C.R., Hirschmann, M.M. (1988) Mg/Mn partitioning as a test for equilibrium between coexisting Fe-Ti oxides. *American Mineralogist* 73, 57-61.

Arató, R., Audétat, A. (2017) Experimental calibration of a new oxybarometer for silicic magmas based on vanadium partitioning between magnetite and silicate melt. *Geochimica et Cosmochimica Acta* 209, 284-295.

Ghiorso, M.S., Evans, B.W. (2008) Thermodynamics of rhombohedral oxide solid solutions and a revision of the Fe-Ti two-oxide geothermometer and oxygen-barometer. *American Journal of Science* 308, 957-1039.

ACKNOWLEDGMENTS

(Eidesstattliche) Versicherungen und Erklärungen

(§ 9 Satz 2 Nr. 3 PromO BayNAT)

Hiermit versichere ich eidesstattlich, dass ich die Arbeit selbständig verfasst und keine anderen als die von mir angegebenen Quellen und Hilfsmittel benutzt habe (vgl. Art. 64 Abs. 1 Satz 6 BayHSchG).

(§ 9 Satz 2 Nr. 3 PromO BayNAT)

Hiermit erkläre ich, dass ich die Dissertation nicht bereits zur Erlangung eines akademischen Grades eingereicht habe und dass ich nicht bereits diese oder eine gleichartige Doktorprüfung endgültig nicht bestanden habe.

(§ 9 Satz 2 Nr. 4 PromO BayNAT)

Hiermit erkläre ich, dass ich Hilfe von gewerblichen Promotionsberatern bzw. -vermittlern oder ähnlichen Dienstleistern weder bisher in Anspruch genommen habe noch künftig in Anspruch nehmen werde.

(§ 9 Satz 2 Nr. 7 PromO BayNAT)

Hiermit erkläre ich mein Einverständnis, dass die elektronische Fassung meiner Dissertation unter Wahrung meiner Urheberrechte und des Datenschutzes einer gesonderten Überprüfung unterzogen werden kann.

(§ 9 Satz 2 Nr. 8 PromO BayNAT)

Hiermit erkläre ich mein Einverständnis, dass bei Verdacht wissenschaftlichen Fehlverhaltens Ermittlungen durch universitätsinterne Organe der wissenschaftlichen Selbstkontrolle stattfinden können.

………………………………………………………………………………………….
Ort, Datum, Unterschrift